

**Manipulation of the motion of polyatomic molecules by AC and DC Stark deceleration**

by

OMID NOURBAKHSH

A THESIS SUBMITTED IN PARTIAL FULFILLMENT OF

THE REQUIREMENTS FOR THE DEGREE OF

DOCTOR OF PHILOSOPHY

in

THE FACULTY OF GRADUATE AND POSTDOCTORAL STUDIES

(Physics)

THE UNIVERSITY OF BRITISH COLUMBIA

(Vancouver)

August 2015

© Omid Nourbakhsh, 2015

## Abstract

A conventional DC Stark decelerator, consisting of 180 stages, was constructed and tested. The experimental setup was characterized using ammonia ( $NH_3$ ) as the reference molecule. Resonance Enhanced Multi-Photon Ionization method (REMPI) was used to detect the ammonia molecules. Deceleration of ammonia molecules was observed and improved by optimizing the design and simulations. Bunching of the molecules with the decelerator electrodes was implemented to improve the signal. The design was optimized by removing the hexapole which was between the nozzle and the decelerator, and also by reducing the distance between the detection point and the decelerator. Finally, deceleration of ammonia molecules from 425  $m/s$  to 27.9  $m/s$  ( $\sim 1.5 K$ ) was demonstrated.

Sulphur deuteride ( $SD$  radical) as a new sample was decelerated. Laser Induced Fluorescence (LIF) of the excited  $SD$  radicals was collected as the detection method. Deceleration of  $SD$  radicals in the  $|X^2\Pi_{3/2}, \nu = 0, J = 3/2, M_J = -3/2\rangle$  energy state from 440  $m/s$  to 301  $m/s$ , and deceleration of  $SD$  radicals in the  $|X^2\Pi_{3/2}, \nu = 0, J = 5/2, M_J = -5/2\rangle$  energy state from 440  $m/s$  to 415  $m/s$  was obtained. A deceleration scheme was presented to obtain separate and pure decelerated packets of  $SD$  radicals in  $J = 3/2$  and  $J = 5/2$ .

The Cavity Enhanced Laser Induced Fluorescence (CELIF) method for measuring the absolute density of the Stark decelerated molecular packets was explained, and the first steps toward its implementation were taken.

In parallel with the DC Stark decelerator a prototype superconducting microwave cavity was designed, constructed, and characterized to be used for future AC Stark deceleration experiments. An electrochemical plating method was used to coat the copper microwave cavity with a lead-tin (Pb-Sn) alloy. An unloaded quality factor of  $10^6$  was obtained for the superconducting cavity. The possibility of deceleration with the superconducting cavity is discussed.

## Preface

This dissertation is based on the simulation, experiment, and data obtained from DC and superconducting AC Stark decelerators, which were constructed at UBC and tested.

I have performed all the experiments, simulations, and data analyses for our DC Stark decelerator under the supervision of my supervisor, T. Momose, which are presented in chapters 2, 4, 5, and 6. The phase-space and non-adiabatic transition analyses presented in chapter 4 are based on the method described respectively by S.Y. T. Van De Meerakker and T. Wall, but I have applied all the presented analyses to our experimental conditions to specifically calculate them for our experimental setup. In chapter 3, the Cavity Enhanced Laser Induced Fluorescence (CELIF) detection scheme for SD radicals was designed in collaboration with D. Carty and E. Werde, and P. Djuricanin. Chapter 5 describes the experimental setup for the DC Stark decelerator. The design of the DC Stark decelerator setup was borrowed from the pioneers of the field at the Fritz Haber Institute in Berlin, Germany. The setup was later modified collaboratively by me, T. Momose, P. Djuricanin, M. Michan, and the electronic and mechanical shops of the Chemistry Department at UBC. T. Mittertreiner developed most of the LabView data acquisition code for the experiment and I modified it. C. Yearwood, B. Kahlon, and K. Enomoto helped me in mechanical polishing of the electrodes for the decelerator.

I performed all the theoretical calculations, analyses, and experiments for the deceleration of SD radical by DC the Stark decelerator. The corresponding experimental results are presented in chapter 6. We have also submitted a manuscript to Molecular Physics including the results for the state purified deceleration of SD radicals. Regarding the CELIF experimental results, we are preparing another manuscript to be submitted to a peer reviewed journal.

The prototype superconducting AC Stark decelerator was designed by K. Enomoto, T. Momose, P. Djuricanin, and W. Hardy. The experiments and data analysis for this experiment were done by me, K. Enomoto, P. Djuricanin, and I. Gerhardt. The results of this experiment are presented in chapter 6. Most of the results of this experiment are contained in the following paper: K. Enomoto, P. Djuricanin, O. Nourbakhsh, I. Gerhardt, Y. Moriwaki, W. Hardy, T. Momose, *Appl. Phys. B* (2012) 109:149–157.

## Table of contents

Abstract.....	ii
Preface.....	iii
Table of contents .....	iv
List of tables.....	vii
List of figures.....	viii
Glossary .....	xv
Acknowledgements .....	xvi
Dedication .....	xvii
<b>Chapter 1: Introduction.....</b>	<b>1</b>
1.1 Cold molecules.....	1
1.1.1 Methods of production of cold molecules.....	3
1.1.1.1 Photo-association .....	4
1.1.1.2 Buffer-gas cooling.....	4
1.1.1.3 Counter-rotating nozzle.....	5
1.1.1.4 Laser cooling.....	5
1.1.1.5 Evaporative cooling .....	6
1.1.1.6 Stark and Zeeman deceleration of a molecular beam .....	6
1.2 Supersonic expansion.....	8
1.3 About the SD radical.....	17
<b>Chapter 2: Stark effect in polar molecules.....</b>	<b>19</b>
2.1 DC Stark effect of molecules .....	19
2.1.1 Symmetric top molecules.....	20
2.1.1.1 Stark effect in symmetric tops .....	21
2.1.1.2 Ammonia molecule .....	23
2.1.1.3 The electronic ground state of ammonia ( $X$ ).....	23
2.1.1.4 The $\tilde{B}$ electronic state of ammonia .....	25
2.1.1.5 Stark effect of ammonia ( $NH_3$ ).....	26
2.1.2 Asymmetric top molecules.....	27
2.1.3 Linear molecules .....	31
2.1.3.1 Hund's case (a).....	32
2.1.3.2 Hund's case (b) .....	33
2.1.3.3 Energy level structure of the SD radical in the electronic ground state .....	34
2.1.3.4 Energy level structure of the SD radical in the first electronic excited state.....	37
2.1.3.5 The Stark effect of the SD radical.....	39

2.2	AC Stark effect of molecules .....	42
<b>Chapter 3: Detection methods .....</b>		<b>46</b>
3.1	Laser Induced Fluorescence (LIF) of <i>SD</i> radical .....	46
3.2	Resonance Enhanced Multi-Photon Ionization (REMPI) of <i>SD</i> radical .....	48
3.3	Cavity Enhanced Laser Induced Fluorescence of <i>SD</i> radical (CELIF).....	49
3.4	Resonance Enhanced Multi-Photon Ionization (REMPI) of ammonia.....	51
<b>Chapter 4: Stark deceleration principle .....</b>		<b>54</b>
4.1	Phase stability diagrams .....	56
4.1.1	Longitudinal phase stability .....	57
4.1.2	Transverse stability .....	60
4.2	Non-adiabatic transitions in a Stark decelerator .....	64
4.3	The principle of microwave Stark deceleration and lens effect .....	66
4.3.1	Superconducting microwave cavity for AC Stark decelerator and lens.....	70
4.3.2	Quality factor of a cylindrical microwave cavity.....	72
<b>Chapter 5: Experimental setup .....</b>		<b>75</b>
5.1	The UBC DC Stark decelerator .....	75
5.1.1	Conditioning .....	76
5.1.2	Complete setup.....	78
5.1.3	Programming and control.....	79
5.1.4	The HV switches and power supplies .....	80
5.1.5	The gas line .....	82
5.1.6	The alignment .....	83
5.1.7	The vacuum.....	83
5.1.8	The nozzle and discharge.....	83
5.1.9	The hexapole.....	87
5.1.9.1	Hexapole as molecular lens.....	88
5.1.9.2	The effect of removing the hexapole .....	90
5.1.10	The lasers .....	93
5.1.11	The optics outside the chamber.....	93
5.1.12	The PMT and its optics .....	97
5.1.13	The test chamber .....	98
5.1.14	The ion optics for the REMPI experiments.....	99
5.1.15	The signal delivery and amplifiers.....	101
<b>Chapter 6: Experimental results .....</b>		<b>103</b>
6.1	Ammonia experiments .....	103
6.1.1	REMPI for ammonia.....	103
6.1.2	Deceleration of ammonia .....	105
6.1.2.1	Deceleration with the first ion optics .....	106
6.1.2.2	Bunching with the decelerator .....	109
6.1.2.3	Deceleration with the second ion optics design .....	113
6.2	Deceleration of <i>SD</i> radical in $J = 3/2$ and $J = 5/2$ rotational states.....	115

6.2.1	LIF signal integration.....	116
6.2.1.1	The fluorescence lifetime of SD radicals.....	117
6.2.2	PMT signal characterization.....	118
6.2.3	Discharge characterization.....	118
6.2.4	LIF frequency scan and rotational temperature of the SD radicals.....	120
6.2.5	Deceleration.....	123
6.2.6	State purity of the decelerated packets.....	130
6.2.7	CELIF detection.....	137
6.2.8	The first CELIF detection of SD radicals after the decelerator.....	141
6.2.9	Future work on CELIF.....	143
6.3	Experimental results for superconducting microwave cavity.....	144
<b>Chapter 7: Conclusion .....</b>		<b>152</b>
7.1	Future work.....	153
<b>References.....</b>		<b>157</b>
<b>Appendices.....</b>		<b>165</b>
	Appendix 1: REMPI detection for formaldehyde.....	165
	Appendix 2: Pb/Sn coating procedure.....	166

## List of tables

<b>Table 1-1:</b> The relation of critical temperature and molecular number density of ammonia.....	1
<b>Table 1-2:</b> The behaviour of the atoms/molecules at different temperatures.....	2
<b>Table 1-3:</b> List of molecules decelerated with Stark or Zeeman decelerators .....	7
<b>Table 1-4:</b> Approximate translational velocity of supersonically expanded noble gases .....	11
<b>Table 1-5:</b> The relation between heat capacity ratio and the flow properties of a supersonically expanded molecular beam.....	14
<b>Table 2-1:</b> Moments of inertia for different geometry types of molecules .....	20
<b>Table 2-2:</b> Rotational constants for $v_2 = 0$ in the electronic ground state of ammonia .....	25
<b>Table 2-3:</b> Different possible symmetries for the $\tilde{B}$ state of ammonia .....	26
<b>Table 2-4:</b> The structure of the Hamiltonian matrix for the Stark effect calculation of ammonia.....	26
<b>Table 2-5:</b> Different representations for asymmetric top molecules.....	27
<b>Table 2-6:</b> Symmetry types of the $D_2$ group .....	28
<b>Table 2-7:</b> Hund's cases for linear molecules.....	32
<b>Table 4-1:</b> Formulae for three modes of a cylindrical cavity with its origin at the centre of the one of the ends of the cavity[111][112][113] .....	71
<b>Table 6-1:</b> Rotational temperature of SD radicals produced at different discharge voltages. The uncertainty for the calculated temperatures is less than 10 %, obtained from the intensity fluctuations of repeated measurements. The uncertainty of the voltages are $\pm 1 V$ , according to the power supply's data sheet. ....	122

## List of figures

<b>Figure 1-1:</b> The structure of supersonic expansion of a gas [64].....	10
<b>Figure 1-2:</b> (a) Approximate velocity of supersonically expanded mixture of ammonia in krypton vs concentration of ammonia in the mixture at T=300 K and T=245 K. (b) The time of flight for part (a). (c) Approximate velocity of supersonically expanded mixture of methyl fluoride in krypton vs concentration of methyl fluoride in the mixture at T=300 K and T=200 K. (d) The time of flight for part (b). .....	12
<b>Figure 1-3:</b> Vapor pressure versus temperature for formaldehyde, methyl fluoride, and ammonia .....	13
<b>Figure 1-4:</b> The variation of Mach number, velocity, internal temperature, and pressure of supersonically expanded Xenon beam after the nozzle with $d = 250 \mu\text{m}$ , and assuming $P_0 = 5 \text{ bars}$ and $T_0 = 300 \text{ K}$	15
<b>Figure 2-1:</b> Molecular frame (x, y, z), lab frame (X, Y, Z), and the Euler angles between them.....	21
<b>Figure 2-2:</b> Stark shift in $\text{CH}_3\text{CN}$ ( $\mu E = 3.92 D$ ) and $\text{CH}_3\text{F}$ ( $\mu E = 1.86 D$ ) as examples for the Stark effect of the rotational levels in symmetric top molecules. The maximum Stark shift for the low field seeking branch (red) is shown on the graph.....	23
<b>Figure 2-3:</b> The potential curve as a function of umbrella angle in ammonia molecule.....	24
<b>Figure 2-4:</b> Stark effect in the $J = 1, K = 1$ state of ammonia ( $\mu E = 1.47 D$ ).....	27
<b>Figure 2-5:</b> Stark shift of formaldehyde molecule in different rotational states ( $\mu E = 2.34 D$ ). Left panel for $m=0$ , middle panel for $m=1$ , and the right panel for $m=2$ . Higher $m$ numbers are not shown. The lowest LFS states of $J=1$ are shown with a different color. ....	31
<b>Figure 2-6:</b> Angular momentum coupling scheme for Hund's case (a) .....	33
<b>Figure 2-7:</b> Angular momentum coupling scheme for Hund's case (b) .....	34
<b>Figure 2-8:</b> Electronic energy level diagram for $SD$ radical [96] .....	35
<b>Figure 2-9:</b> the energy level diagram for the vibrational ground state of $X^2\Pi_{1/2}$ or $3/2$ and $A^2\Sigma^+$ . Note that the splitting in $\rho$ -doubling and $\Lambda$ -doubling are exaggerated to be visible. ....	38
<b>Figure 2-10:</b> The Stark shift for $X^2\Pi_{3/2}, J = 3/2$ state of $SD$ radical ( $\mu E = 0.76 D$ ) (a) from 0 to $200 \text{ kV/cm}$ (b) Zoomed in to show the $\Lambda$ -doubling splitting (the hyperfine structure is ignored).....	41
<b>Figure 2-11:</b> The Stark shift for $X^2\Pi_{3/2}, J = 5/2$ state of $SD$ radical from 0 to $200 \text{ kV/cm}$ (hyperfine structure is ignored). The red lines show LFS states and the blue lines show HFS states. ....	41
<b>Figure 2-12:</b> AC Stark shift of $ 000\rangle$ and $ 100\rangle$ states of $\text{CH}_3\text{CN}$ ( $\mu_{10z} = 2.26 D$ ) calculated by two state model. Left panel for detuning= $+100 \text{ MHz}$ , Right panel for detuning= $-100 \text{ MHz}$ .....	45
<b>Figure 3-1:</b> Some of the possible one photon transitions from $X^2\Pi_{1/2}(\nu'' = 0)$ to $A^2\Sigma^-(\nu' = 0)$ are shown and labeled. Note that the splitting of $\Lambda$ -doubling and $\rho$ -doubling are exaggerated to be visible. .	48
<b>Figure 3-2:</b> Two photon transition from $X\nu_2 = 0$ to $B(\nu_2 = 5)$ and ionization in (2+1) REMPI for ammonia.....	53
<b>Figure 4-1:</b> Top: The front view of our Stark decelerator. Bottom: The electric field magnitude for one pair of electrodes at $\pm 12 \text{ kV}$ in our Stark decelerator (one deceleration stage). In this case the electrodes are assumed to be oriented in the Z direction, and X is assumed to be the beam axis. The center of electrodes are located at $X = 5.5 \text{ mm}$ , $Y = 0 \text{ mm}$ and $Y = 1.825 \text{ mm}$ . Note the confining potentials in the X and Y directions. ....	54
<b>Figure 4-2:</b> The Stark deceleration principle in 2 dimension view. In 3D, the odd electrode pairs are oriented in Y direction, while even electrodes are oriented in the Z direction.....	56

<b>Figure 4-3:</b> (a) Switching scheme and energy loss per stage ( $\Delta W$ ) for phase $\varphi_0$ . (b) The phase ( $\varphi = \varphi_0 + \Delta\varphi$ ) for a molecule close to the synchronous molecule .....	57
<b>Figure 4-4:</b> Phase space plots. Top: Lines of constant energy in phase-space for phase $0^\circ$ . Middle: Lines of constant energy in phase-space for phase $40^\circ$ . Bottom: Separatrices for different phases. The separatrices are shown in colors and are the boundary between the phase-space stable and unstable areas. Note the reduction of the phase-space stable area as the phase increases. The green dashed lines show phases $-\pi/2$ and $+\pi/2$ .....	59
<b>Figure 4-5:</b> The natural longitudinal oscillation frequencies of the UBC Stark decelerator for ammonia molecules as a function of the initial longitudinal position for the phase angles $\varphi_0 = 0^\circ, 20^\circ, 40^\circ, 60^\circ$ , and $80^\circ$ . The green dashed lines show phases $-\pi/2$ and $+\pi/2$ .....	60
<b>Figure 4-6:</b> The transverse oscillation frequency for ammonia an molecule in one period of deceleration versus the initial position (phase) of the molecule. Note that one period of deceleration here is referred to the distance between two parallel adjacent electrode pairs.....	61
<b>Figure 4-7:</b> Left: The solution to the Mathieu equation. The phase-space stable solutions are shown with red color while the phase-space unstable solutions are shown with blue. Right: The phase-space distribution obtained with numerical trajectory simulation of the ammonia molecules for phase= $0^\circ$ . The hollow area in the phase-space corresponds to the unstable solutions of the Mathieu equation. ....	63
<b>Figure 4-8:</b> Top: Simulation for phase-space distribution of 100000 ammonia molecules at nine different snap shots during their deceleration with $\varphi_0 = 45^\circ$ inside the decelerator. First snap shot at the left corresponds to the phase-space distribution at the entrance of the decelerator, and the last snap shot at the right corresponds to right after the last deceleration stage. Bottom: The main decelerated packet which includes the synchronous molecule enlarged. Note the hollow area in the phase-space distribution which is mostly due to the wide spatial distribution of the molecules due to their free flight from nozzle to the decelerator. The red dotted line shows the position of the synchronous molecule.....	64
<b>Figure 4-9:</b> Left: The angular frequency of rotation of the electric field for the UBC Stark decelerator for different phases ( $-90^\circ, -45^\circ, 45^\circ, 90^\circ$ ) at which the switching occurs. Right: (blue) After switching, the electric field magnitude when HV for the electrodes located at $-90^\circ$ and $270^\circ$ is on; (red) the electric field for the electrode pair located at $90^\circ$ before switching the HV. ....	65
<b>Figure 4-10:</b> The normalized magnitude of electric field distribution for $TM_{010}$ mode in a cylindrical cavity. See Figure (4-14) for the cross section view.....	67
<b>Figure 4-11:</b> The normalized magnitude of electric field distribution for $TE_{115}$ mode in a cylindrical cavity with length $L$ and radius $a$ .....	68
<b>Figure 4-12:</b> Principle of AC Stark deceleration by using a MW cavity with length $L$ and with $P$ number of longitudinal modes .....	68
<b>Figure 4-13:</b> The longitudinal phase-space acceptance of a prototype superconducting MW cavity for Acetonitrile molecules and by neglecting the experimental limitations on switching times which can reduce the phase-space stable area.....	69
<b>Figure 4-14:</b> The schematic cross section view for $TE_{11p}, TE_{01p}$ , and $TM_{01p}$ modes. The red lines correspond to E field, and the blue lines correspond to H field.....	71
<b>Figure 5-1:</b> (a) The full view of the UBC Stark decelerator. The electrodes are attached to four long rods. On each rod 90 electrodes are attached that switch on and off simultaneously. Each rod is attached to the holder through a cylindrical ceramic connector which electrically isolates the rod from the rest of the setup. (b) The head of the decelerator. Note the orientation of the electrode pairs. (c) Left: The dimensions	

of the electrodes and the spacing between the electrodes of each pair. Right: The spacing between the adjacent electrodes. (d) The longitudinal electric field magnitude distribution for one electrode pair when the neighbor electrodes are off..... 75

**Figure 5-2:** The conditioning setup for Stark decelerator electrodes..... 77

**Figure 5-3:** The original design for the complete setup of the UBC Stark decelerator that was used for deceleration of ammonia molecules. Note that in this setup the detection method was REMPI for ammonia molecules. The RGA was only used at the beginning to check the arrival of molecules, and was removed later. In the second version of the setup a new design for ion optics was installed. In the third version of the setup the hexapole was removed, and the REMPI detection was replaced with LIF for detecting *SD* radical, therefore the ion optics were replaced with an optical telescope and the MCP was replaced with a PMT..... 78

**Figure 5-4:** Schematic view of the switch box for one polarity of HV for UBC Stark decelerator. The design for the other polarity was similar..... 81

**Figure 5-5:** Right: The measured high voltage at the electrodes and the switching profile of the voltage. Left: Enlarged first two switching voltage profile. Note the +125 V and -125 V floating grounds on the positive and negative sides of the voltage profile. Also note the sharp rise and fall of the voltages, which transition fully in less than 1  $\mu$ s..... 81

**Figure 5-6:** The gas mixing line. Behind the regulator, the mixture of the seed gas in a carrier gas at a pressure of about 10 bar was prepared. The regulator was used to adjust the backing pressure at the nozzle. The typical backing pressure in use was  $\sim$ 5 bar..... 82

**Figure 5-7:** The design for the CRUCS valve. The discharge plate was added for the discharge of *D2S* experiments and was not present for the ammonia experiments. The discharge plate was isolated from the body of the nozzle by a plastic spacer..... 85

**Figure 5-8:** The home-made HV discharge switch box design along with a schematic of the control unit..... 85

**Figure 5-9:** Blue: The trigger pulse from the Stark control unit to the discharge switch box. Red: The monitored glow discharge voltage while discharging through the gas after supersonic expansion. Note that the voltage is scaled down by 100 times using a high voltage probe. Also note that the voltage drops when discharging until it reaches a voltage at which glow discharge is no longer possible. In the case of arcing sharp spikes replaced the smooth exponential decay..... 86

**Figure 5-10:** The 35 cm long hexapole used in ammonia deceleration experiments. The hexapole electrodes were secured by two ceramic holders. The ceramic holder isolated the electrodes from each other. The diameter of each electrode was 2 mm, and the centre to centre spacing between the electrodes was  $\sim$ 5.6 mm. The inner radius of the hexapole was 0.8 mm..... 88

**Figure 5-11:** The electric field magnitude of the hexapole with  $\pm$ 5 kV being applied to its electrodes. The six surrounding cylindrical wells in the figure correspond to the position of the electrodes. Note the low magnitude field amplitude at the centre which guides molecules in LFS states toward the centre of hexapole..... 89

**Figure 5-12:** Top: The free flight path of ammonia molecules after expansion from the nozzle. Bottom: The focusing effect of our 35 cm long hexapole at  $\pm$ 6 kV on ammonia molecules. Note that the position and extension of the waist of the beam can be adjusted by the voltage being applied to the hexapole. The voltage with the highest number of molecules at the phase-space acceptance of the decelerator is preferred..... 90

<b>Figure 5-13:</b> The effect of removing the long hexapole on the (a) signal and (b) the phase-space acceptance of the decelerator. (c) The phase-space distribution of ammonia molecules at the entrance of the decelerator with (blue) and without hexapole (red). .....	92
<b>Figure 5-14:</b> The optics arrangement for the LIF detection of the <i>SD</i> radical. The photo-diode detected the transmitted light through the back side of the prism and its signal was used to trigger the PMT signal recording. ....	94
<b>Figure 5-15:</b> The optics arrangements for delivering the laser to the detection chamber for the CELIF experiments. ....	95
<b>Figure 5-16:</b> The laser beam outside and inside the cavity. Note that the dimensions are exaggerated. ...	95
<b>Figure 5-17:</b> The CRD signal recording arrangement. The photo-diode with internal amplifier was used to collect the weak transmitted light after the back mirror of the cavity. ....	97
<b>Figure 5-18:</b> The PMT and the optics used for collecting the fluorescence light. ....	99
<b>Figure 5-19:</b> The test chamber setup. (a) For LIF experiments in the test chamber. (b) For the CELIF experiments in the test chamber. Note that the two windows in the LIF test chamber setup are replaced with two long tubes on which the cavity mirrors are attached.....	99
<b>Figure 5-20:</b> The two versions of ion optics used for ammonia experiments. Left: the original design. Right: The second version with shorter distance to the decelerator.....	101
<b>Figure 6-1:</b> The frequency spectrum for (2+1) REMPI of ammonia molecules ( $B1E' \leftarrow X1A1'$ 205) after the decelerator. Red: decelerator off. Note the signal is scaled 10 times for clarity and comparison. Blue: decelerator on. Note the signal enhancement for the transitions initiating from $J = 1, K = 1, antisymmetric$ . The peak labeled with a triangle is not assigned. The uncertainty of the wavenumber was $\pm 0.1 \text{ cm}^{-1}$ , which was obtained by the dye laser's minimum possible step size.....	103
<b>Figure 6-2:</b> The (2+1) REMPI signal intensity (obtained at $64032 \text{ cm}^{-1}$ for ammonia molecules in $J = 1, K = 1, antisymmetric$ ) versus the laser power for the purpose of signal calibration. Note the saturation of the signal at $\sim 4 \text{ mJ/pulse}$ . The uncertainties are neglected. ....	105
<b>Figure 6-3:</b> The signal intensity versus the MCP voltage for the purpose of calibration of the signal. Note that the safe limit for voltage was 1850 Volts. intensity (obtained at $64032 \text{ cm}^{-1}$ for ammonia molecules in $J = 1, K = 1, antisymmetric$ , and laser power of $3 \text{ mJ/pulse}$ ). The uncertainties are neglected. ....	105
<b>Figure 6-4:</b> The detected signals after the decelerator for the purpose of comparison between free flight, guiding, and switching modes. For the switching mode, different initial velocities of the synchronous molecules were chosen for the purpose of comparison. Note the different arrival times for the decelerator selected packets at $3500 - 4000 \mu\text{s}$ . The uncertainty for the signal intensity measurements at each data point was $\sim \pm 5 \%$ , that were obtained from the standard deviation of repeated measurements. ....	108
<b>Figure 6-5:</b> Deceleration of ammonia molecules, detected using the first ion optics design. (a) Full time of flight obtained by simulation (red) and experiment (black) for $\text{phase}=0^0$ with initial velocity of $445 \text{ m/s}$ . (b) Deceleration of ammonia molecules from $445 \text{ m/s}$ down to $59 \text{ m/s}$ using different phases for the synchronous molecule. The signal to noise ratio was not high enough to detect a proper signal at lower speeds mostly due to the long distance between the ion optics and the decelerator. The uncertainty for the signal intensity measurements at each data point was $\sim \pm 5 \%$ for velocities higher than $100 \text{ m/s}$ and $\sim \pm 10 \%$ for velocities lower than $100 \text{ m/s}$ , that were obtained from the standard deviation of repeated measurements. ....	109

**Figure 6-6:** Simulation results to show the effect of bunching on improving the signal. The initial velocity in both cases was assumed to be  $445\text{ m/s}$ , and the final velocity was fixed to  $55\text{ m/s}$  in both cases for the purpose of comparison. The blue trace shows the expected signal for no bunching and phase= $51.89^\circ$ , and the red trace shows the expected signal for bunching for the first 10 stages of the decelerator and phase= $54.27^\circ$ . Note the enhancement of the signal in the red trace. Also note the higher phase used for the case with bunching to compensate for the first 10 stages. In this experimental setup bunching particularly helped a lot in improved the signal for final velocities of lower than  $100\text{ m/s}$ .... 112

**Figure 6-7:** Comparison of signals for no bunching (black), first 15 stages for bunching (blue), last 15 stages for bunching (red). Note that bunching improved the signal in both cases, however bunching first had stronger signal than bunching last. This is not a general rule and depends on the spacing of different parts of the experiment. In this case bunching first improves the signal more because of the long distance between the nozzle and the decelerator..... 112

**Figure 6-8:** Time of flight for decelerated ammonia molecules detected by the second ion optics version. (a) The experimental and simulation results for the full time of flight measurement for Phase= $0^\circ$  and initial velocity of  $425\text{ m/s}$ . The top panel shows the phase-space distribution for the main packet and neighboring packets. (b) The experimental and simulation results for the main packet while decelerating from  $425\text{ m/s}$  down to  $27.9\text{ m/s}$ . Note the scale after phase= $49^\circ$ . The uncertainty for the signal intensity measurements at each data point was  $\sim \pm 5\%$  for velocities higher than  $100\text{ m/s}$  and  $\sim \pm 10\%$  for velocities lower than  $100\text{ m/s}$ , that were obtained from the standard deviation of repeated measurements..... 114

**Figure 6-9:** (Red) The typical fluorescence signal seen by the PMT from excited *SD* radicals. (Blue) The fit to the fluorescence decay signal gave a fluorescence lifetime of  $259.46 \pm 8.52\text{ ns}$  for *SD* radicals. Note the sharp peak close to time zero due to the scattered laser light within the PMT gate rise time. ... 117

**Figure 6-10:** The fluorescence signal versus the input laser power measurement for the purpose of finding the saturation limit for the transition in the *SD* molecules ( $X2\Pi3/2, J = 3/2$ ) at the detection point. The PMT gain for this measurement was low to prevent saturating the PMT. The uncertainties are neglected for this measurement..... 118

**Figure 6-11:** Characterizing the discharge signal in the test chamber. Left top: Central velocity of the beam versus the discharge voltage. Right top: width of the velocity distribution versus the discharge voltage. Bottom: the signal intensity versus the discharge voltage. The green circle shows the optimum condition chosen. The experimental conditions for all the graphs are the same. The fluorescence of *SD* radicals after  $q\text{ }Q1P21(1.5)$  transition was collected to obtain the signal for each trace. The uncertainties are neglected for these measurements..... 119

**Figure 6-12:** The frequency spectrum for *SD* radical obtained by LIF method. Red: Simulation at  $T_{rot} = 35\text{ K}$ . Blue: Experimental result. Note that the signal for  $q\text{ }Q1P21(5.5)$  was barely visible and the signals for higher  $J''$  were not seen. The uncertainty for the signal intensity measurements at each data point was less than  $\pm 5\%$ , that were obtained from the standard deviation of repeated measurements. The uncertainty of the wavenumber was  $\pm 0.1\text{ cm}^{-1}$ , which is obtained by the dye laser's minimum possible step size..... 121

**Figure 6-13:** (a) The effect of discharge voltage on the occupation of the rotational states for the *SD* radical. (b) The effect of the discharge voltage on the time of flight profile of the *SD* radical. Note the two dashed lines labelling the curves corresponding to  $490\text{ m/s}$  and  $440\text{ m/s}$ . The velocity spread width for this trace was  $\sim 75\text{ m/s}$ . The uncertainty for the signal intensity measurements at each data point was

$\sim \pm 5 \%$ , that were obtained from the standard deviation of repeated measurements. The uncertainty of the wavenumber was  $\pm 0.1 \text{ cm}^{-1}$ , which is obtained by the dye laser's minimum possible step size. . 123

**Figure 6-14:** The frequency spectrum after the decelerator. Note the difference between decelerator on (blue) and decelerator off (red) spectra, which shows that when the Stark field is on, the molecules in LFS states are guided to the detection point. The uncertainty for the signal intensity measurements at each data point was less than  $\pm 10 \%$ , that were obtained from the standard deviation of repeated measurements. The uncertainty of the wavenumber was  $\pm 0.1 \text{ cm}^{-1}$ , which is obtained by the dye laser's minimum possible step size. .... 126

**Figure 6-15:** Deceleration of *SD* radical. (a) Experimental results for the Stark deceleration of *SD* radical from  $440 \text{ m/s}$  down to  $301 \text{ m/s}$ , along with the free flight (black) and guiding mode (dashed) signals. (b) Right top: Simulation and experimental results for the full time of flight for phase= $0^\circ$ . Left top: the enlarged simulation and experimental results for the main packet with phase= $0^\circ$ . The black circle shows the expected arrival time for the synchronous molecule. Right bottom: the full phase-space distribution of the *SD* radicals that could reach to the detection point for phase= $0^\circ$ . Left bottom: the Phase-space distribution of the main packet for phase= $0^\circ$ . (c) Left panels: The simulation (red), experimental (blue), and free flight (black) for the time of flight of the main packet for different phases. Middle panel: the full phase-space diagram for each phase. Right panel: the phase-space distribution for the main packet for each phase. .... 129

**Figure 6-16:** Top: Deceleration of *SD* radicals in  $X2\Pi3/2, J = 5/2, MJ = -5/2$  state from  $440 \text{ m/s}$  down to  $415 \text{ m/s}$ . Bottom: Corresponding phase-space distribution for the decelerated packets. .... 130

**Figure 6-17:** Stark potential energy for  $X2\Pi3/2, J = 3/2, MJ = -3/2$  and  $X2\Pi3/2, J = 5/2, MJ = -5/2$  ..... 131

**Figure 6-18:** Top: The behaviour of target molecules in  $X2\Pi3/2, J = 3/2, MJ = -3/2$  and  $X2\Pi3/2, J = 5/2, MJ = -5/2$  states. Left: when timing is calculated for  $X2\Pi3/2, J = 3/2, MJ = -3/2$ , Right: When timing is calculated for  $X2\Pi3/2, J = 5/2, MJ = -5/2$ . Bottom: Phase-space distribution for parts (g) and (h), right after the decelerator. .... 135

**Figure 6-19:** Position of target molecules in  $X2\Pi3/2, J = 3/2, MJ = -3/2$  and in  $X2\Pi3/2, J = 5/2, MJ = -5/2$  with respect to the Stark potential period ( $0 - 1.1 \text{ cm}$ ) when the first 130 stages are operated with phase= $10^\circ$ , and the next 50 stages with phase= $70^\circ$ . .... 136

**Figure 6-20:** Simulation and experimental results for the time of flight of the separated *SD* radicals in  $X2\Pi3/2, J = 3/2, MJ = -3/2$  and in  $X2\Pi3/2, J = 5/2, MJ = -5/2$  energy states, when the first 130 stages are operated with phase= $10^\circ$ , and the next 50 stages with phase= $70^\circ$ . The uncertainty for the signal intensity measurements at each data point was  $\sim \pm 10 \%$  for  $J = 3/2$ , and  $\sim \pm 15 \%$  for  $J = 5/2$ , that were obtained from the standard deviation of repeated measurements. .... 136

**Figure 6-21:** Frequency spectrum for the separated decelerated packets; (a) for the decelerated molecules corresponding to  $J = 3/2$  at  $t = 2.78 \text{ ms}$  (b) for the decelerated molecules corresponding to  $J = 5/2$  at  $t = 2.76 \text{ ms}$ . The uncertainty of the wavenumber was  $\pm 0.1 \text{ cm}^{-1}$ , which is obtained by the dye laser's minimum possible step size. The uncertainty for the signal intensity measurements at each data point was  $\sim \pm 10 \%$  for  $J = 3/2$ , and  $\sim \pm 15 \%$  for  $J = 5/2$ , that were obtained from the standard deviation of repeated measurements ..... 137

**Figure 6-22:** Signal recording scheme for CELIF detection method.(a): The experimental cavity ring-down signal. (b): The PMT signal obtained experimentally for the Fluorescence of *SD* radicals by CELIF method, when the gain and density were high at the test chamber. (c): The same as (b), but with lower

concentration and gain. Therefore photon counting scheme was employed. Note that the gate for recording the signal was chosen in a way that includes less noise and stray light..... 140

**Figure 6-23:** Frequency spectrum obtained by CELIF method for *SD* radicals at the test chamber. Note the higher resolution in this spectrum compared to the LIF measurement (figure 6-13). The peaks in this figure are narrower than the LIF measurement due to having less power broadening. The laser power just before hitting the cavity mirror for the first time was  $300 \pm 50 \mu J/pulse$ . The uncertainty of the wavenumber was  $\pm 0.1 \text{ cm}^{-1}$ , which is obtained by the dye laser's minimum possible step size. .... 141

**Figure 6-24:** Time of flight (top) and frequency scan (bottom) for molecules in  $X^2\Pi_{3/2}, J = 3/2, MJ = -3/2$  state after the decelerator and with the decelerator operating at  $\varphi_0 = 0^\circ$ , recorded by CELIF detection method. The laser power just before hitting the cavity mirror for the first time was  $300 \mu J/pulse$ . The uncertainty at each point is  $\pm \sigma$  (standard deviation from the mean value). The uncertainty of the wavenumber was  $\pm 0.1 \text{ cm}^{-1}$ , which is obtained by the dye laser's minimum possible step size. . 143

**Figure 6-25:** Top: The design and dimensions for prototype superconducting microwave cavity. Bottom: The outside view of the actual cavity..... 145

**Figure 6-26:** Top right: Schematic view of the characterizing experiment for the prototype superconducting cavity. Top Left: The actual experimental view. Bottom: The signal delivery and signal collection design. .... 147

**Figure 6-27:** Resonance frequencies between 13.5 GHz to 18 GHz for  $TE_{11p}$  modes of the cavity at room temperature. Note that the peaks for the even-p numbers are shorter than the odd-p numbers. The reason is mainly due to the presence of the antenna at the location of an anti-node at the centre of the cavity for p-even numbers. However one can minimize this effect by adjusting the insertion of the antenna to the cavity. Also note that the resonances from the other modes are not present in this range. 148

**Figure 6-28:** The transmission and reflection signal recorded for the prototype superconducting MW cavity at critical coupling. .... 149

**Figure 6-29:** The power decay signal recorded for prototype superconducting MW cavity. The filled lines refer to reflected signals, while the dashed lines refer to the transmitted signal. Signal for 100 ms long MW pulse (Green), Signal for 10 ms long MW pulse (Red), signal for 1 ms long MW pulse (Blue).... 149

## **Glossary**

AC: Alternating Current  
CELIF: Cavity Enhanced Laser Induced Fluorescence  
DC: Direct Current  
HFS: High Field Seeking  
LFS: Low Field Seeking  
LIF: Laser Induced Fluorescence  
MCP: Micro Channel Plate  
MW: Micro Wave  
PMT: Photo Multiplier Tube  
Ppb: Parts per billion  
Ppq: Parts per quadrillion  
REMPI: Resonance Enhanced Multi-Photon Ionization  
RGA: Residual Gas Analyzer

## **Acknowledgements**

I offer my enduring gratitude to the faculty, staff and my fellow students at UBC, who have inspired me to continue my work in this field. I owe particular thanks my supervisor Dr. Takamasa Momose who supported my project and shared his extensive knowledge with me. I also thank my graduate committee members, Dr. Walter Hardy, Dr. Roman Krems, and Dr. Kirk Madison for their time, help, and support during my PhD studies.

I thank Dr. Katsunari Enomoto and Dr. Walter Hardy for sharing their valuable knowledge with me.

I thank Dr. David Carty, Dr. Eckart Werde, and Dr. Sebastian Y.T Van De Meerakker for their patience in answering my questions and sharing their experience.

I thank Dr. Yang Liu, Dr. Ilja Gerhardt and Dr. Sida Zhou for the great discussions.

I thank Mr. Eric Miller and Mr. Adam Schonewille for their help in my thesis preparation.

Special thanks are owed to Mr. Pavle Djuricanin, Mr. Tony Mittertreiner, Mr. Chris Bedford, Mr Sajjad Haidar, and Dr. Mario Michan for their great technical support, without which this work could not have been done.

This work was supported by an NSERC Discovery Grant and funds from CFI to the Centre for Research on Ultra Cold Systems (CRUCS) at UBC.

## **Dedication**

To my wife and family.

# Chapter 1: Introduction

## 1.1 Cold molecules

There are many unexplored physical phenomena in low temperature physics. Many scientists have joined the interesting field of cold molecules since the mid-1990s. By convention, cold molecules have temperatures in the range  $1\text{ mK} - 1\text{ K}$ . Molecules with temperatures lower than  $1\text{ mK}$  are called ultra-cold, those with temperatures of  $1\text{ K} - 100\text{ K}$  are considered normal low temperature molecules, and those with temperatures higher than  $100\text{ K}$  are called hot. The temperature  $T$  can be used to express the kinetic energy of the molecules (in 3-dimensions) via

$$\frac{3}{2}k_B T = \frac{1}{2}m\langle v \rangle^2. \quad (1.1)$$

Where  $\langle v \rangle$  refers to the average thermal velocity of an ensemble of molecules. The cold and ultra-cold regimes are far below the background temperature of the universe ( $2.7\text{ K}$ ), but are obtainable in laboratories. There is a great interest in the field of cold molecules with the aim of duplicating and even expanding on the successes achieved in the field of cold atoms, such as Bose-Einstein Condensation ( $T < 1\mu\text{K}$ ). The critical temperature for Bose-Einstein Condensation (BEC) for a uniform three dimensional gas consisting of non-interacting particles with no apparent internal degrees of freedom can be estimated by:

$$T_{BEC-critical} = \frac{h^2}{2\pi m k_B} \left( \frac{n}{2.6124} \right)^{0.6667}, \quad (1.2)$$

where  $n$  is the number density of the bosons,  $m$  is the mass, and  $h$  is Planck's constant [1]. As an example consider ammonia ( $\text{NH}_3$ ) with a mass of  $17\text{ amu}$ , and assume it roughly follows the above formula (ignoring the dipolar interaction's perturbation on the critical temperature):

**Table 1-1:** The relation of critical temperature and molecular number density of ammonia

Density ( $n$ ) [ $\text{cm}^{-3}$ ]	$2 \times 10^{22}$	$5 \times 10^{12}$
$T_{BEC-critical}$ [K]	1.28	$0.27 \times 10^{-6}$

Since the cooling process is limited by the crystallization of the molecules, large number densities are not practical; hence a combination of ultra-cold temperatures and relatively low

densities is required to achieve BEC. BEC is a consequence of quantum degeneracy. The criterion for quantum degeneracy is that the mean spacing distance between the atoms or molecules in the gas is on the order of their thermal de-Broglie wavelength. The number of molecules per unit volume and velocity is called phase-space density ( $D$ ), and is given by:

$$D = n\Lambda^3 \quad (1.3)$$

Where  $\Lambda = (2\pi\hbar^2/mk_B T)^{1/2}$  is the thermal de-Broglie wavelength. Table (1-2) summarizes the behaviour of the atoms/molecules at different temperatures:

**Table 1-2:** The behaviour of the atoms/molecules at different temperatures

<b>Temperature</b>	High	Low	$T=T_{cr}$	$T=0$
<b>Behaviour</b>	Thermal velocity	Wave packets	BEC (matter-wave overlap)	Pure BEC (Giant matter-wave)

The first BEC for molecules was reported in 2003 starting from optically trapped fermionic  ${}^6\text{Li}$  atoms, in which a Feshbach resonance allowed pairing of the fermionic atoms to form bosonic  ${}^6\text{Li}_2$  and then Bose condense them by evaporative cooling to below 600 nK [2]. In 2010 the first BEC of photons in an optical micro-cavity was reported, and later in 2012 its theory was developed [3][4].

The applications of cold molecules vary depending on the temperature and the phase-space density of the molecules [5]. Cold molecules have applications in high resolution spectroscopy (including time reversal symmetry violation, parity-violation interaction in chiral molecules, time dependence of fundamental constants, and lifetime measurements), cold collisions (including quantum chemistry, quantum degenerate gases, dipole-dipolar interaction), and quantum computing [6]. In addition, at low temperatures, due to the quantum nature wave behaviour, non-Arrhenius type reactions (such as tunneling) may occur, which enhance the reaction rates and introduce completely new Physics and Chemistry.

Molecules with permanent electric dipole moments ( $\mu$ ) have a long-range dipole-dipole interaction potential in the presence of an external electric field that could be very interesting for the purposes of collision experiments or quantum computation [7][8]. The anisotropic interactions of polar molecules can help in direct control of the intermolecular potential in

collision experiments in an external electric field ( $\vec{E}$ ) [9]. Precision spectroscopy benefits from cold molecules due to increased interaction time, reduced sample temperature, and increased state purity.

### 1.1.1 Methods of production of cold molecules

Cooling refers to the methods that lower the temperature of the gas while increasing the phase-space density. Although cooling molecules is more difficult than cooling atoms, some cooling methods have been demonstrated. Many groups around the world have been working on various techniques to obtain larger ensembles of cold molecules at lower temperatures. There are two general categories for these techniques: direct and indirect.

Indirect cooling methods deal with assembling cold molecules from cold atoms. Cold molecules could be formed from ultra-cold atoms. This could happen through three-body recombination of cold atoms [10], Feshbach resonance association [11], or photo-association [12].

Direct cooling methods deal with cooling molecules in their stable ground state (or their lowest rotational states). This can be done via sympathetic cooling (such as buffer-gas cooling [13]), or evaporative cooling [5]. Pre-cooling methods are used to prepare molecules for cooling by reducing their translational velocity. Some of these methods are deceleration of the molecular beams using an external electric field (Stark [14], velocity filtering [15], Rydberg-state enabled deceleration [16]), external magnetic field (Zeeman [17]), electromagnetic field (optical [18][19]), or using a mechanical deceleration method such as a counter-rotating nozzle. However deceleration methods are not being considered as cooling methods, because they cannot increase the phase-space density of the molecules. Crossed molecular beam collisions is also another example of a direct cooling technique [5]. In the methods dealing with external fields the interaction between the dipole moment of a molecule and the field is employed to decelerate the molecule. The interaction of the field with the dipole moment of the molecule perturbs its energy states. The states for which their energy increases by increasing the field are called Low Field Seeking states (LFS), and the states for which their energy decreases as the field increases are called High Field Seeking states (HFS). The methods based on external fields are various. Stark deceleration has also been applied to molecules in their high field seeking states via the so called Alternating Gradient Decelerator (AGD) [20]. Other methods have been developed in addition to

Stark and Zeeman deceleration. In 2010 a traveling wave decelerator for neutral polar molecules was proposed by Osterwalder et al. on the basis of macroscopic, three dimensional traveling electrostatic traps [21]. In 2011 Riedel et al. showed that it is possible to accumulate decelerated packets of NH molecules in a magnetic trap using a single photon transition [22]. Later in 2012 an optoelectrical cooling method for trapped molecules was demonstrated using the so called Sisyphus effect which allowed the accumulation and cooling of the molecules stored in an electric trap [23]. In 2014 Chervenkov et al. demonstrated a continuous centrifuge decelerator for polar molecules which decelerated  $\text{CH}_3\text{F}$ ,  $\text{CF}_3\text{H}$ , and  $\text{CF}_3\text{CCH}$  from  $200\text{ m/s}$  to  $15\text{ m/s}$ , with an intensity of  $10^9\text{ mm}^2/\text{s}$  [24]. They are now working on combining their centrifuge decelerator with a hydrodynamically enhanced cryogenic buffer-gas source of molecules to enhance the internal-state purity of the decelerated beam. Some of the cooling methods are briefly explained below.

#### **1.1.1.1 Photo-association**

This technique was proposed by Thorsheim et al. 1987 [12]. This method has been used for alkali or earth alkaline metals to form homonuclear or heteronuclear species. In this method, two laser-cooled atoms resonantly absorb one photon (with a frequency slightly below the excitation frequency of the atom) and produce a molecule in an electronically excited state. However, the lifetime of the molecule produced in the excited state is very short (nanosecond range), and the molecule can dissociate into atoms through spontaneous emission. The branching ratio between bound-bound and bound-free transitions is crucial in the formation of stable molecules [6]. The cold molecules produced with this method can have a temperature as low as  $\mu\text{K}$ , but their density is in the order of  $10^4\text{ cm}^{-3}$ , which is too low for most of the interesting applications.

#### **1.1.1.2 Buffer-gas cooling**

Buffer-gas cooling was first developed by John Doyle and his group at Harvard University [13]. Buffer-gas cooling is a cryogenic method in which helium is usually used as the buffer gas. The cooling of the desired sample happens through introducing the sample into the cryogenic cell. Since the sample molecules should thermalize via collisions with the buffer gas before arriving at the walls of the cell, the temperature of the sample molecules is limited by the number density of the buffer gas and the dimensions of the cell. For a cell of the order of  $1\text{ cm}$ , using helium as the

buffer gas, a temperature of a few hundred milli-Kelvins could be achieved. Buffer-gas cooling of at least 15 different molecules has been reported so far. For paramagnetic molecules with large magnetic dipole moments, buffer-gas cooling could be followed by trapping in a superconducting magnetic trap. This is possible if the ratio between the elastic and inelastic cross sections of the sample molecule with helium allow thermalization. The first successful trapping of buffer-gas cooled molecules was demonstrated in 1998 for CaH molecules [25]. The typical range of densities obtained with this method is about  $10^8 \text{ cm}^{-3}$  at a temperature of the order of a few Kelvins. The trapped molecules could be submitted to further cooling through other cooling methods such as evaporative cooling. An intense buffer gas beam has also been developed and characterized [26].

#### **1.1.1.3 Counter-rotating nozzle**

The counter-rotating nozzle was first demonstrated by Gupta in 1999 [27], and later improved by Strebel et al. in 2010 [28]. A counter-rotating nozzle in our lab at the University of British Columbia was also constructed based on Strebel's design. By controlling the rotation frequency of the nozzle, this technique mechanically slows the supersonically expanded molecules to a few tens of metres per second. The final velocity of the beam is tunable and is simply given by  $v_0 = v_s - v_{rot}$ , in which  $v_s$  is the velocity of the molecules after supersonic expansion, and  $v_{rot}$  is the backward velocity of the nozzle with respect to the molecular beam. The typical internal and translational temperatures of the beam produced are in the range of a few tens of Kelvin and a few Kelvin respectively [28]. A combination of counter-rotating nozzle as a pre-cooling method with other cooling methods such as microwave Stark deceleration is currently under investigation in our lab. We have previously coupled the counter-rotating nozzle to a microwave lens to observe the MW lens effect for the  $J = 0$  rotational state of  $\text{CH}_3\text{CN}$  and  $\text{CD}_3\text{CN}$  [29][30].

#### **1.1.1.4 Laser cooling**

Having more degrees of freedom (vibrational and rotational) and possessing electric or magnetic dipole moments, cold molecules are more interesting and complicated than atoms [31]. Cooling atoms usually involves laser cooling in which the photon's momentum transfers to atoms through closed-cycle transitions, and reduces their energy. For molecules these closed-cycle transitions are rare due to their coupled complex vibrational and rotational energy level

structures [32]. For experiments with the aim of BEC for atoms, laser cooling is usually followed by another cooling method such as evaporative cooling. Despite being rare, there are some molecules being proposed that have energy level schemes that could be used for laser cooling, such as NH [33].

#### **1.1.1.5 Evaporative cooling**

Evaporative cooling has been used to produce atom ensembles with temperatures below ten milli-Kelvins. In evaporative cooling, atoms inside a trap cool by transferring their energy to atoms leaving the trap through elastic collisions. Cooling occurs through slowly lowering the depth of the trap and allowing the ensemble to establish a new thermodynamic equilibrium [6]. For cold molecular ensembles, due to unfavorable ratios of elastic to inelastic scattering and slow thermalization rates, evaporative cooling is not easy to achieve. The first observation of evaporative cooling for molecules was reported in 2012 by Stuhl and his colleagues, in which they could see the microwave-forced evaporative cooling of neutral hydroxyl radical (OH) molecules in an extremely high-gradient magnetic quadrupole trap. They reported cooling of at least one order of magnitude in temperature, and a corresponding phase-space enhancement of three orders of magnitude. This observation opens the path to create a BEC from dipolar radicals, and allows cold and ultra-cold chemistry studies of fundamental reaction mechanisms. This group also could successfully applied laser cooling and magneto-optical trapping to molecules [33].

#### **1.1.1.6 Stark and Zeeman deceleration of a molecular beam**

Since the first demonstration of a Stark decelerator by Bethlem et al. [14] and a Zeeman decelerator by Merkt et al. and Raizen et al. [34][35], many groups have begun working on them. The deceleration principles of the Stark and Zeeman decelerators are similar, and will be explained in the next chapter. The difference between Stark and Zeeman decelerators is that Stark decelerators exploit the Stark effect in the presence of an external field to translationally cool the supersonically expanded molecules with non-zero permanent electric dipole moments, while Zeeman decelerators use the Zeeman effect for molecules with non-zero magnetic dipole moments. With these techniques a few molecules and radicals have been decelerated to date, while efforts to optimize the process and decelerate other interesting molecules are still

underway. Since the pulsed molecular beam is supersonically expanded, a high density of molecules in their lowest few quantum states is introduced to the decelerator. Some methods of optimization such as bunching [36] and feedback control [37] have been applied to the Stark decelerators to enhance the density of the decelerated packet. In 2009 a new mode of operation called the  $s = 3$  mode, was introduced to improve the density of the decelerated packet; however, it was beneficial only for final velocities above  $100 \text{ m/s}$  due to the over-focussing of the beam at lower velocities [38]. The decelerator produces a packet of molecules with a tunable longitudinal velocity and with a narrow velocity distribution, which is of interest in many molecular beam experiments. Theoretically, Stark and Zeeman decelerators are capable of bringing the molecules to a standstill, but in reality are limited by the de-Broglie wavelength of the molecules at low velocities, which becomes comparable to the spacing of the decelerator stages. These two methods are capable of producing cold molecules in the milli-Kelvin range with a density of about  $10^6 \text{ cm}^{-3}$ . These typical values are too high and low respectively for many interesting applications of cold molecules, and therefore the decelerated packet should be further cooled, by being loaded into a trap [39].

Table (1-3) lists molecules that have been decelerated by Stark or Zeeman deceleration.

**Table 1-3:** List of molecules decelerated with Stark or Zeeman decelerators

<b>Molecule</b>	<b>Method of deceleration</b>	<b>Reference</b>
$^{12}\text{CO}$	DC/AG <sup>1</sup> /TW <sup>2</sup> Stark	[14][40] [21]
$^{13}\text{CO}$	DC/TW Stark	[41]
<b>OH</b>	DC/AG Stark	[42]
<b>OD</b>	DC Stark	[43]
<b>NH</b>	DC Stark	[44]
$^{14}\text{NH}_3$	DC/MW <sup>3</sup> /TW	[45] [46]
$^{15}\text{NH}_3$	DC Stark	[47]
$^{14}\text{ND}_3$	DC/TW Stark	[48] [46]
$^{15}\text{ND}_3$	DC/AG Stark	[49]
<b>NO</b>	DC Stark	[50]
<b>H<sub>2</sub>CO</b>	DC Stark	[51]
<b>LiH</b>	DC Stark	[52]
<b>CaF</b>	AG/DC Stark	[53]
<b>YbF</b>	AG/TW Stark	[54] [55]
<b>SrF</b>	TW Stark	[56]
<b>SO<sub>2</sub></b>	DC Stark	[57]

Molecule	Method of deceleration	Reference
<b>C<sub>7</sub>H<sub>5</sub>N</b>	AG Stark	[58]
<b>O<sub>2</sub></b>	Zeeman	[59]
<b>CH<sub>3</sub></b>	Zeeman	[60]
<b>CH<sub>3</sub>F</b>	CC <sup>4</sup>	[24]
<b>CF<sub>3</sub>H</b>	CC	[24]
<b>CF<sub>3</sub>CCH</b>	CC	[24]
<b>He<sub>2</sub></b>	Zeeman	[61]
<b>H<sub>2</sub></b>	RB Stark <sup>5</sup>	[62]
<b>SD</b>	DC Stark	This work

<sup>1</sup>Alternating Gradient      <sup>2</sup>Traveling Wave      <sup>3</sup>Microwave  
<sup>4</sup>Continuous Centrifuge      <sup>5</sup>Rydberg

In this thesis I report the construction and characterization of a Stark decelerator at UBC. The decelerator was first characterized by using a previously examined sample, namely ammonia, and then the characterized decelerator was used for the deceleration of a new sample, the *SD* radical. After that, we implement the detection method Cavity Enhanced Laser Induced Fluorescence (CELIF) with which we can experimentally measure the actual number of decelerated/guided molecules with the decelerator. The work on the CELIF detection of the Stark decelerated packet is still in progress in our lab. Finally in this thesis the construction of a prototype superconducting microwave cavity for the purpose of AC Stark deceleration is reported.

## 1.2 Supersonic expansion

In order to produce cold molecules, all the internal and external degrees of freedom must be cooled. External (translational motion) pre-cooling can be obtained by methods such as Stark deceleration, after which external cooling can be obtained by a method such as evaporative cooling. Internal cooling, however, is achieved by bringing the molecules to their lower quantum energy states (electronic, vibrational, and rotational), which can be done by producing supersonically expanded molecular beams. The expansion occurs via expanding the desired gas from a reservoir of high pressure ( $P_0$ ) into a low pressure reservoir ( $P_b$ ) at temperature of  $T_0$ , through a pinhole (nozzle). If the diameter of the orifice of the nozzle ( $d$ ) is much larger than the mean free path of the molecules at pressure  $P_0$  ( $\lambda_0 \ll d$ ), expansion is called supersonic expansion. If  $\lambda_0 \gg d$ , expansion is called effusive. In effusive expansion, since there is no collision between the molecules while expanding, the properties of the beam before and after

expansion are the same. Therefore a Maxwell distribution can describe the velocity distribution of the molecules, while for supersonic expansion the characteristics of the expanded beam are different before and after expansion [63].

In molecular deceleration experiments, pulsed molecular beams are typically used. The advantage of a pulsed molecular beam is to keep the source at high pressure while maintaining high vacuum in the chambers. In addition, since all the other parts of the experiment, such as deceleration and detection, are pulsed, having a pulsed source provides a better timing scheme.

In the case of a supersonic expansion, especially for pulsed molecular beams near a wall and a skimmer in front of the nozzle, analytical estimations for the thermodynamics of a supersonic expansion can be imprecise. To generate an estimate, we begin with the assumption of having an ideal expansion which is continuous and isentropic, and with negligible viscous and heat conduction effects.

The pressure difference between the high pressure reservoir (or stagnation pressure ( $P_0$ )) and the background pressure (inside a vacuum chamber ( $P_b$ )) accelerates the molecules as the area decreases toward the nozzle orifice. At the nozzle exit, if the ratio of the pressures ( $P_0/P_b$ ) exceeds a critical value  $G$  (as defined in Eq. (1.4) ), the mean velocity of the molecules reaches Mach number equal to 1, and the flow becomes so-called “under-expanded”. A subsequent expansion happens to meet the boundary conditions imposed by  $P_b$  and as a result the mean velocity after the nozzle becomes higher than the local speed of sound (supersonic)[64]

$$G = \left( \frac{\gamma + 1}{2} \right)^{\gamma/\gamma-1} \quad (1.4)$$

where  $\gamma$  is the ratio of the specific heats for the gas (for a monoatomic gas it is  $\sim 1.67$ ).  $G$  is less than 2.1 for all the molecules.

The supersonic beam cannot sense the downstream boundary condition and over-expands. A barrel of shock wave at the sides and a Mach disk shock normal to the centreline occurs that changes the direction of the supersonic flow and reduces the Mach number to subsonic values to meet the boundary conditions [64]. The isentropic core of the expansion is not aware of the boundary conditions and is called the “zone of silence”. The molecular beam is usually extracted

from this zone using a skimmer. Skimmers are used to extract the parallel and non-interacting molecules from the central beam. Skimmers also make it possible to differentially pump the chambers from the source chamber. This will lead to better vacuums and less collisions in the following chambers.

The Mach disk location is given by:

$$x = 0.67d\left(\frac{P_0}{P_b}\right)^{1/2} \quad (1.5)$$

For a typical experimental condition, the stagnation pressure is  $P_0 = 3750 \text{ Torr}$ ,  $P_b = 5 \times 10^{-7} \text{ Torr}$ , and  $d = 250 \mu\text{m}$ . The Mach disk will be at  $x = 14.5 \text{ m}$ , which is longer than our decelerator setup. The valve to skimmer distance is usually well below this limit. One can adjust the distance of the skimmer from the nozzle to find the optimum throughput. The optimum position of the skimmer varies depending on the diameter of the source chamber, and the skimmer geometry. However the typical spacing between the skimmer and nozzle is usually between 5 to 10 cm [64].

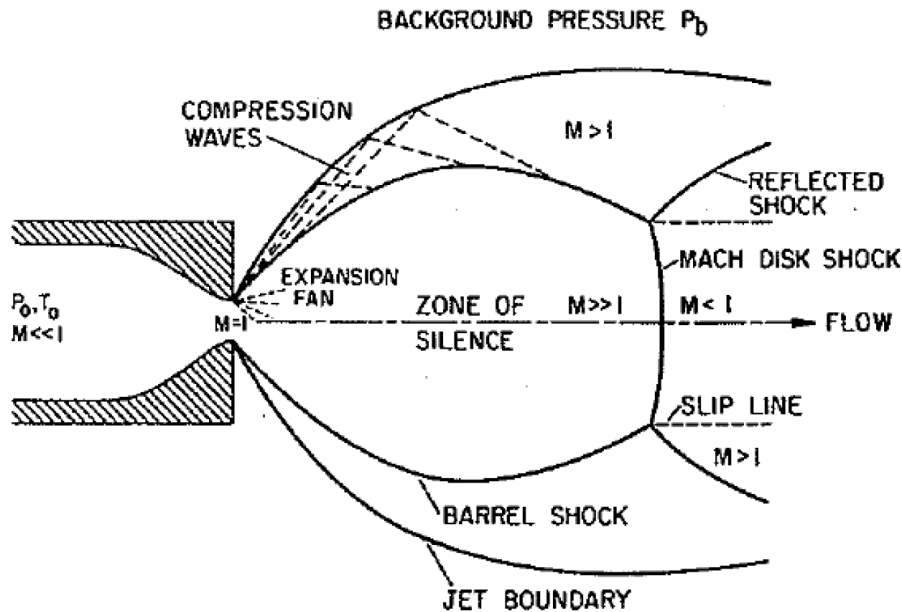


**Figure 1-1:** The structure of supersonic expansion of a gas (Adapted from Ref. [64] under permission)

Since it is assumed that the beam is adiabatically and isentropically expanded, enthalpy is the appropriate thermodynamic quantity to express the flow work, and conservation of the sum of the enthalpy and kinetic energy holds. As the gas expands, it internally cools ( $T \ll T_0$ ) and

enthalpy decreases, therefore the mean velocity increases. It can be shown that the maximum (terminal) velocity for the beam is approximately given by [64]:

$$V_{\infty} = \sqrt{\frac{2RT_0}{W} \frac{\gamma}{\gamma - 1}} , \quad (1.6)$$

with  $R$  the ideal gas constant and  $W$  the molar weight. When using mixtures, these values have to be replaced with their corresponding effective values for the mixture. Table (1-4) shows the values calculated for noble gases using the above formula at 300 K. It must be emphasized that these velocities are calculated for pure noble gases.

**Table 1-4:** Approximate translational velocity of supersonically expanded noble gases

<b>Noble gas</b>	<b>He</b>	<b>Ne</b>	<b>Ar</b>	<b>Kr</b>	<b>Xe</b>
<b>Velocity (m/s)</b>	1764.92	786.21	558.66	385.73	308.16
<b>Atomic mass (gr/mol)</b>	4.002602	20.1797	39.948	83.798	131.293

In a real experiment we mix the noble gas (carrier gas) and the desired sample (seed gas) in a way that the concentration of the sample is a few percent of the mixture. The noble gas cools quickly due to expansion and because of the collisions between the sample molecules with the carrier gas, the molecules cool down and follow the beam properties of the carrier gas. In addition, pre-mixing helps to prevent clustering of the sample molecules. However pre-mixing is not always easy for all samples due to the physical properties of the sample. In order to have enough seed gas molecules to mix, the vapor pressure of the sample at a reasonable and practical temperature must be high enough to allow a mixing ratio of at least a few percent in the carrier gas. For example, many of the metallic hydrides could be good candidates for Stark deceleration due to their large dipole moment, but having a low vapor pressure at practical temperature makes it difficult to directly mix them with the seed gas. However there are some other options such as picking up a sample produced outside the valve by laser ablation [52], heating, or electrical discharge. The pick-up method is not as efficient as pre-mixing since it captures fewer sample molecules, especially in the desired energy state.

In the Stark deceleration experiment, having lower initial velocities for the sample molecules is preferred. One method to produce lower initial velocities with the same carrier gas is to lower the

temperature of the nozzle. Obviously, the temperature cannot be lowered below the boiling point of either the seed gas (sample) or the carrier gas, because a gas phase mixture is needed. In Figure (1-2) I have calculated the estimated most probable speed of mixtures of  $\text{NH}_3$  in krypton and  $\text{CH}_3\text{F}$  in krypton at room temperature and near the boiling point of each sample. The boiling point for krypton is about 120 K, which is lower than the boiling point of the samples. The time of flight for a distance of 167.69 cm (which is our experimental distance between the nozzle and detection) is also plotted.

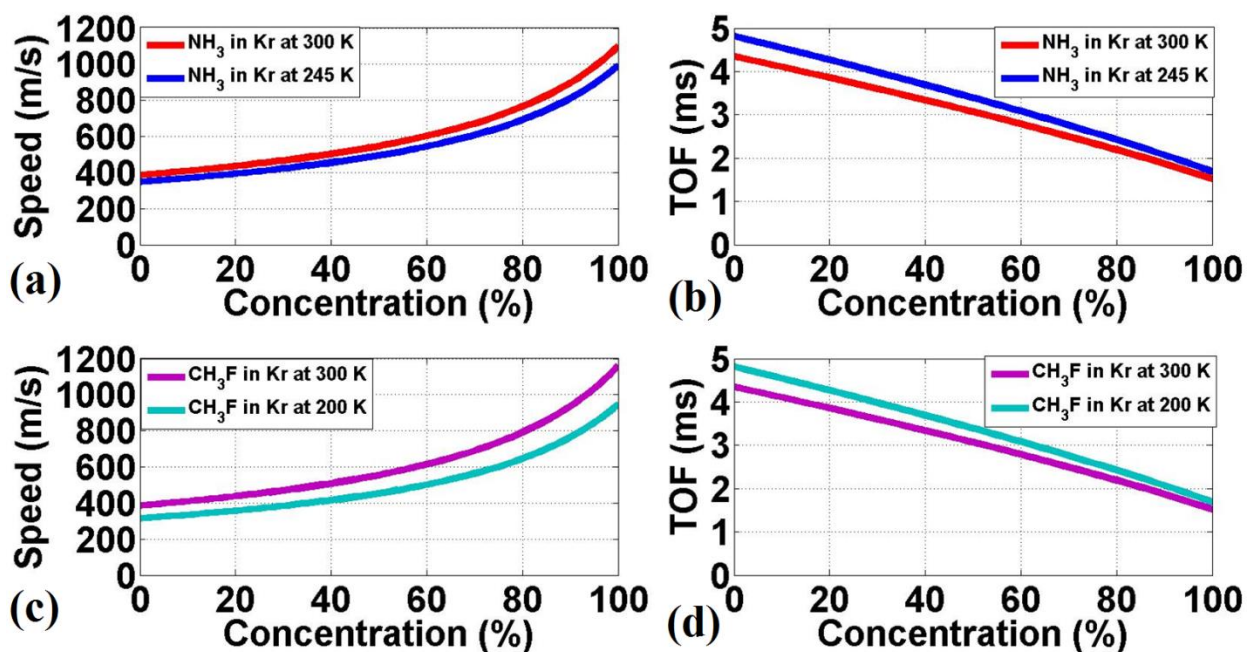


**Figure 1-2:** (a) Approximate velocity of supersonically expanded mixture of ammonia in krypton vs concentration of ammonia in the mixture at  $T=300$  K and  $T=245$  K. (b) The time of flight for part (a). (c) Approximate velocity of supersonically expanded mixture of methyl fluoride in krypton vs concentration of methyl fluoride in the mixture at  $T=300$  K and  $T=200$  K. (d) The time of flight for part (b).

The vapor pressure of a gas at different temperatures can be estimated by the Antoine equation [65]:

$$\text{Log } P = A - \frac{B}{T + C} \quad (1.7)$$

In which  $A$ ,  $B$ , and  $C$  are component-specific constants which also depend on the temperature range,  $P$  is the pressure, and  $T$  is the temperature,

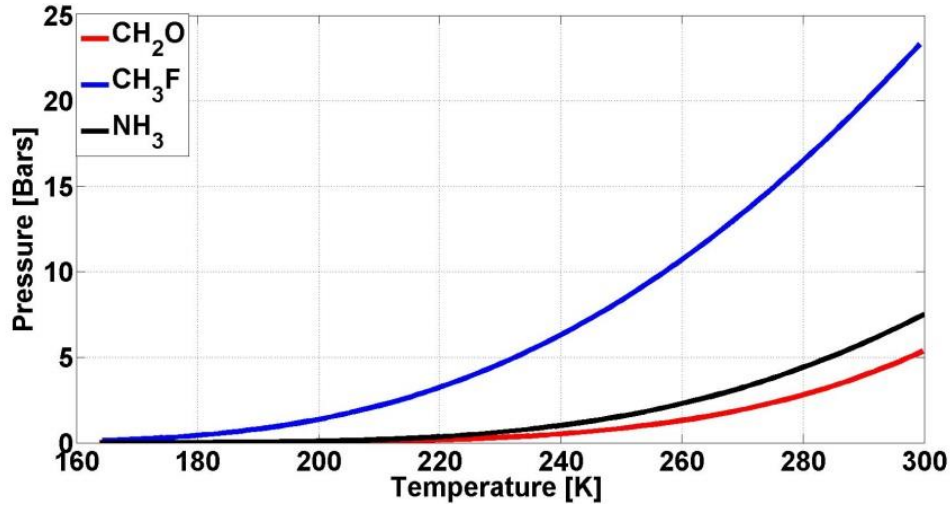


**Figure 1-3:** Vapor pressure versus temperature for formaldehyde, methyl fluoride, and ammonia

Another characteristic of seeded molecular beams is that if the stagnation pressure is not high enough, the seed gas and carrier gas will have slightly different beam properties. If a heavy seed gas is mixed with a light carrier gas at low to moderate pressures, the heavier molecules tend to lag behind the lighter molecules. If the pressure is too low, complete acceleration for the heavy molecule does not occur, and the so called “velocity slip” occurs. In addition to the velocity slip, the heavy species tend to be concentrated on the jet axis [63].

For an ideal gas, the speed of sound is given by:

$$a = \sqrt{\frac{\gamma RT}{W}} \quad (1.8)$$

and the Mach number  $M$  is  $v/a$ . Once  $M$  is known, all the thermodynamic variables in the beam can be calculated. Generally the Mach number varies at different distances from the nozzle:

$$M(x) = A \left( \frac{x - x_0}{d} \right)^{\gamma-1} - \frac{\frac{1}{2} \left( \frac{\gamma+1}{\gamma-1} \right)}{A \left( \frac{x-x_0}{d} \right)^{\gamma-1}} \quad (1.9)$$

In equation (1.9),  $d$  is the nozzle diameter, and  $A$  and  $x_0/d$  are flow properties of the beam which are gas dependent, and experimentally found for different heat capacity ratios [64].

**Table 1-5:** The relation between heat capacity ratio and the flow properties of a supersonically expanded molecular beam

$\gamma$	$x_0/d$	A
1.67	0.075	3.26
1.40	0.4	3.65
1.2857	0.85	3.96
1.2	1.00	4.29
1.1	1.6	5.25
1.05	1.8	6.44

Using  $M(x)$  we can find the thermodynamic quantities as below:

$$\begin{aligned}
 T &= T_0 \left(1 + \frac{\gamma - 1}{2} M^2\right)^{-1} \\
 V &= M \sqrt{\frac{\gamma R T_0}{W}} \left(1 + \frac{\gamma - 1}{2} M^2\right)^{-\frac{1}{2}} \\
 P &= P_0 \left(\frac{T}{T_0}\right)^{\gamma/\gamma-1} = P_0 \left(1 + \frac{\gamma - 1}{2} M^2\right)^{-\gamma/\gamma-1} \\
 \frac{\rho}{\rho_0} &= \frac{n}{n_0} = \left(\frac{T}{T_0}\right)^{\frac{1}{\gamma-1}} = K \frac{d^2}{x^2}
 \end{aligned} \tag{1.10}$$

where  $K$  is equal to 0.15 for monoatomic gas ( $\gamma = 5/3$ ), or 0.086 for a diatomic gas ( $\gamma = 7/5$ ). It can be seen that the density decreases with increasing distance from the nozzle as  $x^{-2}$ .

Figure (1-4) shows the results for the case of our nozzle with  $d = 250 \mu m$ , and assuming  $P_0 = 5 \text{ bars}$  and  $T_0 = 300 \text{ K}$  for Xenon carrier gas. The plots are truncated at the position of our skimmer (4.78 cm). As we can see from the figure, the velocity of the beam quickly reaches a maximum of 308.16 m/s, and the temperature drops close to zero.

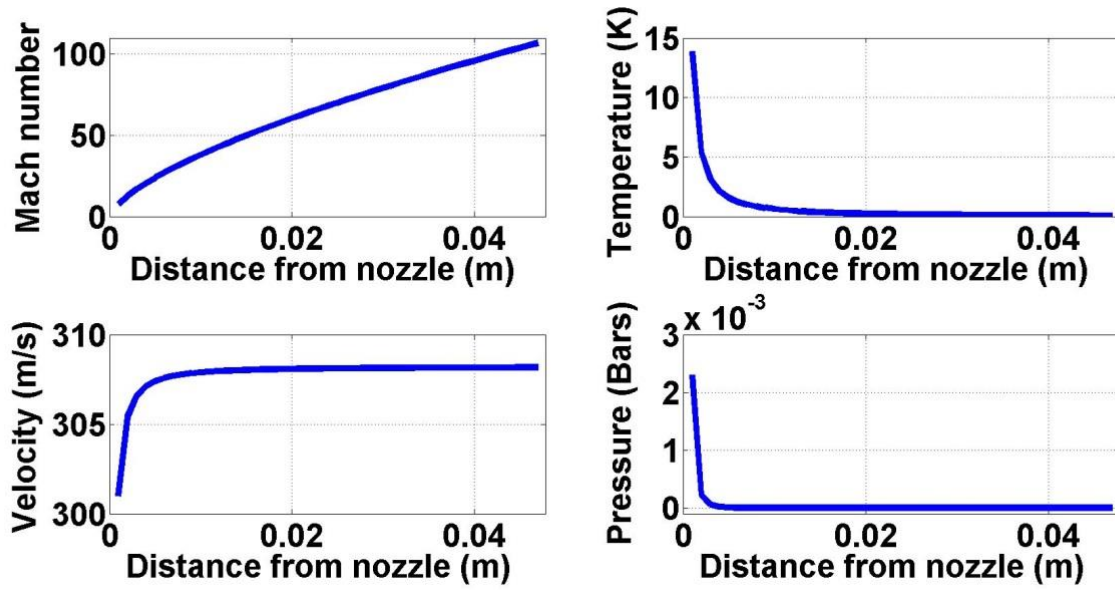


**Figure 1-4:** The variation of Mach number, velocity, internal temperature, and pressure of supersonically expanded Xenon beam after the nozzle with  $d = 250 \mu m$ , and assuming  $P_0 = 5 \text{ bars}$  and  $T_0 = 300 \text{ K}$

We can use Maxwell-Boltzmann distribution to obtain the velocity distribution of the supersonically expanded beam. The ratio of the longitudinal mean velocity of the supersonic beam to the longitudinal velocity width is called the parallel speed ratio ( $S_{||} = V_{\infty}/\Delta V_{||}$ ). For the direct deceleration methods such as Stark and Zeeman deceleration, we would like  $S_{||}$  to be as large as possible. In other words, since the longitudinal velocity acceptance of the decelerator is finite, a narrower velocity width is preferred. The parallel speed ratio can be predicted using:

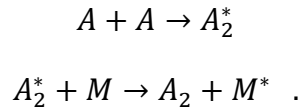
$$S_{||} \sim 5.4(P_0 d)^{0.32} \quad (1.11)$$

where  $P_0$  is in Torr, and  $d$  in  $cm$  [66]. For example if the stagnation pressure is 5 bars ( $\sim 3750 \text{ Torr}$ ), and  $d$  is  $250 \mu m$  ( $0.025 \text{ cm}$ ), the resulting beam spread is 4.33 %. The expression above suggests that if the stagnation pressure is higher, the longitudinal beam velocity spread is narrower. In addition to that, in 2008 Christen and Rademann showed that high pressure supersonic jets could provide a method for efficient generation of intense, slow, and extremely monochromatic molecular beams [67]. In their method they applied stagnation conditions slightly above the critical point of the gas. In a real system, the gas density in the reservoir influences the mutual particle interactions, and therefore results in a pressure dependent heat capacity ratio, which in turn affects the terminal velocity and velocity spread of the beam.

However many of the chemically interesting molecules have a critical point which is too high for this method to be achievable [67].

Based on considerations above, it appears that increasing the stagnation pressure, choosing a large nozzle exit diameter, and using heavy carrier gases should always be useful. But unfortunately it is not. The heavier noble gases have larger polarizabilities and therefore higher clustering rates. Higher clustering rates result in inefficient cooling, which means higher rotational temperature, larger mean velocity, and larger velocity spread.

The formation of a cluster has two steps [68]



The gas expands isentropically until it is supersaturated. Due to the collisions, an excited-state dimer forms. Then through a collision with a third body ( $M$ ) the complex becomes stabilized. The number of collisions plays an important role in cluster formation. It is impossible to exactly predict the cluster formation rate in a mixture of gases, but it is possible to investigate the effect of pressure, temperature and nozzle geometry on the cluster formation. A higher cluster density and a less rapid expansion will enhance the cluster formation rate. The so called ‘‘Hagena parameter ( $\Gamma^*$ )’’ is a measure that scales the clustering rate [69]:

$$\Gamma^* = kP_0 \frac{d^{0.85}}{(\tan \alpha)^{0.85} T_0^{2.29}} \quad (1.12)$$

where  $d$  is the nozzle diameter ( $\mu m$ ),  $\alpha$  the expansion half angle,  $P_0$  the backing pressure (mbar),  $T_0$  the stagnation temperature (Kelvin), and  $k$  a species-dependent constant related to bond formation. The formula shows that increasing the stagnation pressure or nozzle diameter will increase the clustering rate. If  $\Gamma^* < 100$  we can be sure that clustering does not happen [69]. For example, for Kr,  $k = 2890$ . Assume  $\alpha = 20^\circ$ ,  $T_0 = 300 K$ ,  $d = 250 \mu m$ , and  $P_0 = 5000 mbar$ . In this case  $\Gamma^* = 7917.8$ . For He which has a small  $k = 3.85$ , with the same condition  $\Gamma^* = 10.55$ . So the clustering rate for helium is much less than for krypton.

For more effective deceleration it is preferred to have lower initial velocities for the molecular beam. However, although heavier carrier gases (such as Kr or Xe) provide lower initial

velocities, they produce higher clustering rates. Therefore having some clusters in the beam is inevitable when using the heavy carrier gases. In our experiment we initially used a Residual Gas Analyzer (RGA) to detect the molecules. The presence of some clusters and also velocity slip for our molecular beam was observed. However due to the difficulties in interpreting the behaviour of our RGA for different gain settings, it was not possible to investigate them quantitatively.

The velocity dispersion ( $\Delta V_{||}$ ) is related to the translational temperature ( $T_{||}$ ):

$$\Delta V_{||} = \sqrt{\frac{2RT_{||}}{W}} \quad (1.13)$$

Generally, during the expansion through the nozzle, the translational temperature of the molecules thermalizes to  $T_{||}$  after several collisions, but the rotational temperature of the supersonic beam depends on the rotational structure of the molecule, carrier gas, and external sources of energy such as heating, excitation, etc. [70].

For our typical experimental conditions, the velocity dispersion of the supersonically expanded beam is about 7 % of the mean velocity of the beam. This ratio corresponds to  $\Delta V_{||} \sim 31 \text{ m/s}$  for a molecular beam pulse with a mean velocity of  $445 \text{ m/s}$ . If we assume the molar mass of krypton, this velocity dispersion corresponds to  $T_{||} \sim 5 \text{ K}$ .

### 1.3 About the SD radical

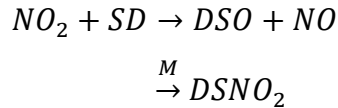
Investigating radicals has been an interesting subject for many physicists and chemists. Radicals play an important role in the studies of chemical reactions and collision experiments.

Unlike the majority of stable molecules, the ground electronic state of many free radicals has nonzero electronic orbital and/or spin angular momentum, which results in observable effects of coupling between rotation and electronic motion, such as  $\Lambda$ -doubling in a  $^2\Pi$  state and  $\rho$ -doubling in a  $^2\Sigma$  state. Experimental investigations of the spectra of free radicals range from ultraviolet (UV) spectroscopy, to electron paramagnetic resonance (EPR) and microwave spectroscopy [71].

Unlike OH and OD radicals [70][72][39][73][74], mercapto radicals (SH/SD) have not been extensively investigated. SH and SD have one of the smallest dipole allowed rotation-vibration transitions between the lowest vibrational states of the electronic ground state, which has made

them interesting for investigating their rotation-vibration transition probabilities [75]. These radicals play an important role in interstellar interactions, coal combustion, and the atmospheric sulphur cycle [76][77]. The physics and chemistry of sulfur-containing species in outer space is especially interesting because of their chemical activity and relatively high abundance [78]. The mercapto radical plays an important role in the ultraviolet photochemistry of sulfur-containing species released into the atmosphere from natural and anthropogenic sources [79].

The rate of some reactions, such as [80]:



has a negative temperature effect, which was interpreted as a result of the formation of a recombination intermediate [81]. The negative temperature effect is referred to reactions for which the reaction rate increases by decreasing the temperature. However, details of the reaction mechanism, especially below 200 K, have not yet been understood. Creation of cold SD beams will significantly contribute to understanding of the chemistry of the sulfur-containing molecules at medium low temperature (10 K – 100 K) relevant to atmospheric and interstellar chemistry.

Given the applications mentioned above and the relatively good Stark shift/mass ratio, we decided to choose the SD radical as one of our target molecules for Stark deceleration.

In our experiment, we preferred to work with SD radical due to the fact that it has a longer fluorescence lifetime (~ 250 ns), which makes the detection easier. The SH radical has a short fluorescence lifetime of about 3 ns.

## Chapter 2: Stark effect in polar molecules

The supersonically expanded molecular beam is directional. Supersonic expansion cools the internal degrees of freedom of the molecules, and brings the beam temperature to about 1 K. At this temperature molecules are in their ground electronic and vibrational states, and the few lowest rotational states are occupied. Stark deceleration is only applicable to polar molecules (with non-zero permanent electric dipole moment), and is a state selective method in which only molecules in the low field seeking states (with positive Stark shift), or only molecules in the high field seeking states (with negative Stark shift) are translationally decelerated or accelerated.

The absolute ground state of any molecule, which is very interesting for many scientists, is always a high field seeking state. Therefore molecules in the absolute ground state cannot be decelerated in a conventional DC Stark decelerator; instead we work with some of the lowest (low field seeking) rotational energy states which are also populated in the supersonically expanded beam. On the other hand, alternating gradient Stark decelerators only work for high field seeking states. Interestingly, AC Stark decelerators such as microwave decelerator are capable of decelerating molecules of both types, depending on the detuning of their frequency.

### 2.1 DC Stark effect of molecules

The effective Hamiltonian for a molecule in our desired range of external electric field (less than 150 kV/cm) is given by:

$$H = H_{Rotational} + H_{Stark} \quad (2.1)$$

The rotational basis set is used when calculating the Stark shift of the energy states. In a semi-classical approach, the rotational Hamiltonian for a rigid rotor, with  $I_a$ ,  $I_b$ , and  $I_c$  as its moments of inertia about the principal axes (a, b, c), is given by [82]:

$$H_{rigid\ rotor} = \hbar^2 \left( \frac{J_a^2}{2I_a} + \frac{J_b^2}{2I_b} + \frac{J_c^2}{2I_c} \right) = h(AJ_a^2 + BJ_b^2 + CJ_c^2) \quad (2.2)$$

where  $J_a$ ,  $J_b$ , and  $J_c$  are the angular momentum operators about the principal axes ( $J^2 = J_a^2 + J_b^2 + J_c^2$ ), and  $A$ ,  $B$ , and  $C$  are rotational constants (in units of wavenumber ( $cm^{-1}$ )) which are defined as:

$$A = \frac{h}{8\pi^2 I_a} \quad , \quad B = \frac{h}{8\pi^2 I_b} \quad , \quad C = \frac{h}{8\pi^2 I_c} \quad (2.3)$$

Table (2-1) classifies the molecules based on their rotational constants:

**Table 2-1:** Moments of inertia for different geometry types of molecules

Geometry	Moments of inertia	Rotational constants
<b>Linear top</b>	$I_b = I_c, I_a = 0$	$B = C, A = \infty$
<b>Asymmetric top</b>	$I_a \neq I_b \neq I_c$	$A \neq B \neq C$
<b>Spherical top</b>	$I_a = I_b = I_c$	$A = B = C$
<b>Oblate Symmetric top</b>	$I_a = I_b < I_c$	$A = B > C$
<b>Prolate symmetric top</b>	$I_a < I_b = I_c$	$A > B = C$

The Stark Hamiltonian is in the form:

$$H_{Stark} = -\vec{\mu}_E \cdot \vec{E} \quad (2.4)$$

where  $\vec{\mu}_E$  is the permanent electric dipole moment of the molecule. The difficulty of calculation arises from the fact that the vector  $\vec{\mu}_E$  is well defined in the body-fixed frame of the molecule while  $\vec{E}$  is defined in the lab frame of reference.

### 2.1.1 Symmetric top molecules

Polar symmetric top molecules are of interest in cold molecule studies for several reasons, one of which is that they are good candidates for qubits in the field of quantum computing [83]. In order to calculate the Stark effect for symmetric top molecules, one must first determine what their eigenstates are. If we define the lab frame coordinates as (X, Y, Z) and the molecule-fixed frame as (x, y, z), we can relate the two frames using the Euler angles of rotation (figure2-1). The time-dependent Schrodinger equation for a rotating molecule is:

$$H\psi_{rot}(\varphi, \theta, \chi) = E_{rot}\psi_{rot}(\varphi, \theta, \chi) \quad (2.5)$$

for which the eigen-functions are of the form [84] [92]:

$$\begin{aligned} \psi_{rot}(\varphi, \theta, \chi) &= \sqrt{\frac{2J+1}{8\pi^2}} D_{MK}^{J*}(\varphi, \theta, \chi) \\ D_{MK}^{J*}(\varphi, \theta, \chi) &\equiv e^{iM\varphi} d_{MK}^J(\theta) e^{iK\chi} \end{aligned} \quad (2.6)$$

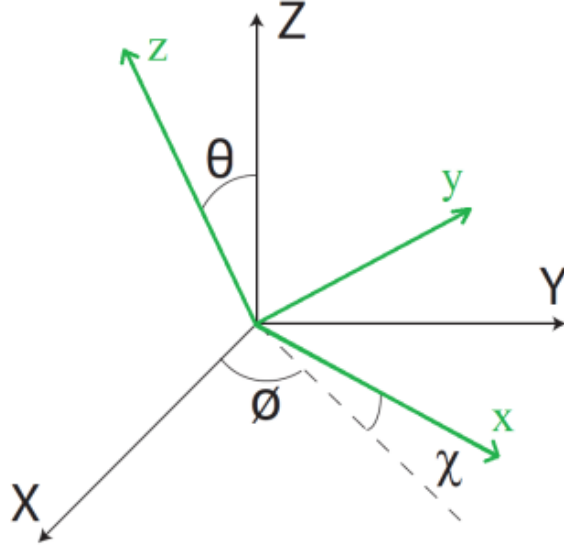


**Figure 2-1:** Molecular frame (x, y, z), lab frame (X, Y, Z), and the Euler angles between them

where  $D_{MK}^{J*}$  and  $d_{MK}^J$  are the Wigner D-matrices [92], and  $K$  ( $K = -J, -j + 1, \dots, J - 1, J$ ) and  $M$  ( $M = -J, -j + 1, \dots, J - 1, J$ ) are the projections of the orbital angular momentum ( $J$ ) on the molecular z-axis and the lab-frame Z-axis. Therefore  $J$ ,  $K$ , and  $M$  are good quantum numbers for representing the rotational energy of the symmetric top molecules. Using Dirac notation  $|JKM\rangle$  is the normalized wave-function:

$$|JKM\rangle = \sqrt{\frac{2J+1}{8\pi^2}} D_{MK}^{J*}(\varphi, \theta, \chi) \quad (2.7)$$

The semi-classical zero-field rotational energy of an oblate symmetric top is given by [82]:

$$E_{rot} = BJ(J+1) + (C-B)K^2 - \Delta_J J^2(J+1)^2 - \Delta_{JK} J(J+1)K^2 - \Delta_K K^4 \quad (2.8)$$

where  $\Delta_J$ ,  $\Delta_{JK}$ , and  $\Delta_K$  are centrifugal distortion constants. For a prolate top the rotational constant  $C$  has to be replaced with rotational constant  $A$ .

### 2.1.1.1 Stark effect in symmetric tops

The matrix elements for the Stark effect of symmetric tops are given by [84]:

$$\langle J_2 K_2 M_2 | -\vec{\mu}_E \cdot \vec{E} | J_1 K_1 M_1 \rangle = -\mu_E |\vec{E}| \langle J_2 K_2 M_2 | \cos\theta | J_1 K_1 M_1 \rangle \quad (2.9)$$

$$= -\mu_E |\vec{E}| (-1)^{M-K} \sqrt{(2J_1 + 1)(2J_2 + 1)} \begin{pmatrix} J_1 & J_2 & 1 \\ M & -M & 0 \end{pmatrix} \begin{pmatrix} J_1 & J_2 & 1 \\ K & -K & 0 \end{pmatrix}$$

The only non-vanishing matrix elements are:

$$\begin{aligned} \langle J + 1, K, M | \cos\theta | J, K, M \rangle &= \langle J, K, M | \cos\theta | J + 1, K, M \rangle \\ &= \left( \frac{[(J + 1)^2 - K^2][J + 1 - M^2]}{(J + 1)^2(2J + 1)(2J + 3)} \right)^{1/2} \end{aligned} \quad (2.10)$$

$$\langle J, K, M | \cos\theta | J, K, M \rangle = \frac{KM}{J(J + 1)} \quad (2.11)$$

$$\langle J - 1, K, M | \cos\theta | J, K, M \rangle = \left( \frac{[J^2 - K^2][J^2 - M^2]}{J^2(2J + 1)(2J - 1)} \right)^{1/2} \quad (2.12)$$

The results of the calculation for the  $J = 1$  state of  $CH_3F$  and  $CH_3CN$  as examples of the DC Stark shift in symmetric tops are shown in figure (2-2). Note that in the case of  $CH_3F$  and  $CH_3CN$ , the low field seeking states become high field seeking at higher electric fields. Therefore, the Stark deceleration of the molecules in these states is limited to electric fields below the turning point of the Stark shifts.

Equation (2.11) shows the first order Stark effect, and equations (2.10) and (2.12) refer to second order Stark effect. The first order Stark effect is non-zero for symmetric top molecules (for non-zero  $M$  and  $K$ ), while for linear molecules it is zero, unless the rotational state is mixed (such as  $\Lambda$ -doubling). The Stark shift calculation for SD radical (linear molecule) is presented in section (2.1.3.5).

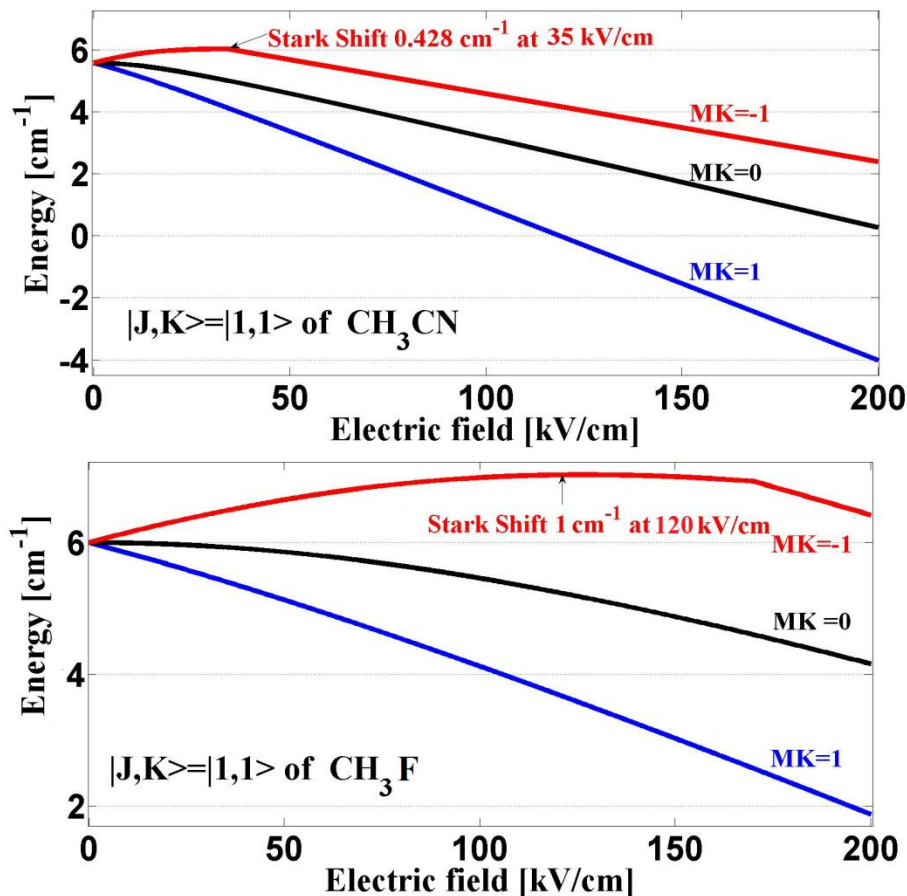


**Figure 2-2:** Stark shift in CH<sub>3</sub>CN ( $\mu_E = 3.92 D$ ) and CH<sub>3</sub>F ( $\mu_E = 1.86 D$ ) as examples for the Stark effect of the rotational levels in symmetric top molecules. The maximum Stark shift for the low field seeking branch (red) is shown on the graph.

### 2.1.1.2 Ammonia molecule

Ammonia was chosen for characterizing our Stark decelerator because it has been well studied, and has a low mass and a large dipole moment ( $m = 17.031 amu$ ,  $\mu_E = 1.47 Debye$ ).

### 2.1.1.3 The electronic ground state of ammonia ( $\tilde{X}$ )

Ammonia in its ground state has  $C_{3v}$  symmetry and a pyramidal structure with nitrogen as its apex and an equilateral triangle formed by the hydrogen atoms at its base. The inversion of the molecule is associated with a particular vibrational motion in the ground state that resembles the movement of an umbrella which is being opened and closed. During these oscillations the nitrogen atom tunnels through the barrier, and oscillation begins on the other side. The angle between the line connecting the centroid of the base with the apex and one of the  $NH$  bonds is

called umbrella angle ( $\rho$ ). The potential energy curve as a function of umbrella angle is illustrated in Figure (2-3) [85]:

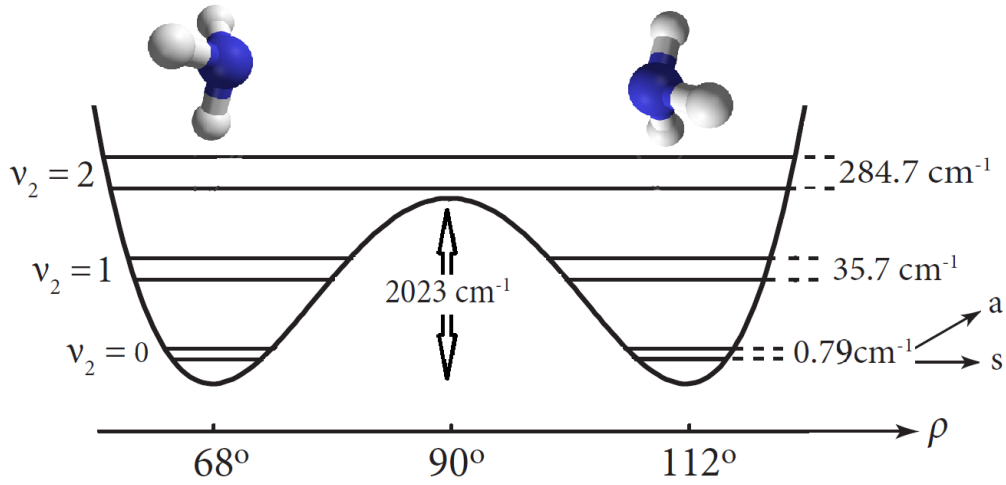


**Figure 2-3:** The potential curve as a function of umbrella angle in ammonia molecule

The finite barrier in the potential corresponds to the situation where the nitrogen atom is in the plane of the hydrogen atoms. Due to the coupling between the two wells by tunneling through a finite barrier, the eigenfunctions must be either symmetric or anti-symmetric. In order to obtain a symmetrized wave function with a well-defined parity, the  $|JKM\rangle$  functions linearly combine:

$$|JKM, \alpha\rangle = \frac{1}{\sqrt{2}} (|JKM\rangle + \alpha|J - KM\rangle) \quad (2.13)$$

where  $\alpha = \pm(-1)^J$  is the parity index and - and + refer to the symmetric and anti-symmetric inversions respectively. For the ammonia molecule the rotational eigenstates can be written as:

$$|JKM, \alpha\rangle = \frac{1}{\sqrt{1 + \delta_{K,0}}} (|JKM\rangle + \alpha|J - KM\rangle) \quad (2.14)$$

The relation between parity and  $\alpha$  is:

$$parity = \alpha(-1)^{J-K+1}. \quad (2.15)$$

The rotational energies of ammonia are given to a good approximation by [86]

$$E_v(J, K) = T_v + B_v J(J + 1) + (C_v - B_v)K^2 - D_{JJv}J^2(J + 1)^2 - D_{JKv}J(J + 1)K^2 - D_{KKv}K^4 \quad (2.16)$$

where  $T_v$  denotes the inversion splitting between symmetric and anti-symmetric inversion doublets (so-called  $l$ -doublet).  $C_v$  and  $B_v$  are the rotational constants, and  $D_{JJv}$ ,  $D_{JKv}$ , and  $D_{KKv}$  are centrifugal distortion constants.

**Table 2-2:** Rotational constants for  $\nu_2 = 0$  in the electronic ground state of ammonia

Rotational constant	Symmetric ( $cm^{-1}$ )	Anti-symmetric ( $cm^{-1}$ )
$T_v$	0	0.7932
$C_v$	6.22675	6.22950
$B_v$	9.94655	9.94160
$D_{JJv}$	$849.4 \times 10^{-6}$	$831.4 \times 10^{-6}$
$D_{JKv}$	$1577.0 \times 10^{-6}$	$1529.0 \times 10^{-6}$
$D_{KKv}$	$810.2 \times 10^{-6}$	$880.6 \times 10^{-6}$

For the vibronic ground state of ammonia it is common to use the labels  $\tilde{X}(0)$  for the symmetric doublet (its symmetry is  $A'_1$ ) and  $\tilde{X}(1)$  for the anti-symmetric doublet (its symmetry is  $A''_2$ ). It must be noted that for ammonia, due to the Pauli Exclusion Principle, ortho-ammonia only has  $A_1$  or  $A_2$  symmetries ( $K_{ortho} = 0, 3n$ ) whereas para-ammonia only has  $E$  symmetry ( $K_{para} = 3n \pm 1, 2$ ). In the case of  $\tilde{X}(0)$  with  $K_{ortho} = 0$ , all the *even*  $-J$  numbers are Pauli forbidden, while for  $\tilde{X}(1)$  with  $K_{ortho} = 0$ , all the *odd*  $J$  numbers are Pauli forbidden. Therefore when plotting the energy diagram, these states are absent.

#### 2.1.1.4 The $\tilde{B}$ electronic state of ammonia

Two photon excitation of ammonia from its ground state  $\tilde{X}$  to its  $\tilde{B}$  excited state was used for detection purposes in this thesis. The  $\tilde{B}$  state belongs to the  $D_{3h}$  symmetry group and has a flat geometry; therefore it has no tunnelling barrier and no inversion splitting. However strong rotation-vibration interactions at this level shift the rigid rotor energy levels and cause splitting. Considering this effect, the Hamiltonian of ammonia in its  $\tilde{B}$  state becomes [86]:

$$H_v^{rot} = T_v + B_v \vec{J}^2 + (C_v - B_v) J_z^2 - D_{JJv} \vec{J}^4 - D_{JKv} \vec{J}^2 J_z^2 - D_{KKv} J_z^2 - 2C_v \zeta_v \vec{l} \cdot \vec{J} + \frac{q_v}{2} \{ \vec{l}_+^2 \vec{J}_-^2 + \vec{l}_-^2 \vec{J}_+^2 \} \quad (2.17)$$

where  $B_v, C_v, D_{JJv}, D_{JKv}, D_{KKv}$  are the rotational and centrifugal distortion constants,  $q_v$  is the rotation-vibration constant,  $\zeta_v$  is the strength of the Coriolis interaction, and  $T_v$  is the term value of the vibronic state. The values for these constants are reported by Ashfold et al. [87].  $\vec{l}$  is the vibrational angular momentum along the molecular axis which is 0 for the ground state but  $\pm 1$  for the  $\tilde{B}$  state. In this formalism the wavefunctions are of the form  $|JKM\rangle|l\rangle$  [88].

The different possible symmetries for the  $\tilde{B}$  state are given in table (2-3) [89]

**Table 2-3:** Different possible symmetries for the  $\tilde{B}$  state of ammonia

$K$	$0, J \text{ even}$	$0, J \text{ odd}$	$6n \pm 1$	$6n \pm 2$	$6n \pm 3$	$6n \pm 6$
<b>Symmetry</b>	$A'_1$	$A'_2$	$E''$	$E'$	$A''_1 \oplus A''_2$	$A'_1 \oplus A'_2$

### 2.1.1.5 Stark effect of ammonia ( $NH_3$ )

For ammonia in the electronic ground state the inversion splitting of the rotational states should be considered, in which the rotation and inversion motions are superimposed on the vibrational structure. For the typical range of electric fields used in the Stark decelerator (low electric fields), and for a rotational state  $|JKM\rangle$ , the Stark shift for ammonia can be approximated by:

$$\Delta E_{stark} = \pm \sqrt{\left(\frac{W_{inv}}{2}\right)^2 + \left(\mu_E |\vec{E}| \frac{MK}{J(J+1)}\right)^2} \quad (2.18)$$

where  $W_{inv}$  is the inversion doubling [90]. However, in this thesis the method described by Hojer et al. for the ammonia molecule is used to calculate the energies more accurately [91]. In order to calculate the Stark shift for ammonia the method used for symmetric tops is modified to include the difference between the calculation of the Stark effect for ammonia and for typical symmetric tops, which is due to the inversion splitting in ammonia and the symmetric and anti-symmetric behaviour of its wavefunction. Table (2-4) summarizes the method of calculation considering the inversion splitting. Our target state is the  $|J = 1, K = 1\rangle$  in the vibrational and electronic ground state of  $\tilde{X}(\nu = 0)$ . For this state  $E_{vib_{a/s}}^M = 0$ ,  $E_{inv_s}^M = 0$ , and  $E_{inv_a}^M = 0.79 \text{ cm}^{-1}$ . Figure (2-4) shows the result of the calculation for the Stark effect in the  $|J = 1, K = 1\rangle$  state of ammonia.

**Table 2-4:** The structure of the Hamiltonian matrix for the Stark effect calculation of ammonia

$J + 1, K, M$		$J, K, M$		$J - 1, K, M$	
$a$	$s$	$a$	$s$	$a$	$s$
$E_{tot_a}^M(J+1, K)$	$a_{j+1}^M$	0	$b_{j+1}^M$	0	0
$a_{j+1}^M$	$E_{tot_s}^M(J+1, K)$	$b_{j+1}^M$	0	0	0
0	$b_{j+1}^M$	$E_{tot_a}^M(J, K)$	$a_j^M$	0	$b_j^M$
$b_{j+1}^M$	0	$a_j^M$	$E_{tot_s}^M(J, K)$	$b_j^M$	0
0	0	0	$b_j^M$	$E_{tot_a}^M(J-1, K)$	$a_{j-1}^M$
0	0	$b_j^M$	0	$a_{j-1}^M$	$E_{tot_s}^M(J-1, K)$

Where  $E_{tot_{a/s}}^M = E_{vib_{a/s}}^M + E_{inv_{a/s}}^M + E_{rot_{a/s}}^M$ .

$$a_j^M = -\mu |\vec{E}| \langle J, K, M | \cos\theta | J, K, M \rangle = -\mu |\vec{E}| \frac{KM}{J(J+1)}$$

$$b_j^M = -\mu|\vec{E}| \langle J-1, K, M | \cos\theta | J, K, M \rangle = -\mu|\vec{E}| \left( \frac{[J^2 - K^2][J^2 - M^2]}{J^2(2J+1)(2J-1)} \right)^{1/2} \quad (2.19)$$

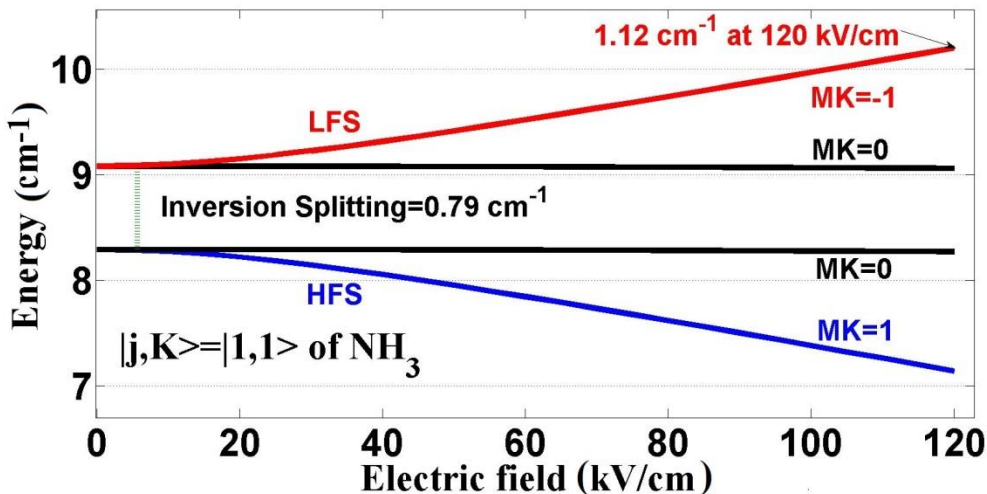


Figure 2-4: Stark effect in the  $|J = 1, K = 1\rangle$  state of ammonia ( $\mu_E = 1.47 D$ )

### 2.1.2 Asymmetric top molecules

Formaldehyde, which is an asymmetric top molecule, is a good sample for Stark deceleration experiments. Initially formaldehyde was one of the candidates for our deceleration experiments, but we decided to decelerate *SD* radical instead. However it is instructive to present the calculations done for this molecule. Since Formaldehyde is an asymmetric top molecule here I briefly explain the rotational structure and the Stark shift calculation for this molecule. The rotational Hamiltonian for asymmetric top molecules is given by:

$$H_{\text{rigid-rotation}} = AJ_a^2 + BJ_b^2 + CJ_c^2 \quad (2.20)$$

Where  $A$ ,  $B$ , and  $C$  are the rotational constants about  $a$ ,  $b$ , and  $c$ , the principal axis of the molecule [92]. This equation has the property that a rotation by  $180^\circ$  about  $a$ ,  $b$ ,  $c$  leaves the Hamiltonian unchanged, which means that all the asymmetric tops belong to the  $D_2$  symmetry group.

Table 2-5: Different representations for asymmetric top molecules

Representation	x	y	z	Most natural for
I	b	c	a	In the limit of a prolate top
II	c	a	b	Between prolate and oblate
III	a	b	c	In the limit of oblate top

The Schrodinger equation for an asymmetric top molecule has no trivial analytical solution. The field-free symmetric top wavefunctions ( $|JKM\rangle$ ) combine to make a basis set for the Hamiltonian matrix of an asymmetric top. However, the quantum number  $M$  still remains a good quantum number and there are no off-diagonal elements in  $M$  in the matrix. This means that the block of each value of  $M$  in the matrix can be diagonalized separately. It can be shown that the rotational eigenstates have a form as shown below [92]:

$$\begin{aligned}\psi_{JM}(\theta, \varphi, \chi) &= |J\tau M\rangle = \sum_K A_K |JKM\rangle \\ &= \frac{1}{\sqrt{2}} [|JKM\rangle + (-1)^s |J - KM\rangle]\end{aligned}\quad (2.21)$$

Where  $s = 0$  or  $1$  for non-zero  $K$  values, and  $s = 0$  for  $k = 0$ . The value of  $\tau$  is given by:

$$\tau = K_{-1} - K_1 \quad (2.22)$$

and runs from  $J$  to  $-J$  in unit steps.  $K_{-1}$  and  $K_1$  are the values of  $|K|$  in the limits of a prolate top and an oblate top respectively. The other familiar notation is in the form of  $|J_{K_{-1}K_1}M\rangle$ . The symmetrized basis functions can be constructed from the symmetric top basis functions by using Wang transformation [82]:

$$X = X^{-1} = \tilde{X} = \frac{1}{\sqrt{2}} \begin{bmatrix} \ddots & & \dots & & \ddots \\ & -1 & 0 & 1 & \\ \vdots & 0 & \sqrt{2} & 0 & \vdots \\ & -1 & 0 & 1 & \\ \ddots & & \dots & & \ddots \end{bmatrix} \quad (2.23)$$

$$\psi_{wang} = \tilde{X} \psi_{Symmetric\ top} \quad (2.24)$$

It can be shown that the secular determinant factors divide into four blocks, each belong to one of the symmetry species of the  $D_2$  group which are shown below [92]:

**Table 2-6:** Symmetry types of the  $D_2$  group

Secular determinant	K	s	$J_{even}$	$J_{odd}$
$E^+$	Even	0	A	$B_z$
$E^-$	Even	1	$B_z$	A
$O^+$	Odd	0	$B_x$	$B_y$
$O^-$	Odd	1	$B_y$	$B_x$

In order to make the rotational Hamiltonian matrix, the expectation value of the Hamiltonian for matrix elements are needed. Calculating the rotational energies and their Stark shift for asymmetric tops is more complicated than the symmetric tops. The general Hamiltonian takes the form:

$$H_{tot} = H_{rigid-rotation} + H_{distortion-rotation} + H_{Stark} \quad (2.25)$$

where  $H_{distortion-rotation}$  represents the non-rigid part of the rotational Hamiltonian, and is described using Watson's  $A$  reduction [93]:

$$\begin{aligned} \langle J, K, M | H_{distortion-rotation} | J, K, M \rangle \\ = \left[ \Delta_J (J(J+1))^2 + \Delta_{JK} J(J+1)K^2 + \Delta_K K^4 \right] \end{aligned} \quad (2.26)$$

$$\begin{aligned} \langle J, K+2, M | H_{distortion-rotation} | J, K, M \rangle &= \langle J, K, M | H_{distortion-rotation} | J, K+2, M \rangle \\ &= \left[ \delta_J J(J+1) + \frac{\delta_K}{2} ((K+2)^2 \right. \\ &\quad \left. + K^2) \right] \sqrt{J(J+1) - K(K+1)} \sqrt{J(J+1) - (K+1)(K+2)} \end{aligned} \quad (2.27)$$

where  $\Delta_J$ ,  $\Delta_{JK}$ ,  $\Delta_K$ ,  $\delta_J$ , and  $\delta_K$  are the centrifugal distortion constants. The dipole moment might have components along each of the principal axes of the molecule,  $\mu = (\mu_a, \mu_b, \mu_c)$ , hence we have to consider their effect.

$$H_{Stark} = H_{Stark}^a + H_{Stark}^b + H_{Stark}^c \quad (2.28)$$

The contribution from each element for the representation  $I$ , where  $\mu_a$  is the dipole moment component along the principal axis  $a$ , is given as below [82]:

$$\begin{aligned} \langle J, K, M | H_{Stark}^a | J, K, M \rangle &= -\mu_a |\vec{E}| \frac{KM}{J(J+1)} \\ \langle J+1, K, M | \cos\theta | J, K, M \rangle &= \langle J, K, M | H_{Stark}^a | J+1, K, M \rangle \\ &= -\mu_a |\vec{E}| \left( \frac{[(J+1)^2 - K^2][(J+1)^2 - M^2]}{(J+1)^2(2J+1)(2J+3)} \right)^{1/2} \\ \langle J, K+1, M | H_{Stark}^b | J, K, M \rangle &= -\mu_b |\vec{E}| \frac{M}{2J(J+1)} \sqrt{(J-K)(J+K+1)} \\ \langle J+1, K \pm 1, M | H_{Stark}^b | J, K, M \rangle &= \pm \mu_b |\vec{E}| \frac{\sqrt{(J \pm K + 1)(J \pm K + 2)} \sqrt{(J+1)^2 - M^2}}{2(J+1) \sqrt{2(J+1)(2J+3)}} \end{aligned}$$

$$\begin{aligned}
\langle J, K \pm 1, M | H_{Stark}^c | J, K, M \rangle &= \pm i \frac{M \sqrt{(J \mp K)(J \pm K + 1)}}{2J(J + 1)} \mu_c |\vec{E}| \\
\langle J + 1, K \pm 1, M | H_{Stark}^c | J, K, M \rangle &= -i \frac{\sqrt{((J \pm K + 1)(J \pm K + 2))} \sqrt{(J + 1)^2 - M^2}}{2(J + 1) \sqrt{(2J + 1)(2J + 3)}} \mu_c |\vec{E}|
\end{aligned}
\tag{2.29}$$

In order to find the rotational energy eigenvalues, first the rotational matrix elements as mentioned above for the matrix with the basis of a symmetric top are needed. Then the result is transformed to the basis set of the asymmetric top using a Wang transformation:

$$H_{Wang-rotation} = \tilde{X} (H_{rigid-rotation} + H_{distortion-rotation}) X \tag{2.30}$$

The result basis has four sub-matrices corresponding to the four different symmetries. By diagonalizing the transformed Hamiltonian we obtain the rotational eigenvalues and eigenstates, considering the distortions. In order to calculate the Stark effect, again the Stark Hamiltonian matrix in the symmetric top basis is constructed, and then it is transformed via Wang transformation. Then we transform the summation of the Wang-transformed rotational and Stark matrices into the basis set of which the rotational matrix is diagonal. Now by diagonalizing this matrix for different values of the electric field we can find the Stark shift of each rotational state. This method is used to calculate the Stark shift for Formaldehyde as shown in figure (2-5).

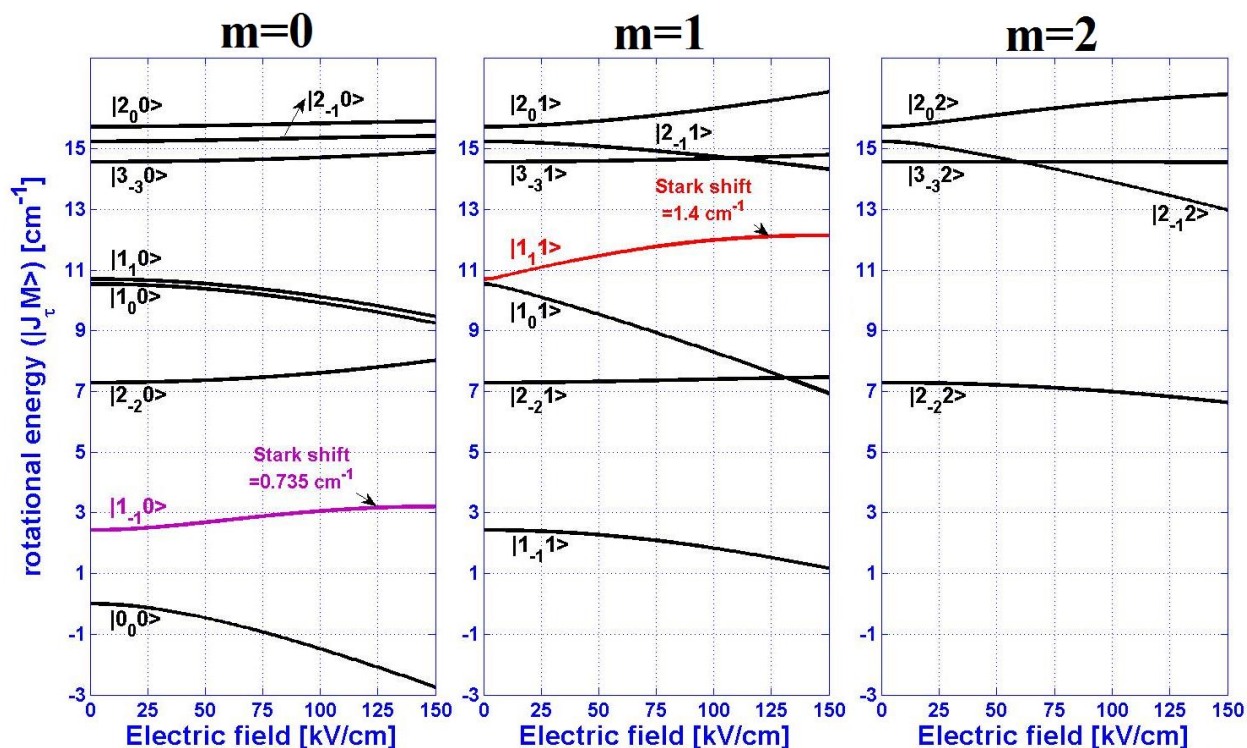


**Figure 2-5:** Stark shift of formaldehyde molecule in different rotational states ( $\mu_E = 2.34 D$ ). Left panel for  $m=0$ , middle panel for  $m=1$ , and the right panel for  $m=2$ . Higher  $m$  numbers are not shown. The lowest LFS states of  $J=1$  are shown with a different color.

### 2.1.3 Linear molecules

As a sample for Stark deceleration we used the *SD* radical which is a linear molecule. In order to discuss the Stark effect in linear molecules, first it is necessary to understand the coupling of the electronic and rotational motions of the diatomic molecule, so called Hund's cases. The Hund's cases are idealized cases that describe the different ways that the angular momenta can be coupled in a diatomic molecule[94]. Here are the definitions of the angular momenta in use:

$S$ , Total spin electronic angular momentum

$\Sigma$ , Projection of  $S$  on the internuclear axis

$L$ , Electronic orbital angular momentum

$\Lambda$ , Projection of  $L$  on the internuclear axis

$J$ , Total angular momentum ( $J = L + S + R$ )

$N$ , Total orbital rotational angular momentum ( $N = J - S$ )

$R$ , Nuclear rotational angular momentum ( $R = N - L$ )

$\Omega$ , Projection of  $(L + S)$  on the internuclear axis

$J_a=L + S$ , in the absence of coupling to the internuclear axis

$I$ , Nuclear spin

There are five major Hund's cases (a, b, c, d, e). Considering the coupling of the nuclear spin ( $I$ ) will extend these cases further. Generally, for a given diatomic molecule, the strengths of the rotational coupling of  $L$  and  $S$  to  $J$ , spin-orbit coupling, and electrostatic coupling of  $L$  to the internuclear axis determine which case is the proper case:

**Table 2-7:** Hund's cases for linear molecules

Hund's case	Condition	Proper quantum number
(a)	$A_v\Lambda \gg B_vJ$	$\beta, \Lambda, S, \Sigma, J, \Omega$
(b)	$A_v\Lambda \ll B_vJ$	$\beta, \Lambda, N, S, J$
(c)	$A_v\Lambda \gg \Delta E_{el}$	$\beta, (J_a), J, \Omega$
(d)	$B_vJ \gg \Delta E_{el}$	$\beta, N, S, L, R, J$
(e)	$A_v\Lambda \gg B_vJ \gg \Delta E_{el}$	$\beta, J_a, R, J$

Where  $B_v$  is the rotational constant and  $A_v$  is the spin-orbit coupling coefficient. These numbers depend on the vibrational quantum number ( $v$ ). The quantum number  $\beta$  represents all the other quantum numbers such as vibrational and electronic. In addition to the quantum number above sometimes  $M_J$ , the projection of  $J$  on the space-fixed axis  $Z$  (such as the external field direction), is used.  $M_J$  takes the values  $-J, -J + 1, \dots, +J$ . In the absence of the external field and for a given  $J$  the rotational energies are degenerate in  $M_J$ .

Our target molecule for Stark deceleration was  $SD$  radical. Here I also present the values for  $SH$  radical in the brackets, just in case one is interested. For this linear molecule in the ground state ( $^2\Pi_{3/2}$ ) the ratio of  $A_v/B_v \approx 76.887$  (39.836), which indicates that its Hund's case is closer to the case (a). However, as the  $J$  increases it gets closer to the Hund's case (b). Here I briefly explain the Hund's cases (a) and (b).

### 2.1.3.1 Hund's case (a)

In this case,  $L$  is strongly coupled to the molecular axis due to the electrostatic forces, while  $S$  is strongly coupled to  $L$  through spin-orbit coupling. Also, as it is shown in figure (2-6),  $\Omega = \Lambda + \Sigma$ . The total angular momentum ( $J$ ) is the result of the coupling between  $\Omega$ , which is along the molecular axis, and  $R$ . The nutation of  $R$  and  $\Omega$  about  $J$  are much slower than the precession of  $L$

and  $S$  about the molecular axis. The so called  $\Lambda$ -doubling for this case happens due to the fact that the precession of  $L$  and  $S$  about the molecular axis can proceed in either direction, in a way that their projections on the molecular axis can be positive or negative ( $\pm\Lambda, \pm\Sigma$ ). This two-fold degeneracy for  $\Lambda$  is called  $\Lambda$ -doubling. Also, as a result, the sign of  $\Omega$  can also be positive or negative. This is so called  $\Omega$ -doubling.

Considering the hyperfine structure by including the nuclear spin ( $I$ ), the total angular momentum  $F$  of the molecule will be  $F = J + I$  [95]. As a result each  $\Lambda$ -doublet component of the rotational state splits further due to the hyperfine interaction. Also the projection of the  $F$  on the external quantization axis (such as electric field direction) is shown by  $M_F$  which take the values  $-F, -F + 1, \dots, F$ . When there is no external quantization axis the rotational level is degenerate in  $M_F$ .

The diagram below describes the situation for Hund's case (a):

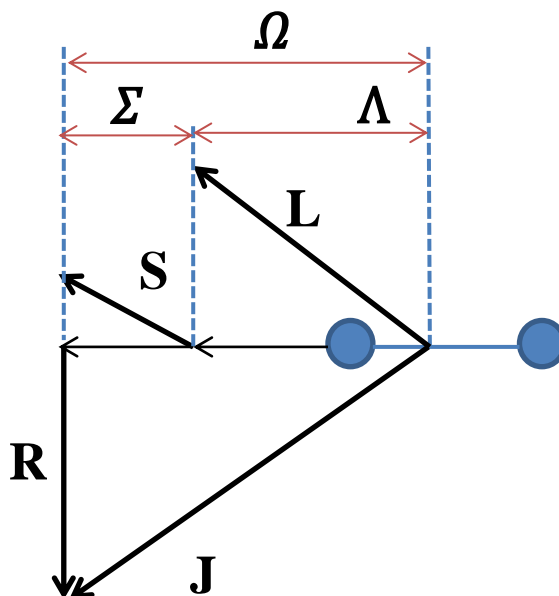


**Figure 2-6:** Angular momentum coupling scheme for Hund's case (a)

### 2.1.3.2 Hund's case (b)

This case is a proper choice when spin-orbit coupling does not exist or it is very weak ( $\Lambda = 0$  or  $\Lambda \approx 0$ ), and  $S$  is non-zero. Since  $S$  no longer couples to the internuclear axis  $\Omega$  is not defined. In

this picture,  $\Lambda$  couples to  $R$  and forms  $N$ , such that the projection of  $N$  on the inter-nuclear axis is  $\Lambda$ . Then  $N$  couples with  $S$  to form  $J$ . The rotational Hamiltonian is:

$$\begin{aligned} H_{rot} &= B_v R^2 = B_v [N - L]^2 + \gamma N \cdot S \\ &= B_v [N(N + 1) + L^2 - 2N \cdot L] + \gamma N \cdot S \end{aligned} \quad (2.31)$$

in which  $\gamma N \cdot S$  is the spin-rotation interaction which applies when  $S = 1/2$  and  $N \geq 1$ . In this case each  $N$  level splits into a so called  $\rho$ -doublet, characterized by the total angular momentum  $J$ , such that the so called  $F_1(J)$  corresponds to series with  $J = N + 1/2$ , and the so called  $F_2(J)$  corresponds to series with  $J = N - 1/2$ . The parity of the rotational levels follows:

$$parity = (-1)^N \quad (2.32)$$

The spin-rotation splitting also exists for  $S \geq 1$  which is more complicated, but is not discussed here. Figure (2-7) shows the vector diagram for Hund's case (b):

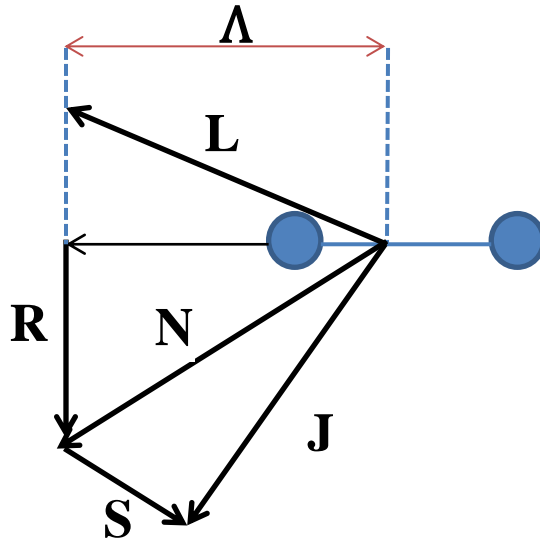


**Figure 2-7:** Angular momentum coupling scheme for Hund's case (b)

### 2.1.3.3 Energy level structure of $SD$ radical in the electronic ground state

$SD$  radical is best described by Hund's case (a) for low rotational states in the electronic ground state. The configuration of the electrons in the ground state of the  $SD$  molecule ( $X^2\Pi_{3/2}$ ) is in the form of:  $(1\sigma)^2(2\sigma)^2(3\sigma)^2(1\pi)^4(5\sigma)^2(2\pi)^3$ . The electronic energy level structure is shown in figure (2-8) [96]:

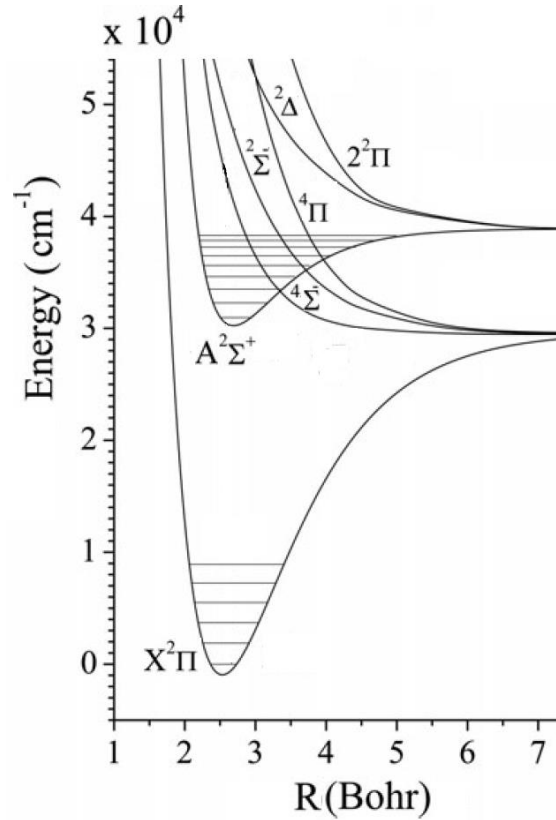


**Figure 2-8:** Electronic energy level diagram for *SD* radical [96]

Since  $(2\pi)^3$  is an open shell, the total electronic ( $L$ ) and spin ( $S$ ) angular momenta are not zero. The projections of  $L$  on the molecular axis are  $\Lambda = \pm 1$ , and the projections of  $S$  on the molecular axis are  $\Sigma = \pm 1/2$ . Therefore the electronic ground state is denoted by  $X^2\Pi$ . The  $^2\Pi$  state has two spin-orbit manifolds  $F_1$  and  $F_2$  ( $^2\Pi_{1/2}$  and  $^2\Pi_{3/2}$ ) corresponding to  $\Omega = \pm 1/2$  and  $\Omega = \pm 3/2$  respectively, which arise from the coupling of  $\Lambda$  and  $\Sigma$  along the inter-nuclear axis. The rotational energy of the molecule is given by  $H_{Rotation}$  as [39]:

$$H_{Rotation} = B_v(\vec{J} - \vec{L} - \vec{S})^2 + A_v\vec{L} \cdot \vec{S} \quad (2.33)$$

$B_v$  is the rotational constant,  $A_v$  is the spin-orbit constant, and  $\nu$  is the vibrational quantum number. For *SD* vibrational ground state  $B_v = 146885.297 \text{ MHz}$  and  $A_v = -11293540 \text{ MHz}$ . (for *SH*,  $B_v = 283587.62 \text{ MHz}$  and  $A_v = -11297139 \text{ MHz}$ ). The negative spin-orbit constant indicates that the  $^2\Pi_{3/2}$  state has lower energy than  $^2\Pi_{1/2}$ . This energy difference is  $388 \text{ cm}^{-1}$  (for *SH*,  $375 \text{ cm}^{-1}$ ) [97]. There are only two rotational degrees of freedom for linear molecules. As a result we can set the Euler angle  $\chi$  to zero and use the rigid body rotational basis functions [92]:

$$|J\Omega M_J\rangle = \left(\frac{2J+1}{4\pi}\right)^{1/2} D_{M_J,\Omega}^{J*}(\phi, \theta, 0) \quad (2.34)$$

In order to use a symmetrized wave function a linear combination of the wave functions is used:

$$|J\Omega M_J \alpha\rangle = \frac{1}{\sqrt{2}} (|J\Omega M_J\rangle + \alpha |J - \Omega M_J\rangle) \quad (2.35)$$

Where  $\alpha = \pm 1$  defines the symmetry that is labeled by  $e$  and  $f$  for  $\alpha = +1$  and  $\alpha = -1$  respectively, and is related to the parity by:

$$Parity = \alpha(-1)^{J-S} \quad (2.36)$$

Toby et. al calculated the eigenfunctions of the rotational Hamiltonian for the  $OH$  molecule [72] which has the same structure as  $SD$  radical. However here the work done on the  $OH$  molecule presented by Van De Meerakker [39] is applied to the  $SD$  radicals. Following his notation:

$$\begin{aligned} |{}^2\Pi_{3/2}, JM_J \alpha\rangle &= C_1(J) \left| J\Omega = \frac{1}{2}, M_J \alpha \right\rangle + C_2(J) \left| J\Omega = \frac{3}{2}, M_J \alpha \right\rangle \\ |{}^2\Pi_{1/2}, JM_J \alpha\rangle &= -C_2(J) \left| J\Omega = \frac{1}{2}, M_J \alpha \right\rangle + C_1(J) \left| J\Omega = \frac{3}{2}, M_J \alpha \right\rangle \end{aligned} \quad (2.37)$$

Where by defining  $Q = A_v/B_v$  and  $P = (4(J + 1/2)^2 + Q(Q - 4))^{1/2}$ ,

$$\begin{aligned} C_1(J) &= \left(\frac{P + Q - 2}{2P}\right)^{1/2} \\ C_2(J) &= \left(\frac{P - Q + 2}{2P}\right)^{1/2} \end{aligned} \quad (2.38)$$

This mixing of the basis wavefunctions with different values for  $\Omega$  occurs due to the spin-orbit term in the rotational Hamiltonian. However, for low values of  $J$  the degree of the mixing is low and  $\Omega$  can be considered as a good quantum number. The energies of the rotational levels are given by:

$$E({}^2\Pi_{3/2}, JM_J \alpha) = B_v \left[ \left(J + \frac{1}{2}\right)^2 - \frac{P}{2} - 1 \right]$$

$$E(^2\Pi_{1/2}, JM_J\alpha) = B_v \left[ \left( J + \frac{1}{2} \right)^2 + \frac{P}{2} - 1 \right] \quad (2.39)$$

By considering the gyroscopic effect of  $J$  on  $S$  and  $L$ , the degeneracy of the rotational energies with  $\alpha = +1$  and  $\alpha = -1$  are lifted [98][99]. This effect results in off-diagonal elements in  $\Lambda$ , which results in mixing the electronic ground state with the first electronically excited state. As a result  $|^2\Pi_{\Omega}, JM_J\alpha = +1\rangle$  and  $|^2\Pi_{\Omega}, JM_J\alpha = -1\rangle$  split. This splitting forms a  $\Lambda$ -doublet which is much smaller than the rotational energy spacing. For low  $J$  numbers energies with  $\alpha = -1$  (with symmetry label  $f$ ) are higher in energy than  $\alpha = +1$  (with symmetry label  $e$ ). For the case of  $SD$  radical, the target state is  $^2\Pi_{3/2}, J = 3/2$  for which the splitting is  $0.00166 \text{ cm}^{-1}$  (For  $SH$  and the same state  $0.00370 \text{ cm}^{-1}$ ). For further information on the rotational spectrum of  $SH$  and  $SD$  the works done by Klisch et al. [97], and also by D.A. Ramsay are suggested [100].

#### 2.1.3.4 Energy level structure of the $SD$ radical in the first electronic excited state

The electronic structure of the  $SD$  molecule in its first excited state ( $A^2\Sigma^+$ ) is  $(1\sigma)^2(2\sigma)^2(3\sigma)^2(1\pi)^4(5\sigma)^1(2\pi)^4$  which results from the excitation of the valence electron from  $5\sigma$  to  $2\pi$ . Because for this state  $\Lambda = 0$ , it is best described by Hund's case (b). The interaction between the orbital angular momentum ( $N$ ) and the electron spin results in  $\rho$ -doubling as described in Hund's case (b). The rotational energies for the  $A^2\Sigma^+$  state are given by [100]:

$$\begin{aligned} F_1(N) &= B_v N(N+1) - D_v N^2(N+1)^2 - \frac{1}{2} \gamma_v N \\ F_2(N) &= B_v N(N+1) - D_v N^2(N+1)^2 - \frac{1}{2} \gamma_v (N+1) \end{aligned} \quad (2.40)$$

Where  $F_1(N)$  refers to the  $J = N + 1/2$  components,  $F_2(N)$  refers to  $J = N - 1/2$  components,  $B_v$  and  $D_v$  are rotational constants, and  $\gamma_v$  is the spin-rotation constant. For  $A^2\Sigma^+$  vibrational ground state of  $SD$  ( $SH$ ) are:

$$B_0 = 4.304 \text{ cm}^{-1} (8.283 \text{ cm}^{-1}), D_0 = 0.00018 \text{ cm}^{-1} (0.00066 \text{ cm}^{-1}), \text{ and } \gamma_0 = 0.163 \text{ cm}^{-1} (0.313 \text{ cm}^{-1}).$$

Figure (2-9) shows the energy level diagram for the vibrational ground state of  $X^2\Pi_{1/2 \text{ or } 3/2}$  and  $A^2\Sigma^+$ :

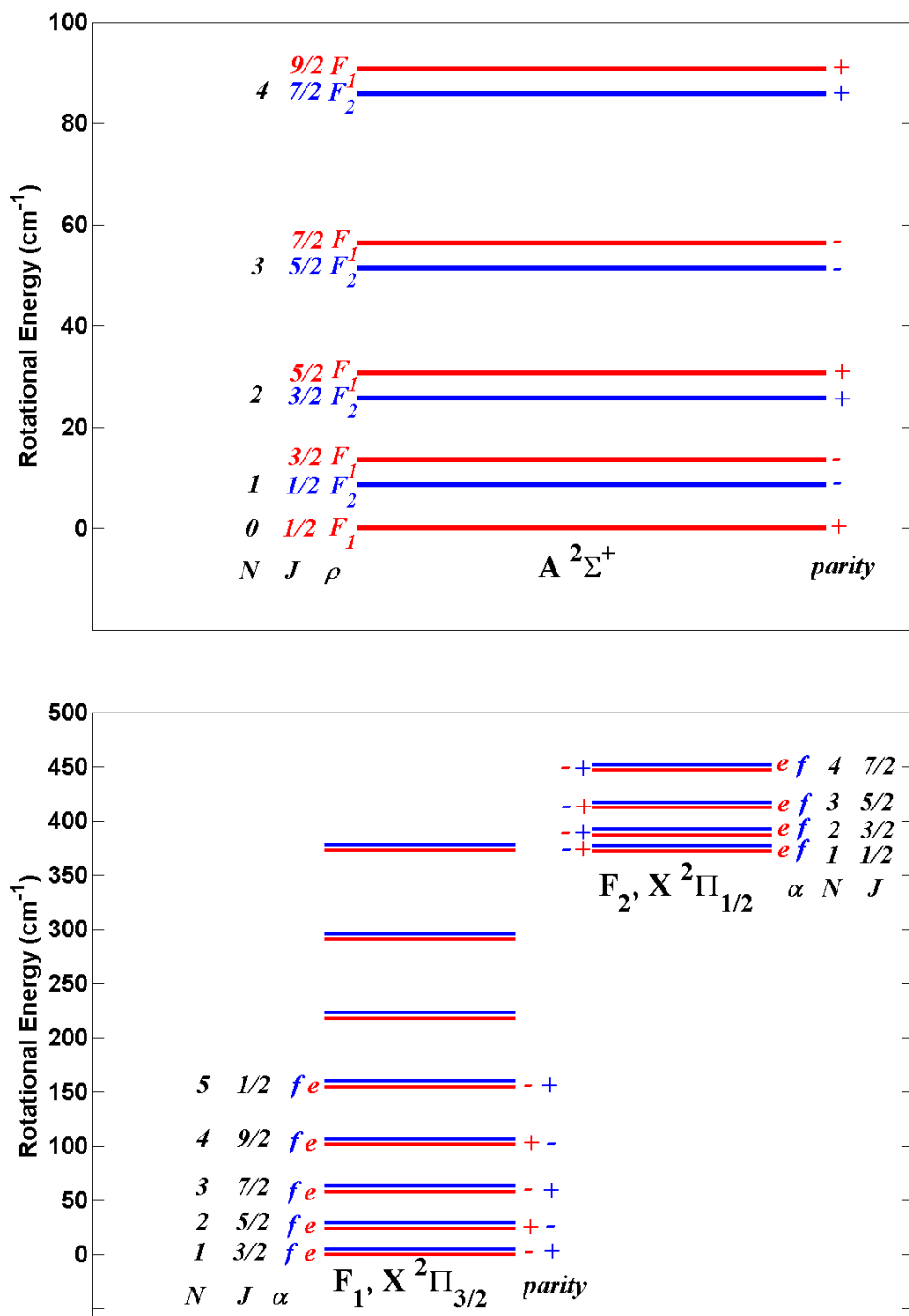


**Figure 2-9:** the energy level diagram for the vibrational ground state of  $X^2\Pi_{1/2 \text{ or } 3/2}$  and  $A^2\Sigma^+$ . Note that the splitting in  $\rho$ -doubling and  $\Lambda$ -doubling are exaggerated to be visible.

### 2.1.3.5 The Stark effect of the $SD$ radical

In the presence of external electric fields with magnitudes greater than  $1 \text{ kV/cm}$  the total angular momentum ( $J$ ) decouples from the nuclear spin ( $I$ ), hence the hyperfine structure of the polar molecules can be ignored for Stark shift calculations. Therefore for  $X^2\Pi_{1/2}$  or  $3/2$  the symmetrized eigenfunctions introduced for Hund's case (a) can be used ( $|J\Omega M_J \alpha\rangle = \frac{1}{\sqrt{2}}(|J\Omega M_J\rangle + \alpha|J - \Omega M_J\rangle$ ). These wavefunctions are similar to the ones for the symmetric tops (the only difference is that  $K$  is replaced by  $\Omega$ ). Assuming that the external field is along the  $z$ -axis in the lab frame, using the Wigner rotation matrices the selection rules are:

$$J = J' \text{ or } J = J' \pm 1, \quad M_J = M_J', \quad \Omega = \Omega' \quad (2.41)$$

However, due to the large rotational spacing in  $SD$ , the couplings between  $J = J' \pm 1$  are weak and can be neglected under typical Stark decelerator electric field conditions. Therefore for calculating the Stark effect of our target state  $X^2\Pi_{3/2}$  only  $\Lambda$ -doublet components ( $e$  and  $f$ ) of each  $M_J$  are dealt with:

$$\begin{aligned} \langle {}^2\Pi_{3/2}, JM_J \alpha | -\mu \cdot E | {}^2\Pi_{3/2}, JM_J \alpha' \rangle &= \left( C_1(J) \left\langle J\Omega = \frac{1}{2}, M_J \alpha \right| + C_2(J) \left\langle J\Omega = \frac{3}{2}, M_J \alpha \right| \right) \\ &- |\mu||E| \cos\theta \left( C_1(J) \left\langle J\Omega = \frac{1}{2}, M_J \alpha' \right| + C_2(J) \left\langle J\Omega = \frac{3}{2}, M_J \alpha' \right| \right) \\ &= -|\mu||E| \left[ \left( C_1(J)^2 \left\langle J\Omega = \frac{1}{2}, M_J \alpha \right| \cos\theta \left\langle J\Omega = \frac{1}{2}, M_J \alpha' \right| \right) \right. \\ &\quad + \left( C_2(J)^2 \left\langle J\Omega = \frac{3}{2}, M_J \alpha \right| \cos\theta \left\langle J\Omega = \frac{3}{2}, M_J \alpha' \right| \right) \\ &\quad + \left( C_1(J)C_2(J) \left\langle J\Omega = \frac{1}{2}, M_J \alpha \right| \cos\theta \left\langle J\Omega = \frac{3}{2}, M_J \alpha' \right| \right) \\ &\quad \left. + \left( C_2(J)C_1(J) \left\langle J\Omega = \frac{3}{2}, M_J \alpha \right| \cos\theta \left\langle J\Omega = \frac{1}{2}, M_J \alpha' \right| \right) \right] \end{aligned} \quad (2.42)$$

The result will be in the form of [39]:

$$\begin{pmatrix} E_\Lambda & X \\ X & 0 \end{pmatrix} \quad (2.43)$$

Where  $E_\Lambda$  is the  $\Lambda$ -doublet splitting of the  $X^2\Pi_{3/2}$  for each  $M_J$ , and  $X$  is given by:

$$X = \langle {}^2\Pi_{3/2}, JM_J e | -\mu \cdot E | {}^2\Pi_{3/2}, JM_J f \rangle = -|\mu||E| \frac{M_J}{J(J+1)} \left( \frac{C_1(J)^2 + 3C_2(J)^2}{2} \right) \quad (2.44)$$

The target state in the ground state of the *SD* radical is  $X^2\Pi_{3/2}, J = 3/2$ , for which  $C_1(3/2) = 0.0413$  and  $C_2(3/2) = 0.9991$ . The dipole moment of *SD* radical is  $0.76 D$ , and  $E_A = 50 \text{ MHz}$  for  $X^2\Pi_{3/2}, J = 3/2$  [97]. Note that the Stark shift can be well described by first order Stark effect ( $-|\mu||E| \frac{M_J \Omega}{J(J+1)}$ ) for high electric fields (because  $\Omega$  is non-zero). However, by using equation (2.44), after diagonalizing the matrix the Stark shifted energies are given by:

$$\Delta E_{Stark} = \frac{E_A}{2} \pm \sqrt{\left(\frac{E_A}{2}\right)^2 + X^2} \quad (2.45)$$

Where the plus sign is used for the upper  $\Lambda$ -doublet which is a LFS state, while minus sign is used for the lower  $\Lambda$ -doublet which is a HFS state. The calculated Stark shift for our target state for deceleration  $|X^2\Pi_{3/2}, J = 3/2, M_J = -3/2\rangle$  at  $126 \text{ kV/cm}$  is about  $0.96 \text{ cm}^{-1}$ . Figure (2-10) demonstrates the Stark shift for  $X^2\Pi_{3/2}, J = 3/2$ . The  $|X^2\Pi_{3/2}, J = 3/2, M_J = -1/2\rangle$  state is also LFS, but it is not preferred since its Stark shift is less than  $|X^2\Pi_{3/2}, J = 3/2, M_J = -3/2\rangle$ . In a supersonic expansion the lowest rotational levels of the molecules are populated. The population of each energy level depends on the rotational temperature of the beam. Therefore at the presence of external electric fields it is possible to guide the molecules in rotational energy levels higher than the ground state. Figure (2-11) shows the Stark effect for  $J = 5/2$ , which is the next rotational level after  $J = 3/2$  in  $X^2\Pi_{3/2}$ . For this state  $C_1(5/2) = 0.0358$ ,  $C_2(5/2) = 0.9994$ , and  $E_A = 64 \text{ MHz}$  [97]. The calculated Stark shift for our target state for deceleration  $X^2\Pi_{3/2}, J = 5/2, M_J = -5/2$  at  $126 \text{ kV/cm}$  is about  $0.68 \text{ cm}^{-1}$ .

In this thesis we neglect the hyperfine structure of the *SD* radical because, as I will explain in the experimental setup in chapter (5), the electric field in our Stark decelerator never approaches zero, in order to prevent unwanted non-adiabatic transitions. However it is instructive to mention the Stark shift of the hyperfine structure for this molecule at very weak electric fields (less than  $0.5 \text{ kV/cm}$ ).

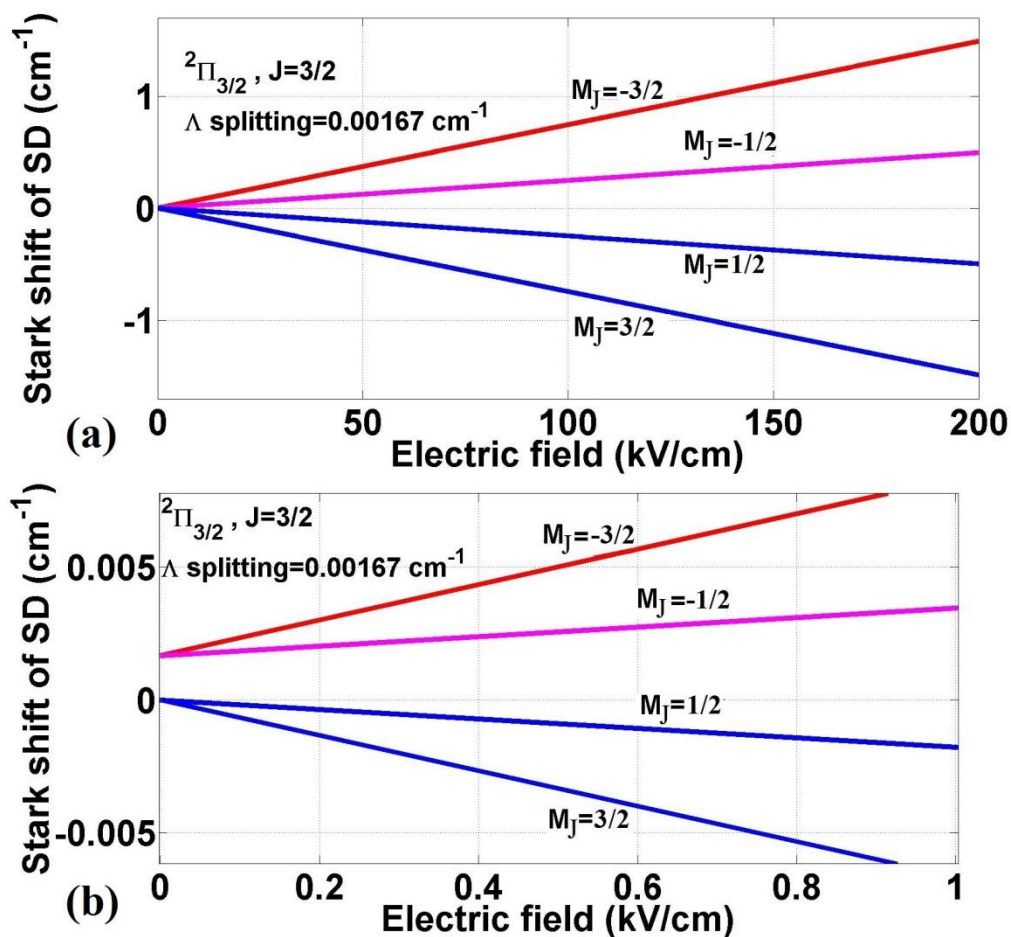


Figure 2-10: The Stark shift for  $X^2\Pi_{3/2}, J = 3/2$  state of the  $SD$  radical ( $\mu_E = 0.76 D$ ) (a) from 0 to 200  $\text{kV/cm}$  (b) Zoomed in to show the  $\Lambda$ -doubling splitting (the hyperfine structure is ignored)

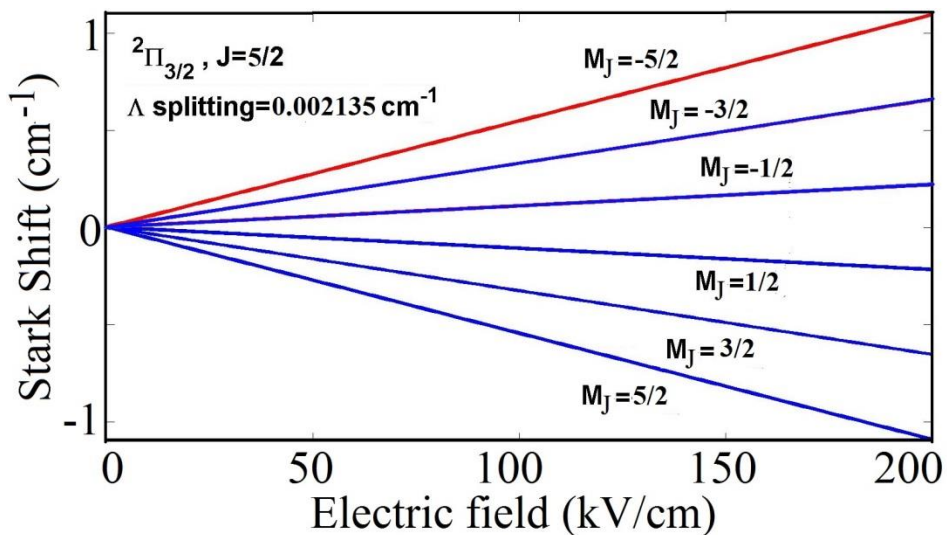


Figure 2-11: The Stark shift for  $X^2\Pi_{3/2}, J = 5/2$  state of the  $SD$  radical from 0 to 200  $\text{kV/cm}$  (hyperfine structure is ignored). The red lines show LFS states and the blue lines show HFS states.

If one considers the hyperfine structure of  $SD$ , the nuclear spin  $\vec{I}$  couples to the rotational angular momentum  $\vec{J}$  and gives  $\vec{F} = \vec{I} + \vec{J}$ , which splits each  $\Lambda$ -doublet component of  $X^2\Pi_{3/2}, J = 3/2$  into two hyperfine levels  $F = 1$  and  $F = 2$ , and transforms the basis sets  $|JM_J\Omega\alpha\rangle$  to  $|FM_F\alpha\rangle$ .  $M_F$  is the projection of  $F$  on the electric field axis. For very low electric fields the Stark effect of the  $SD$  molecule in a  $\Pi$  state can be obtained by:

$$\begin{aligned}
& \langle FM_F\alpha | -\mu \cdot E | F'M'_F\alpha' \rangle \\
&= -\mu E (-1)^{J+J'+F+F'+I-|\Omega|-M_F+1} \left( \frac{\alpha\alpha'(-1)^{J+J'+2|\Omega|+1} + 1}{2} \right) \\
&\times ((2J'+1)(2J+1)(2F'+1)(2F+1))^{1/2} \\
&\times \begin{Bmatrix} F & F' & 1 \\ J' & J & 1 \end{Bmatrix} \begin{pmatrix} J & 1 & J' \\ -|\Omega| & 0 & |\Omega'| \end{pmatrix} \begin{pmatrix} F' & 1 & F \\ M'_F & 0 & M_F \end{pmatrix}
\end{aligned} \tag{2.46}$$

In which Clebsch-Gordon coefficients and  $3j$  (parntheses) and  $6j$ (brackets) symbols are used [39] [70].

## 2.2 AC Stark effect of molecules

The AC Stark shift is associated with a rotational transition due to an electromagnetic wave such as a microwave field. A linearly polarized electric field can be obtained by using a microwave cavity. The optical selection rule for a linearly polarized microwave field allows transitions by  $\Delta j = \pm 1, \Delta M = 0$ , and  $\Delta K = 0$  for a symmetric top molecule. After the supersonic expansion, the ground state of the molecule is highly populated. The transition rules limit the transition to the state  $|JKM\rangle = |100\rangle$  from the ground state  $|JKM\rangle = |000\rangle$ . The Hamiltonian of the molecule at the presence of an electromagnetic wave is in the form of [101]:

$$\hat{H} = \hat{H}_{rot} - \vec{\mu} \cdot \vec{E} \tag{2.47}$$

Here,  $E$  is not DC, and has a form of:

$$E_z = E_{0z} \cos(\omega t) \tag{2.48}$$

where  $\omega$  is the angular frequency of the oscillation for the electromagnetic wave, and  $E_{0z}$  is the electric field amplitude. Therefore:

$$-\vec{\mu} \cdot \vec{E} = -\mu_z E_z = -\mu_z E_{0z} \cos(\omega t) = -\frac{\mu_z E_{0z}}{2} (e^{-i\omega t} + e^{i\omega t}) \quad (2.49)$$

We will elaborate the Hamiltonian more. The total Hamiltonian of a system consisting of a molecule and electromagnetic field in a cavity can be written as:

$$\hat{H} = \hat{H}_{rot} + \hat{H}_{radiation} + \hat{H}_{Interaction} \quad (2.50)$$

in which  $\hat{H}_{radiation}$  represents the energy of the electromagnetic field, and  $\hat{H}_{Interaction}$  represents the interaction between the molecule and the field. The classical Hamiltonian of an electromagnetic field is in the form of:

$$H_{radiation} = \frac{\epsilon_0}{2} \int (|E|^2 + c^2 |B|^2) dv \quad (2.51)$$

where  $c$  is the speed of light in the medium. One can show that the quantum mechanical version of this Hamiltonian behaves similar to a classical harmonic oscillator, which can be represented by photon creation and annihilation operators ( $\hat{a}^\dagger$  and  $\hat{a}$ ) as:

$$\hat{H}_{radiation} = \sum_{i=1}^{\infty} \hbar \omega_i \left( \hat{a}_i^\dagger \hat{a}_i + \frac{1}{2} \right) \quad (2.52)$$

In which  $i$  represents the cavity modes and  $\omega_i$  represents the frequency of each mode. By introducing  $|n_i\rangle$  as a state having  $n_i$  photons of mode  $i$ , the creation and annihilation operators act as  $\hat{a}_i^\dagger |n_i\rangle = \sqrt{n_i + 1} |n_i + 1\rangle$  and  $\hat{a}_i |n_i\rangle = \sqrt{n_i} |n_i - 1\rangle$ , which are equivalent to creation and annihilation of a photon. The first two parts of the total Hamiltonian are not coupled; therefore we can use the so called dressed states as the basis set of the total Hamiltonian matrix. However, the interaction part of the Hamiltonian can couple different states, and as a result shifts their energy, which is called AC Stark shift. The dressed state formalism has a form of  $|JKM\rangle |\bar{N} + n\rangle$  for symmetric top molecules, in which  $\bar{N}$  is the average number of photons in the field, and  $n = \dots, -2, -1, 0, 1, 2, \dots$ . One can show that the interaction Hamiltonian after quantization has a form of:

$$\hat{H}_{Interaction} = -\frac{1}{2\sqrt{\bar{N}}}\vec{\epsilon}\cdot\vec{\mu}(\hat{a}^\dagger + \hat{a}) \quad (2.53)$$

Where (since  $\bar{N} \gg 1$ )

$$\begin{aligned} \hat{a}_i^\dagger |\bar{N} + n\rangle &= \sqrt{\bar{N} + n + 1} |\bar{N} + n + 1\rangle \sim \sqrt{\bar{N}} |\bar{N} + n + 1\rangle \\ \hat{a} |\bar{N} + n\rangle &= \sqrt{\bar{N} + n} |\bar{N} + n - 1\rangle \sim \sqrt{\bar{N}} |\bar{N} + n - 1\rangle \end{aligned} \quad (2.54)$$

For linearly polarized radiation the transition rules for the rotational states of a symmetric top molecule are  $\Delta j = \pm 1$ ,  $\Delta M = 0$ , and  $\Delta K = 0$ . The selection rule related to the ladder operators of the field is  $\Delta n = \pm 1$ . Therefore the matrix elements will be:

$$\begin{aligned} \langle J'K'M', \bar{N} + n' | \hat{H}_{Interaction} | J''K''M'', \bar{N} + n'' \rangle &= -\frac{1}{2} \langle J'00 | \vec{\epsilon}\cdot\vec{\mu} | J''00 \rangle \langle n' | (\hat{a}^\dagger + \hat{a}) | n'' \rangle = \\ &= -\frac{1}{2} E_{0z} \mu \langle J'00 | \cos \theta | J''00 \rangle \langle n' | (\hat{a}^\dagger + \hat{a}) | n'' \rangle \\ &= \delta_{J'J''} \delta_{n'n''} [BJ'(J'+1) + nh\vartheta] - (\delta_{J'J''+1} + \delta_{J'J''-1}) (\delta_{n'n''-1} + \delta_{n'n''+1}) \\ &\quad \times \frac{1}{2} E_{0z} \mu \sqrt{(2J'+1)(2J''+1)} \begin{pmatrix} J' & 1 & J'' \\ 0 & 0 & 0 \end{pmatrix}^2 \end{aligned} \quad (2.55)$$

Therefore using the dressed state formalism for linearly polarized radiation we can show that the Hamiltonian is in the form of:

$$H = \begin{bmatrix} \ddots & \vdots & 0 & 0 \\ \cdots & E_{rot} + n\hbar\omega & -\frac{1}{2}\mu_z E_{0z} & 0 \\ 0 & -\frac{1}{2}\mu_z E_{0z} & E_{rot} + (n+1)\hbar\omega & \cdots \\ 0 & 0 & \vdots & \ddots \end{bmatrix} \quad (2.56)$$

where  $\hbar\omega$  is the photon energy, and  $\mu_z = \langle JKM | \mu \cos \theta | J'K'M' \rangle$ . For the case of the transition between the two dressed states  $|000\rangle|\bar{N} + 1\rangle$  and  $|100\rangle|\bar{N}\rangle$ , the above Hamiltonian can be approximated by:

$$H = \begin{pmatrix} 2B + n\hbar\omega & -\frac{1}{2}\mu_{10z}E_{0z} \\ -\frac{1}{2}\mu_{10z}E_{0z} & (n+1)\hbar\omega \end{pmatrix} \quad (2.57)$$

Here  $\mu_{10z}$  is the transition dipole moment between the two desired states, which is given by:

$$\mu_{10z} = \langle 100 | \mu \cos \theta | 000 \rangle = \mu \langle 100 | \cos \theta | 000 \rangle = \frac{\mu}{\sqrt{3}} \quad (2.58)$$

where  $\mu_0$  is the permanent dipole moment of the molecule, and  $\theta$  is the angle between the molecular axis and the polarization of the field. After diagonalization, the Stark shift of each of the states is found to be:

$$\begin{aligned} \Delta E_{|000\rangle} &= -\frac{\delta}{2} \pm \frac{1}{2} \sqrt{\delta^2 + E_{0z}^2 \mu_{10z}^2} \\ \Delta E_{|100\rangle} &= +\frac{\delta}{2} \mp \frac{1}{2} \sqrt{\delta^2 + E_{0z}^2 \mu_{10z}^2} \end{aligned} \quad (2.59)$$

where  $\delta = \hbar(\omega - \omega_{10})$  is the frequency detuning of the radiation relative to the resonant frequency of the transition between the two states ( $\omega_{10} = 2B/\hbar$ ). In each case, the upper sign is for the blue-detuning ( $\delta > 0$ ), and the lower sign is for the red-detuning ( $\delta < 0$ ). It is interesting that each state can be a high field seeking state or low field seeking state, depending on the sign of the detuning. The result of AC Stark shift calculations for a two-state model for  $\text{CH}_3\text{CN}$ , with  $\mu_0 = 3.92 \text{ D}$  and  $100 \text{ MHz}$  detuning are shown in figure (2-11).

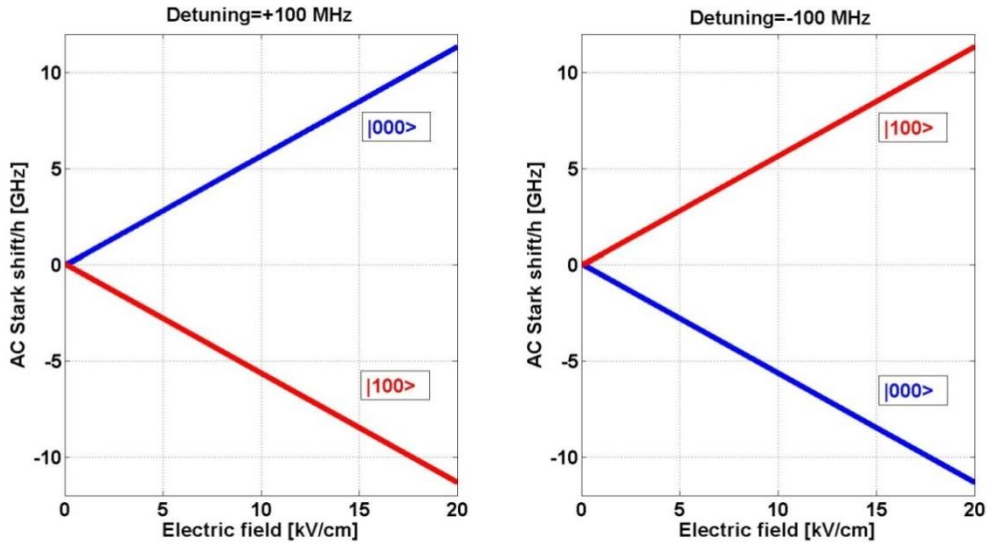


**Figure 2-12:** AC Stark shift of  $|000\rangle$  and  $|100\rangle$  states of  $\text{CH}_3\text{CN}$  ( $\mu_{10z} = 2.26 \text{ D}$ ) calculated by two state model. Left panel for detuning=  $+100 \text{ MHz}$ , Right panel for detuning=  $-100 \text{ MHz}$ .

## Chapter 3: Detection methods

### 3.1 Laser Induced Fluorescence (LIF) of *SD* radical

Laser induced fluorescence of *SD* radicals via excitation of the rotational bands in  $X^2\Pi_{3/2}(v'' = 0) \rightarrow A^2\Sigma^-(v' = 0)$  was used to probe the *SD* molecules in the desired state ( $X^2\Pi_{3/2}, J = 3/2$ ), which lies between 322 – 324 nm in UV. The fluorescence life time of the *SD* (*SH*) radical in the  $A^2\Sigma^-(v' = 0)$  is reported to be less than 200 (3) ns [102]. A detailed description of  $X^2\Pi_{3/2} \rightarrow A^2\Sigma^-$  transitions for *OH* molecule, that has similar structure as *SD* molecules, is reported by Dieke [103]. The selection rules for electric dipole allowed transitions are:

$$\begin{aligned} \Delta J &= \pm 1, 0 \\ \text{parity: } &\text{even}(+) \rightleftharpoons \text{odd}(-) \\ \Delta N &= \pm 2, \pm 1, 0 \end{aligned} \quad (3.1)$$

The notation for transition labels used by Dieke was,

$$\Delta N_{F'F''}(N'') \quad (3.2)$$

In which  $F'$  and  $F''$  refer to the  $\rho$ -doublet component of the  $A^2\Sigma^-$  state and the manifold ( $\Omega$ ) of the  $X^2\Pi_{\Omega}$  respectively, and  $N''$  shows the value of  $N$  for  $X^2\Pi_{\Omega}$ . If  $F'$  and  $F''$  are equal in any transition, only one subscript is shown. Also  $\Delta N = 2$  is labeled by  $S$ ,  $\Delta N = 1$  is labeled by  $R$ ,  $\Delta N = 0$  is labeled by  $Q$ ,  $\Delta N = -1$  is labeled by  $P$ , and  $\Delta N = -2$  is labeled by  $O$ . This labeling method along with the transition rules gives twelve possible branches:

$$O(N), P_1(N), P_2(N), P_{12}(N), Q_1(N), Q_{21}(N), Q_2(N), Q_{12}(N), R_1(N''), R_{21}(N''), R_2(N''), S_{21}(N'')$$

However in some other literatures and some simulation software the notation is different and is in the form of:

$$\Delta N \Delta J_{F'F''}(J'') \quad (3.3)$$

Where everything is the same as Dieke's notation, except that  $J''$  ( $J$  for  $X^2\Pi_{\Omega}$ ) is used instead of  $N''$ , and  $\Delta J$  is added. In this case  $\Delta J = -1, 0, +1$  is referred to with the capital letters  $P, Q, R$  respectively, while  $\Delta N = -2, -1, 0, +1, +2$  is referred to by small letters  $o, p, q, r, s$ . Again for convenience whenever  $\Delta J = \Delta N$  only the capital letter is used. For example, assume a transition from  $X^2\Pi_{3/2}, J = 3/2$  ( $N = 1$ ) to  $A^2\Sigma^-, N = 3, J = 5/2$ . This means:

$\Delta N \rightarrow s, \Delta J \rightarrow R, F' = F_2 \rightarrow 2, F'' = F_1 \rightarrow 1, J'' = 3/2 = 1.5$ . Therefore this transition is labeled by  $sR_{21}(1.5)$ . The latter notation is used to show some of these transitions in figure (3-1) for the *SD* radical. The excitations are shown for the rotational bands in  $X^2\Pi_{\Omega}(v'' = 0) \rightarrow A^2\Sigma^-(v' = 0)$  transition. The green and orange arrows in the figure refer to the transitions from *e* symmetry and from *f* symmetry in the  $X^2\Pi_{\Omega}$  state, respectively.

Assume the  $Q_1(1.5)$  transition is used to excite the molecules in our Stark deceleration preferred state,  $X^2\Pi_{3/2}, J = 3/2$ . After excitation the molecules relax through fluorescence and emit photons. However there are different channels for the fluorescence to happen that can satisfy the transition rules. In the case of  $Q_1(1.5)$  excitation, the fluorescence channels could be through off-resonance transitions  $P_1(2.5), pQ_{12}(1.5), oP_{12}(2.5), qR_{12}(0.5)$ , and on-resonance through  $Q_1(1.5)$ . Each of these fluorescence transitions could be used to detect the molecules after the decelerator. However in the case of *SD* radical the Frank-Condon factors are such that about 95 percent of the fluorescence appears on-resonance. This could experimentally cause some difficulties which will be discussed later.

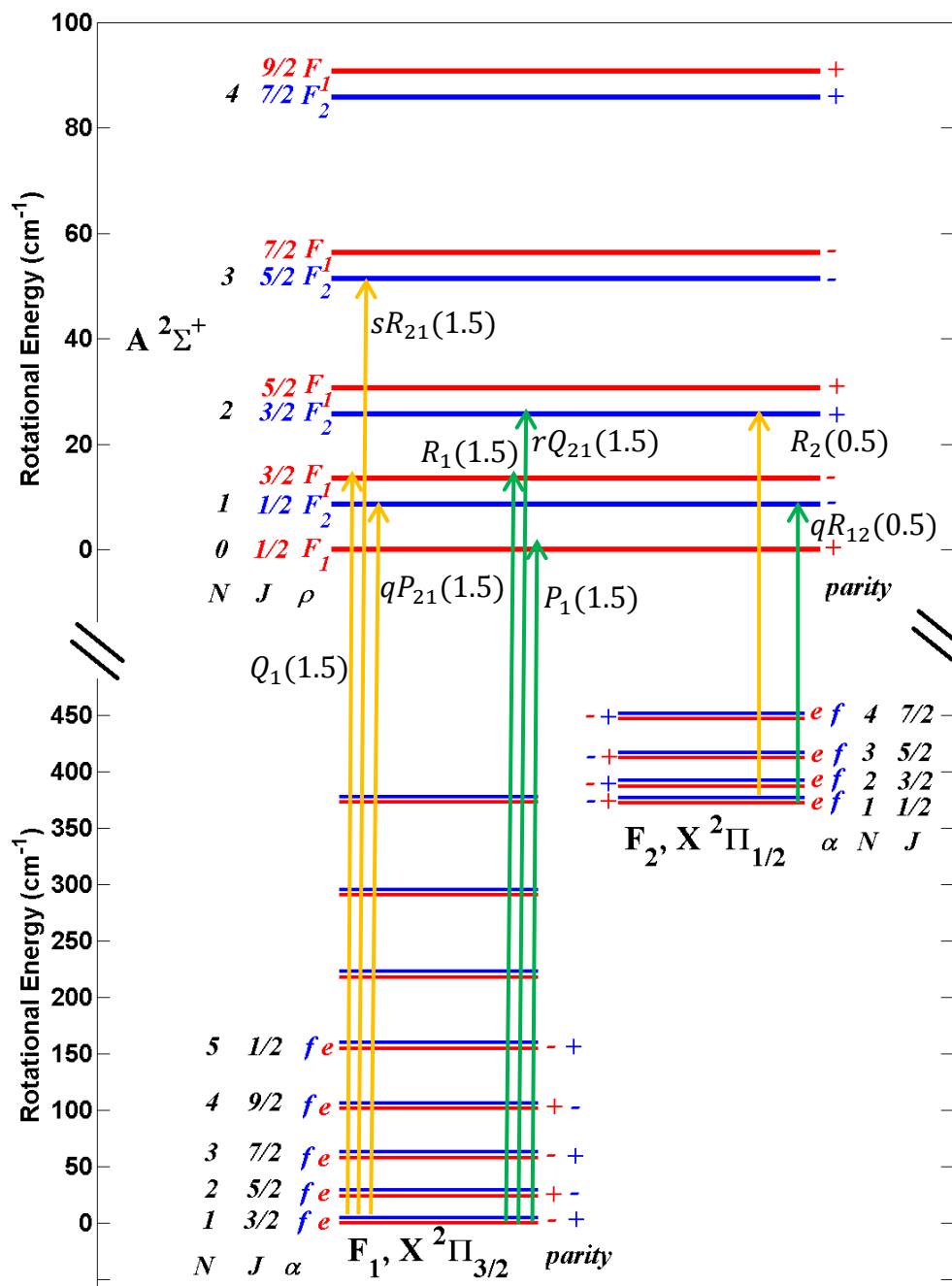


**Figure 3-1:** Some of the possible one photon transitions from  $X^2\Pi_{\Omega}(v'' = 0)$  to  $A^2\Sigma^-(v' = 0)$  are shown and labeled. Note that the splitting of  $\Lambda$ -doubling and  $\rho$ -doubling are exaggerated to be visible.

### 3.2 Resonance Enhanced Multi-Photon Ionization (REMPI) of *SD* radical

Although REMPI was not used as the detection method in our experiments on *SD*, it is useful to make mention of the method. The first (2 + 1) REMPI study on *SD* was done by Milan et al. [104]. Later in 1996 they reported a more extensive study on the two-photon REMPI

photoelectron spectroscopy of the *SD* (*SH*) radical [79]. In their method they used a (2 + 1) REMPI scheme to investigate the rotationally resolved Rydberg states converging upon the  $a^1\Delta$  or  $b^1\Sigma^+$  in a one photon energy range of 208 – 258 nm. According to Milan's report a two-photon energy between 77500 – 78500  $cm^{-1}$  can be used to investigate the  $[a^1\Delta]3d\pi^2\phi(v' = 0) \leftarrow X^2\Pi(v'' = 0)$  transition, between 80100 – 80800  $cm^{-1}$  can be used to investigate the  $[a^1\Delta]3d\pi^2\Pi(v' = 0) \leftarrow X^2\Pi(v'' = 0)$  transition, between 81400 – 82400  $cm^{-1}$  can be used to investigate the  $[b^1\Sigma^+]4p\sigma^2\Sigma^+(v' = 0) \leftarrow X^2\Pi(v'' = 0)$  transition, and between 82000 – 82700  $cm^{-1}$  can be used to investigate the  $[a^1\Delta]3d\delta^2\Sigma^+(v' = 0) \leftarrow X^2\Pi(v'' = 0)$  transition in *SD* radical. The reported results are rotationally resolved and can be used for the detection of *SD* radical after Stark deceleration. There are advantages for REMPI over LIF measurements, such as elimination of the detection of scattered laser light, better collection efficiency and sensitivity, but when considering the disadvantages such as low transition probabilities and the small size focused UV light, the advantages are minimal. However in our experiments REMPI for *SD* was not used due to our ultimate goal to implement the CELIF method, which relies on the LIF detection.

### 3.3 Cavity Enhanced Laser Induced Fluorescence of *SD* radical (CELIF)

To my knowledge no one has yet experimentally and accurately measured the absolute density of molecules in a Stark decelerated packet. The main problem is that all the detection methods used so far for Stark deceleration are not designed to precisely measure the absolute density of the packet. This could result in some difficulties for certain applications of Stark decelerated packets, such as finding the absolute cross sections in scattering experiments. The estimations reported so far are mostly the result of simulations, or found by rough estimations for carefully calibrated LIF measurements which can still be an order of magnitude wrong [70]. Therefore we decided to measure the absolute density of the Stark decelerated packet using a well calibrated method called CELIF. The CELIF method combines the LIF and cavity ring-down methods (CRD). This method was first introduced by Sanders et al. to measure the absolute absorption coefficients of 1,4-bis(Phenylethynyl)benzene (BPEB), and is claimed to be effective for molecules with fluorescence lifetimes on the order of hundreds of nanosecond [105].

Although LIF detection is a good way for detecting low density species, calibrating the LIF setup to give absolute densities is frustrating and has large uncertainty [73]. On the other hand, the

Cavity Ring-Down (CRD) method has been widely used to measure the absolute densities ( $\rho$ ) in different phases of matter by measuring the absorption coefficient  $\alpha = \sigma\rho$ , where the absorption cross-section  $\sigma$  is known.

Fortunately Mizouri et al. have performed CELIF measurement of *SD* radicals in a supersonic jet and have reported the limit of detection (LOD) for that to be  $10^5 \text{ cm}^{-3}$  [106], which makes it suitable for measuring the density of the Stark decelerated packet. In collaboration with their group at Durham University in England, we would like to implement the density measurement of the Stark decelerated packet using the CELIF method. The theory of the method is explained here, and the experimental setup and results obtained so far are described in the experimental results.

CELIF detection combines two other methods, CRD and LIF. The CRD method is known for measuring absolute absorption coefficients, being immune to laser power fluctuations, not being background free, and having up to sub-ppb sensitivity. On the other hand, the LIF method is known for being principally background free, having sub-ppq sensitivity, needing to compensate for laser power fluctuation, and being difficult to calibrate. The CELIF method takes advantage of the positive characteristics of these two methods and provides a measurement with easier calibration while giving the same signal to noise ratio as the LIF measurement. A CRD measurement cannot be used alone to find the absolute density of the molecules due to the low concentrations of the sample for a Stark decelerated packet.

Put simply, in the CELIF method the signal recorded from the integrated LIF signal is normalized shot-to-shot to the corresponding integrated CRD intensity:

$$CELIF \text{ signal}(sig^{CELIF}) = \frac{LIF \text{ signal}(sig^{LIF})}{CRD \text{ signal}(sig^{CRD})} \quad (3.4)$$

where  $sig^{LIF} = I^{LIF} \alpha \Gamma g$ , and  $I^{LIF}$  is the intensity of the light interacting with the molecules,  $\Gamma$  is the fluorescence quantum yield, and  $g$  is the instrument factor, that includes all the instrument related factors such as geometry and quantum efficiency of the PMT. It can be shown that for a cavity with highly reflecting mirrors and with low photon loss,  $sig^{CELIF}$  can be given by [105]:

$$sig^{CELIF} = \frac{2\alpha\Gamma g}{T} = \frac{2\sigma\rho\Gamma g}{T} \quad (3.5)$$

where  $T$  is the transmission of the cavity mirrors. The difficult part of working with the above formula is the determination of  $g/T$ . In order to solve this problem Mizouri et al. suggested performing a separate Rayleigh scattering measurement with dry  $N_2$  filled chamber, with a known pressure and consequently a known density, while keeping all the other experimental conditions the same. The angle between the linear polarization of the incident laser light and the LIF detection axis is set to the so-called magic angle ( $\theta = 54.7^\circ$ ) for which the difference between the fluorescence light and the scattered light due to the angular distribution vanishes [92]. Since all the other experimental conditions are the same  $g = g'$ . After taking the ratio of the two measurements, the ratio no longer depends on  $g$  and  $T$ :

$$\frac{sig_{SD}^{CELIF}}{sig_{N_2}^{CELIF}} = \frac{\sigma_{SD} \rho_{SD} \Gamma_{SD}}{\sigma_{N_2} \rho_{N_2} \Gamma_{N_2}} \quad (3.6)$$

Also, it is known that  $\Gamma_{N_2} = 1$ . The value for  $\rho_{N_2}$  can be found from the pressure reading of the chamber, and  $\sigma_{N_2} = (4.1 \pm 0.2) \times 10^{-26} cm^2$  and  $\sigma_{SD} = (7.0 \pm 0.5) \times 10^{-16} cm^2$  and  $\Gamma_{SD} = 0.2 \pm 0.01$  can be found in the literature [106]. Therefore the only unknown parameter remaining is  $\rho_{SD}$ :

$$\rho_{SD} = \frac{sig_{SD}^{CELIF} \sigma_{N_2} \rho_{N_2}}{sig_{N_2}^{CELIF} \sigma_{SD} \Gamma_{SD}} \quad (3.7)$$

In order to obtain a more accurate signal we must subtract the background signal from our CELIF readings:

$$sig'_{SD}{}^{CELIF} = sig_{SD}^{CELIF} - sig_{Background}^{CELIF} \quad (3.8)$$

and then use  $sig'_{SD}{}^{CELIF}$  in the calculations. Sanders et al. have shown that the signal to noise ratio of the CELIF method is similar to that for the LIF measurement [105].

### 3.4 Resonance Enhanced Multi-Photon Ionization (REMPI) of ammonia

Since the experiments presented in this thesis are the first experiments done with the Stark decelerator at UBC after its assembly, it was necessary to characterize the setup with a well-known sample such as ammonia. The availability of the resources for the Stark deceleration of ammonia plus its low mass and good Stark effect made it the best candidate for characterizing our decelerator. Detailed versions of the theory of the REMPI experiments on ammonia

molecules have been presented by several groups [70][107]. The two photon selection rules for the rotational states are:

$$\begin{aligned}\Delta J &= 0, \pm 1, \pm 2 \\ \Delta K &= \pm 1 \\ \Delta l &= \pm 1\end{aligned}\tag{3.9}$$

(2 + 1) REMPI via  $\tilde{B}(v_2 = 5)$  Rydberg state was used to detect the ammonia molecules in our experiments. The  $\tilde{B}(v_2 = 5)$  state has a flat geometry and has no inversion splitting. The vibronic wave-function of  $\tilde{B}$  is two-fold degenerate and has  $E''$  symmetry for even  $v_2$  and  $E'$  symmetry for odd  $v_2$ . The symmetry for the lower levels of the electronic ground state inversion doublets  $\tilde{X}(0)$  is  $A_1''$ , while for the upper inversion doublets  $\tilde{X}(1)$  it is  $A_1'$ . Therefore, the upper levels can only be probed via a  $\tilde{B}(v_2 = \text{odd})$  band and the lower levels via a  $\tilde{B}(v_2 = \text{even})$  band:

$$\begin{aligned}\tilde{B}(v_2 = \text{even}) &\leftarrow \tilde{X}(0) \\ \tilde{B}(v_2 = \text{odd}) &\leftarrow \tilde{X}(1)\end{aligned}\tag{3.10}$$

Since the upper level of  $|J, K \rangle = |1, 1 \rangle$  is our low field seeking target state,  $\tilde{X}(1)$ , the required two-photon transition is  $\tilde{X}(v_2 = 0) = 0 \rightarrow \tilde{B}(v_2 = \text{odd})$ . A two-photon transition such as  $\tilde{X}(v_2 = 0) = 0 \rightarrow \tilde{B}(v_2 = \text{even})$  will probe the lower level,  $\tilde{X}(0)$ , of  $|J, K \rangle = |1, 1 \rangle$ . By choosing  $v_2 = 5$  the transition can be labeled by  $2_{v''}^{v'''} = 2_0^5$ . The two photon energy required for this transition is about  $64032 \text{ cm}^{-1}$ . Figure (3-2) schematically shows this transition:

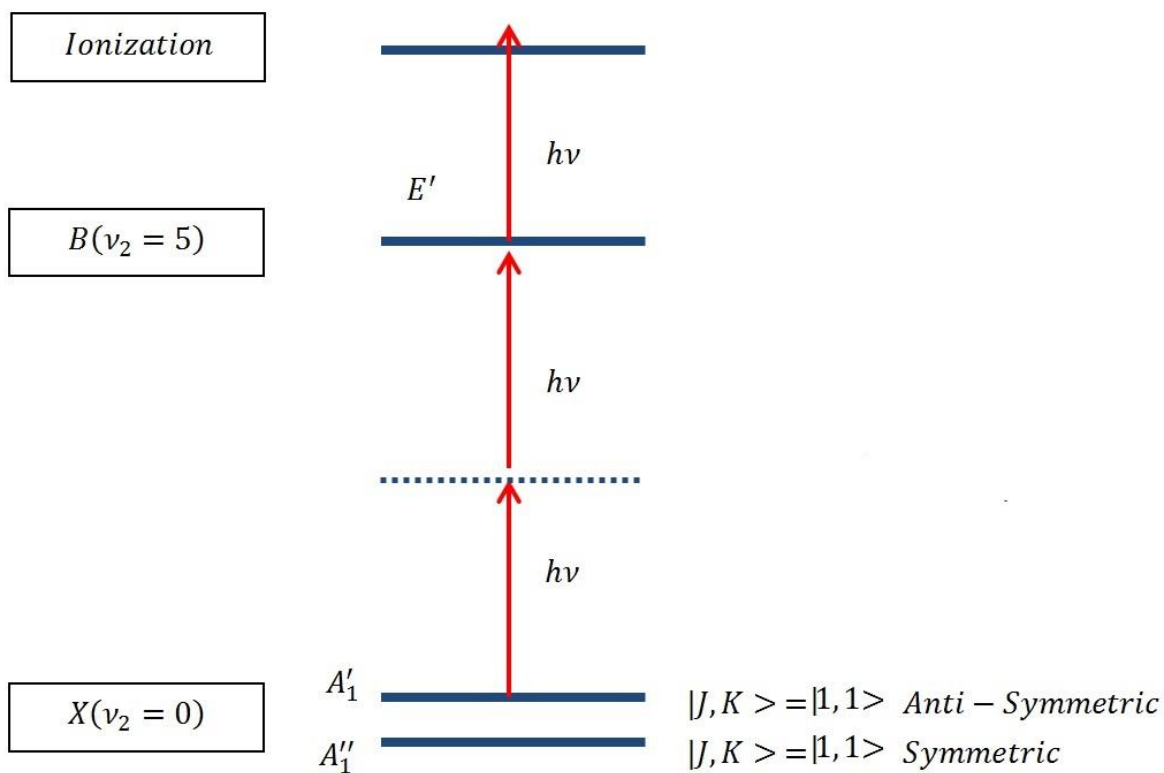


**Figure 3-2:** Two photon transition from  $\tilde{X}(\nu_2 = 0)$  to  $\tilde{B}(\nu_2 = 5)$  and ionization in (2+1) REMPI for ammonia

## Chapter 4: Stark deceleration principle

The Stark decelerator is an array of cylindrical electrode pairs, equally spaced in the longitudinal direction of the molecular beam, that provide electric field stages for deceleration. If we assume  $X$  is the direction of the molecular beam, the two poles of the electrodes of each stage are oriented alternately in the  $Y$  and  $Z$  directions. The electric field distribution for one electrode pair of our decelerator at  $\pm 12$  kV is plotted in Figure (4-1). Figure (5-1) provides more details about the design of our decelerator.

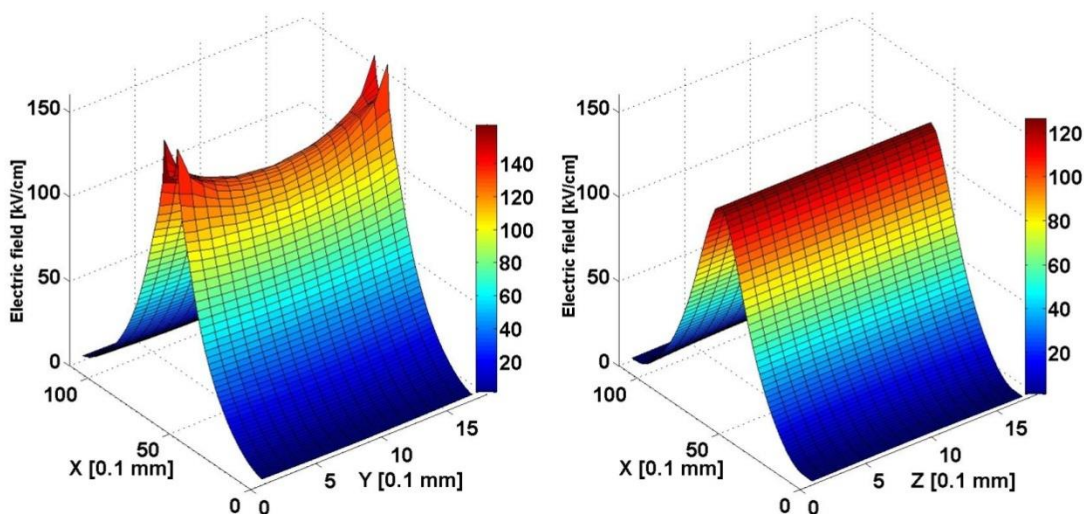
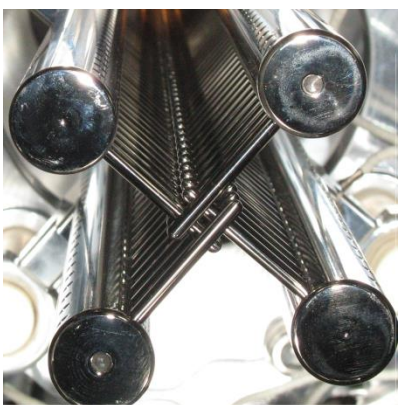


**Figure 4-1:** Top: The front view of our Stark decelerator. Bottom: The electric field magnitude for one pair of electrodes at  $\pm 12$  kV in our Stark decelerator (one deceleration stage). In this case the electrodes are assumed to be oriented in the  $Z$  direction, and  $X$  is assumed to be the beam axis. The center of electrodes are located at  $X = 5.5$  mm,  $Y = 0$  mm and  $Y = 1.825$  mm. Note the confining potentials in the  $X$  and  $Y$  directions.

As we can see in Figure (4-1), the electric field in the longitudinal direction ( $X$ ) increases from zero to some peak value, and goes back to zero. In the transverse direction, there is a potential well in the  $Y$  direction, but for the  $Z$  direction there is no confining potential. Hence the orientation of the electrodes is alternately rotated by  $90^\circ$  degrees to provide the confining potential in both of the transverse directions ( $Y$  and  $Z$ ). Molecules in the low field seeking states see a potential hill due to their positive Stark effect as they pass through each stage. When molecules climb up the potential, they lose kinetic energy. In order to prevent them from gaining the energy back, the voltage on the electrodes in front of the molecule switches off before the molecule leaves the upward side of the potential, and at the same time the next pair of electrodes switches on to provide the next deceleration stage. After the molecule passes through all the stages, it will lose part of its kinetic energy. The amount of energy loss per stage depends on the position of the molecule in each period of deceleration. If we assume  $d$  is the distance between each adjacent electrode pairs, then  $2d$  is one period of the potential, similar to the figure (4-1). The position of the target molecule, which we call the Synchronous molecule, with respect to the potential is represented by a phase as shown in figure (4-2). The zero for the phase is defined in the middle of the two adjacent electrode pairs, and the phase at any point is given by  $x\pi/d$ . By this definition electrode pairs at  $\varphi = \pi/2$  and  $\varphi = 5\pi/2$  are grounded.

The force experienced by the molecule at each point is simply given by:

$$\vec{F} = -\vec{\nabla}W_{Stark}(E(\vec{r})) \quad (4.1)$$

In which  $W$  is the Stark energy of the molecule, and  $\vec{r}$  is the position of the molecule inside the decelerator.

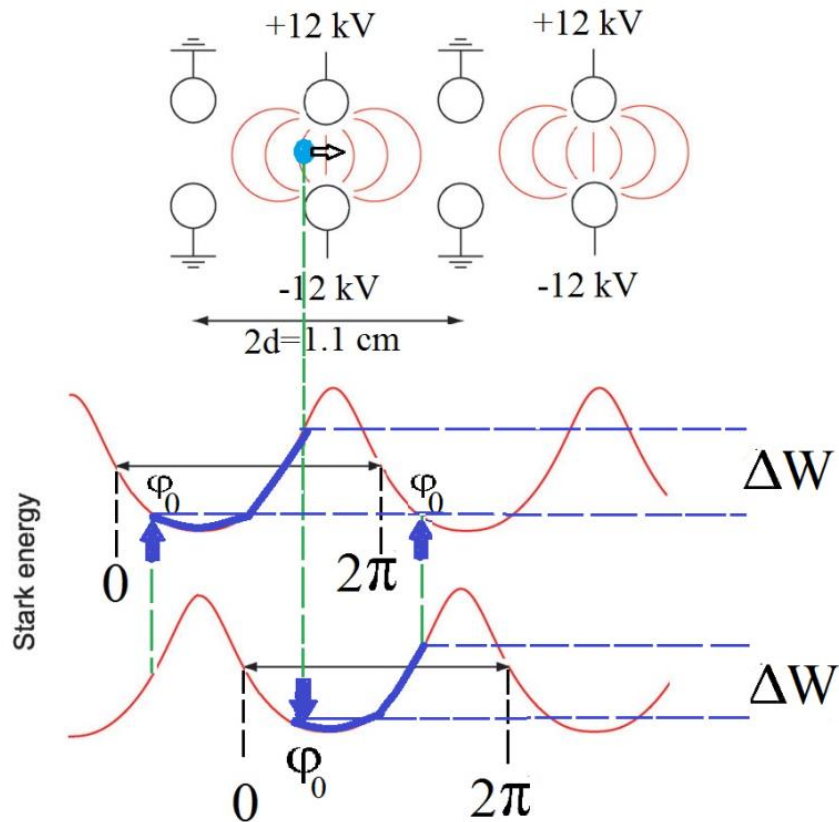


**Figure 4-2:** The Stark deceleration principle in 2 dimension view. In 3D, the odd electrode pairs are oriented in  $Y$  direction, while even electrodes are oriented in the  $Z$  direction.

#### 4.1 Phase stability diagrams

Our phase-space has six dimensions  $(x, y, z, v_x, v_y, v_z)$ , where  $x$  is the molecular beam axis, and  $y$  and  $z$  are the transverse directions. A Stark decelerator not only decelerates the synchronous molecule, but also decelerates other molecules within its phase-space acceptance. Phase-space acceptance of the decelerator is referred to the phase-space volume that is accepted initially at the entrance of the decelerator. These accepted molecules that are close to the synchronous molecule experience oscillatory motions around the synchronous molecule in phase-space. In an ideal decelerator the number of oscillatory molecules in this volume is conserved throughout the deceleration process, and the molecules in that volume are called phase-stable. The molecules that are not phase-stable cannot follow the decelerator's periodic potential, and will leave the decelerated packet. It is of interest to obtain the highest possible phase-space density for the decelerated beam; however conventional decelerators are not able to compress the phase-space. In order to obtain higher phase-space density and more cooling, we need to combine the Stark

decelerator with some other cooling methods. In other words, a Stark decelerator can be used as the first stage of cooling, and if a more cold and dense ensemble is needed, we can load the molecules into a secondary stage where we apply another cooling method such as evaporative cooling. Hence a good understanding of the decelerated beam profile is required to design and match the phase-space acceptance of the decelerated beam and thus the next stage of the experiment. If interested, there are some good references for further studying of the phase-space stability of Stark decelerators [39][14][108]. In this thesis some of their results are utilized to characterize our Stark decelerator.

#### 4.1.1 Longitudinal phase stability

The longitudinal phase-space is a two dimensional space  $(x, v_x)$ . Here we neglect the effect of the transverse motion of the molecules on the longitudinal motion, and investigate the longitudinal phase stability. The phase of the synchronous molecule inside the potential is given by  $\varphi_0 = x\pi/d$ , where  $d$  is the distance between two adjacent electrode pairs. It is known that the energy loss per stage for the synchronous molecule can be estimated by [39]:

$$\Delta W(\varphi_0) = W(\varphi_0 + \pi) - W(\varphi_0) = 2a_1 \sin \varphi_0 \quad (4.2)$$

Where  $2a_1$  can be found from the height of the potential, as shown in Figure (4-3):

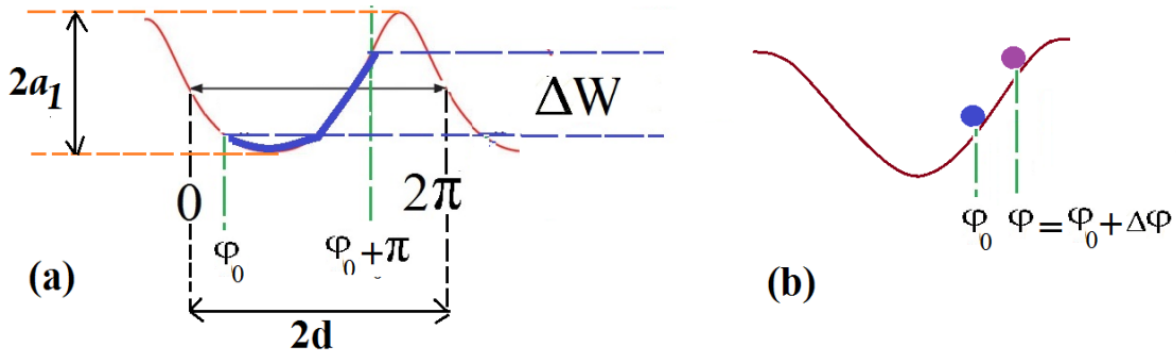


**Figure 4-3:** (a) Switching scheme and energy loss per stage ( $\Delta W$ ) for phase  $\varphi_0$ . (b) The phase ( $\varphi = \varphi_0 + \Delta\varphi$ ) for a molecule close to the synchronous molecule

A non-synchronous molecule with a phase  $\varphi = \varphi_0 + \Delta\varphi$  experiences more of the upward side of the potential hill, and therefore will lose more kinetic energy than the synchronous molecule, and over time its velocity decreases below the velocity of the synchronous molecule. At this point, its new phase becomes  $\varphi_0 - \Delta\varphi$ , and the molecule loses less energy compared to the synchronous

molecule while climbing the potential, and over time its velocity becomes higher than the synchronous molecule. This cycle continues until the end of the decelerator. For a molecule close to the synchronous molecule, the longitudinal oscillation frequency of the molecule around the synchronous molecule can be approximated by:

$$\frac{\omega_x}{2\pi} = \left( \frac{a_1 \cos \varphi_0}{2m\pi d^2} \right)^{\frac{1}{2}} \quad (4.3)$$

In our case, for ammonia molecule ( $|J = 1, MK = -1 \rangle$ ) with  $m = 17.031 \text{ gr/mol}$ , maximum of  $|\vec{E}| = 126 \text{ kV/cm}$  on the molecular axis, and  $d = 5.5 \text{ mm}$ , the potential depth is  $2a_1 = 2.4 \times 10^{-23} \text{ Joules}$ . Ideally with these numbers, the maximum possible oscillation frequency, which occurs at phase zero, will be about 1494 Hz. The equation of motion of the molecule with respect to the synchronous molecule can be approximated by [39]:

$$\frac{md}{\pi} \frac{d^2 \Delta\varphi}{dt^2} + \frac{2a_1}{d} (\sin(\varphi_0 + \Delta\varphi) - \sin(\varphi_0)) = 0 \quad (4.4)$$

where  $m$  is the mass of the molecule. After solving the differential equation we can obtain the phase stability diagrams for different choices of the synchronous molecule phase. The results of the calculations for our decelerator operating at  $\pm 12 \text{ kV}$  for the case of ammonia molecules are shown in Figure (4-4). The red lines in figure (4-4) show the boundary of the phase stable area for each phase that is called the Separatrix. The Separatrixes for a few other phases are also shown.

The natural longitudinal oscillation frequencies of our decelerator for ammonia molecules as a function of the initial longitudinal position for the phase angles  $\varphi_0 = 0^\circ, 20^\circ, 40^\circ, 60^\circ, \text{ and } 80^\circ$  are also calculated and shown in Figure (4-5).

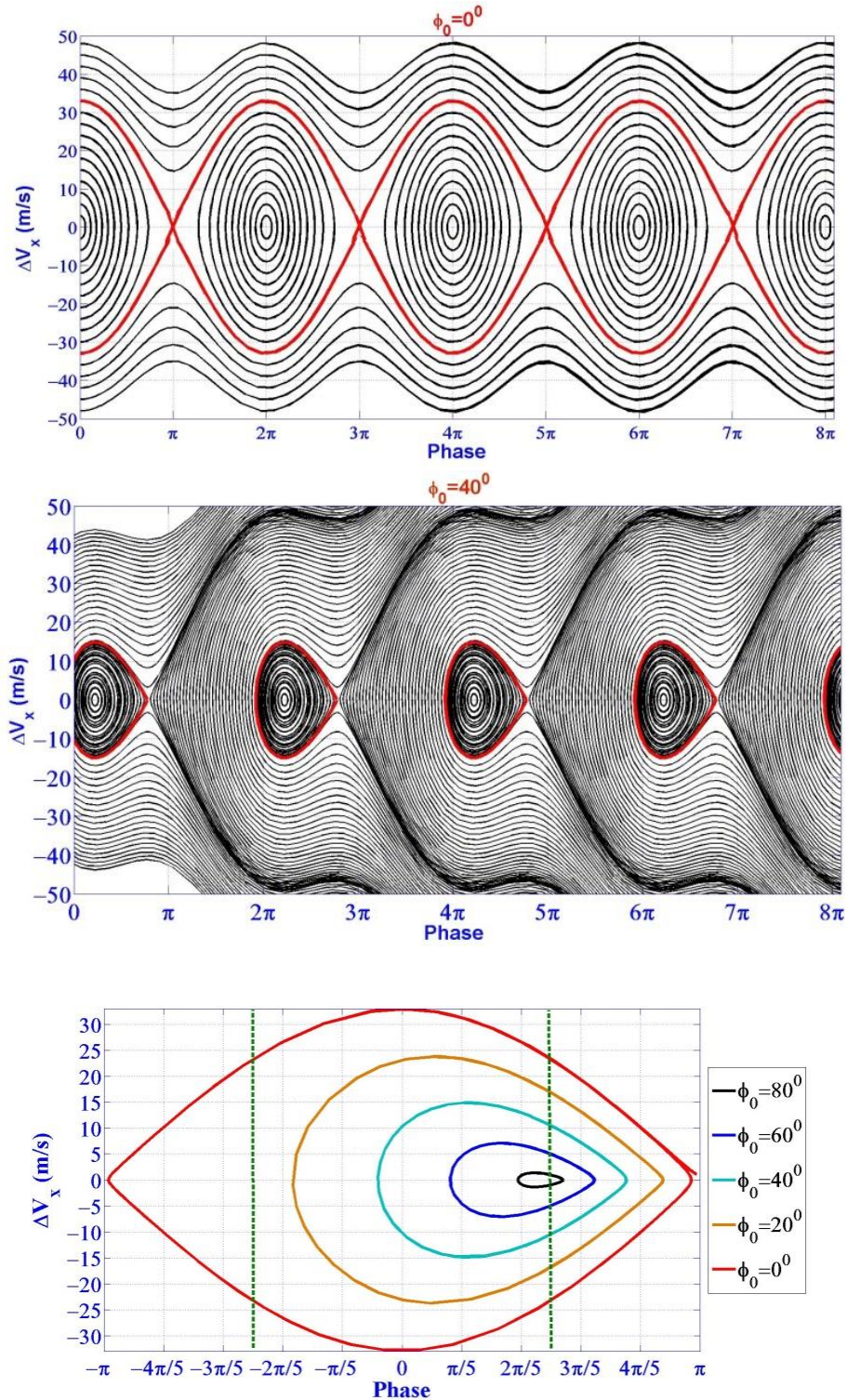


**Figure 4-4:** Phase space plots. Top: Lines of constant energy in phase-space for phase  $0^\circ$ . Middle: Lines of constant energy in phase-space for phase  $40^\circ$ . Bottom: Separatrices for different phases. The separatrices are shown in colors and are the boundary between the phase-space stable and unstable areas. Note the reduction of the phase-space stable area as the phase increases. The green dashed lines show phases  $-\pi/2$  and  $+\pi/2$

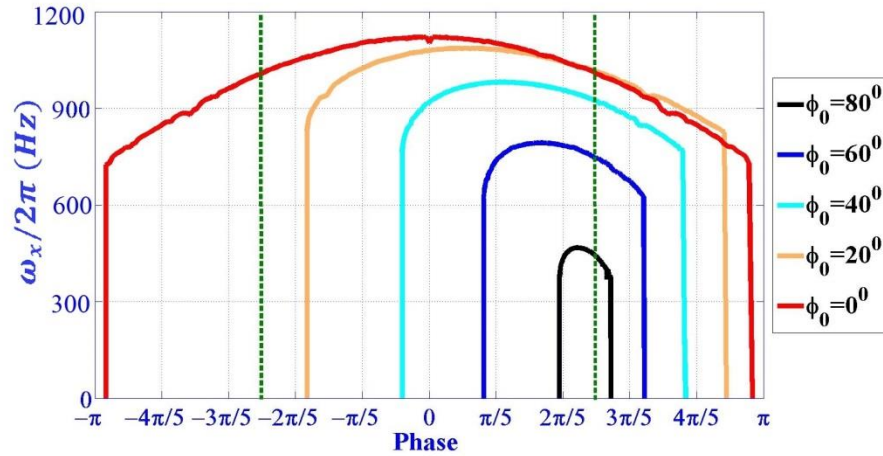


**Figure 4-5:** The natural longitudinal oscillation frequencies of the UBC Stark decelerator for ammonia molecules as a function of the initial longitudinal position for the phase angles  $\varphi_0 = 0^\circ, 20^\circ, 40^\circ, 60^\circ,$  and  $80^\circ$ . The green dashed lines show phases  $-\pi/2$  and  $+\pi/2$

The amount of deceleration depends on the phase of the synchronous molecule, and since it determines the velocity of the target molecule, all of the timings of the experiment depend on this phase. The higher the phase is, the slower the beam that can be obtained. However, as we can see from figure (4-4), increasing the phase is equivalent to decreasing the phase stable area, which means fewer molecules are getting decelerated. Therefore there is a trade-off between the number of decelerated molecules and their final velocity.

#### 4.1.2 Transverse stability

In a real experiment, the motions of the molecules inside the decelerator in longitudinal and transverse directions are not independent. Since the electric field is higher close to the electrodes, molecules will undergo oscillations around the synchronous molecule in the transverse direction. As the molecules change their position in the transverse direction their longitudinal potential gradient changes. It is possible that the molecules leave the phase stable region when they are oscillating in the transverse direction, due to the switching of the field which changes the orientation of the potential well in the transverse direction. The method introduced by Bethlem et al. is followed to obtain an estimate for the natural transverse oscillation frequency ( $\omega_{transverse}/2\pi$ ) of ammonia molecules in our Stark decelerator, in order to get a quantitative measure of the focussing behaviour of our decelerator, [49]. In this method the average force experienced by the ammonia molecule in one of the transverse directions over one period of deceleration (two stages with one switching) is calculated. Assuming that the longitudinal

oscillation frequency is low ( $2d/v_x \ll 2\pi/\omega_t$ ), and assuming that the transverse force is linear in displacement from the molecular axis, the frequency of transverse oscillation only depends on the phase of the molecule. The dependence of this frequency on the phase can be easily understood if we think about the longitudinal motion of the molecule, and the amount of time it spends in different parts of the field distribution during its flight. If the phase is close to zero, then the molecule will spend most of its time near the grounded electrodes which have the modest focussing force. On the other hand, at higher phases the molecule spends more time close to the HV electrodes, and therefore feels more focusing force.

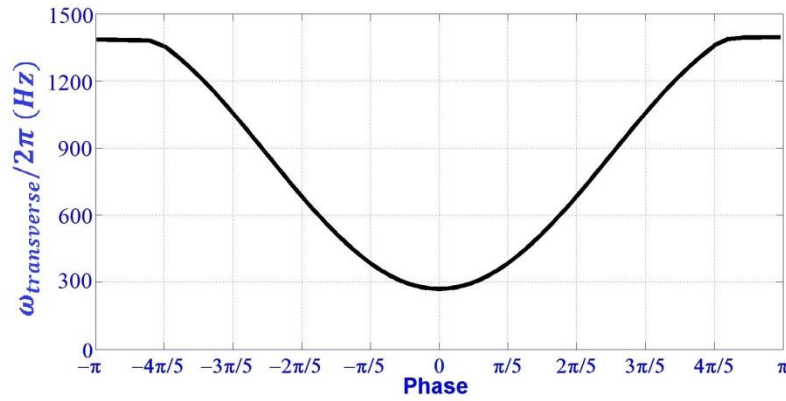


**Figure 4-6:** The transverse oscillation frequency for ammonia an molecule in one period of deceleration versus the initial position (phase) of the molecule. Note that one period of deceleration here is referred to the distance between two parallel adjacent electrode pairs.

When the longitudinal and transverse oscillation frequencies are close, a parametric amplification can occur, which results in unstable regions in the phase-space acceptance of the decelerator [39]. Since this behaviour is well explained in [39], the theory is not included here. However, the results for our decelerator operating at phase zero for the ammonia molecule are presented. It is assumed that the longitudinal frequency ( $\omega_x/2\pi$ ) does not depend on the transverse position ( $z$ ) of the molecule, and the non-synchronous molecule has phase ( $\varphi$ ). The temporal oscillation frequency in the transverse direction ( $z$ ) can be approximated by (assuming mass=1) [49]:

$$\frac{d^2z}{dt^2} = -\omega_z^2(t)z$$

$$\omega_z^2(t) = \omega_0^2 - A\cos(2\omega_x t) \quad (4.5)$$

Where the values of  $\omega_0$  and  $A$  can be obtained from combining the transverse oscillation frequency as a function of phase (the same as figure (4-6)), and the phase corresponding to the longitudinal oscillation frequency ( $\omega_x/2\pi$ ). The equation of motion for the transverse motion of the molecule driven by its longitudinal motion is given by the so-called ‘‘Mathieu equation’’ [39]:

$$\frac{d^2z}{d\tau^2} + (a - 2q\cos(2\tau))z = 0$$

where

$$a = \left(\frac{\omega_0}{\omega_x}\right)^2, \quad q = \frac{A}{2\omega_x^2}, \quad \tau = \omega_x t \quad (4.6)$$

If the solution to this equation is stable (oscillatory) then the molecule will remain confined during the deceleration process. Since the stability of the solutions to the Mathieu equation depend on the value of  $\omega_x$ , the particle will be lost during the deceleration if the solution is unstable for a chosen  $\omega_x$  (or its equivalent phase). The lost molecules will be absent in the phase-space acceptance of the decelerator, and therefore the phase-space will be ring-like. The result for our case is shown in figure (4-7). In the Mathieu diagram, the blue area is where the solution of the equation is unstable and the red area shows the stable solutions. Due to the unstable solutions the decelerated packet cannot accept all of the values within its separatrix, so it will have a hollow shape. This hollow shape is not expected for a 1D simulation since it does not deal with the transverse oscillation. Also the actual shape of the phase-space distribution depends on the initial phase-space distribution of the molecules, and may look different than what is presented in figure (4-7), which assumes that the entire phase-space acceptance area is filled at the entrance of the decelerator.

Figure (4-8) illustrates the time evolution of the deceleration process at phase  $45^\circ$  from the initial velocity of about  $418 \text{ m/s}$  at nine different snap shots during the deceleration. The nozzle introduces a  $6D$  phase-space distributed molecular packet that arrives to the decelerator. The initial phase-space distribution  $(x, v_x)$  right before the decelerator is shown in the first shot from the left. Shown to the right are the eight shots from the molecules taken at equal time intervals, until the decelerated packet exits the decelerator. The position of the synchronous molecule is shown by the red dashed line.

It is interesting to note what happens to the molecules that leave the decelerated packet. As we can see in figure (4-8), these molecules continue their flight to the end of the decelerator while

they are accelerated, not affected, or partially decelerated. The other important feature of this figure is the presence of multiple decelerated packets, arriving at different times with different final velocities. The reason is that the initial packet of molecules introduced to the decelerator is spatially stretched, due to the free flight of the molecules from the nozzle to the decelerator.

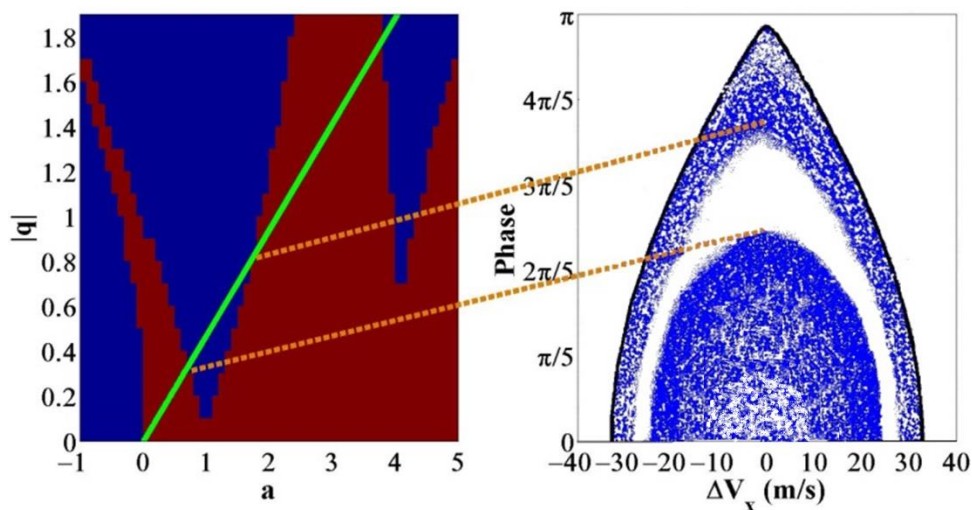


**Figure 4-7:** Left: The solution to the Mathieu equation. The phase-space stable solutions are shown with red color while the phase-space unstable solutions are shown with blue. Right: The phase-space distribution obtained with numerical trajectory simulation of the ammonia molecules for phase= $0^\circ$ . The hollow area in the phase-space corresponds to the unstable solutions of the Mathieu equation.

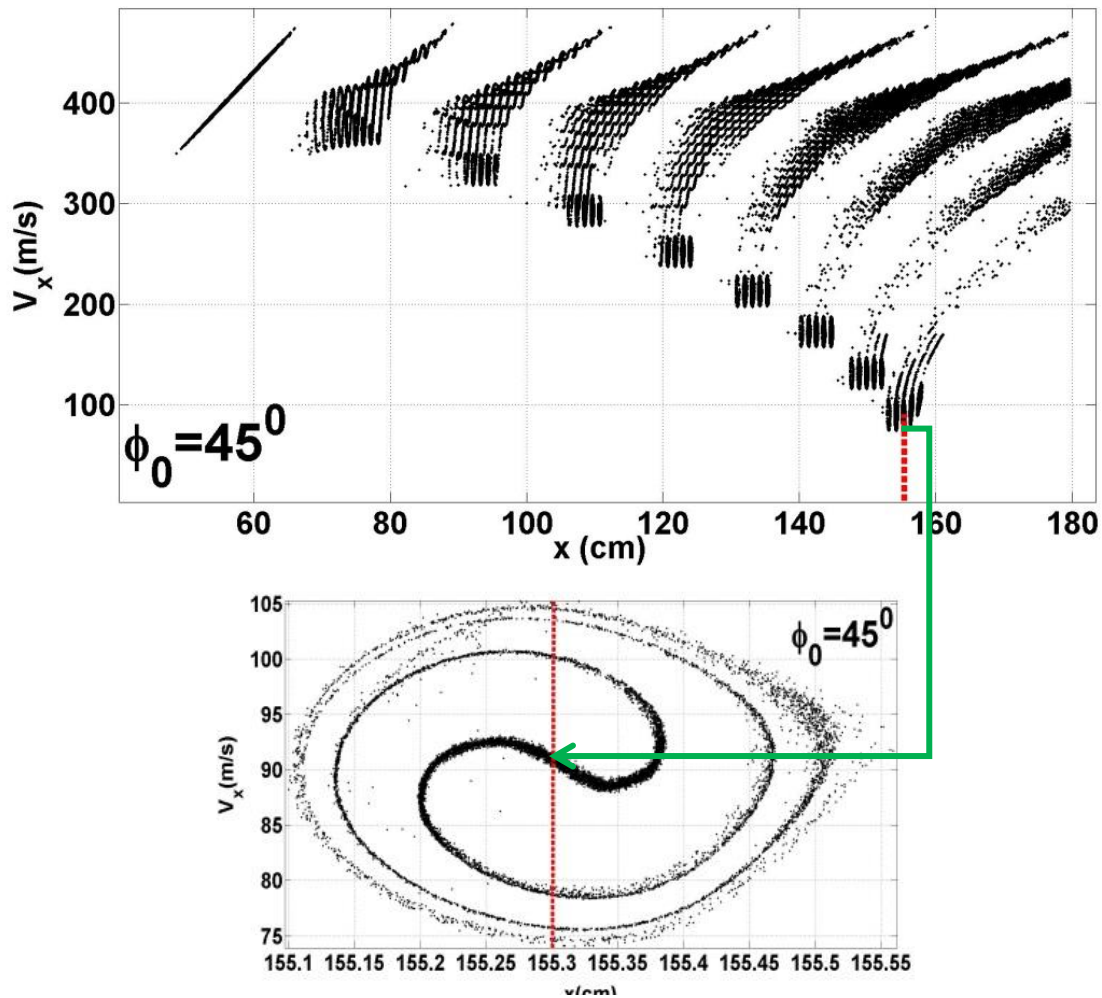


**Figure 4-8:** Top: Simulation for phase-space distribution of 100000 ammonia molecules at nine different snapshots during their deceleration with  $\phi_0 = 45^\circ$  inside the decelerator. First snapshot at the left corresponds to the phase-space distribution at the entrance of the decelerator, and the last snapshot at the right corresponds to right after the last deceleration stage. Bottom: The main decelerated packet which includes the synchronous molecule enlarged. Note the hollow area in the phase-space distribution which is mostly due to the wide spatial distribution of the molecules due to their free flight from nozzle to the decelerator. The red dotted line shows the position of the synchronous molecule.

## 4.2 Non-adiabatic transitions in a Stark decelerator

In a Stark decelerator, the Stark shift of the energy states adiabatically follows the electric field. This is true until the switching happens. At this point, the electric field quickly changes its magnitude and direction which can cause non-adiabatic transitions from the desired energy state to an undesired one. These transitions become significant if the time-varying electric field has frequency components that are close to the energy splitting of the energy states. A non-adiabatic transition can occur due either to a quick rotation of the field, or quick change in the magnitude

of the field. Since the Stark shift of the rotational energy states correspond to frequencies in the  $GHz$  region, if the switching of the voltage electrodes is fast (less than  $1 \mu s$ ) a non-adiabatic transition may occur, especially when the switching is from a low field to a high field magnitude (the typical rise time of the voltages on the electrodes are on the order of a few hundred nanoseconds). This is possible at avoided crossings of the energy states, or at very low electric fields. In the case of non-adiabatic transitions at low electric fields, rotation of the field plays the main role. Fortunately, at low fields it is possible to eliminate the transitions by using a bias field. The bias field ensures that the electric field magnitude never becomes small enough to bring the two Stark-split states very close to each other, or to energies comparable with the frequency of the rotation. Following the method described by Wall et al. [109], the bias voltage required for our decelerator was calculated for ammonia molecules in the  $|J, K \rangle = |1, 1 \rangle$  state. In our case the rise time of the voltage on the electrodes was about  $150 ns$ , which implied that a bias voltage of  $150 V$  ( $1.61 kV/cm$ ) would suffice for our goal. To provide the bias electric field, an adjustable floating ground circuit was added to our HV switch circuits. Having a bias voltage helps in removing the possibility of the adiabatic transitions at zero electric field. The angular frequency of rotation of the electric field for our Stark decelerator for different phases at which the switching happens is presented in figure (4-9).

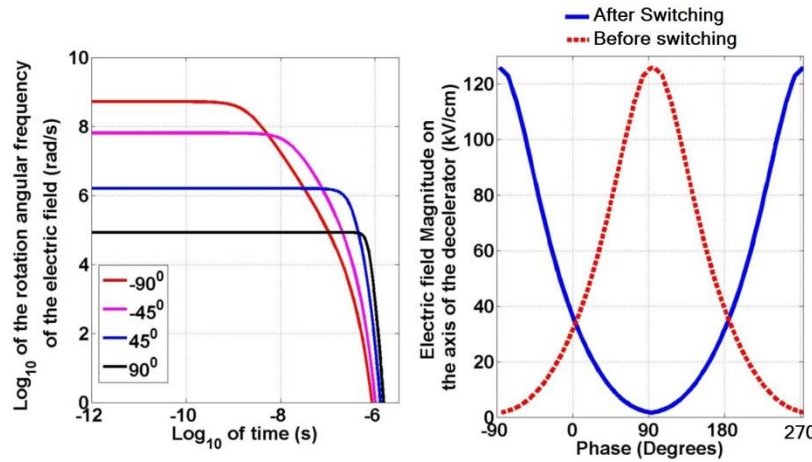


**Figure 4-9:** Left: The angular frequency of rotation of the electric field for the UBC Stark decelerator for different phases ( $-90^\circ$ ,  $-45^\circ$ ,  $45^\circ$ ,  $90^\circ$ ) at which the switching occurs. Right: (blue) After switching, the electric field magnitude when HV for the electrodes located at  $-90^\circ$  and  $270^\circ$  is on; (red) the electric field for the electrode pair located at  $90^\circ$  before switching the HV.

### 4.3 The principle of microwave Stark deceleration and lens effect

The advantage of using a microwave field is the possibility of having an absolute maximum of a field in free space, which is impossible for a DC electric field (Earnshaw' theorem). Using a microwave trap for polar molecules was first proposed by DeMille et al. [101], and later in 2005 a microwave Stark decelerator was proposed by Enomoto and Momose [18]. A microwave decelerator has an advantage over the DC Stark decelerators since its three dimensional trapping potential eliminates the loss of the molecules in the transverse direction. In 2010 Odashima et al. experimentally demonstrated a microwave lens for polar molecules, and in 2012 Merz et al. demonstrated the first experimental deceleration of polar molecules using microwave fields [110][45]. The lens effect for pre-cooled (using the counter-rotating nozzle method) CH<sub>3</sub>CN and CD<sub>3</sub>CN molecules in their ground state has already been demonstrated in our lab using a non-superconductive MW cavity [29]. In this experiment the pre-cooling was essential in order to observe the effect of the dipole force, since the potential was on the order of 1 K. Due to the shape of the standing wave inside the MW cavity, the focusing experiments required  $TM_{01P}$  and  $TE_{01P}$  modes of the cavity while the deceleration is best done with  $TE_{11P}$ . Assume that the AC Stark shift of the desired energy state (which is usually the ground state of the molecule) is given by  $\Delta U$ . The translational motion of the molecules can be affected by the microwave dipole force  $\vec{F}$ :

$$\vec{F}(\rho, z, t) = -\vec{\nabla}U(\vec{E}(\rho, z, t)) \quad (4.7)$$

Therefore any focusing effect or deceleration can happen with the same scheme as the DC hexapole or DC Stark decelerator. The only difference here is that the shape of the potential is defined by the mode of the cavity, and the strength of the potential depends on the detuning of the rotational transition frequency from the cavity resonance frequency, the MW power, and the Q-factor of the cavity. The radial component of the force is responsible for the focussing or defocusing effects, while the longitudinal part of the force (cavity axis direction) is responsible for the deceleration or acceleration.

Consider the two-dimensional motion of an acetonitrile molecule with no azimuthal velocity. Assume that the  $TM_{010}$  mode of the cavity is chosen for focusing the molecules. This mode is ideal for this purpose because it does not have any nodes that causes non-adiabatic transitions

among degenerate internal states in zero electric field [110]. The magnitude of the electric field distribution for this mode is shown in figure (4-10):

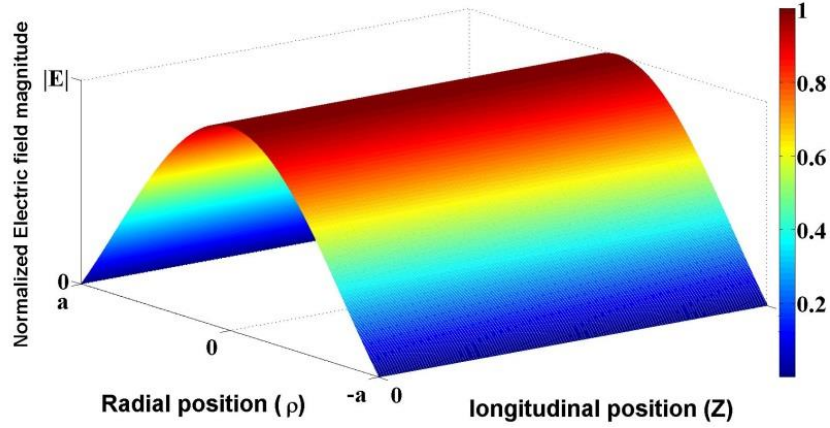


**Figure 4-10:** The normalized magnitude of electric field distribution for  $TM_{010}$  mode in a cylindrical cavity. See Figure (4-14) for the cross section view.

Because the maximum electric field strength is at the centre of the cavity, this mode can focus molecules in HFS states. The focusing effect of the microwave cavity can be calculated by use of a transfer matrix. For near resonant and high-power microwaves ( $h|\nu_{eg} - \nu| \ll |E_0\mu_{eg}|$ ), the AC Stark shift is not sensitive to detuning ( $\nu_{eg} - \nu$ ), and the radial trapping potential can be assumed to be harmonic, and the transfer matrix can be expressed as [111]:

$$\begin{pmatrix} \rho_{out} \\ \nu_{\rho out} \end{pmatrix} = \begin{pmatrix} \cos \frac{\alpha d}{\nu_z} & \frac{1}{\alpha} \sin \frac{\alpha d}{\nu_z} \\ -\alpha \sin \frac{\alpha d}{\nu_z} & \cos \frac{\alpha d}{\nu_z} \end{pmatrix} \begin{pmatrix} \rho_{in} \\ \nu_{\rho in} \end{pmatrix} \quad (4.8)$$

Where

$$\alpha = \sqrt{\frac{E_0\mu_{eg}x_{01}^2}{4a^2m}} \quad (4.9)$$

The  $TE_{11p}$  mode can be used both for focusing and deceleration purposes. The electric field has nodes and anti-nodes along the longitudinal direction (the same as cavity axis) that provides focusing and deceleration potentials for molecules in HFS states. The electric field distribution of this mode for  $p = 5$  of a cavity with length ( $L$ ) and radius ( $a$ ) is shown below (Calculated for  $\theta = 45^\circ$  of cylindrical coordination):

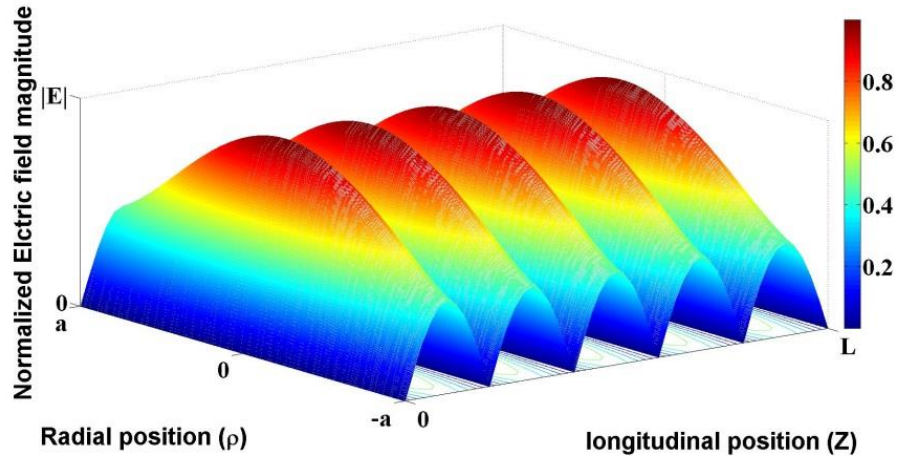


**Figure 4-11:** The normalized magnitude of electric field distribution for  $TE_{115}$  mode in a cylindrical cavity with length  $L$  and radius  $a$ .

In order to decelerate the molecules a switching scheme is required to prevent the molecules from regaining their kinetic energy by going through the downward side of the potential. During the deceleration the microwave potential is turned off and on in a way that the molecule only sees a portion of each period of the potential that satisfies the desired deceleration, acceleration, or guiding. The switching scheme is shown below for a cavity with length  $L$  and  $p$  nodes in the longitudinal direction.  $\phi_0$  is the phase of the synchronous molecule.

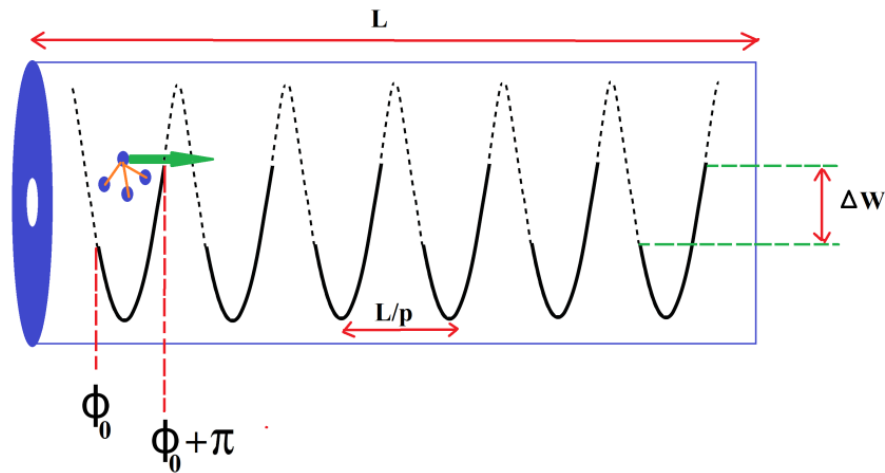


**Figure 4-12:** Principle of AC Stark deceleration by using a MW cavity with length  $L$  and with  $P$  number of longitudinal modes

By defining phase  $90^\circ$  at nodes and  $-90^\circ$  at anti-nodes, and assuming that  $W$  is the depth of the potential between a node and anti-node,  $\lambda$  is the microwave wavelength, and  $m$  is the mass of the molecule, one can show that the equation of motion for a nonsynchronous molecule (located at phase  $\phi$ ) with respect to the synchronous molecule is given by [18]:

$$\Delta\varphi = \frac{4\pi(z - z_{synchronous})}{\lambda} \quad (4.10)$$

$$\frac{d^2\Delta\varphi}{dt^2} + \frac{8\pi W}{m\lambda^2}(\sin(\varphi_0 + \Delta\varphi) - \sin(\varphi_0)) = 0 \quad (4.11)$$

The rotational transition frequency of acetonitrile between  $|100\rangle$  and  $|000\rangle$  states is about  $18.4 \text{ GHz}$ . Assume the mode  $TE_{11p}$  is used for our proposed superconducting cavity (its prototype version is described in the experimental results) for decelerating acetonitrile molecules with  $m = 41 \text{ gr/mol}$  in their ground state. Also assume the detuning to be  $100 \text{ MHz}$ , and  $P \times Q = 2 \times 10^7$  for the cavity. By neglecting the delay time effect in rise and fall times of the field inside the cavity we expect  $W \sim 0.3 \text{ K}$  in equation (4.11). The longitudinal phase-space acceptance of superconducting microwave decelerator with these assumptions is shown in figure (4-13):

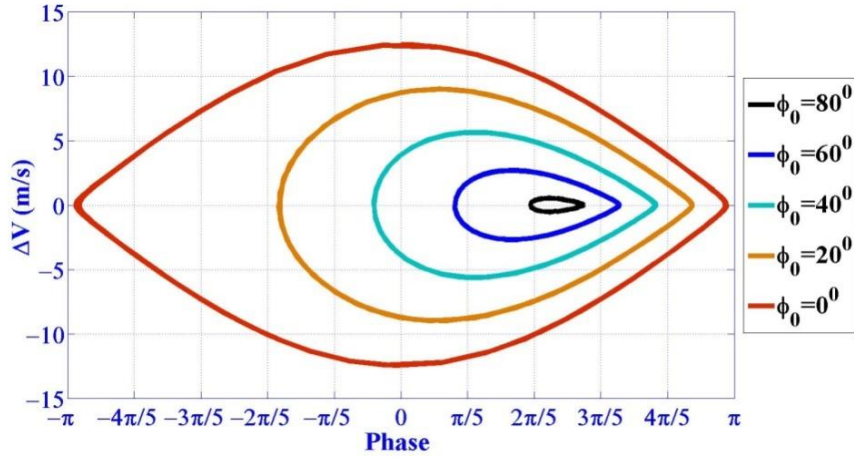


**Figure 4-13:** The longitudinal phase-space acceptance of a prototype superconducting MW cavity for Acetonitrile molecules and by neglecting the experimental limitations on switching times which can reduce the phase-space stable area.

In a real experiment the switching is not instantaneous. Enomoto and Momose have previously discussed an amplitude modulation of the field [18]. In addition, the evolution of the quality factor during the experiment due to the heating caused by the surface current should be considered. It is especially important when we want to use the microwave cavity as a trap for molecules. We have experimentally investigated this effect for our prototype superconducting cavity.

We are currently working on a combination of our superconducting microwave decelerator and a counter rotating nozzle for deceleration purposes. However, the experimental results presented in this thesis are limited to the measurements done for characterizing the superconducting MW cavity.

### 4.3.1 Superconducting microwave cavity for AC Stark decelerator and lens

In order to generate sufficiently large microwave fields microwave cavities are needed. In all of the previous studies the microwave cavities in use had quality factors of  $\sim 10^4$  or less which limited the application of this method to the so called “pre-cooled” molecular beams. The pre-cooled molecular beam refers to a molecular packet which is already partially decelerated with another cooling method such as Stark deceleration or counter rotating nozzle. Therefore, when it arrives at the microwave cavity, the translational velocity of the beam in the pre-cooled molecular packet is already reduced. Since the translational energy of the pre-cooled beam is lower and molecules spend more time within the cavity, the AC Stark potential becomes effective and can manipulate the motion of the molecules. In 2012 it was proposed to use a superconducting microwave cavity to enhance the Q-factor of the cavity and hence increase the potential depth of the cavity [111] which is presented in this thesis.

Table (4-1) shows the basic formulae for three modes of a cylindrical cavity with its origin at the centre of one of the ends of the cavity, in which  $\nu_p$  is the resonant frequency,  $E_\rho$ ,  $E_\theta$ , and  $E_z$  are the electric field component amplitudes,  $W$  is the total energy stored in the cavity,  $Q_r$  is the quality factor due to the surface resistance,  $J_m$  and  $J'_m$  are the  $m$ -th order Bessel function and its derivative,  $x_{mn}$  and  $x'_{mn}$  are the  $n$ -th roots of  $J_m$  and  $J'_m$  respectively ( $x'_{11} = 1.8412$ ,  $x'_{01} = 3.8317$ , and  $x_{01} = 2.4048$ ),  $a$ ,  $d$  and  $V$  are the radius, length, and volume of the cavity  $\epsilon_0$  and  $\mu_0$  are permittivity and permeability of vacuum,  $c$  is the speed of light in vacuum,  $s_p = 1$  for  $p = 0$  and  $s_p = 2$  for  $p \neq 0$ . The maximum electric field is  $E_0/2$  for the  $TE_{11p}$  mode,  $0.582 E_0$  for the  $TE_{01p}$  mode, and  $E_0$  for the  $TM_{010}$  mode.  $p$  is the number of longitudinal modes. Figure (4-14) illustrates the cross section view of these modes.

Among the modes mentioned in table (4-1)  $TM_{010}$  has the maximum AC field amplitude on the longitudinal cavity axis, which provides a radial confinement harmonic potential for molecules in high field seeking states. In addition, this mode does not have a node in the longitudinal cavity

axis direction, and its field is axially symmetric, which means that  $TM_{010}$  is a good candidate for focussing molecules in high field seeking states. The  $TE_{01p}$  mode has zero electric field amplitude along the longitudinal cavity axis, which provides a two dimensional radial confinement potential for the molecules in low field seeking states. The  $TE_{11p}$  mode has the lowest cut-off frequency, and has its maximum AC field amplitude on the centre axis which periodically changes from zero to maximum. This mode can provide a three-dimensional trapping potential for the molecules in their high field seeking states at every antinode, so can be used for deceleration of molecules with the same scheme as the DC Stark decelerator. The static radial confinement in this mode is an advantage of the microwave decelerator over the alternating gradient decelerators (works for molecules in high field states), which conserves the phase-space density of the decelerated packets, especially near zero velocity.

**Table 4-1:** Formulae for three modes of a cylindrical cavity with its origin at the centre of the one of the ends of the cavity[111][112][113]

	TE <sub>11p</sub> mode ( $p \geq 1$ )	TE <sub>01p</sub> mode ( $p \geq 1$ )	TM <sub>01p</sub> mode ( $p \geq 0$ )
$v_p$	$\frac{c}{2a} \sqrt{\left(\frac{x'_{11}}{\pi}\right)^2 + \left(\frac{pa}{d}\right)^2}$	$\frac{c}{2a} \sqrt{\left(\frac{x'_{01}}{\pi}\right)^2 + \left(\frac{pa}{d}\right)^2}$	$\frac{c}{2a} \sqrt{\left(\frac{x_{01}}{\pi}\right)^2 + \left(\frac{pa}{d}\right)^2}$
$E_\rho$	$E_0 \frac{J_1(x'_{11}\rho/a)}{x'_{11}\rho/a} \sin \theta \sin \frac{\pi pz}{d}$	0	$-E_0 \frac{\pi pa}{x_{01}d} J'_0(x_{01}\rho/a) \sin \frac{\pi pz}{d}$
$E_\theta$	$E_0 J'_1(x'_{11}\rho/a) \cos \theta \sin \frac{\pi pz}{d}$	$E_0 J'_0(x'_{01}\rho/a) \sin \frac{\pi pz}{d}$	0
$E_z$	0	0	$E_0 J_0(x_{01}\rho/a) \cos \frac{\pi pz}{d}$
$W$	$\frac{\epsilon_0 E_0^2 \pi a^2 d}{8} \left(1 - \frac{1}{x_{11}^2}\right) J_1^2(x'_{11})$ $\simeq 0.02984 \epsilon_0 E_0^2 V$	$\frac{\epsilon_0 E_0^2 \pi a^2 d}{4} J_0^2(x'_{01})$ $\simeq 0.04055 \epsilon_0 E_0^2 V$	$\frac{\epsilon_0 E_0^2 \pi a^2 d}{2s_p} \left[1 + \left(\frac{\pi pa}{x_{01}d}\right)^2\right] J_1^2(x_{01})$ $\simeq 0.1348 \epsilon_0 E_0^2 V$ ( $p = 0$ )
$Q_r$	$\frac{c\mu_0}{2R_s} \frac{(x'_{11}{}^2 - 1)x'_{11}{}^2 + (\pi pa/d)^2}{x'_{11}{}^4 + 2\pi^2 p^2 x'_{11}{}^2 a^3/d^3 + (\pi pa/d)^2(1 - 2a/d)}$	$\frac{c\mu_0}{2R_s} \frac{[x'_{01}{}^2 + (\pi pa/d)^2]^3}{x'_{01}{}^2 + 2\pi^2 p^2 a^3/d^3}$	$\frac{c\mu_0}{2R_s} \frac{\sqrt{x_{01}{}^2 + (\pi pa/d)^2}}{1 + s_p a/d}$

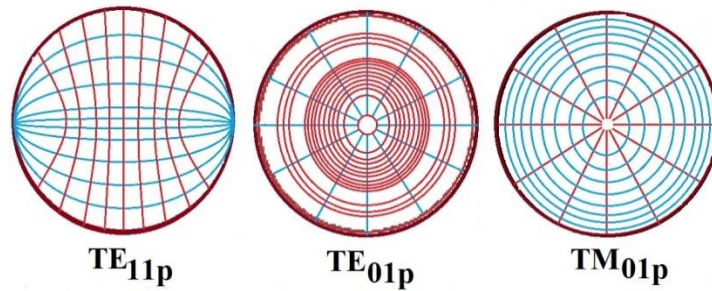


**Figure 4-14:** The schematic cross section view for  $TE_{11p}$ ,  $TE_{01p}$ , and  $TM_{01p}$  modes. The red lines correspond to E field, and the blue lines correspond to H field.

The electric field strength of the microwave field in a cylindrically symmetric resonator is given by [114]:

$$E_{MW} = \sqrt{\frac{4.2 Q P_{MW}}{\pi \epsilon_0 \nu_{mnp} V}} \quad (4.12)$$

In which  $Q$  is the quality factor of the system,  $P_{MW}$  is the power of the microwave field, and  $\nu_{mnp}$  is the frequency of the  $TE_{11p}$  mode which is given by:

$$\nu_{mnp} = \frac{c}{2} \sqrt{\left(\frac{x'_{lm}}{a\pi}\right)^2 + \left(\frac{p}{L}\right)^2} \quad (4.13)$$

Where  $x_{lm}$  (replaces  $x'_{lm}$  in equation (4-13)) is 2.4048 for  $TM_{01p}$  modes, and  $x'_{lm} = 1.8412$  for  $TE_{11p}$  modes,  $p$  is the node number of the standing wave,  $a$  is the radius of the cavity, and  $L$  is the length of the cavity. Since the AC Stark shift is proportional to the electric field magnitude, higher electric field magnitudes are preferred (as long as the Stark shift increases). According to equation (4.12), the electric field strength inside the cavity can be set by the MW power applied to the cavity and the quality factor of the cavity. Improving the quality factor of the cavity can help in generating higher electric field magnitudes. Our proposed superconducting cavity has a much higher quality factor than the ordinary cavities, and hence provides higher electric field magnitudes. A prototype version of such cavity was characterized in our lab. The experimental results of the prototype cavity are presented in section (6-3).

### 4.3.2 Quality factor of a cylindrical microwave cavity

The quality factor of the cavity is defined as:

$$Q = \frac{2\pi W}{P} \quad (4.14)$$

Where  $P$  is the power loss of the cavity and  $W$  is the total energy stored in the cavity. The unloaded quality factor ( $Q_0$ ) of the cavity depends on the power loss due to the finite surface resistance (expressed by  $Q_r$ ), the end holes (expressed by  $Q_d$ ), and other effects such as contact resistance among the cavity parts (expressed by  $Q_{others}$ ). If  $P_i$  represents the power loss due to each effect, the relation between  $Q_0$  and the above power losses can be expressed as below:

$$Q_i = \frac{2\pi W}{P_i} \quad (4.15)$$

$$\frac{1}{Q_0} = \frac{1}{Q_r} + \frac{1}{Q_d} + \frac{1}{Q_{others}} \quad (4.16)$$

As shown in table (4-1),  $Q_r$  depends on the cavity dimensions ( $a$  and  $d$ ), and the surface resistance ( $R_s$ ).  $R_s$  can be approximated by [115]:

$$R_s = R_{res} + R_{BCS} \quad (4.17)$$

$$R_{BCS} \propto \frac{v^b}{T} \exp\left(-\frac{\Delta}{k_B T}\right) \quad (4.18)$$

Where  $R_{res}$  is the residual resistance at  $T = 0 K$ , and according to Bardeen-Cooper-Schrieffer theory,  $R_{BCS}$  is the temperature dependence part of  $R_s$ ,  $b$  is the frequency dependence factor,  $k_B$  is the Boltzmann constant, and  $2\Delta$  is the energy gap [116]. Although having a smaller hole (radius  $a_{hole}$ ) and longer hole length ( $d_{hole}$ ) minimizes the energy loss through the holes [112][117], having a larger hole diameter and shorter hole length is preferred for introducing more molecules to the cavity. The power loss for a hole with small radius and long length in a cavity for  $TE_{11p}$  and  $TM_{01p}$  modes can be approximated by [112]:

$$P_{hole-TE_{11p}} = \frac{32\epsilon_0\pi^3v^4}{27c^3} a_{hole}^2 E_0^2 \left[ 1 - \left( \frac{cx'_{11}}{2\pi va} \right)^2 \right] e^{-2\gamma_m d_{hole}}$$

$$P_{hole-TM_{01p}} = \frac{32\epsilon_0\pi^3v^4}{27c^3} a_{hole}^2 E_0^2 e^{-2\gamma_e d_{hole}} \quad (4.19)$$

Where  $\gamma_m = \sqrt{\left(\frac{x'_{11}}{a_{hole}}\right)^2 - \left(\frac{2\pi v}{c}\right)^2}$  and  $\gamma_e = \sqrt{\left(\frac{x_{01}}{a_{hole}}\right)^2 - \left(\frac{2\pi v}{c}\right)^2}$ . The diffraction loss ( $P_d$ ) is the sum of the losses of the two holes. An antenna is responsible for injecting microwaves into the cavity. The loaded quality factor ( $Q_L$ ) is referred to the total quality factor of the cavity at the presence of an antenna (with  $Q_c$  as the quality factor of the input coupler), and is given by:

$$\frac{1}{Q_L} = \frac{1}{Q_0} + \frac{1}{Q_c} = \frac{Q_0}{1 + \beta} = \frac{v_p}{\delta v} \quad (4.20)$$

where  $\beta = Q_0/Q_c$  is called the coupling parameter,  $v_p$  is the resonant frequency, and  $\delta v$  is the full width at half maximum of the resonant frequency in the frequency domain. In the time domain the decay of the stored energy  $W(t)$  as a function of time after turning the input power off can be given by:

$$W(t) = W(0)e^{-2\pi v t / Q_L} \quad (4.21)$$

The relationship between the stored energy in the cavity and the quality factor of the cavity at resonance and in the steady state is:

$$W = \frac{P_{input} Q_0}{2\pi\nu} (1 - |\Gamma|^2) = \frac{P_{input} Q_L}{2\pi\nu} \frac{4\beta}{1 + \beta} \quad (4.22)$$

Where  $\Gamma$  is the voltage reflection coefficient of the coupling antenna and is given by  $|\Gamma|^2 = \left(\frac{1-\beta}{1+\beta}\right)^2$ . Critical coupling happens when there is no reflection and all the microwave power goes into the cavity. At critical coupling  $\Gamma$  is zero, and  $Q_L = Q_0/2$ . Our prototype cavity has a superconducting lead-tin (Pb/Sn) coating that helps improve our quality factor. The design and characteristics of this cavity are presented in section (6-3).

## Chapter 5: Experimental setup

### 5.1 The UBC DC Stark decelerator

The DC Stark decelerator at UBC consists of 180 electrode pairs oriented alternately at 90 degrees to each other ( $Y$  and  $Z$  axis) and perpendicular to the molecular beam direction ( $X$  axis).

Figure (5.1) shows the design for the decelerator electrodes:

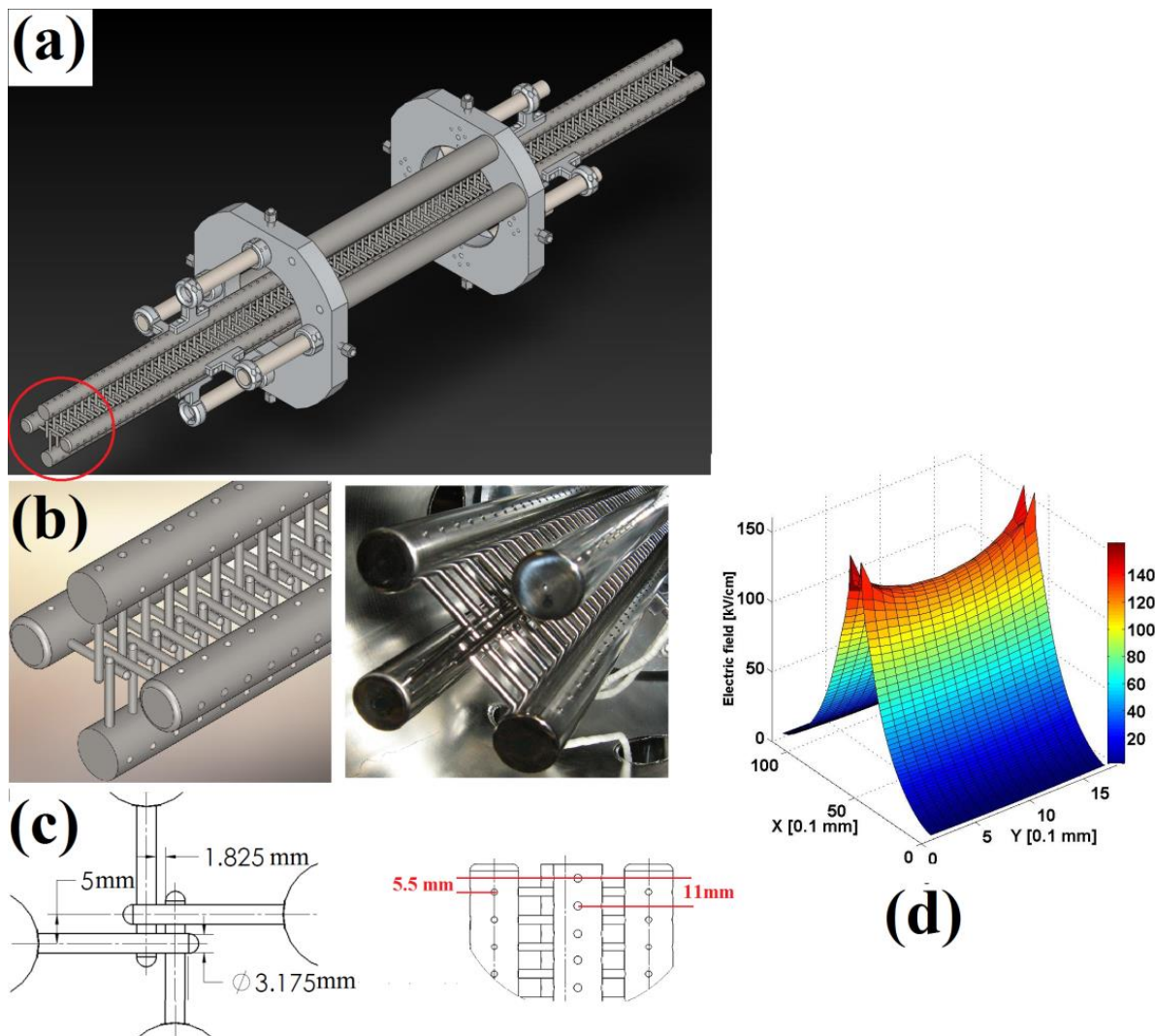


**Figure 5-1:** (a) The full view of the UBC Stark decelerator. The electrodes are attached to four long rods. On each rod 90 electrodes are attached that switch on and off simultaneously. Each rod is attached to the holder through a cylindrical ceramic connector which electrically isolates the rod from the rest of the setup. (b) The head of the decelerator. Note the orientation of the electrode pairs. (c) Left: The dimensions of the electrodes and the spacing between the electrodes of each pair. Right: The spacing between the adjacent electrodes. (d) The longitudinal electric field magnitude distribution for one electrode pair when the neighbor electrodes are off.

The decelerator has four highly polished one meter long stainless steel rods. Each of these rods holds a set of 90 parallel highly polished stainless steel electrodes that are carefully attached to the rod by tiny adjustable screws. In order to make a better adjustment we designed a set of jigs that set the height and also the spacing between adjacent electrodes. All of the 90 electrodes on each rod are connected to the same high voltage polarity through a fast high voltage switch that controls the timing of the voltage. Assuming that we refer to the  $X$  axis as the molecular beam axis, two of the 90 electrode sets together will make a set of 90 electrode pairs (positive and negative polarity) in  $Y$  direction, and the other two form a set of 90 electrode pairs in the  $Z$  direction, as are shown in the figure (5-1). These two sets form 180 electrode pairs together, and each pair is one deceleration stage. We refer to the electrode pairs in the  $Y$  direction as odd electrodes, and the electrode pairs in the  $Z$  direction as even. The separation between successive odd pairs or successive even pair is 11  $mm$  centre to centre. Any of the adjacent odd and even electrode pairs are separated by 5.5  $mm$  centre to centre. The surface-to-surface spacing between the positive and negative electrodes of each electrode pair is 1.825  $mm$ . Each of the stainless steel rods are connected to an adjustable holder in the middle through two ceramic connectors. The adjustable holder has eight screws that allow adjusting the position of the decelerator when it is inside the chamber. The connectors are made of ceramic, so the four rods are not electrically connected. The four high voltage switches are connected to each rod by wires. The wires are attached to the clamps that hold the rods, and are isolated from the holder of the decelerator by ceramic spacers.

### **5.1.1 Conditioning**

Since high positive and negative voltages are applied to the electrodes with a very small spacing between them, it is necessary to highly polish the electrodes. One can improve the surface smoothness by electrochemical polishing to prevent any unwanted discharge between the electrodes during the experiment. Fortunately, mechanical polishing was sufficient in our case. The reason for a high polish is that the resistance in the circuit is very small while operating the switches and any discharge can cause large surges of current in the circuit which can damage the electronics and also the electrodes. After mechanically polishing the electrodes outside the chamber, it is required to condition the electrodes after assembly in vacuum in order to minimize the possibility of discharge between electrodes. Conditioning means that the voltages applied to

the electrodes is slowly increased in several steps, while holding the voltage constant at each step until there is no micro-discharge. It is required to monitor the current flowing through the electrodes whenever high voltage is applied to the electrodes. Ideally the current should be zero, but due to possible micrometer-scale scratches remaining on the surface of the electrodes discharge is still possible. It was easier and safer to build a separate conditioning circuit that did not include switches. In order to monitor the current first we limited the current by adding a resistor to the circuit, which in our case was a  $500\text{ M}\Omega$  resistor. At each step the voltage was increased slowly and the current was monitored until it was dropped below  $100\text{ nA}$ . Then it was held at this condition for some time. By this method, weak micro-discharges can further smooth the surface of the electrodes further. The voltage was then slowly raised to the next step, and the procedure repeated. As the voltage was ramped up, the discharge became more frequent, and as a result the waiting time was increased. Whenever a current higher than  $1\text{ }\mu\text{A}$  was observed, the voltage was reduced to the previous step. The operational voltage of the decelerator while switching in our case was  $\pm 12\text{ kV}$ . In order to assure an operation without any discharge it was better to condition the electrodes for a voltage higher than the operational voltage. So our decelerator was conditioned to  $\pm 14.5\text{ kV}$ . Every time the chamber was opened the entire conditioning procedure had to be repeated. Figure (5-2) schematically shows the circuit in use for conditioning. Using this setup the current could be read both manually (by using ammeters) and with LabView code (using the optical current sensor). Sometimes conditioning with the method mentioned above cannot remove the discharge fully. In that case a more sophisticated method such as glow conditioning might be useful [118].

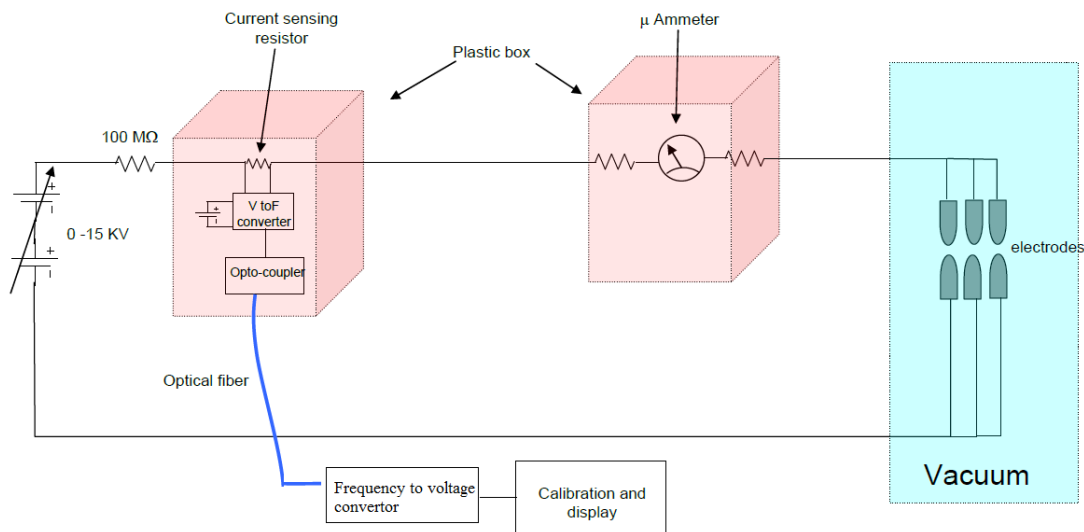


**Figure 5-2:** The conditioning setup for Stark decelerator electrodes.

### 5.1.2 Complete setup

The main body of the experiment is shown in Figure (5-3):

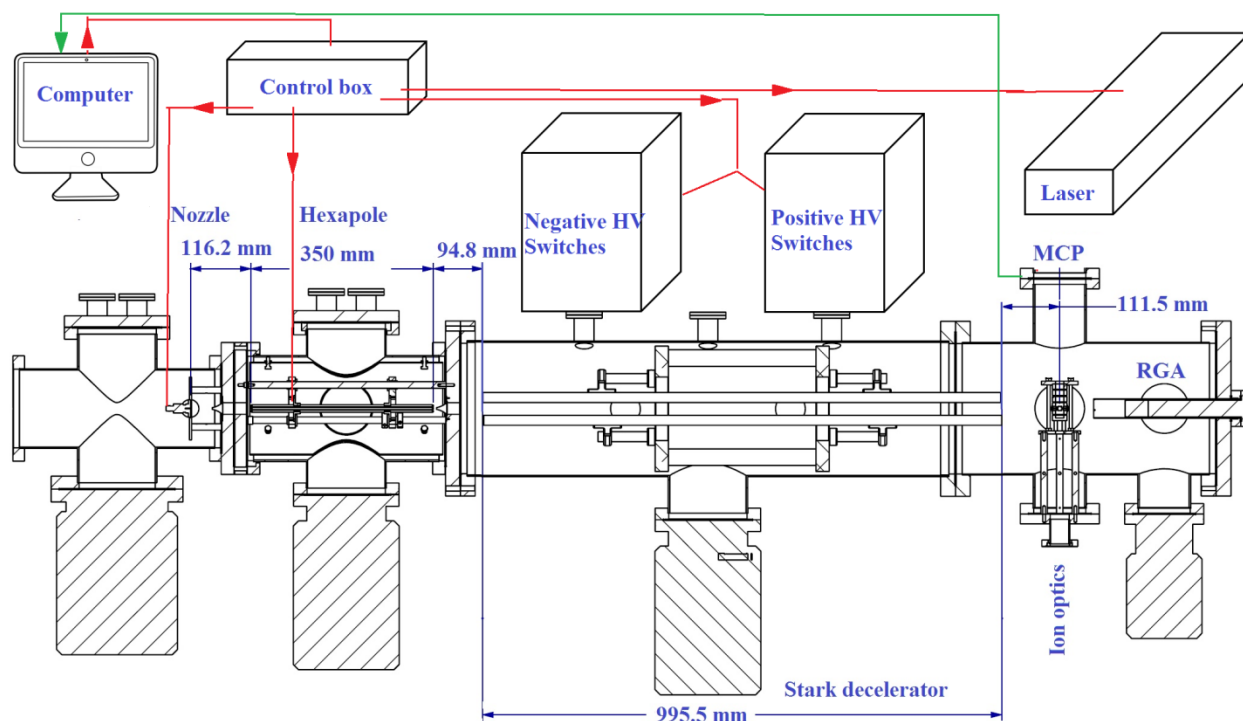


**Figure 5-3:** The original design for the complete setup of the UBC Stark decelerator that was used for deceleration of ammonia molecules. Note that in this setup the detection method was REMPI for ammonia molecules. The RGA was only used at the beginning to check the arrival of molecules, and was removed later. In the second version of the setup a new design for ion optics was installed. In the third version of the setup the hexapole was removed, and the REMPI detection was replaced with LIF for detecting *SD* radical, therefore the ion optics were replaced with an optical telescope and the MCP was replaced with a PMT.

Figure (5-3) schematically shows the original design for our Stark deceleration experiment. In this design the molecular beam that is produced by the nozzle is skimmed twice before arriving at the decelerator, once before and once after the hexapole. This improves the differential pumping of the chambers and results in a better vacuum on the detection side. Then the molecules pass through the decelerator and finally arrive at the detection point. The laser light passes through the windows on the detection side and hits the molecules. The REMPI detection components, including ion optics and a Micro-Channel Plate detector (MCP), are shown in the figure. The position of the Residual Gas Analyzer (RGA) is shown since it might be required for future experiments. We only used the RGA at beginning to ensure the presence of the molecular beam at the detection point. In the LIF experiments, as it will be explained in section (5-1-12), the ion optics were replaced with an assembly of optical lenses, the MCP was replaced with a

photomultiplier (PMT), and the hexapole was removed. In the Cavity Enhanced Laser Induced Fluorescence (CELIF) experiment the windows on the detection chamber were replaced with two cavity mirrors attached to two extended arms. Each part is briefly explained in the following sections.

### 5.1.3 Programming and control

The entire Stark deceleration experiment is run by a user-programmed computer controller. Since everything in the experiment has to be accurately timed, one has to first make a numerical simulation that generates a timing file to time and control the different parts of the experiment, from the expansion of the molecules to the signal recording. The timing is calculated by numerical methods, such as *4th* order Runge-Kutta (*RK4*), to calculate the dynamics of the molecules while flying from the nozzle to detection. *RK* methods are usually preferred over the other integrators when external forces exist [17]. In our simulations the *4th* order Runge-Kutta was chosen over the higher orders, such as the *8th* order, because it was more time efficient while producing the same result as the *8th* order.

Stark deceleration is a result of the interaction of the dipole moment of the molecules with the external electric field. One essential part of our simulation was to simulate the electric field strength distribution inside the decelerator. For this simulation the SIMION software was used and its results were exported to the timing simulation. The timing simulation was responsible for generating a file that controlled the timing of the experiment, such as timing for the nozzle, discharge, hexapole, each electrode pair of the decelerator, and the detection. LabView code designed for the experiment imported the resulting timing file and applied the timings to the instruments through a National Instrument Digital Input/Output card (NI PCIe-6537 DIO card) and a control box (interface box) which was designed by our departmental electronics shop (UBC Chemistry). The DIO card provided 20 ns edge resolution for signals that drove the nozzle, discharge, Stark electrodes, PMT, laser flash lamp and Q-Switch. The interface box converted the 3.3 V signals from the DIO card to 50 ohm standard output signals, for transmission through a coaxial cable to the laser, nozzle, discharge, and Stark controllers. The LabView code controlled all the settings required for the instruments, such as the time or frequency range over which the signal was scanned, the number of averages, the gating of the PMT, the laser timing and power, the repetition rate of the experiment, the mode of operation

(Stark on/off), the nozzle and discharge duration, the scope settings (which in our case was a AlazarTech AT9350 scope card installed on the computer), and finally recording the data into files for later analysis. After recording the data another code was used to analyze the data. The experimental result had to be compared with a numerical simulation for the experiment. That means another code was responsible to do the numerical simulations. Code was also required to give the optimized timing for the decelerator by optimization techniques. For the experiments presented in this thesis, all of the programming mentioned above required the writing of thousands of lines of codes.

#### **5.1.4 The HV switches and power supplies**

Two Spellman SL300 high voltage power supplies were connected to two  $2\mu F - 20 kV$  capacitors to provide steady high voltage required for the experiment. Four Behlke HTS-151-03-GSM HV switches were used to switch the voltages on and off on the electrodes. Two of the switches controlled the positive high voltage, and the other two controlled the negative high voltage. The ground for the electrodes was connected to a home-made adjustable floating ground circuit which maintained a minimum of  $\pm 125 V$  on the electrodes to prevent the loss of the molecules in the desired rotational state through unwanted non-adiabatic transitions. The switch activation signal from the interface box first arrives at a low voltage control circuit board and then is relayed from there to the switch. Figure (5-4) schematically shows the Stark electronics layout for two switches connected to the same polarity voltage. The other two switches had the same structure but were connected to a different voltage polarity.

In order to be able to find a more accurate switching timing sequence and also to match the simulation conditions with the experiment, the rise time and fall time of the voltages on the electrodes were measured. Figure (5-5) shows a typical switching profile of the voltages measured at the Stark electrodes, from which the rise time and fall time can be measured. By fitting an exponential function, a typical rise and fall time with a time constant of  $150 ns$  was obtained. This means that it takes about  $1 \mu s$  for the electrodes to reach the full high voltage ( $\pm 12 kV$ ) or to return to low voltage ( $\pm 125 V$ ). These values were considered in the trajectory and timing simulations.

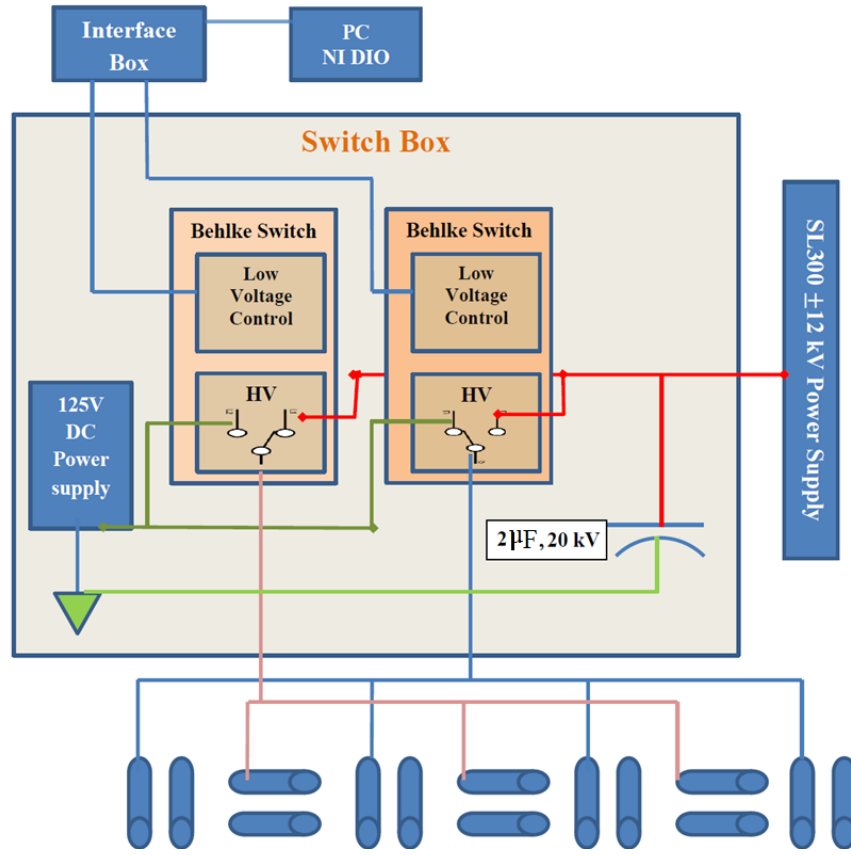


**Figure 5-4:** Schematic view of the switch box for one polarity of HV for UBC Stark decelerator. The design for the other polarity was similar.

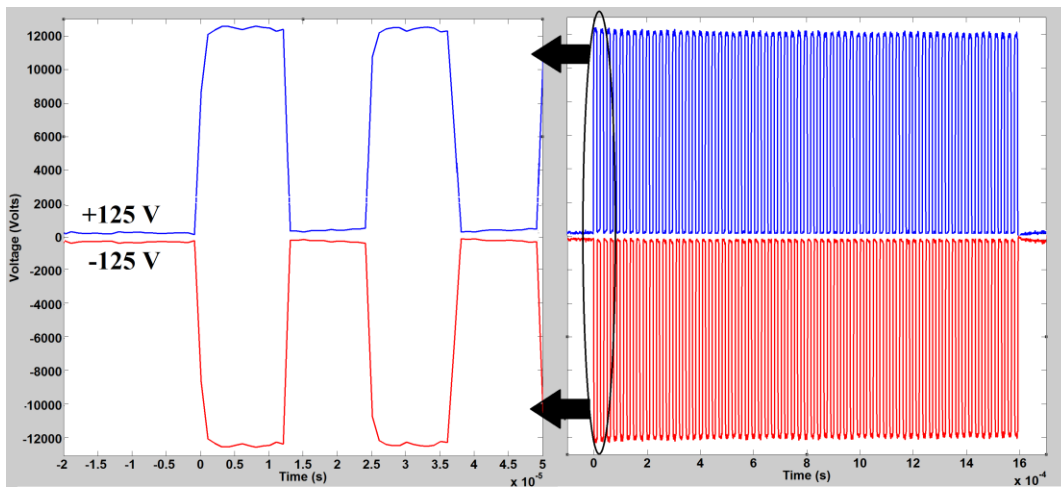


**Figure 5-5:** Right: The measured high voltage at the electrodes and the switching profile of the voltage. Left: Enlarged first two switching voltage profile. Note the **+125 V** and **-125 V** floating grounds on the positive and negative sides of the voltage profile. Also note the sharp rise and fall of the voltages, which transition fully in less than **1  $\mu$ s**.

### 5.1.5 The gas line

The typical concentration of the seed gas ( $NH_3$ (%99.999) or  $D_2S$ (98 %)) was between 1% and 10 %, that was mixed with a carrier gas. The typical pressure at the nozzle was 4 – 5 bars (backing pressure). The carrier gas in most of the experiments was krypton. Because krypton was less expensive than xenon, it was used as the carrier gas, although its expansion produces molecules with higher translational velocities than xenon. For some frequency measurement purposes it was better to use lighter carrier gases, such as argon or even helium, because they travel faster along the beam axis. As a result the transverse loss during the flight, due to the transverse motion of the molecules, was less. In addition, the rotational temperature of the sample molecules are expected to be lower for lighter carrier gases, which increases the population in the desired state of the seed gas (which is usually one of its lowest rotational states) and increases the signal-to-noise ratio. Moreover, lighter carrier gases benefit from a lower clustering rate. The higher longitudinal translational velocity of these gases makes it difficult for them to be used for Stark deceleration purposes. As a result, in most of the experiments in this field, xenon or krypton has been used as the carrier gas. Figure (5-6) shows the gas line that prepared the gas for the nozzle. In order to keep a continuous and steady flow of gas to the nozzle, a reservoir containing the mixture at a pressure higher than the pressure behind the nozzle was added to the line, and a regulator adjusted the pressure behind the nozzle. Circulating the gas inside the reservoir can result in a better gas mixture; however it was not implemented in our setup.

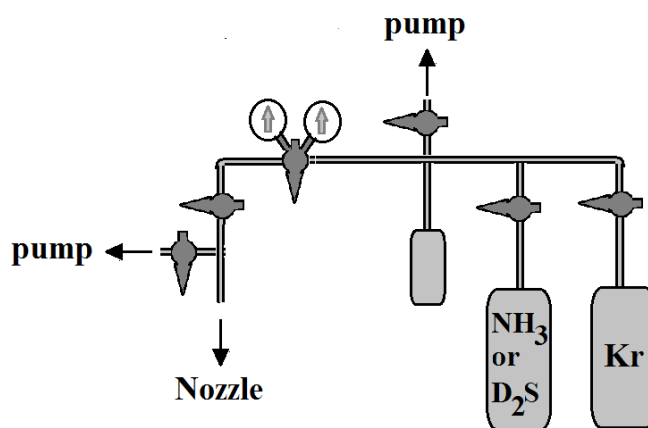


**Figure 5-6:** The gas mixing line. Behind the regulator, the mixture of the seed gas in a carrier gas at a pressure of about **10 bar** was prepared. The regulator was used to adjust the backing pressure at the nozzle. The typical backing pressure in use was **~5 bar**.

### 5.1.6 The alignment

After all the elements of the setup were ready, the next step was to align the decelerator with the nozzle, hexapole, and the detection. In our design the positions of the nozzle and hexapole were fixed, but carefully placed at the centre of the chambers. In order to align the decelerator to the nozzle, a combination of alignment by eye through a telescope and laser alignment was utilized. For the laser alignment two set points were required. A jig was inserted at the nozzle position that had a  $0.5\text{ mm}$  hole in the middle that resembled the centre of the actual nozzle. This was the first set point. The second set point was chosen to be at the centre of the detection chamber at the position designed for the RGA. The laser had to pass through the nozzle jig and hit the centre of the detection chamber. By adjusting the screws attached to the decelerator's holders the position of the decelerator was adjusted in a way that the laser light could pass through the decelerator until the maximum flux was observed. To verify the alignment, it was also checked by a telescope located at the centre of the detection chamber. In order to do that, the laser was removed and instead a light was turned on inside the source chamber. Then, by using the telescope it was confirmed that the decelerator was fully centred. The detection laser alignment for REMPI or LIF measurements were completed outside the chambers using optical elements.

### 5.1.7 The vacuum

The vacuum pumps of our setup were Varian Turbo-V 1001 Navigator ( $1050\text{ L/s}$ ) for the source chamber, plus three Varian Turbo-V551 Navigator ( $550\text{ L/s}$ ) for the hexapole, decelerator, and detection chambers. All of the turbo pumps were connected to an Extra-Dry Pfeiffer D35614 Asslar vacuum pump. The typical pressures for the source, hexapole, decelerator, and detection chambers while the nozzle was operating were  $5 \times 10^{-6}\text{ Torr}$ ,  $5 \times 10^{-7}\text{ Torr}$ ,  $8 \times 10^{-8}\text{ Torr}$ , and  $2 \times 10^{-8}\text{ Torr}$ . When the nozzle was not operating the pressures were  $1 \times 10^{-8}\text{ Torr}$ ,  $5 \times 10^{-8}\text{ Torr}$ ,  $5 \times 10^{-8}\text{ Torr}$ , and  $1 \times 10^{-9}\text{ Torr}$ , respectively.

### 5.1.8 The nozzle and discharge

The nozzle is responsible for producing the molecular beam through the supersonic expansion of the gas. In this thesis the terms “nozzle” and “valve” are used interchangeably. A nozzle that can provide a short and intense pulse of molecular beam is required for Stark deceleration experiments. A nozzle with a cold, sharp and intense molecular beam is preferred, because it

provides more molecules of interest within the phase-space acceptance of the decelerator. The higher number of molecules in the phase-space acceptance means more decelerated molecules, and a better signal to noise ratio at the detection point. In our experiment a Parker General Valve series 99 was tried first, however it needed hundreds of microseconds of opening time to produce an intense beam. Therefore it was replaced with a valve developed at CRUCS (Canadian Centre for Research on Ultra-Cold Systems). In contrast to the Even Lavie design [119], our valve has a different sealing technique, a different spring for the plunger and different plunger mass. Our nozzle can produce pulses as short as  $35 \mu s$ , can handle a backing pressure of up to  $10 \text{ bar}$ , and can be cooled down to  $80 \text{ K}$  without leaking. The typical nozzle opening times used in our experiments were between  $50$  and  $60 \mu s$ .

For the discharge experiments a thin circular stainless steel plate ( $\sim 0.5 \text{ mm}$  thickness) with a hole in the middle was placed after the nozzle. A plastic spacer separated the discharge plate from the body of the nozzle ( $3 \text{ mm}$  thickness). The discharge plate was connected to a home-made discharge switch that could switch positive voltages, and was controlled by the computer through the interface box. The discharge occurs between the discharge plate and the body of the nozzle (grounded). It was important to polish the surface of the discharge plate and the front side of the nozzle to prevent unwanted arcs between them. The plate and the plastic spacers were attached to the body of the nozzle by using plastic screws.

It is important to distinguish between a glow discharge and arcing. In the molecular discharge experiments a glow discharge is needed. Glow discharge refers to a discharge through a gas medium in which the voltage difference between two electrodes (plates in our case) causes ionization of the molecules in the gas, usually accompanied by a glowing light. Arcing refers to the direct discharge between the two plates due to the voltage difference. Since the purpose of the molecular discharge experiments is usually to use the molecular fragments after the discharge, a glow discharge is required. The glow discharge occurs at lower voltages than arcing. Finding the proper voltage and switching scheme is part of the calibration procedure of the discharge experiments, which depends on the gas type, gas density, and the spacing of the electrodes. In our experiment  $SD$  molecules were produced from the discharge of  $D_2S$  molecules. The typical voltage used for the discharge in the experiments was  $\sim + 620 \text{ V}$ . The nozzle, discharge plate, and the discharge switch are schematically shown in figure (5-7) and

figure (5-8) respectively. The discharge behaviour was experimentally measured by probing the voltage drop of the plate versus time. Figure (5-9) shows the experimental measured voltage behaviour of the discharge plate for a  $40 \mu\text{s}$  long discharge pulse of  $+620 \text{ V}$  and for a nozzle opening time of  $55 \mu\text{s}$  with a  $4 \text{ bars}$  backing pressure.

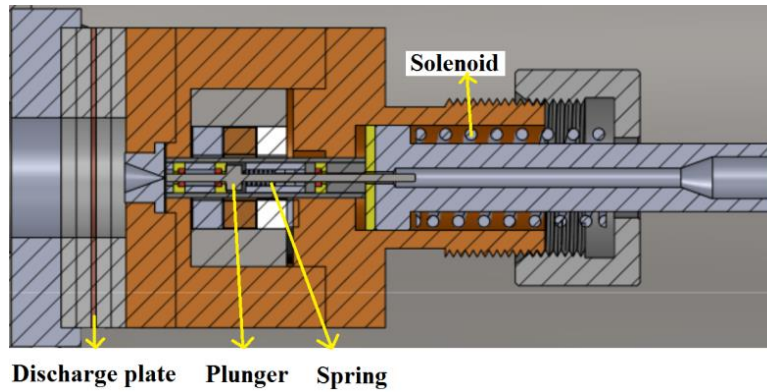


**Figure 5-7:** The design for the CRUCS valve. The discharge plate was added for the discharge of  $D_2S$  experiments and was not present for the ammonia experiments. The discharge plate was isolated from the body of the nozzle by a plastic spacer.

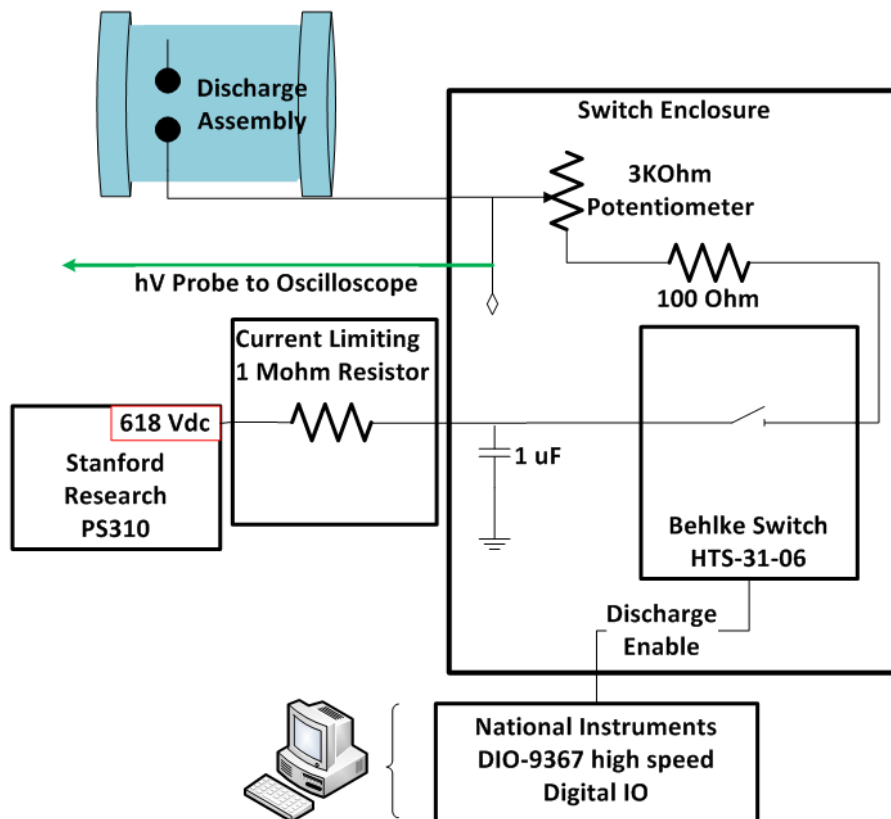


**Figure 5-8:** The home-made HV discharge switch box design along with a schematic of the control unit.

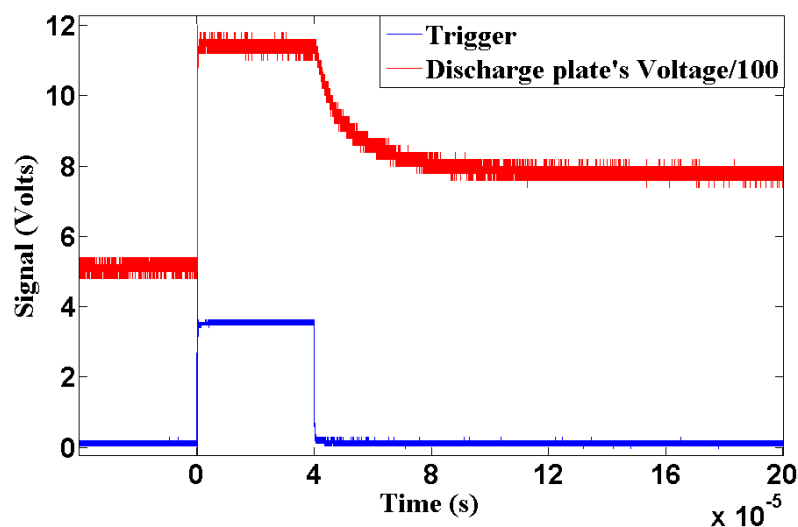


**Figure 5-9:** Blue: The trigger pulse from the Stark control unit to the discharge switch box. Red: The monitored glow discharge voltage while discharging through the gas after supersonic expansion. Note that the voltage is scaled down by 100 times using a high voltage probe. Also note that the voltage drops when discharging until it reaches a voltage at which glow discharge is no longer possible. In the case of arcing sharp spikes replaced the smooth exponential decay.

The behaviour of the discharge depends on the voltage on the discharge plate, the nozzle opening time, the backing pressure of the nozzle, and the current limiting resistance in the discharge switch circuit. If for any reason no discharge occurs, such as when the discharge voltage is too low, the exponential decay shown in figure (5-9) will disappear and the plate stays charged. If for any reason discharge changes to arcing, such as having too much voltage on the plate, then again the exponential decay vanishes, but this time the discharge voltage sharply drops to zero due to the arcing. When a glow discharge occurs, as it is shown in figure (5-9), the exponential decay of the voltage continues until the voltage on the plate reaches a value for which a discharge is no longer possible, and the voltage on the plate levels off. The faster the discharge decays, the higher is the temperature and velocity of the molecules in the beam. Therefore, although increasing the discharge voltage might help in increasing the number of *SD* radical molecules in the beam, it would not necessarily improve the Stark deceleration experiment. Further discussion on the discharge behaviour is presented in section (6-2-3). Cooling the body of the nozzle to a temperature higher than the boiling point of the gas mixture can be useful in increasing the number of molecules in the expanded beam. It is also beneficial in preparing the molecules with lower initial velocity; therefore less deceleration is required to reach to a certain final velocity. This means a lower phase angle can be used for deceleration, and as a result there is less loss

during the deceleration with high phases. The boiling point of  $D_2S$  is  $-60^\circ C$ . Assuming that the nozzle is cooled to  $-50^\circ C$ , the central velocity of the beam is reduced by about 9%. In most of the experiments presented in this thesis, the central velocity was about  $490\text{ m/s}$ . By keeping all the other conditions the same, cooling the nozzle can bring the central velocity down to  $446\text{ m/s}$ . However for the experiments in this thesis, cooling the nozzle was not performed.

The backing pressure at the nozzle can also impact the molecular beam's density. It is known that higher backing pressure at the nozzle produces a higher density of the molecules after expansion. Practically, the mechanical design of the nozzle limits the maximum backing pressure that we can apply. If the pressure is too high the plunger of the nozzle cannot move. In addition to the mechanical limitations of the setup, the sample molecule clustering rate increases at higher pressures. In our experiments it was found that the best backing pressure for the nozzle was  $4 - 6\text{ bars}$ .

### **5.1.9 The hexapole**

Our hexapole was  $35\text{ cm}$  long and was placed in a separate chamber from the nozzle. A skimmer skimmed the molecular beam before it arrived at the hexapole, hence the chambers were differentially pumped. A home-made high voltage power supply that could provide HV up to  $\pm 10\text{ kV}$  was connected to the hexapole. The typical voltage applied to the hexapole was about  $\pm 3\text{ kV}$  to  $\pm 7\text{ kV}$ . However because the hexapole effect is velocity dependent, the best voltage setting was first determined by a numerical trajectory simulation for each experiment, and then the best condition was then found experimentally by changing the hexapole voltage around the value given by the simulation until the maximum signal was obtained.

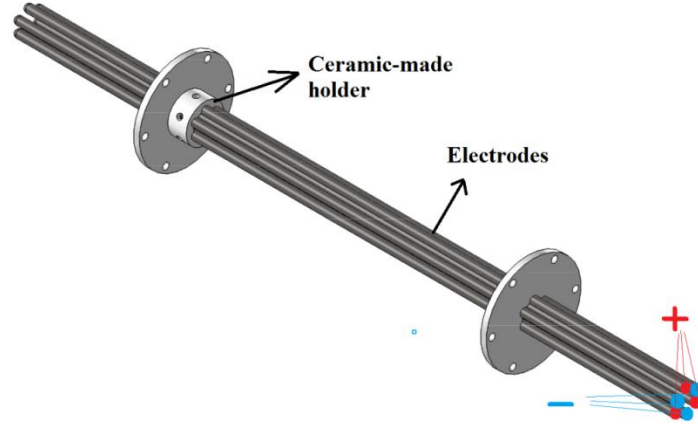


**Figure 5-10:** The 35 cm long hexapole used in ammonia deceleration experiments. The hexapole electrodes were secured by two ceramic holders. The ceramic holder isolated the electrodes from each other. The diameter of each electrode was **2 mm**, and the centre to centre spacing between the electrodes was **~5.6 mm**. The inner radius of the hexapole was **0.8 mm**.

### 5.1.9.1 Hexapole as molecular lens

A hexapole was implemented in our setup to focus the molecules toward the entrance of the Stark decelerator. This increased the density of the molecules within the phase-space acceptance of the decelerator. Among the molecules guided to the decelerator some have higher transverse velocity than what the decelerator can transversely trap, so they will be lost; however there are other molecules which can be trapped transversely and hence increase the density. The other benefit of a hexapole is that it filters molecules in low field seeking states from high field seeking states. In addition by adding a hexapole chamber between the nozzle and decelerator chambers we were able to differentially pump the chambers and provide a better signal-to-noise ratio at the detection point. Experimentally, the signal with hexapole on was enhanced by  $\sim 75$  times larger than to when the hexapole was off.

A hexapole can also be used for velocity filtering purposes. In this method the molecules from a source are introduced to a bent hexapole. The bent hexapole acts as a filter due to the fact that only those molecules which have less longitudinal and transverse translational energy than the potential depth at the bend can be guided through the hexapole. In our experiments the application of the hexapole was only to focus and guide the molecules and not to velocity filter them. Therefore it had no bend. The electric hexapole exploits the Stark effect of the molecule and is well-described in the literature [120]. The force that the molecule experiences is given by:

$$\vec{F} = -\vec{\nabla}W_{Stark}(E(r, \theta)) \quad (5.1)$$

The electric field distribution inside a hexapole to a very good approximation is given by:

$$E(r, \theta) = \frac{V_0}{r} \left(\frac{r}{r_0}\right)^2 \left[ 2.9498398 - 0.1122901 \left(\frac{r}{r_0}\right)^6 \cos(6\theta) - 0.0376238 \left(\frac{r}{r_0}\right)^{12} \cos(12\theta) \right] \quad (5.2)$$

where  $r_0$  is the internal radius of the hexapole, and  $V_0$  is the voltage on the electrodes. To include the effect of the finite size of the electrode rods a numerical simulation using SIMION software was carried out. The result of the simulation for voltage of  $\pm 5 \text{ kV}$  and with the actual dimensions of our hexapole is shown in figure (5-11).

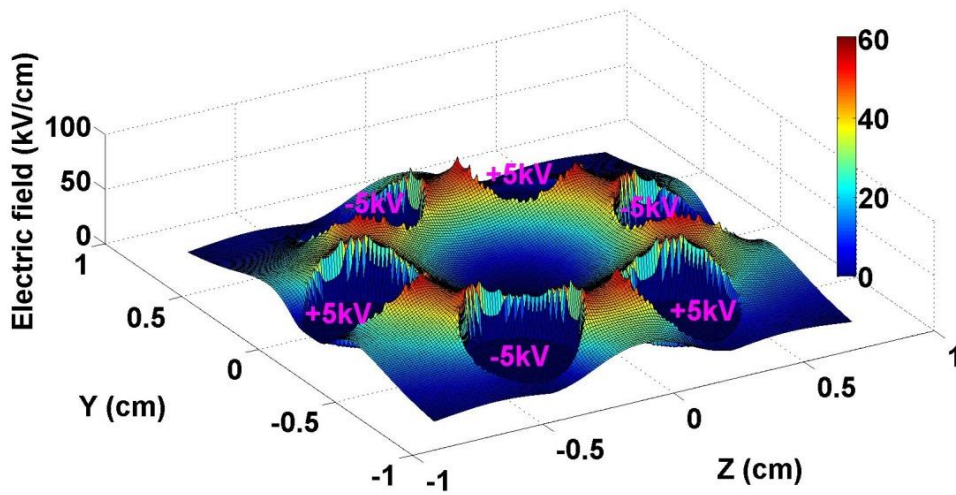


**Figure 5-11:** The electric field magnitude of the hexapole with  $\pm 5 \text{ kV}$  being applied to its electrodes. The six surrounding cylindrical wells in the figure correspond to the position of the electrodes. Note the low magnitude field amplitude at the centre which guides molecules in LFS states toward the centre of hexapole.

With the  $\pm 5 \text{ kV}$  being applied to our hexapole, in the case of ammonia molecule, a maximum transverse velocity of about  $25 \text{ m/s}$  was guidable. The typical transverse velocities of the supersonically expanded beams in our experiment are on the order of less than 10 % of the longitudinal velocity of the beam. For a beam with longitudinal velocity of  $400 \text{ m/s}$ , a maximum transverse velocity of  $40 \text{ m/s}$  and transverse position of  $3.5 \text{ cm}$  from the beam axis is expected at the decelerator's entrance. This position is far beyond the acceptance of the decelerator ( $\sim 0.9 \text{ mm}$  from the beam axis). However, since the hexapole can focus the molecules toward the entrance of the decelerator, by turning the hexapole on at  $\pm 5 \text{ kV}$ , ammonia molecules with transverse velocity of less than  $25 \text{ m/s}$  could be introduced to the decelerator. The focal point of hexapole for each molecule depends on its position in phase-space. Figure (5-

12) shows the effect of a 35 cm long hexapole on LFS state ammonia molecules in  $|1,1\rangle$ . The hexapole is located between 12.5 cm – 47.5 cm, and one can clearly see the focusing at about 50 cm. Both focal point and transverse velocity acceptance can vary by changing the voltage applied to the hexapole. Based on simulations for a molecular beam with mean velocity of  $\sim 400$  m/s, the best phase-space matching for our decelerator was occurred when  $V = \pm 4.5 - \pm 5.5$  kV was applied to the hexapole. Although a hexapole can be useful in confining the molecules in transverse direction, depending on its design, it is not necessarily beneficial to use. This will be discussed more in the next section.

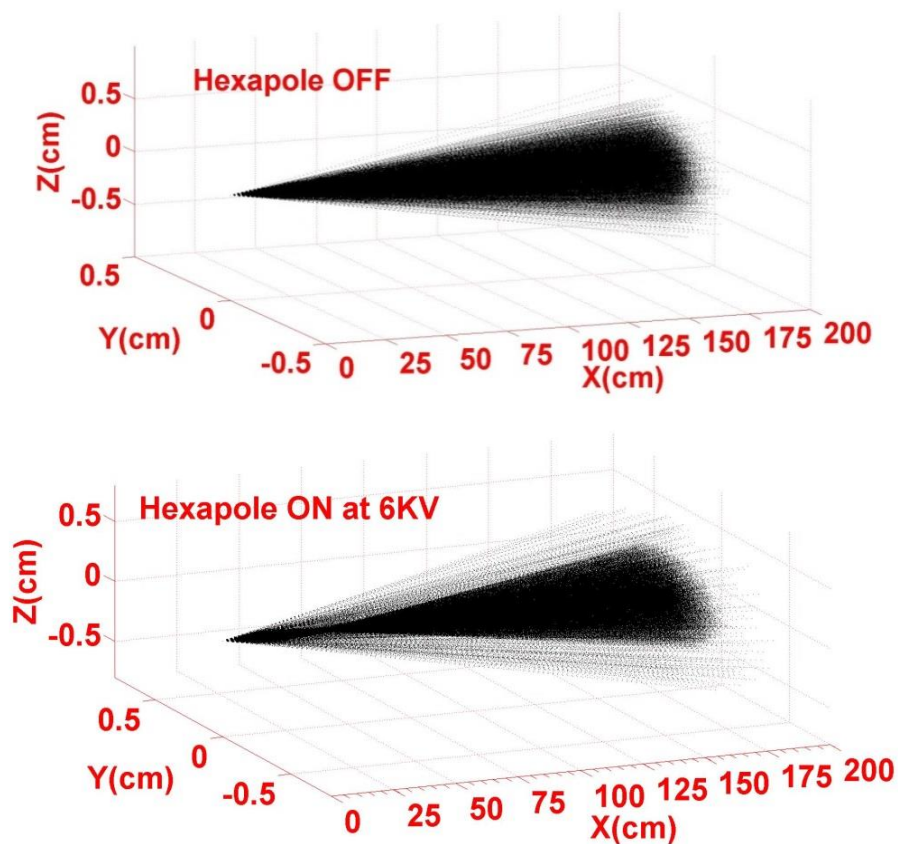


**Figure 5-12:** Top: The free flight path of ammonia molecules after expansion from the nozzle. Bottom: The focusing effect of our 35 cm long hexapole at  $\pm 6$  kV on ammonia molecules. Note that the position and extension of the waist of the beam can be adjusted by the voltage being applied to the hexapole. The voltage with the highest number of molecules at the phase-space acceptance of the decelerator is preferred.

### 5.1.9.2 The effect of removing the hexapole

Although the hexapole transversely focuses the molecules toward the entrance of the decelerator and increases the number of molecules within the phase-space acceptance of the decelerator, it

was determined from the simulations that the signal intensity might be even better without our long hexapole (35 cm). The reason is that as the molecules fly through the hexapole, they get more and more separated in the longitudinal (beam axis) direction due to their different longitudinal velocities. By the time that molecules arrive at the decelerator they are not longitudinally close to the synchronous molecule and will not be accepted in the longitudinal phase-space acceptance of the decelerator. As a result there is a trade-off between the signal enhancement obtained by focusing in the transverse direction by using a long hexapole and the decrease in signal due to the larger separation of the molecules in the longitudinal direction.

Removing our long hexapole (35 cm) can improve the signal by reducing the longitudinal flight path that reduces the longitudinal spatial divergence of the molecules. The decision to remove the hexapole from the setup was made after the setup was already set for the *SD* measurements; therefore deceleration without the hexapole was only performed on *SD* and not for ammonia. Although no experiment was done with ammonia to experimentally show the improvement of the signal, the success of previous simulations in predicting the behaviour of the molecule indicated that the simulation results were reliable. The comparison between the results for the setup with and without a hexapole ( $\pm 4.5$  kV) is shown in figure (5-13). As the figure shows, removing the hexapole had two major effects on the signal; first, the peak intensity of the desired packet increased by a factor of two, and second, the side bands of the main packet merged. The side bands are the molecular packets that are up to a few stages ahead or behind the synchronous molecule. The side bands are less stable compared to the main packet due to the fact that the timings are set for the velocity and the position of the synchronous molecule. Therefore the sidebands have different final velocities compared to the main packet. By removing the hexapole, the molecules have less rotation in their phase-space distribution when arriving at the decelerator. This means that more molecules are around the synchronous molecule, and hence more are within the phase-space acceptance of the main packet.

In section (6-2-5) the experimental and simulation results for deceleration of *SD* radicals are presented. The phase-space distributions of the decelerated packets are also shown, in which merging the sidebands, improved phase-space distribution, and matching with the experimental results can be seen.

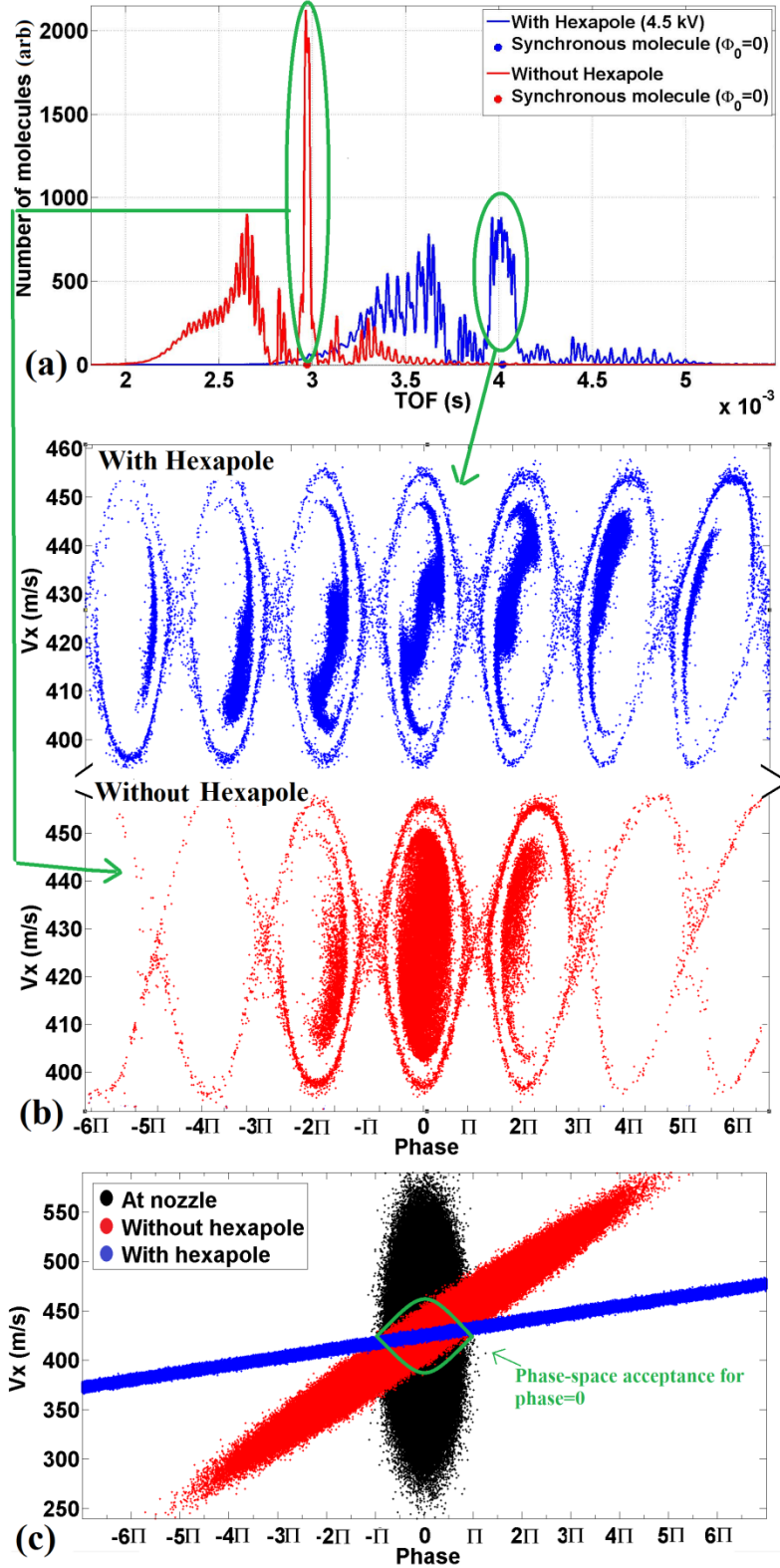


**Figure 5-13:** The effect of removing the long hexapole on the (a) signal and (b) the phase-space acceptance of the decelerator. (c) The phase-space distribution of ammonia molecules at the entrance of the decelerator with (blue) and without hexapole (red).

### 5.1.10 The lasers

The range of required laser wavelengths for our experiments was between 310 *nm* to 330 *nm*. This range was produced by using a frequency doubled pulsed dye laser (Sirah PricissionScan (DCM), or Radiant NarrowScan (DCM)) that was pumped by a nano-second pulsed Nd-Yag laser (Spectra Physics, Quanta Ray Pro-230-10) operating at its second harmonic (532 *nm*). With this setup the Sirah dye laser could produce up to about 20 *mJ/pulse*. Since such a high power output would saturate the MCP or PMT, the laser was operated well below this maximum output ( $\sim$  few milli-Joules for REMPI and hundreds of micro-Joules for LIF). However since another experiment in our lab required 20 *mJ/pulse* energy range, the Sirah dye laser which was initially in use for the Stark experiments was replaced with a Radiant dye laser available with a maximum power of 7 *mJ/pulse* for the same dye and frequency range. In my experiments all the REMPI measurements were done with the Sirah dye laser, while all the LIF and CELIF measurements were done with a Radiant dye laser. The maximum repetition rate of the laser pulses depends on the maximum repetition rate of the Nd-Yag laser. In our experiments the maximum possible repetition rate was 10 *Hz*. However this rate was never used for the deceleration measurements in order to prevent damage to the electronics of the Stark switches from overheating of the resistors used in its circuit. The maximum repetition rate used in our experiments was 3.3 *Hz*.

### 5.1.11 The optics outside the chamber

Three different optical setups were used for the three different experiments in this thesis. REMPI detection was used for the first characterization experiments of the Stark decelerator with ammonia molecules. The optics used for this experiment were simply prisms for alignment, apertures, and a fused silica convex lens with 400 *mm* focal point. The lens focused the laser beam at the centre of the ion optics to ionize molecules in the molecular beam. The lens was attached to an X-Y-Z stage for fine adjustments of its position.

The second optical setup was used for the LIF experiment. In this experiment, prisms were responsible for the laser alignment, and apertures were used to reduce the diameter of the laser beam (which typically had a diameter of about 5 *mm*). Although having a larger laser beam diameter ensures that most of the molecules at the detection point will be hit by the laser, reducing the diameter of the laser beam can help in reducing the scattered light that arrives at the

PMT. Since the spacing between the electrodes in our Stark decelerator is less than 2 mm, a laser beam with about the same diameter was enough for the LIF experiments. The laser beam hit the molecules at the centre of the detection chamber and the collimating lens of the PMT telescope collected the fluorescence light of the molecules.

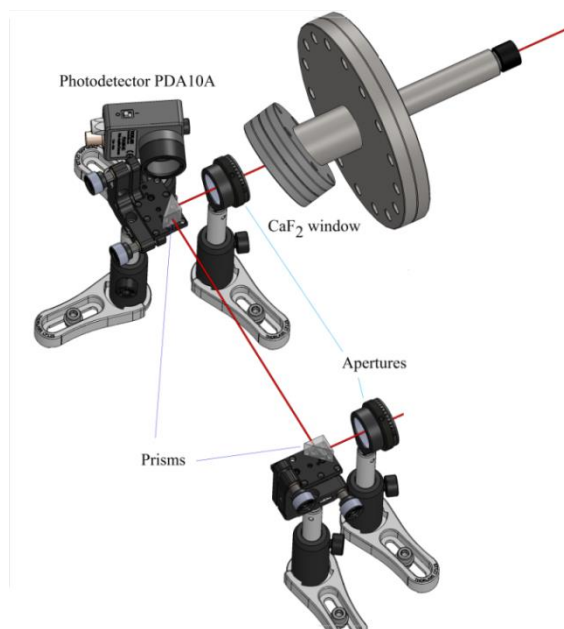


**Figure 5-14:** The optics arrangement for the LIF detection of the *SD* radical. The photo-diode detected the transmitted light through the back side of the prism and its signal was used to trigger the PMT signal recording.

The third set of optics that was used for the CELIF experiments was more complicated than the other two (figures (5-15) and (5-16)). The reason for that was the necessity to match the mode of the cavity with the mode of the incident laser. The laser beam after the dye laser has a bandwidth and includes a range of different longitudinal and transverse laser modes. If the mode of the laser is not purified, then different modes of the cavity will be present inside the cavity with a random behaviour. In the cavity ring-down experiments this is equivalent to non-exponential decay for the cavity ring-down signal due to mode beating and hence unstable cavity ring-down measurements. We used a spatial filter to spatially match the laser beam to the  $TEM_{00}$  mode of the cavity. For this purpose the method suggested by Greaves et al. [121] was used, in which a telescope and pinhole arrangement were used as the spatial filter to form a Gaussian laser beam. In order to couple the laser beam into the transverse mode of the cavity, the focus of the incident

light to the cavity had to match the waist of the electric field with the correct spot size, which was achieved by using a coupling lens.

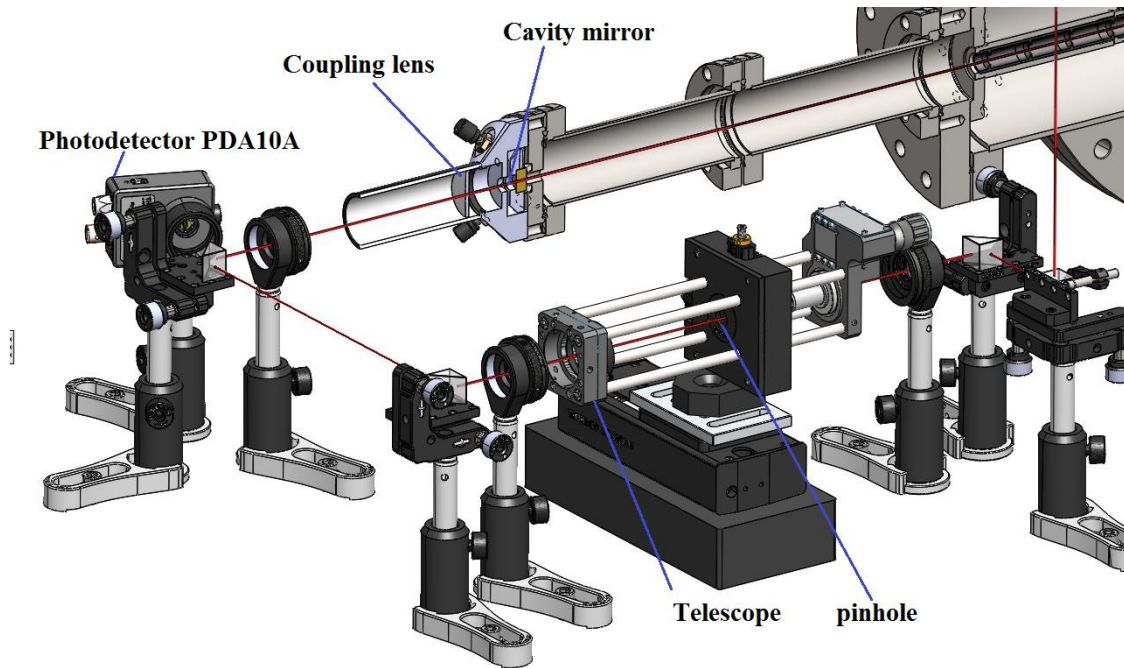


**Figure 5-15:** The optics arrangements for delivering the laser to the detection chamber for the CELIF experiments.

When calculating the proper position for the coupling lens the diverging effect of the plano-concave cavity mirror on the focal point of the coupling lens should also be considered. Figure (5-16) illustrates the optical path of the beam outside and inside the cavity.

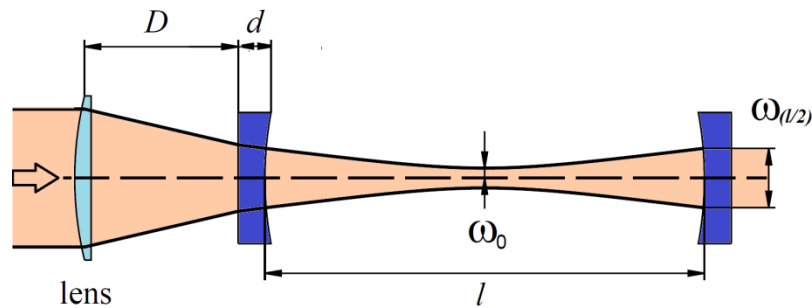


**Figure 5-16:** The laser beam outside and inside the cavity. Note that the dimensions are exaggerated.

In figure (5-16)  $\omega_0$  is the beam waist at the centre of the cavity, and is given by:

$$\omega_0 = \sqrt{\frac{\lambda z_0}{n_0 \pi}} \quad (5.3)$$

Where  $z_0$  is the characteristic length of the cavity,  $n_0$  is the refractive index of vacuum, and  $\lambda$  is the wavelength of the incident light.  $z_0$  depends on the geometry of the cavity:

$$z_0 = \frac{l(2R - l)}{4} \quad (5.4)$$

where  $l$  is the length of the cavity and  $R$  is the radius of the mirror surface.  $\omega(l/2)$  is the beam spot size at the mirror surface:

$$\omega(l/2) = \omega_0 \sqrt{\frac{2z_0 + l}{2z_0}} \quad (5.5)$$

One can show that the ray matrix for this configuration at the lens position is given by [121]:

$$\begin{pmatrix} r \\ r' \end{pmatrix} = \begin{pmatrix} \frac{\omega(l/2)(Rn_2 + dn_2 + Dn_1)}{Rn_2} \\ \frac{\omega(l/2)(-Rn_2 - dn_2 - Dn_1 + fn_1)}{Rn_2f} \end{pmatrix} \quad (5.6)$$

Where  $r$  is the distance of the ray from the propagation axis and  $r'$  is the slope of the ray at the lens position when it arrives at the lens.  $f$  is the focal length of the lens,  $n_1$  is the refractive index of the mirror substrate,  $n_2$  is the refractive index of the air,  $d$  is the thickness of the mirror, and  $D$  is the distance between the coupling lens and the mirror. In our case  $r' = 0$  because the incident beams to the lens are parallel. Since all the element in the matrix above are known, it is easy to solve the above equations to find  $D$ . In our experiment  $f = 71.4 \text{ cm}$ ,  $l = 90 \text{ cm}$ ,  $R = 100 \text{ cm}$ ,  $d = 0.635 \text{ cm}$ ,  $\lambda = 323.17 \text{ nm}$ ,  $n_1 = 1.482978$ , and  $n_2 = 1.000277$ , which results in  $z_0 = 24.75 \text{ cm}$ ,  $\omega_0 = 0.159 \text{ mm}$ ,  $\omega(l/2) = 0.268 \text{ mm}$ ,  $D = 3.52 \text{ cm}$ , and  $r = 0.283 \text{ mm}$  at the coupling lens position, which was equivalent to an incident beam diameter of  $4.2 \text{ mm}$ . The cavity ring down signal was an extra measurement for the CELIF measurements compared to the LIF alone experiments. In our CELIF experiments the ring-down signal was collected by using a Thorlabs PDA36A photodiode which had an internal adjustable amplifier. The tiny fraction of light that passed through the end cavity was guided and focused to the photodiode by using two convex lenses in a telescope form. The detection scheme of the CRD signal is shown in figure (5-17).

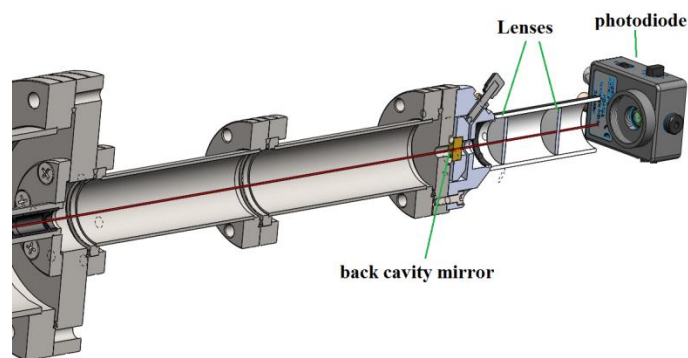


**Figure 5-17:** The CRD signal recording arrangement. The photo-diode with internal amplifier was used to collect the weak transmitted light after the back mirror of the cavity.

### 5.1.12 The PMT and its optics

A PMT plus telescope optics was used to collect the fluorescence light of the *SD* radical at the detection point. The telescope consisted of a collimating lens (Thorlabs LA4464-UV, Fused Silica, Plano-Convex,  $D = 50.8\text{ mm}$ ,  $F = 60\text{ mm}$ ), a focusing lens (Thorlabs LA4545-UV, Plano-Convex,  $D = 50.8\text{ mm}$ ,  $F = 100\text{ mm}$ ), and an optional imaging lens and optical filter that were not used. The PMT that was used for the *SD* radical experiments was a Hamamatsu H11526-010NF which had a gate function ( $70\text{ ns}$  rise time and  $8\text{ ns}$  fall time). The collimating lens collected the fluorescence photons, and was positioned at its focal point distance from the detection point to properly collimate the light towards the focusing lens. The focusing lens then focused the light to the PMT detection area. In order to get a good signal in the LIF measurement experiments it is necessary to separate the laser light (direct or reflected) from the fluorescence light, to prevent the PMT from including laser light in the fluorescence signal. One way to remove the stray light is to block the transmittance of the light with the same wavelength as the incident laser to the PMT by using band-pass or low/high pass optical filters. The filter can be a single filter or a combination of different filters that limits the wavelength range of the light arriving to the PMT. This is a good method if the molecule of interest fluoresces at wavelengths other than the one that excited the molecule. If the detection wavelength includes the excitation wavelength, using a filter means removing most of the signal. In the case of *SD* radical using an optical filter could not help, since about 95 % of the fluorescence light has the same wavelength as the incident light due to a favorable Franck-Condon factor for  $(\nu = 0) \rightarrow (\nu = 0)$  electronic transitions. In such cases using a gated PMT can be very useful, as it was in our experiment. By using a gated PMT it is possible to open the PMT gate after the laser light hits the sample. One

can remove most of the stray light from the signal by choosing the right time to open the gate. In addition, gating the PMT helps in reducing the nonlinear after-pulsing effects due to the huge number of photons of the stray light. This nonlinear behaviour happens due to the large current gain of the PMT ( $\sim 10^7$ ). This behaviour can be compared to the human eye being exposed to a very intense pulse of visible light (such as the flash of a camera), which makes the person to go blind for a short while. Gating with a proper timing prevents the PMT from capturing the intense incident laser light. This method is especially useful if the fluorescence life time of the sample is much longer than the time duration for which the laser pulse is in the PMT field of view. In the case of *SD* radical the fluorescence life time was about 250 ns which was much longer than the few nanosecond that it takes for the laser pulse to pass the field of view of the telescope. Although most of the stray light was removed by gating the PMT, the remaining stray light from the scattered light from the reflective surfaces in the chamber plus the fluorescence light from the windows could still ruin the signal. In order to minimize these effects, it was needed to use a window which does not fluoresce in the range of the wavelengths used in the experiment. In our experiment a *CaF<sub>2</sub>* window was used which had almost no fluorescence for the range of the wavelengths in use ( $\sim 320$  nm). Using optical baffles reduced the scattered light arriving to the field of view of the telescope. In our experiment, in addition to using the baffles, the field of view of the telescope was reduced by adding a 3 cm long optical lens tube after the collimating lens of the telescope. The reason for that was the presence of the Stark electrodes with shiny surfaces close to the detection point. A better signal to noise ratio was obtained by reducing the field of view of the telescope to the area around the point where molecules hit the laser light. Figure (5-18) shows the PMT and telescope configuration for the LIF and CELIF experiments.

### **5.1.13 The test chamber**

A test chamber was initially used for the LIF and CELIF measurements to characterize the detection and discharge behaviour. It resembled the actual deceleration setup design, only with having the hexapole and Stark decelerator removed, and leaving two chambers for the source and detection. The nozzle and discharge plate had the same assembly as section (5-1-8), and the LIF and CELIF detection assemblies were the same as section (5-1-11). This aided an easier characterization of the molecular beam and detection by providing stronger signal due to the short distance ( $\sim 30$  cm) between the nozzle and the detection (figure (5-19)).

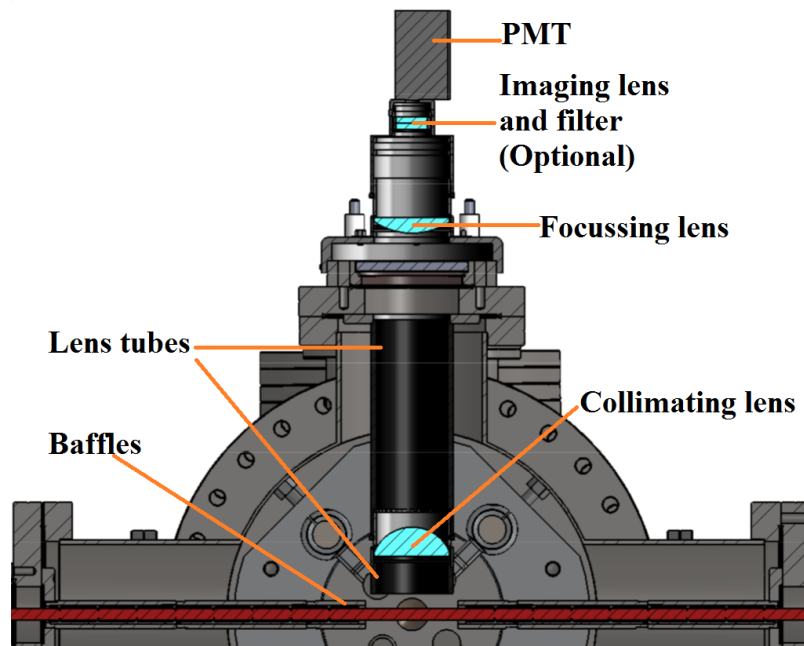


**Figure 5-18:** The PMT and the optics used for collecting the fluorescence light.

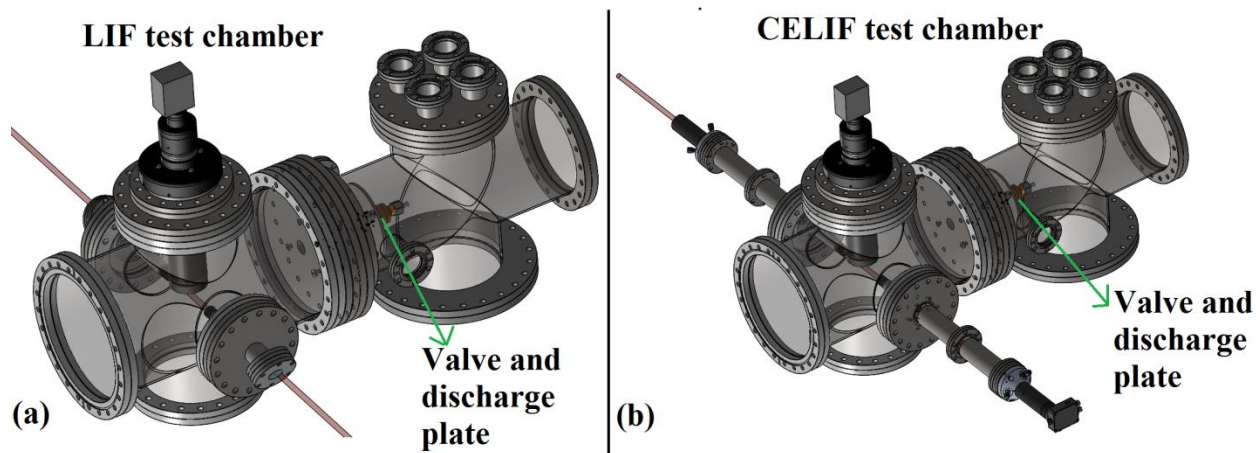


**Figure 5-19:** The test chamber setup. (a) For LIF experiments in the test chamber. (b) For the CELIF experiments in the test chamber. Note that the two windows in the LIF test chamber setup are replaced with two long tubes on which the cavity mirrors are attached.

#### 5.1.14 The ion optics for the REMPI experiments

In order to probe the molecules at the detection point, ionization with time-of-flight mass spectrometry was used for the sensitive detection of the molecules. The ion optics at the detection point guided the ionized molecules produced by the REMPI to the MCP. The efficiency of guiding ions to the detector with this method is reported to be near unity [122]. Two

different ion optics designs were used in our experiments, one with three electrodes, and one with six electrodes. The original design of our ion optics was the six electrode version, in which 1200 V was applied to the electrode at its base. All the electrodes were connected to each other in series via 2 M $\Omega$  resistors in between. Therefore the voltage dropped to zero at the top electrode. This configuration repelled and focused the positive ions at the MCP. The role of the field-free region between the top electrode of the ion optics and MCP was to separate the ions with different charge-to-mass ratios while traveling toward the MCP. The mass resolution of the MCP detected signal depends on the length of the free path. In our case this free path length was 18.44 cm which resulted in 2.7  $\mu$ s arrival time for the NH<sub>3</sub><sup>+</sup> ions after their ionization. The mass-resolution of the signal from MCP was not very critical in our case due to having a clean setup with negligible background ions.

After several experiments and simulations it was realized that the long distance (11.5 cm) between the ion optics and the detection point in the original design reduces the signal to noise ratio at the detection point. This problem mainly happened due to the spatial expansion of the molecules along the beam axis due to their different velocities. The over-focusing of molecules after the last deceleration stage could be another reason for losing molecules. This means that some of the molecules were lost due to their transverse position by the time they arrived at the detection point. Therefore a second version of the ion optics was designed that was attached to the decelerator via an isolator. This version had only three ring electrodes, in which the bottom electrode was connected to +1300 V, the middle plate to +650 V, and the top electrode to the ground. The distance between the decelerator to the centre of the new ion optics was 4 cm. The free path distance for ions in this design was 20.8 cm, and the corresponding ion arrival time to the MCP was 2.8  $\mu$ s. An isolating spacer prevented discharge between the decelerator and the ion optics. The simulations showed that the guiding efficiency were the same for both of the ion optics designs. Figure (5-20) shows the structure of both versions.

It is unfortunate that determining the absolute densities of the detected samples with a REMPI measurement is not possible, because when multiple photon transitions are used to ionize the molecules, the ionization efficiency highly depends on the laser beam profile (beam waist and transverse profile of the beam). Unfortunately pulsed dye lasers have unstable beam profile which makes the measurement inaccurate.

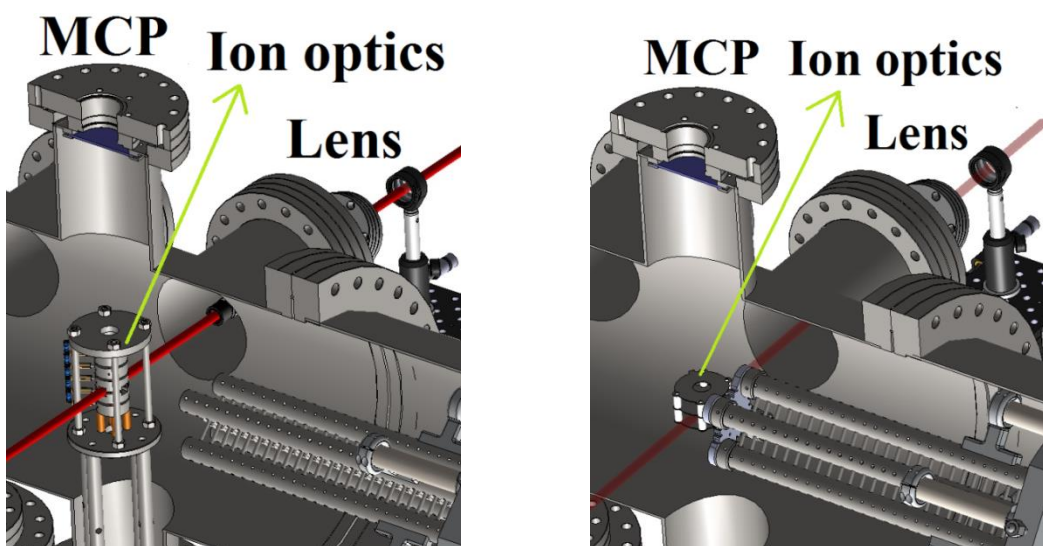


**Figure 5-20:** The two versions of ion optics used for ammonia experiments. Left: the original design. Right: The second version with shorter distance to the decelerator.

### 5.1.15 The signal delivery and amplifiers

In the REMPI experiments an MCP (Del Mar Venture's MCP-GPS46) was used. The typical voltages applied to the cathode and anode of the MCP were between  $-1500$  to  $-1850$  V and  $0$  –  $300$  V, respectively. Dark current was seen when voltages on cathode and anode were around  $-1850$  and  $+300$  V respectively. Increasing the voltage on the cathode and anode increases the gain of the MCP, however if the gain is too high for a measurement it might damage the MCP. So each experiment began with lower MCP gains, and then gradually the gain was increased until a good signal-to-noise ratio was obtained. The output of the MCP after passing through a home-made current to voltage convertor arrived at a set of two amplifiers, Mini-Circuit ZFL-500HLN+ ( $10$  –  $500$  MHz), and Mini-Circuits ZRL-400+ ( $150$  –  $400$  MHz). These two amplifiers low passed and band passed the signal respectively. The scope card installed on the computer was Alazar ATS9350 (12 bit,  $500$  MS/s,  $250$  MHz full power bandwidth). The trigger for the scope to record the signal from the MCP was provided by using a photomultiplier (Thorlabs Si Transimpedance Amplified Photodetector PDA10A) which was located on the laser beam path outside the chamber and after the detection point. The output signal from the MCP had a width of about  $3$  ns. The scope card on the computer did not have enough resolution to capture the signal properly. In order to fix this problem a  $22$  MHz low pass

filter (BLP-21.4+) was attached right before the scope. The combination of this filter together with the other amplifiers produced a signal wide enough (tens of nanosecond) and strong enough (from millivolts to a few volts depending on the gain of the MCP) to be seen by the scope. The LabView code then captured the signal and calculated the integrated signal for each single shot and recorded it for further processing.

One important problem at the beginning of our measurements was the RF noise produced by the fast switching of the electrodes. The noise showed up as very sharp peaks with the same frequency as the Stark electrode switching. The switching noise was not removable by grounding the switches circuits. The main source of the noise was the HV cables that were working as strong antennas. After several attempts we stopped trying to remove the noise by hardware and instead used a software trick. The trick was to force the decelerator to stop switching a few microseconds before the laser was triggered. Therefore with the switching off, the associated noise disappeared from detection.

In the case of LIF and CELIF measurements, the PMT signal produced from the molecular fluorescence passed through only one amplifier (Mini-Circuit ZFL-500HLN+) and then went through the 20 MHz filter. However, for the LIF measurements if the signal was strong, such as the experiments done at the test chamber with a detection point close to the nozzle, the 20 MHz filter was unnecessary, because the fluorescence signal was so strong that it looked like a continuous decay for about one microsecond. Using the filter would only smooth the signal coming from the PMT.

For the CELIF cavity ring-down measurements the ring-down signal was collected by a photodiode (Thorlabs Si Transimpedance Amplified Photodetector PDA36A ). The photodiode had an internal amplifier which made it easy to adjust its signal intensity. The signal was then captured by the scope card on the computer for further processing with the LabView program and recording.

## Chapter 6: Experimental results

### 6.1 Ammonia experiments

#### 6.1.1 REMPI for ammonia

The  $B^1E' \leftarrow X^1A'_1 2_0^5$  one color two-photon resonant, three-photon ionization transition ((2 + 1) REMPI) of ammonia molecules was used in the Stark decelerator characterization experiments. To initially find the signal the  $B^1E' \leftarrow X^1A'_1 2_0^4$  transition was used, since it was already well studied [123]. After finding the right alignments for the laser and Stark decelerator, the  $B^1E' \leftarrow X^1A'_1 2_0^5$  transition was then used. It was possible to find a two photon transition from our desired LFS state ( $|J = 1, K = 1, \textit{antisymmetric}\rangle$ ) that was separated enough from the other transitions, in a way that power broadening could not mix them. In the REMPI measurements in this thesis, the two photon wavenumber  $64050 \text{ cm}^{-1}$  was used. Figure (6-1) shows the frequency spectrum of ammonia around this wavenumber.

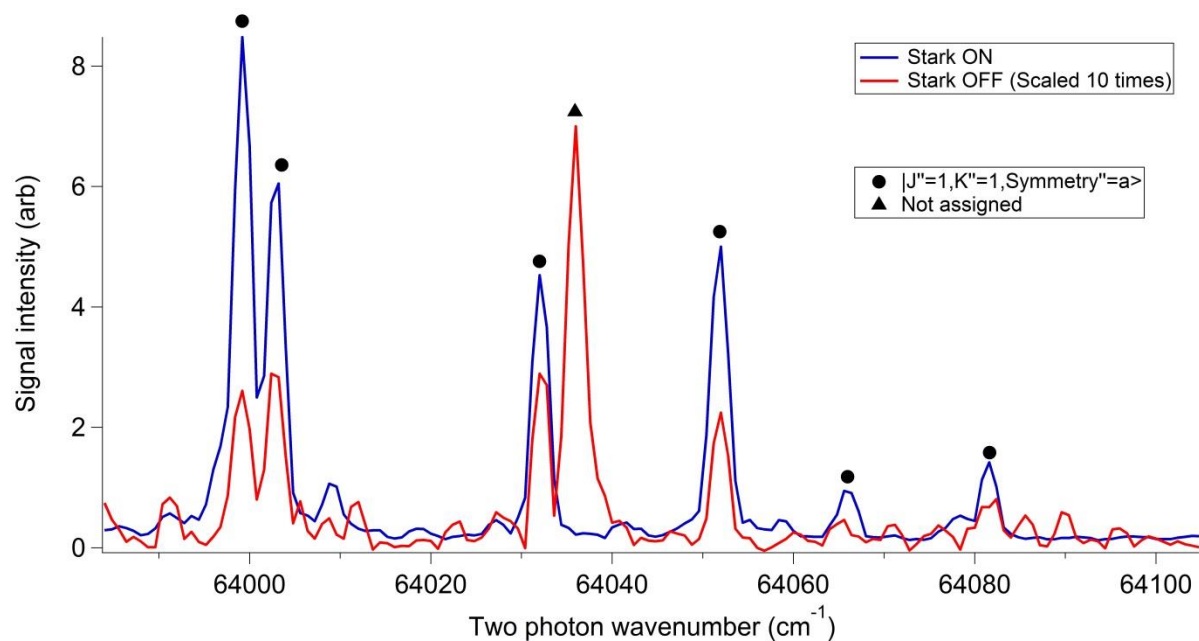


**Figure 6-1:** The frequency spectrum for (2+1) REMPI of ammonia molecules ( $B^1E' \leftarrow X^1A'_1 2_0^5$ ) after the decelerator. Red: decelerator off. Note the signal is scaled 10 times for clarity and comparison. Blue: decelerator on. Note the signal enhancement for the transitions initiating from  $|J = 1, K = 1, \textit{antisymmetric}\rangle$ . The peak labeled with a triangle is not assigned. The uncertainty of the wavenumber was  $\pm 0.1 \text{ cm}^{-1}$ , which was obtained by the dye laser's minimum possible step size.

The peaks located at  $64032 \text{ cm}^{-1}$  and  $64036 \text{ cm}^{-1}$  merit a closer look. The origin of the transition for the peak located at  $64036 \text{ cm}^{-1}$  (labeled by a triangle in a Stark off spectrum) is not known, but we know that it is originating from a HFS state since it is suppressed when the decelerator is on. This transition cannot belong to  $B^1E' \leftarrow X^1A'_1 2_0^5$ , because  $B^1E' \leftarrow X^1A'_1 2_0^5$  is only possible by symmetry for ammonia molecules in  $\tilde{X}(1)$ . Therefore the unknown transition could belong to higher vibrational or rotational states. According to figure (6-1), this transition was absent when the decelerator was on which indicates its HFS behaviour, while all the other transitions which originate from  $|J = 1, K = 1, \textit{antisymmetric}\rangle$  were present and pronounced due to being LFS. In our experiments the transitions at  $64050 \text{ cm}^{-1}$  and  $64000 \text{ cm}^{-1}$  were selected for detecting ammonia molecules in the desired state as they were well isolated and pronounced after the decelerator.

One may think that higher laser powers could produce stronger signal, but as we increased the laser power the two-photon transition saturated after a specific power. A measurement was made to characterize the signal versus laser power to find the power range in which the transition was not saturated and the signal intensity would be linearly proportional to the density of the molecules. All of these characterization measurements were made with a low gain setting for the MCP and amplifier to avoid saturating the signal sent to the scope. The results are shown in figure (6-2). In this measurement a mixture of 1% ammonia in krypton was used. As we can see in figure (6-2), a laser power of  $\sim 4 \text{ mJ/pulse}$  saturated the transition for this measurement. As a result, the typical laser power used in our experiments was set to be  $\sim 3 \text{ mJ/pulse}$ . However, depending on the concentration of the sample and other experimental conditions this setting was changed. The MCP voltage used for this measurement was  $1550 \text{ V}$ .

MCP gain was measured after characterizing the laser power. Figure (6-3) shows the characterization result for the MCP gain. The laser power used for this measurement was set to  $3 \text{ mJ/pulse}$ . Since the dark current for MCP was observed at  $\sim 1900 \text{ V}$ , voltages higher than  $1850 \text{ V}$  were not used.

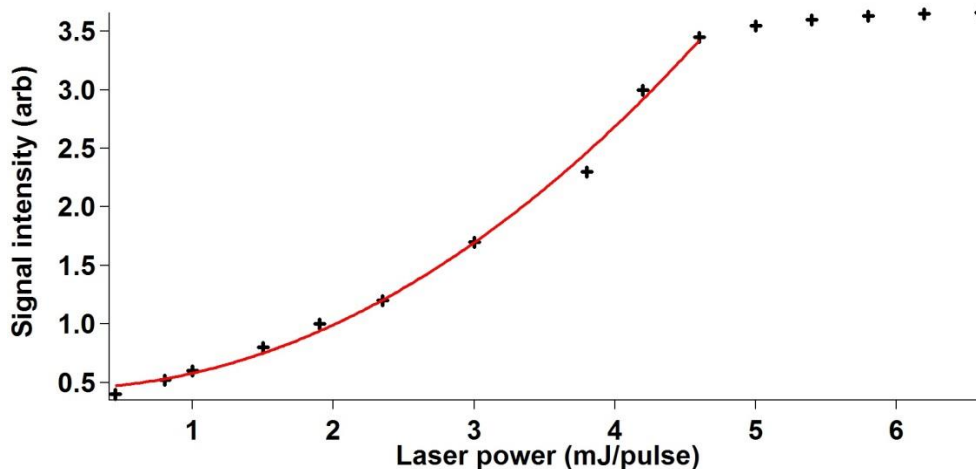


**Figure 6-2:** The (2+1) REMPI signal intensity (obtained at  $64050\text{ cm}^{-1}$  for ammonia molecules in  $|J = 1, K = 1, \textit{antisymmetric}\rangle$ ) versus the laser power for the purpose of signal calibration. Note the saturation of the signal at  $\sim 4\text{ mJ/pulse}$ . The uncertainties are neglected.

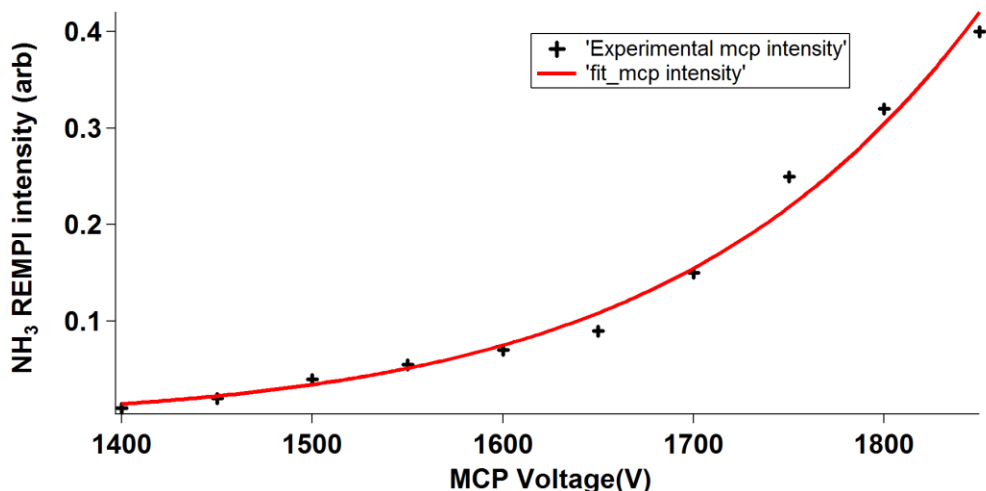


**Figure 6-3:** The signal intensity versus the MCP voltage for the purpose of calibration of the signal. Note that the safe limit for voltage was 1850 Volts. (Obtained at  $64050\text{ cm}^{-1}$  for ammonia molecules in  $|J = 1, K = 1, \textit{antisymmetric}\rangle$ , and laser power of  $3\text{ mJ/pulse}$ ). The uncertainties are neglected.

### 6.1.2 Deceleration of ammonia

Conditioning of the Stark decelerator was the first step in preparing the decelerator for the deceleration experiments. A LabView code was used to monitor the conditioning current. Conditioning was performed every time the chamber was opened.

Proper characterization of the DC Stark decelerator required matching our simulation results with the experimental results, which means several trials of both the measurement and simulation were done until we confirmed that the behaviour of the decelerator was predictable by the

simulation. For this purpose and for our experimental setup the best candidate was ammonia due to its availability, low mass, good Stark shift, and its easy detection via REMPI, which made the characterization of the decelerator easier.

In order to find the uncertainty for the final velocity calculations, it is required to know the details of all the uncertainties in timing and spacing. The uncertainty in the mean velocity,  $\Delta V$ , of the molecular packet is simply given by:  $\Delta V/V = \Delta X/X + \Delta t/t$ , in which  $t$  and  $\Delta t$  are time and its uncertainty, and  $X$  and  $\Delta X$  are distance from the nozzle to the detection point and its uncertainty. In our experiment the timing is controlled by a computer for which the uncertainty is negligible (fast clock). However there are time delays corresponding to the nozzle, switches, laser, and detection. We knew that in our typical experimental conditions our nozzle had  $50 \pm 5 \mu\text{s}$  delay from the nozzle characterization experiments previously done by our lab technician. In our numerical timing sequence calculations, the delay of the nozzle has been accounted for. Also, in the worst case scenario the delays of the HV switches and detection elements are typically on the order of tens of nanosecond. The time of flight for molecules in our measurements is a few milliseconds. Therefore the contribution of the time in the uncertainty is less than 1 %. If we assume an exaggerated uncertainty of 1 cm for  $\Delta X$ ,  $\Delta X/X$  will be less than 1 %. Therefore by assuming an exaggerated uncertainty for time and the distance, we assume an exaggerated uncertainty of 2 % for the velocities calculated in this thesis. Please note that since the experimental results are compared to the numerical simulation results, the experimental results are reliable within the uncertainty of the numerical calculations.

#### **6.1.2.1 Deceleration with the first ion optics**

For the first ion optics design, the distance between the last electrode pair of the decelerator and the centre of the ion optics was 11.15 cm. This distance caused the decelerated packets to become lost or elongated along the beam axis after the decelerator, and made the signal weak. This became especially problematic for the detection molecules at final velocities lower than 80 m/s. The reason this setup was initially chosen was to leave enough space for the future experiments where a microwave decelerator or trap is added. For the experiments done in this thesis, the DC Stark decelerator was used alone.

The first measurement prior to any deceleration was to find the velocity of the molecular packet after the supersonic expansion. The theory of the supersonic expansion can give some rough estimate of the most probable velocity of the beam, but it is also necessary to experimentally find the time of flight distribution and extract the longitudinal velocity distribution from that. This determines the initial velocity of the synchronous molecule.

For our Stark decelerator we could choose between the guiding mode (when all the electrodes were connected to high voltages but without switching) and the deceleration mode (when odd and even electrode pairs go on and off with the switching scheme). The guiding mode can guide the molecules in the LFS states along the decelerator to the detection point, and produce a strong signal. We could then choose the desired initial velocity by looking at the guided beam, as illustrated in figure (6-4). In this figure a coarse ( $5 \mu\text{s}$  step size) time of flight scan of the molecular beam is shown. In the figure the signal enhancement when the decelerator was on compared to when it was off can be easily seen. The signal corresponding to  $\varphi_0 = 0^\circ$  of the initial velocity  $V_i = 445 \text{ m/s}$  was the strongest among the others for this molecular beam. So the velocity for the synchronous molecule in the deceleration experiments was set to  $V_i = 445 \text{ m/s}$ . However, as we can see later for SD radicals, choosing the initial velocity of the synchronous molecule depends on the final goal of the experiment and the experimental conditions.

By choosing  $V_i = 445 \text{ m/s}$  as the initial velocity of the synchronous molecule and calculating the switching times for different phases, we experimentally observed deceleration of ammonia molecules down to  $\sim 59 \text{ m/s}$ . In figure (6-5) the full time of flight is shown for phase zero. For clarity only the decelerated packet is shown for the other phases. For the lower final velocities bunching for first stages was done. The so-called “bunching” of the molecular packets, which was used to improve the signal, is explained in the next section (6-1-2-2). For the lower final velocities the signals are scaled to be clearly seen. The gas mixture used for these experiments was a mixture of 2% ammonia in krypton. The backing pressure of the nozzle was 5 bars, and the nozzle was open for  $50 \mu\text{s}$  for each shot. In all of the measurements the laser power was fixed to  $3 \text{ mJ/pulse}$ , and the measurements were made with a repetition rate of 3 Hz. The effective detection area in the simulation was assumed to be 1 mm to be comparable with the laser beam waist at the detection point. The number of averages per point was different for each measurement. The number of averages for  $\varphi_0 = 0^\circ$  was 15 shots/point, for  $\varphi_0 = 30^\circ$  and  $\varphi_0 =$

$45^\circ$  was 50 *shots/point*, for  $\varphi_0 = 52^\circ$  and  $\varphi_0 = 53.3^\circ$  was 100 *shots/point*, and for  $\varphi_0 = 57.6^\circ$  was 200 *shots/point*. The result presented here was obtained after several attempts to match the simulation with the experiment and characterize the dimensions and the time delays. After optimizing the variables in the simulation, a delay time of 50  $\mu\text{s}$  for the nozzle was found to be practical. For  $\varphi_0 = 57.6^\circ$ , the signal to noise ratio was lower due to the spatial expansion of the decelerated packet, which limited the detection for further deceleration. Therefore the second version of the ion optics was designed to reduce the free flight path of the molecules and reduce this expansion.

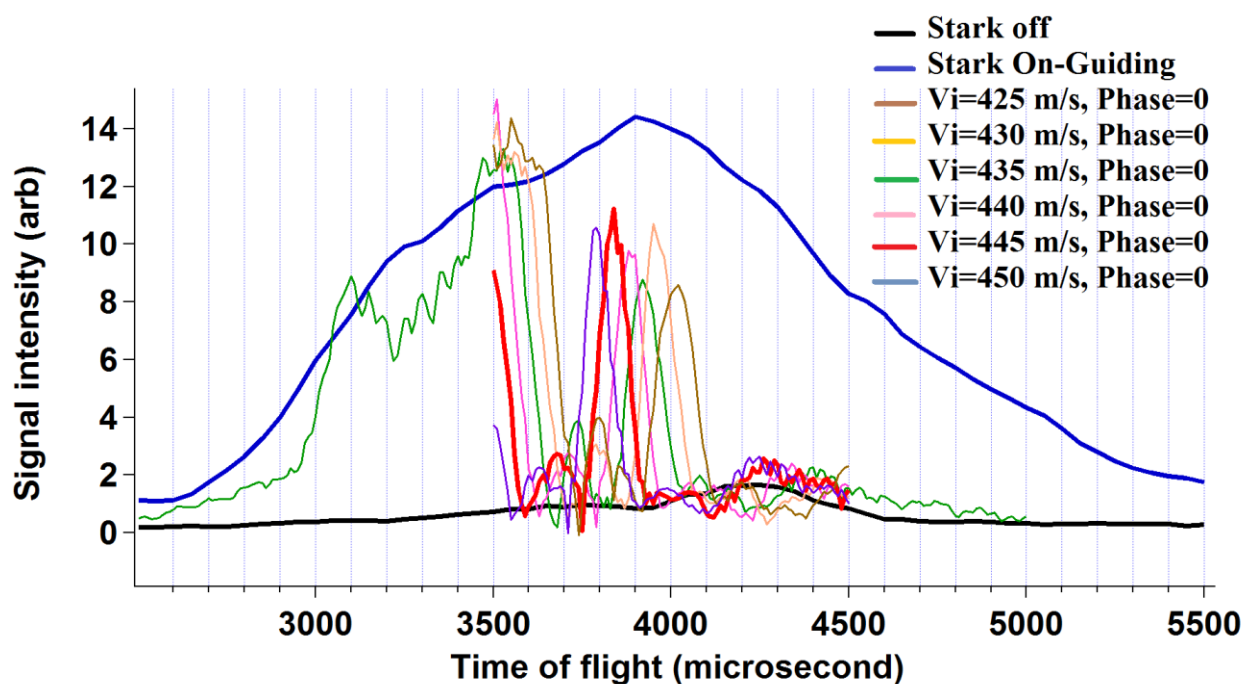


**Figure 6-4:** The detected signals after the decelerator for the purpose of comparison between free flight, guiding, and switching modes. For the switching mode, different initial velocities of the synchronous molecules were chosen for the purpose of comparison. Note the different arrival times for the decelerator selected packets at **3500 – 4000  $\mu\text{s}$** . The uncertainty for the signal intensity measurements at each data point was  $\sim \pm 5\%$ , that were obtained from the standard deviation of repeated measurements.

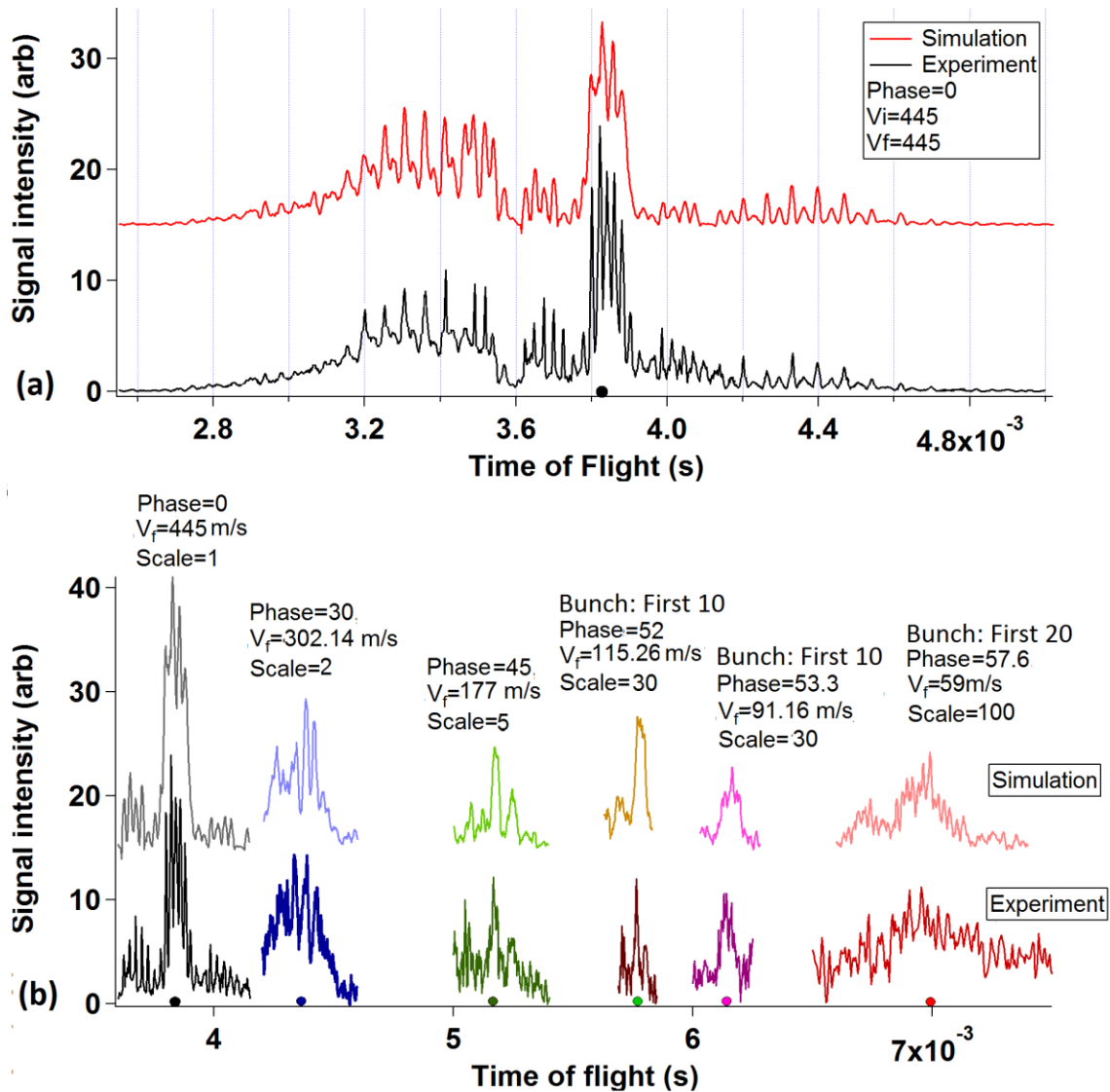


**Figure 6-5:** Deceleration of ammonia molecules, detected using the first ion optics design. (a) Full time of flight obtained by simulation (red) and experiment (black) for phase= $0^0$  with initial velocity of  $445$  m/s. (b) Deceleration of ammonia molecules from  $445$  m/s down to  $59$  m/s using different phases for the synchronous molecule. The signal to noise ratio was not high enough to detect a proper signal at lower speeds mostly due to the long distance between the ion optics and the decelerator. The uncertainty for the signal intensity measurements at each data point was  $\sim \pm 5\%$  for velocities higher than  $100$  m/s and  $\sim \pm 10\%$  for velocities lower than  $100$  m/s, that were obtained from the standard deviation of repeated measurements.

### 6.1.2.2 Bunching with the decelerator

In a free flight, due to the velocity spread of the molecules, the molecular beam diverges in the longitudinal and transverse directions while traveling toward the entrance of the decelerator, and also traveling from the decelerator's exit to the detection point. Inside the decelerator, the molecules in LFS states are focused in the transverse direction by the force exerted on them by

the decelerator's electrodes. In the longitudinal direction, however, the velocity spread is larger and the confining field is phase dependent. This means that the molecules around the synchronous molecule can diverge in the longitudinal direction and will be lost from the target packet. In the case of deceleration with high phases a large number of molecules get lost, especially the ones ahead of the synchronous molecule, because the potential hill is not extended enough to capture them. The molecules that pass the potential peak are no longer confined and will be lost. Therefore it is desirable to find a way to focus the molecules longitudinally toward the synchronous molecule. This can be done by using a so-called "buncher". A buncher can be separated from the decelerator and be located after the decelerator as described by Crompvoets et al. [124], or can be some of the electrode pairs of the decelerator itself working at phase zero, as explained below. A combination of bunching and deceleration has been tried before with the aim of reducing the operational length of the decelerator [36], where bunching was applied to the last electrodes of the decelerator. However to my knowledge the work done in this thesis is the first attempt to use the decelerator electrode pairs both as buncher and velocity reducer, especially for the first set of electrodes.

The structure of the buncher is the same as the Stark decelerator. The operation of the buncher is similar to the decelerator working with phase zero. A buncher rotates the phase-space distribution of those molecules around the synchronous molecule which are within the phase-space acceptance of the buncher. The molecular packet can become focussed toward the synchronous molecule spatially or in velocity, depending on the amount of time that the buncher is on. The benefit of a separate buncher is that its dimension and voltage can be controlled separately from the decelerator, and can be designed to be more effective. A separate buncher has been previously used after the decelerator to shape the phase-space profile of the decelerated packet [124]. In our case, especially for the experiments at the presence of hexapole, a buncher was needed before the decelerator to squeeze the molecules spatially in the longitudinal direction, in order to increase the number of molecules within the phase-space acceptance of higher operational phases. Since our Stark decelerator has 180 stages of deceleration, using some of the electrode pairs for bunching would not impose a large increase in its operational phase for the same final velocity.

In our experiments a separate buncher was not used because it was not necessary for the characterization experiments. Instead, the bunching principle was applied to some of the

decelerator's stages, in which some of the electrode pairs were switched on and off at phase zero. The timing sequence generated by numerical simulation controls the switching of the Stark electrodes. This means any number of electrode pairs at any part of the decelerator could be used for bunching, while the rest could be used for deceleration.

In this method there are two important things to mention. First, due to the coupling of the longitudinal and transverse motions of the molecules this method is not very effective for low velocity packets ( $\sim < 80$  m/s). Second, although bunching can increase the signal by reducing the spread of molecules in phase-space, it leaves fewer stages available for deceleration. This means that if a certain final velocity is desired, the measurement with bunching has to operate at a higher deceleration phase than the one without bunching. I wrote an optimization code to determine the best combination of bunching and deceleration stages. The simulations showed that this method was mostly useful for the decelerated packets with a low final velocity, as explained below. The optimum number of stages required to get the best signal was obtained from the simulation in which the geometry of the setup and the velocity of the molecular beam were the main factors. Figure (6-6) shows a simulation result that demonstrates the difference that bunching can make to the intensity of the signal. The simulation was done for a molecular packet with initial velocity of  $445$  m/s and final velocity of  $55$  m/s. As we can see, bunching for the first 10 stages (electrode pairs) has increased the signal; although a slightly higher phase was used for deceleration. Figure (6-7) shows the agreement of the experiment with the simulation for a molecular packet decelerated to  $\sim 76$  m/s from  $445$  m/s. As the graph shows, for this case the bunching is most effective when it was done for the first stages. This makes sense when thinking of a molecular packet which has freely traveled for about  $\sim 55$  cm in the longitudinal direction to arrive at the decelerator. Bunching at the beginning helps to rotate the phase-space distribution in a way that molecules are spatially more close to the synchronous molecule. Therefore the number of molecules within the phase-space acceptance of the decelerator increases, and a better signal is obtained.

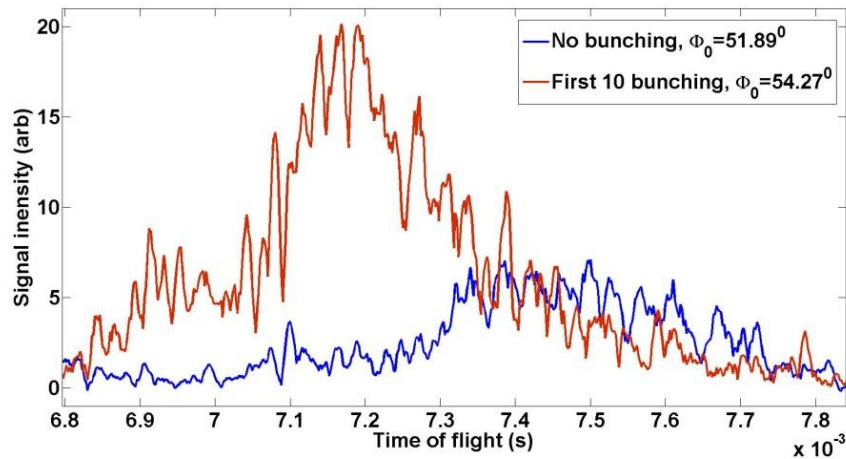


**Figure 6-6:** Simulation results to show the effect of bunching on improving the signal. The initial velocity in both cases was assumed to be **445 m/s**, and the final velocity was fixed to **55 m/s** in both cases for the purpose of comparison. The blue trace shows the expected signal for no bunching and phase=**51.89°**, and the red trace shows the expected signal for bunching for the first 10 stages of the decelerator and phase=**54.27°**. Note the enhancement of the signal in the red trace. Also note the higher phase used for the case with bunching to compensate for the first 10 stages. In this experimental setup bunching particularly helped a lot in improving the signal for final velocities of lower than **100 m/s**.

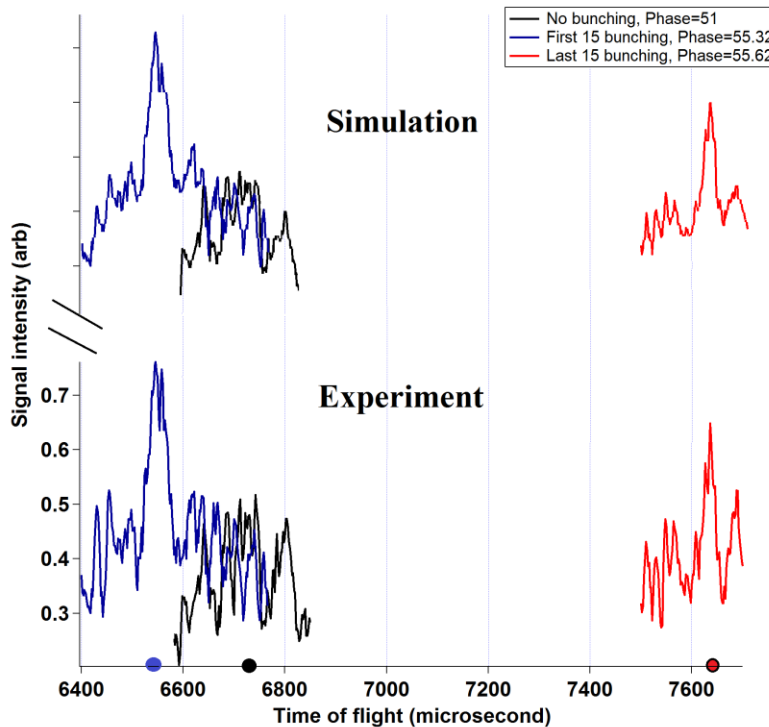


**Figure 6-7:** Comparison of signals for no bunching (black), first 15 stages for bunching (blue), last 15 stages for bunching (red). Note that bunching improved the signal in both cases, however bunching first had stronger signal than bunching last. This is not a general rule and depends on the spacing of different parts of the experiment. In this case bunching first improves the signal more because of the long distance between the nozzle and the decelerator.

The arrival time of the decelerated packet with the same final velocity can be tuned by the number of bunching stages in use. The general trend is that if bunching happens at the first stages, the decelerated packet arrives earlier, and if the last stages are used the decelerated packet arrives later than the one with no bunching. The reason is that when bunching is applied at the first stages, the molecules travel at high velocity for a longer time, while when bunching is applied at the last stages, the molecules travel at low velocity for a longer time.

### **6.1.2.3 Deceleration with the second ion optics design**

In order to reduce the distance between the decelerator and the detection point a second version of the ion optics was designed. The new ion optics was  $\sim 3.8\text{ cm}$  away from the last electrode pair, which is about one third of the previous distance. It was also necessary for the new design to move the decelerator back toward the hexapole by  $1.67\text{ cm}$  to match the centre of the new ion optics with the window on the chamber. After several attempts to find the optimum timing, deceleration from  $V_i = 425\text{ m/s}$  to  $V_f = 27.9\text{ m/s}$  was obtained. This became possible by the new design of the ion optics, and the fact that a lower initial velocity was chosen for the synchronous molecule. The lower initial velocity means a molecular packet with lower initial translational energy was chosen. Therefore a lower phase was required to reach a specific final velocity. A lower phase for the deceleration is equivalent to a larger phase-space acceptance for the decelerator, which resulted in a larger number of molecules at the detection point and an enhanced signal. In all of the measurements the laser power was fixed to  $3\text{ mJ/pulse}$ , the repetition rate to  $3\text{ Hz}$ , the nozzle backing pressure to  $5\text{ bars}$ , and hexapole to  $5\text{ kV}$ . The number of averages per point was higher for the lower final velocity measurements to enhance the signal to noise ratio.

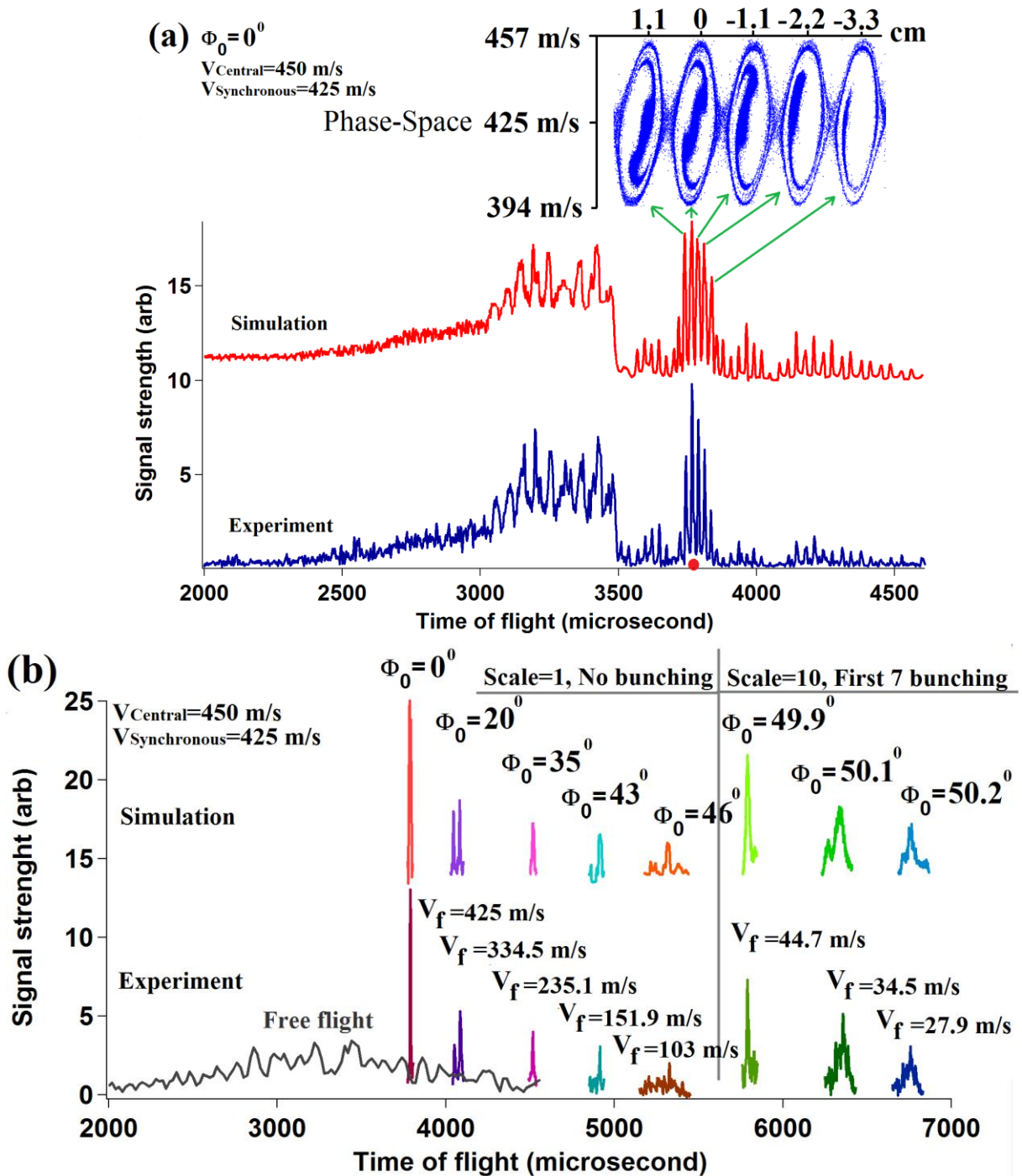


**Figure 6-8:** Time of flight for decelerated ammonia molecules detected by the second ion optics version.

(a) The experimental and simulation results for the full time of flight measurement for Phase= $0^\circ$  and initial velocity of  $425 \text{ m/s}$ . The top panel shows the phase-space distribution for the main packet and neighboring packets. (b) The experimental and simulation results for the main packet while decelerating from  $425 \text{ m/s}$  down to  $27.9 \text{ m/s}$ . Note the scale after phase= $49^\circ$ . The uncertainty for the signal intensity measurements at each data point was  $\sim \pm 5 \%$  for velocities higher than  $100 \text{ m/s}$  and  $\sim \pm 10 \%$  for velocities lower than  $100 \text{ m/s}$ , that were obtained from the standard deviation of repeated measurements.

## 6.2 Deceleration of *SD* radical in $J = 3/2$ and $J = 5/2$ rotational states

Deceleration of the *SD* radical for the first time is demonstrated in this thesis. In these experiments the *SD* radical was produced by an electric glow discharge of supersonically expanded deuterium sulfide ( $D_2S$ ) in a carrier gas such as argon or krypton. The velocity distribution of the produced *SD* radical highly depends on the discharge condition and the concentration of the deuterium sulfide in the mixture. For the deceleration experiments in this thesis typically a mixture of 10 % deuterium sulfide in krypton was used. In order to discharge the supersonically expanded gas a discharge plate was placed after the nozzle. The discharge method does not produce radicals with 100% efficiency. In addition, although lowering the concentration would help in obtaining a lower mean velocity for the molecular packet, it might not produce enough *SD* radicals. Therefore, a discharge characterization was necessary.

The Stark deceleration of *OH* radicals with the molar mass of  $\sim 17.008 \text{ gr/mol}$ , electric dipole moment of  $1.67 \text{ D}$  in the  $|X^2\Pi_{3/2}, J = 3/2, M_J = -3/2\rangle$  state, and Stark shift of  $3.22 \text{ cm}^{-1}$  at  $200 \text{ kV/cm}$  has been previously reported [39]. Although the *OH* radical is theoretically similar to the *SD* radical in Stark effect calculations, it is lighter in weight, has higher electric dipole moment, and has higher Stark shift than the *SD* radical. The *SD* radical has a molar mass of  $34.0791 \text{ gr/mol}$  which is two times more than the hydroxide radical. The electric dipole moment of *SD* radical is  $0.76 \text{ D}$ , which is about two times less than the hydroxide radical. As a result the Stark shift for this state for *SD* radical is  $1.49 \text{ cm}^{-1}$  at  $200 \text{ kV/cm}$ , which is about half of that for the *OH* radical. This means that deceleration of the *SD* radical to a given final velocity is more difficult than for the *OH* radical. An additional difficulty with the *SD* radical is in its detection. About 95 % of the UV excited *SD* radicals relax to the same initial state after the fluorescence. The fluorescence light for this transition has the same wavelength as the incident laser, which reduces the signal-to-noise ratio of the collected fluorescence light (LIF). Although it is possible to use filters and monitor the off-resonant fluorescence light for detecting the molecules, we preferred to use the transition with higher fluorescence intensity since the number of molecules was already so low after the deceleration. Therefore gating the PMT and baffles were employed to reduce the signal from the stray and scattered light as much as possible. However since the shiny surfaces such as the Stark electrodes are close to the detection point, detecting some scattered light was inevitable. In order to improve the signal-to-noise ratio a large

number of averages per point was used. We decided to use the LIF detection scheme because we plan to measure the absolute density of the Stark decelerated molecules by CELIF method for the next step, even-though the REMPI scheme for detecting SD radicals was available.

In the case of CELIF experiments, the background light was less problematic due to the presence of the cavity which reduced the laser intensity inside the chamber. However since the laser intensity at the detection point was about one hundred times less, the emitted fluorescence light intensity per pass (each time the laser bounces back and forth between the cavity mirrors) was also much less than the LIF measurement. The CELIF measurements therefore required a photon counting scheme, as will be explained in section (6-2-7).

### **6.2.1 LIF signal integration**

For each single laser shot an integrated LIF signal was recorded. The average integrated LIF signal per point was calculated using a computer code written specifically for data analysis of the LIF experiment. The rise time of the PMT gate for our PMT was  $\sim 70$  ns and the fall time was  $\sim 8$  ns. Since the rise time of the PMT is long, it was necessary to open the gate some time before the fluorescence occurs. It was possible to remove most of the stray light from the signal by setting the rise time carefully. The PMT was turned on a few tens of nanoseconds before the arrival time of the laser to the detection point. In other words the stray light arrived in the middle of the rise time, during which the PMT was still not operating at full efficiency, and as a result could not blind the PMT with a huge signal. The integrated signal was recorded in a window between the time that PMT gate was fully open and the off time of the PMT. Any integration window between these two times also works. Figure (6-9) illustrates the signal recording scheme for the LIF measurements.

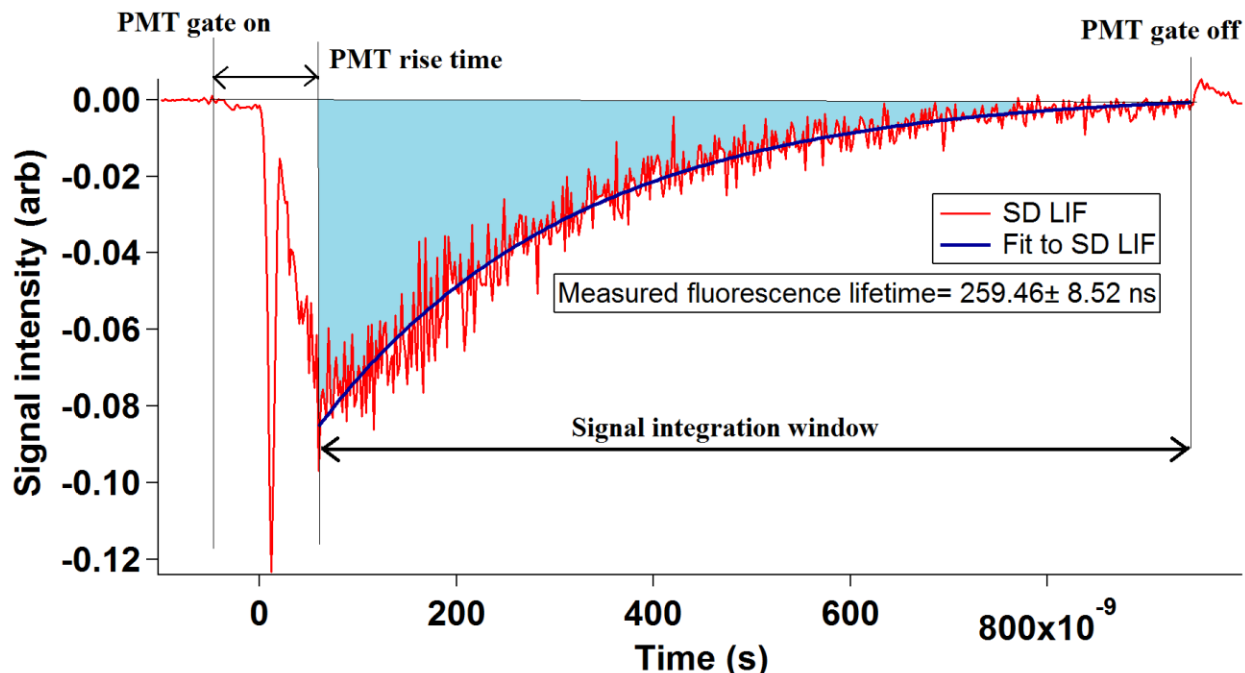


**Figure 6-9:** (Red) A typical fluorescence signal seen by the PMT from excited *SD* radicals. (Blue) The fit to the fluorescence decay signal gave a fluorescence lifetime of  $259.46 \pm 8.52 \text{ ns}$  for *SD* radicals. Note the sharp peak close to time zero due to the scattered laser light within the PMT gate rise time.

### 6.2.1.1 The fluorescence lifetime of *SD* radicals

To my knowledge there are a few reports on the fluorescence lifetime measurement of *SD* radicals in  $|A^2\Sigma^+, \nu' = 0, N' = 0 - 13\rangle$ , all of which were made in the 1980s [125] [126]. Kawasaki et al. reported that the fluorescence lifetimes of *SD* radical decreased monotonically from  $198 \text{ ns}$  to  $44 \text{ ns}$  with increasing the rotational energies by pre-dissociation through tunneling. In their measurement  $198 \text{ ns}$  is reported to be the maximum fluorescence lifetime for *SD* radicals in  $|A^2\Sigma^+, \nu' = 0, N' = 0 - 13\rangle$  [126]. On the other hand Friedl et al. reported an average fluorescence lifetime of  $194 \text{ ns}$  for  $|A^2\Sigma^+, \nu' = 0, N' = 0 - 10\rangle$  energy states, while claiming that the fluorescence lifetime is roughly constant for all the rotational levels [125].

The measured fluorescence life time of  $A^2\Sigma^+, \nu' = 0, N' = 1\rangle$  obtained from our experiment is  $\sim 259.5 \text{ ns}$  which is close to the values ( $\sim 200 \text{ ns}$ ) reported by the previous groups, but slightly higher than theirs. Figure (6-9) shows the typical decay behaviour of fluorescence light in our case along with its fitted line.

The fluorescence lifetime of *SH* radical is reported to be  $\sim 3 \text{ ns}$ . The substantial difference between the lifetimes of *SH* and *SD* radicals has been interpreted as an indication that *SH* pre-

dissociates even in  $\nu' = 0$  of the  $A$  state. The pre-dissociation is believed to be caused by the crossing with the  $^4\Sigma^-$  state [127].

### 6.2.2 PMT signal characterization

The PMT used in our experiments was a Hamamatsu H11526-010NF which could be gated. In order to reduce the scattered light captured by the PMT it was necessary to reduce the laser power to a range that gave the best signal while still not saturating the transition. A measurement was done at the test chamber to characterize the PMT signal versus the incident laser power at a low PMT gain. The low gain on the PMT insured that the saturation of the signal was not due to the PMT saturation.

As figure (6-10) shows, the transition became saturated at a laser power of  $\sim 400 \mu\text{J}/\text{pulse}$ . Using higher laser powers not only could not improve our signal intensity, but could also reduce the signal to noise ratio by producing more scattered light. As a result, the laser powers used in the experiments were always chosen to be below this level.

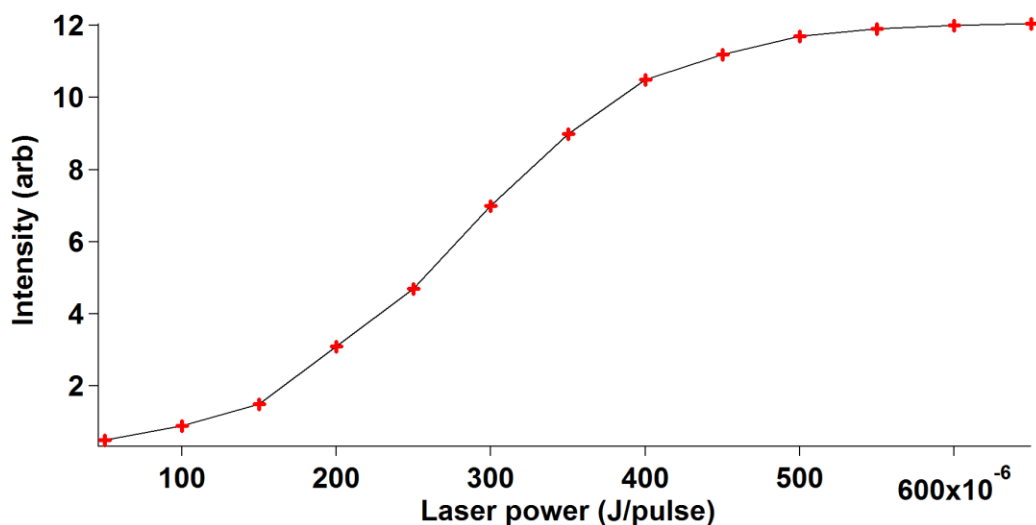


**Figure 6-10:** The fluorescence signal versus the input laser power measurement for the purpose of finding the saturation limit for the transition in the  $SD$  molecules ( $|X^2\Pi_{3/2}, J = 3/2\rangle$ ) at the detection point. The PMT gain for this measurement was low to prevent saturating the PMT. The uncertainties are neglected for this measurement.

### 6.2.3 Discharge characterization

A test chamber was used to characterize the glow discharge of the supersonically expanded mixture of 10 %  $D_2S$  in krypton. The goal of the discharge characterization was to find the

optimum voltage at which the molecular beam was not too fast, not rotationally hot, and produced a strong signal. Although increasing the voltage of the discharge plate generally increased the number of  $SD$  radicals produced, it was at the expense of producing a faster beam with a higher rotational temperature. The typical discharge voltage for the experiments after characterization was  $+618\text{ V}$ . At this voltage the central velocity of the molecular beam was  $490\text{ m/s}$ , and the maximum observed occupied rotational number that was visible from the fluorescence signal was  $J'' = 5.5$ , as we can see from the frequency spectrum in figure (6-12). The width of the velocity spread for this voltage was obtained from the time of flight measurement and was  $\sim 75\text{ m/s}$ . This made it possible to use  $V_i = 440\text{ m/s}$  as the initial velocity for the deceleration experiments. Figure (6-11) shows the experimental results for the characterization of the discharge at different voltages.

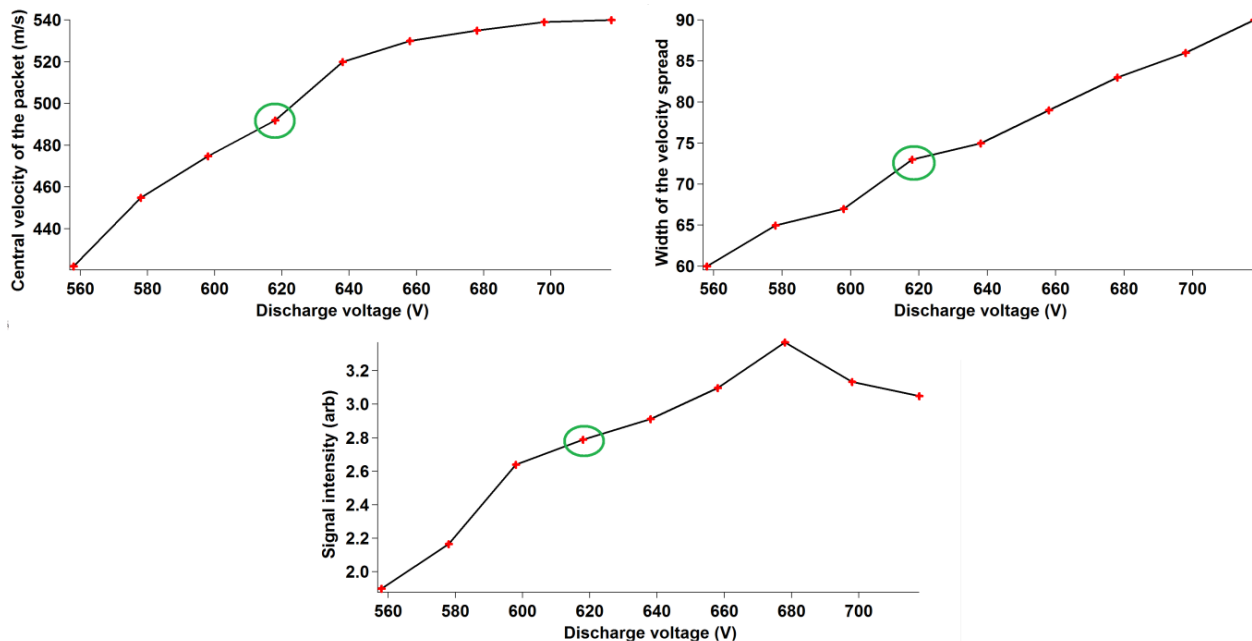


**Figure 6-11:** Characterizing the discharge signal in the test chamber. Left top: Central velocity of the beam versus the discharge voltage. Right top: width of the velocity distribution versus the discharge voltage. Bottom: the signal intensity versus the discharge voltage. The green circle shows the optimum condition chosen. The experimental conditions for all the graphs are the same. The fluorescence of  $SD$  radicals after  $q\ Q_1P_{21}(1.5)$  transition was collected to obtain the signal for each trace. The uncertainties are neglected for these measurements.

Another thing that had to be characterized for the nozzle was the timing for the discharge pulse. A long discharge pulse would increase the risk of arcing, and a short pulse might not produce enough radicals. After several attempts a pulse length of  $40\ \mu\text{s}$  with  $+618\text{ V}$  being applied to the

discharge plate was determined to be optimal. The discharge typically happened from 80  $\mu s$  to 120  $\mu s$  after the nozzle activation pulse.

#### 6.2.4 LIF frequency scan and rotational temperature of the SD radicals

The frequency spectrum of the *SD* radical in the  $X^2\Pi_{3/2}$  manifold was measured at the test chamber. For this measurement the discharge plate's voltage was +618 V, the nozzle opening time 55  $\mu s$ , and the laser power 300 mJ/pulse. The transitions are shown and labeled on the spectrum in figure (6-12). The simulation for the transitions at a rotational temperature of  $T = 35 K$  is also shown on the graph. As we can see from the figure, the transition intensities do not exactly follow the simulation; however it is possible to estimate the rotational temperature of the beam by comparing the feature of the simulated spectrum at different rotational temperatures with the experimental result. Using this method, an estimation for the rotational temperature was obtained. The  $q Q_1 P_{21}(5.5)$  transition at 30917.2  $cm^{-1}$  is barely visible in the spectrum. This transition begins to show up in the simulation at  $T \sim 35 K$ . The feature of the spectrum stays the same for the temperature range of  $T \sim 35 K - 45 K$ . In the simulation spectrum at  $T = 45 K$  a transition from  $J'' = 6.5$  appeared at 30966.2  $cm^{-1}$  which corresponded to the  $r R_1 Q_{21}(6.5)$  transition. Since this transition was absent in the experimental result, the rotational temperature of the beam was roughly estimated to be between 35 K – 45 K. A more accurate estimation is presented on next page.

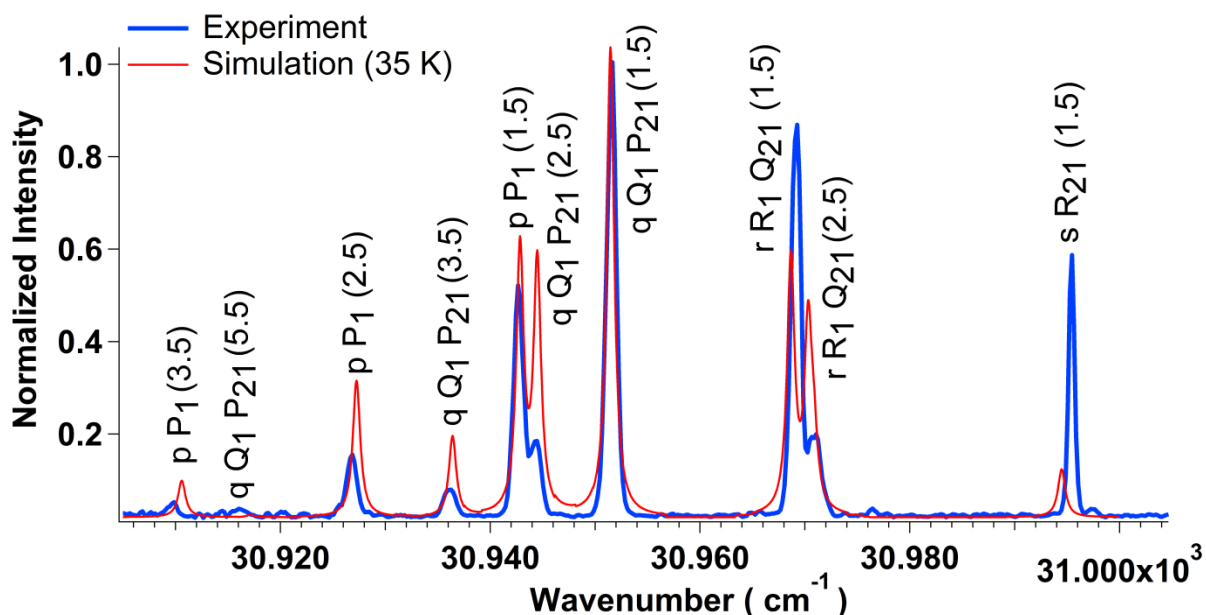


**Figure 6-12:** The frequency spectrum for *SD* radical obtained by LIF method. Red: Simulation at  $T_{rot} = 35\text{ K}$ . Blue: Experimental result. Note that the signal for  $q Q_1 P_{21}(5.5)$  was barely visible and the signals for higher  $J''$  were not seen. The uncertainty for the signal intensity measurements at each data point was less than  $\pm 5\%$ , that were obtained from the standard deviation of repeated measurements. The uncertainty of the wavenumber was  $\pm 0.1\text{ cm}^{-1}$ , which is obtained by the dye laser's minimum possible step size.

The rotational temperature of the beam is important because we would like to have most of the molecules in the lowest rotational state ( $J = 1.5$ ) in the  $X^2\Pi_{3/2}$  manifold. The frequency spectrum for the beam was measured at different discharge voltages in order to see the effect of the discharge voltage on the rotational temperature of the beam. The results are shown in figure (6-13). In the spectrum the  $q Q_1 P_{21}(5.5)$  transitions are scaled ten times for clarity. As we can see from the spectrum, the  $q Q_1 P_{21}(5.5)$  transitions increase in intensity as the discharge voltage passes 620 V.

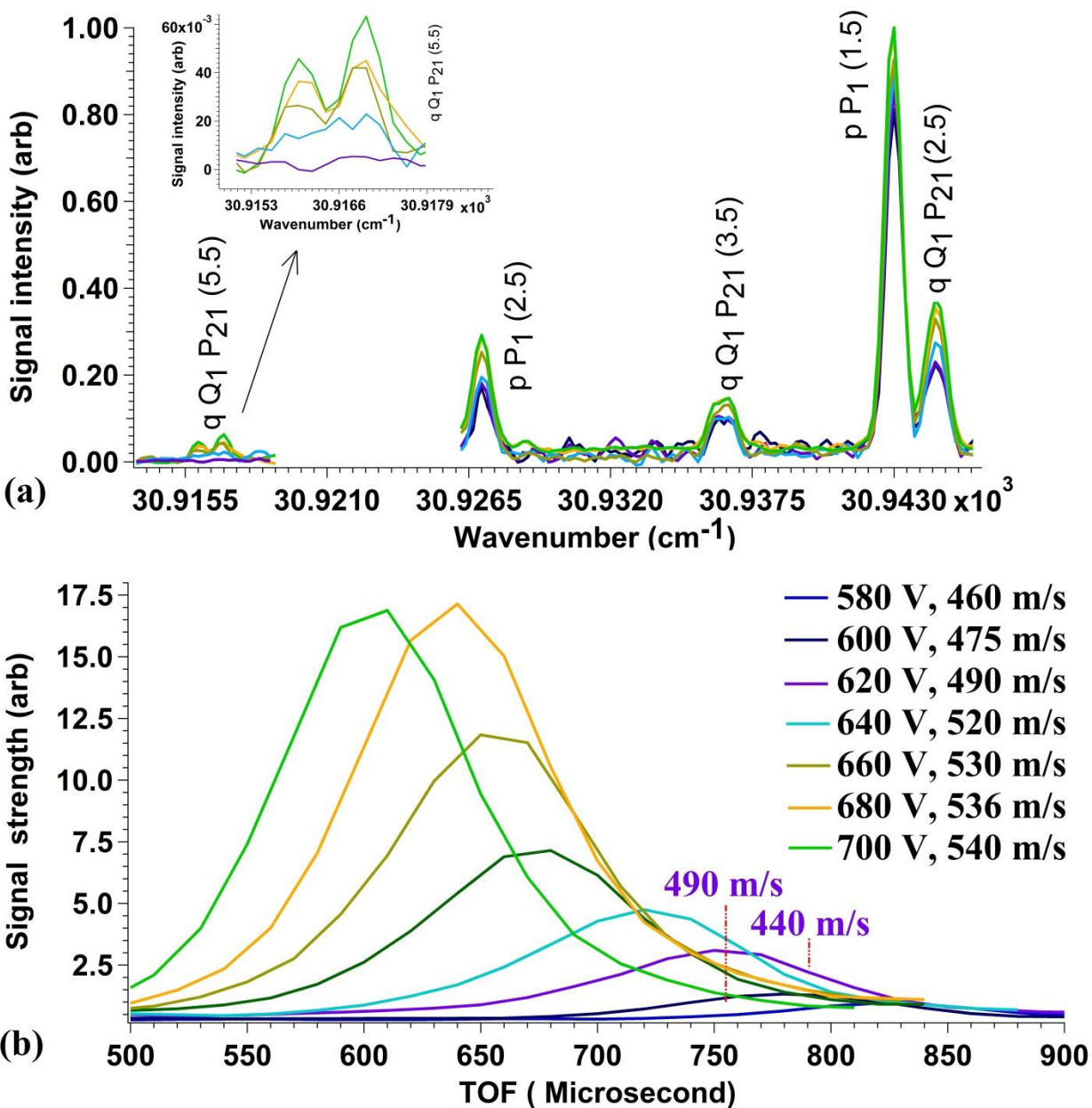
Although higher discharge voltages provided stronger signal for all the transitions, the associated higher temperatures produced higher translational velocities. By considering the characterization graphs shown in figure (6-11), 620 V was chosen to be the operational voltage for the experiments done in this thesis. Part (b) of the figure (6-13) demonstrates the effect of increasing the discharge voltage on the velocity of the molecular beam. For discharge voltage  $\sim 620\text{ V}$ , the central velocity (490 m/s) and the typical velocity used in the deceleration experiments (440 m/s) are shown on the graph. As we can see the voltage  $\sim 620\text{ V}$  has moderate signal strength, but it provides the maximum signal strength at 440 m/s among all.

Figure (6-13 (a)) shows the normalized signal intensities for the frequency spectrum of SD radicals at different discharge voltages. The signal for each trace is normalized to the intensity of the  $p P_1(1.5)$  transition signal of the same trace. For voltages lower than 620 V the signal for  $q Q_1 P_{21}(5.5)$  transition was in the noise level, so it was not possible to deduce any information from it. The signal enhancement, by increasing the discharge voltage for transitions from  $J$  values higher than 1.5, demonstrates the population growth in these levels.

The rotational temperature of the SD radicals produced at each discharge voltage was estimated with calculating the relative population of rotational energy levels (Boltzmann distribution), and by taking the ratio of the integrated signal in  $q Q_1 P_{21}(5.5)$  with respect to the integrated signal in  $p P_1(1.5)$ . The results are shown in table (6-1). For the discharge voltage of 620 V, the estimated temperature from this method is 29 K which is close to the estimation discussed above ( $\sim 35$  K).

**Table 6-1:** Rotational temperature of SD radicals produced at different discharge voltages. The uncertainty for the calculated temperatures is less than **10** %, obtained from the intensity fluctuations of repeated measurements. The uncertainty of the voltages are  $\pm 1$  V, according to the power supply's data sheet.

<b>Discharge Voltage (Volts)</b>	<b>Estimated <math>T_{rot}</math> (Kelvin)</b>
620	29
640	41
660	46
680	48
700	51



**Figure 6-13:** (a) The effect of discharge voltage on the occupation of the rotational states for the *SD* radical. (b) The effect of the discharge voltage on the time of flight profile of the *SD* radical. Note the two dashed lines labelling the curves corresponding to **490 m/s** and **440 m/s**. The velocity spread width for this trace was  $\sim 75$  m/s. The uncertainty for the signal intensity measurements at each data point was  $\sim \pm 5\%$ , that were obtained from the standard deviation of repeated measurements. The uncertainty of the wavenumber was  $\pm 0.1$   $\text{cm}^{-1}$ , which is obtained by the dye laser's minimum possible step size.

### 6.2.5 Deceleration

Stark deceleration of the *SD* radical molecular beam for the first time is discussed in this section. The detection scheme used for the deceleration experiments was LIF. This work continues on

similar experiments using the CELIF detection method, with the goal of measuring the absolute density of the decelerated packets.

All of the experimental deceleration results were reproduced by the simulation, and are presented in this section.

After characterizing the discharge behaviour and finding the frequency spectrum with the test chamber, the detection assembly was installed in the detection chamber of the Stark decelerator. The centre of the LIF collecting optics was located at  $\sim 4$  cm away from the last electrode pair of the decelerator. In order to reduce the scattered light from the shiny surfaces of the decelerator electrodes, the plastic spacer that was used before for the ammonia experiments to attach the ion optics to the body of the decelerator was left attached to the decelerator. Also, all the windows of the setup, except the laser entrance, were blocked to reduce the background light inside the chambers. The baffles used in the laser line reduced the scattered light and the unwanted fluorescence from the windows. A field of view reducer for the PMT optics was also used to limit the field of view of the PMT optics to the detection point as much as possible.

In addition to the different detection scheme compared to the ammonia experiments, the *SD* radical experiments were performed without the hexapole to improve the signal. Therefore it was necessary to align the parts again, and optimize the simulation with the new dimensions. To make sure the dimensions and spacing used in the simulation match with the experiment, the arrival time and the shape of the Stark decelerated packets were compared and adjusted to find the optimum condition.

Molecules in our desired state ( $|X^2\Pi_{3/2}, J = 3/2, M_J = -3/2\rangle$ ) were monitored. The transitions from the *f* symmetry of  $J = 3/2$  are Stark favoured and the molecules at this state can be guided through the decelerator because of being LFS. Since the distance from the nozzle to the detection point was long (116.1 cm), the signal at the detection point with decelerator off was weak because of the loss in the transverse direction. The signal of the Stark guided molecules was strong because the decelerator confined the molecules in the transverse direction, and guided the molecules in the LFS states to the detection point. When comparing the decelerator on and decelerator off frequency spectrum measurements (figure (6-14)), an enhancement in the signals originating from *f* symmetry of the  $J = 3/2$  is seen. The transitions  $s R_{21}(1.5)$  and

$q Q_1 P_{21}(1.5)$  when the decelerator was on were enhanced due to originating from the LFS part of the  $J = 3/2$ . Any of these transitions could have been used for monitoring the Stark decelerated packets, among which the  $q Q_1 P_{21}(1.5)$  was chosen due to its higher intensity. The frequency spectrum signal when the decelerator was off was very close to the noise limit, and did not have good signal-to-noise ratio.

The molecules in energy states with higher  $J$  values that have  $f$  symmetry are also Stark favoured, and can be guided by the decelerator. For example, the  $q Q_1 P_{21}(2.5)$  transition which originates from the  $f$  symmetry part of  $J = 5/2$  state also shows signal enhancement after the decelerator. Figure (6-14) shows the signal enhancement for this transition. The signal intensity for this transition is much less than the  $q Q_1 P_{21}(1.5)$  due to the lower population in  $J = 5/2$  compared to  $J = 3/2$ . In section (6-2-6) the frequency spectrum is discussed further. In addition, the Stark shift at  $126 \text{ kV/cm}$  for  $|X^2\Pi_{3/2}, J = 5/2, M_J = -5/2\rangle$  is about  $0.3 \text{ cm}^{-1}$  less than the Stark shift for  $|X^2\Pi_{3/2}, J = 3/2, M_J = -3/2\rangle$ . These two states have the highest positive Stark shift among the other components for  $J = 5/2$  and  $J = 3/2$ , respectively. The confining potential depth for the molecules in  $|X^2\Pi_{3/2}, J = 5/2, M_J = -5/2\rangle$  is shallower than the one for  $|X^2\Pi_{3/2}, J = 3/2, M_J = -3/2\rangle$ , which results in less deceleration for it. Figure (6-16) shows the deceleration result for the  $|X^2\Pi_{3/2}, J = 5/2, M_J = -5/2\rangle$  state of SD radicals. Due to the low population of molecules in the  $|X^2\Pi_{3/2}, J = 5/2, M_J = -5/2\rangle$  state and low signal-to-noise ratio for its measurement, it was not possible to monitor decelerations with phases higher than  $20^\circ$ . All the experimental conditions for this measurement were the same as the ones used for  $|X^2\Pi_{3/2}, J = 3/2, M_J = -3/2\rangle$ , except the switching times which were calculated specifically for  $|X^2\Pi_{3/2}, J = 5/2, M_J = -5/2\rangle$ .

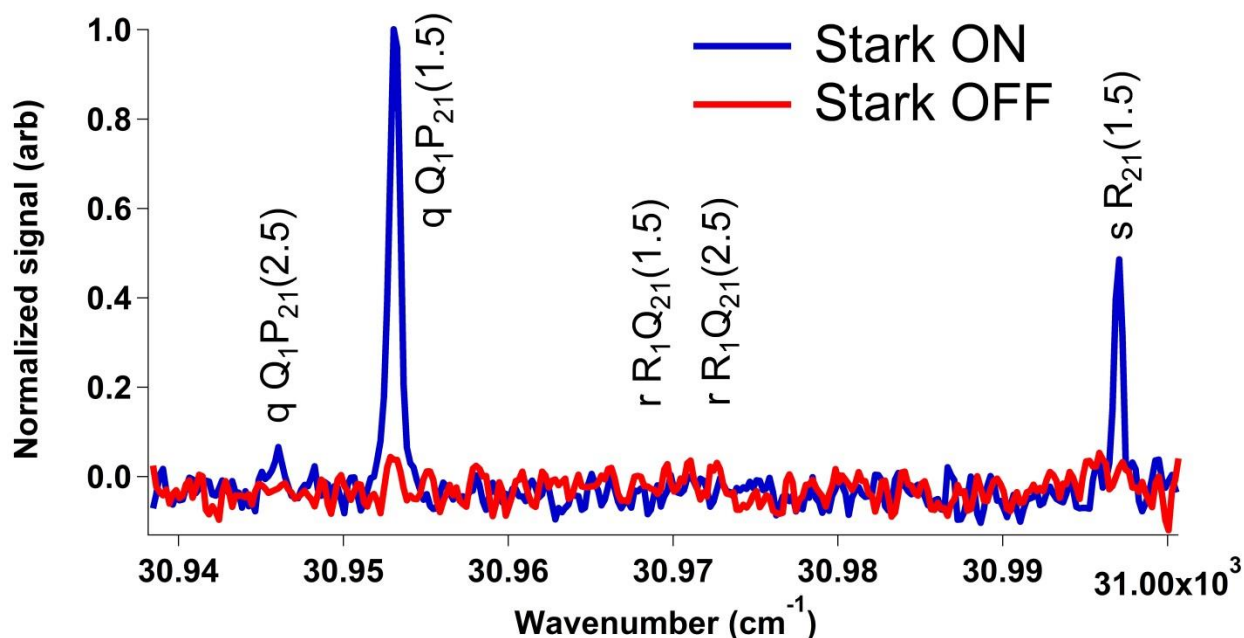


**Figure 6-14:** The frequency spectrum after the decelerator. Note the difference between decelerator on (blue) and decelerator off (red) spectra, which shows that when the Stark field is on, the molecules in LFS states are guided to the detection point. The uncertainty for the signal intensity measurements at each data point was less than  $\pm 10\%$ , that were obtained from the standard deviation of repeated measurements.

The uncertainty of the wavenumber was  $\pm 0.1 \text{ cm}^{-1}$ , which is obtained by the dye laser's minimum possible step size.

The experimental conditions for the Stark deceleration experiments were as below:

Nozzle:  $55 \mu\text{s}$  opening, backing pressure 4 bars, gas mixing ratio 10 %  $D_2S$  in Krypton.

Discharge: duration:  $40 \mu\text{s}$ , voltage +618 V

Pressures of the chambers while operating: source chamber:  $5 \times 10^{-5} \text{ Torr}$ , decelerator chamber:  $5 \times 10^{-6} \text{ Torr}$ , detection chamber:  $1 \times 10^{-7} \text{ Torr}$ . The pressure in the decelerator and detection chambers were higher than the previous REMPI experiments for two reasons: one was the removed hexapole chamber which was equivalent to removing one stage of differential pumping, and the other was the presence of the plastic parts of the baffles which were outgassing in the detection chamber.

Repetition rate of the experiment:  $0.7 \text{ s/shot}$ . A higher repetition rate was not used for two main reasons: first to prevent heating the nozzle and producing instability in the molecular beam generation, and second to keep the pressure of the decelerator chamber low enough to be safe while switching the electrodes.

For deceleration of SD radicals in  $|X^2\Pi_{3/2}, J = 3/2, M_J = -3/2\rangle$ :

Number of averages: depending on the phase chosen between 50 to 500 *shots/point*.

Laser: power: 300  $\mu\text{J/pulse}$ , wavenumber: 30953.3  $\text{cm}^{-1}$ .

PMT gate: opened 150 *ns* after the Q-Switch of the Nd-Yag laser, closed after 1  $\mu\text{s}$ .

Calculated central velocity of the molecular beam: 490 *m/s*.

Velocity of the synchronous molecule: 440 *m/s*.

Phase of the synchronous molecule: from 0° to 70°.

Deceleration down to: 301 *m/s*.

The uncertainty for the signal intensity measurements at each data point was  $\sim \pm 10\%$  for phases lower than 40° and  $\sim \pm 12\%$  for phases higher than 40°, that were obtained from the standard deviation of repeated measurements.

Further deceleration was not detectable due to the poor signal to noise ratio at larger phases. In addition, since recording the entire time of flight trace of the beam required very long measurement times, the full time of flight was only experimentally recorded for the  $\phi_0 = 0^\circ$  to make sure that the simulation and experiments were in agreement. For the rest of the phases the experimental measurements were limited to the decelerated packets. The experimental deceleration results for all phases are shown in figure (6-15) (aggregated in part (a), and individually in part (b) and (c), with comparisons to simulation).

For deceleration of molecules in  $|X^2\Pi_{3/2}, J = 5/2, M_J = -5/2\rangle$ :

Number of averages: 500 *shots/point*.

Laser: power: 300  $\mu\text{J/pulse}$ , wavenumber: 30946  $\text{cm}^{-1}$ .

PMT gate: opened 150 *ns* after the Q-Switch of the Nd-Yag laser, closed after 1  $\mu\text{s}$ .

Calculated central velocity of the molecular beam: 490 *m/s*.

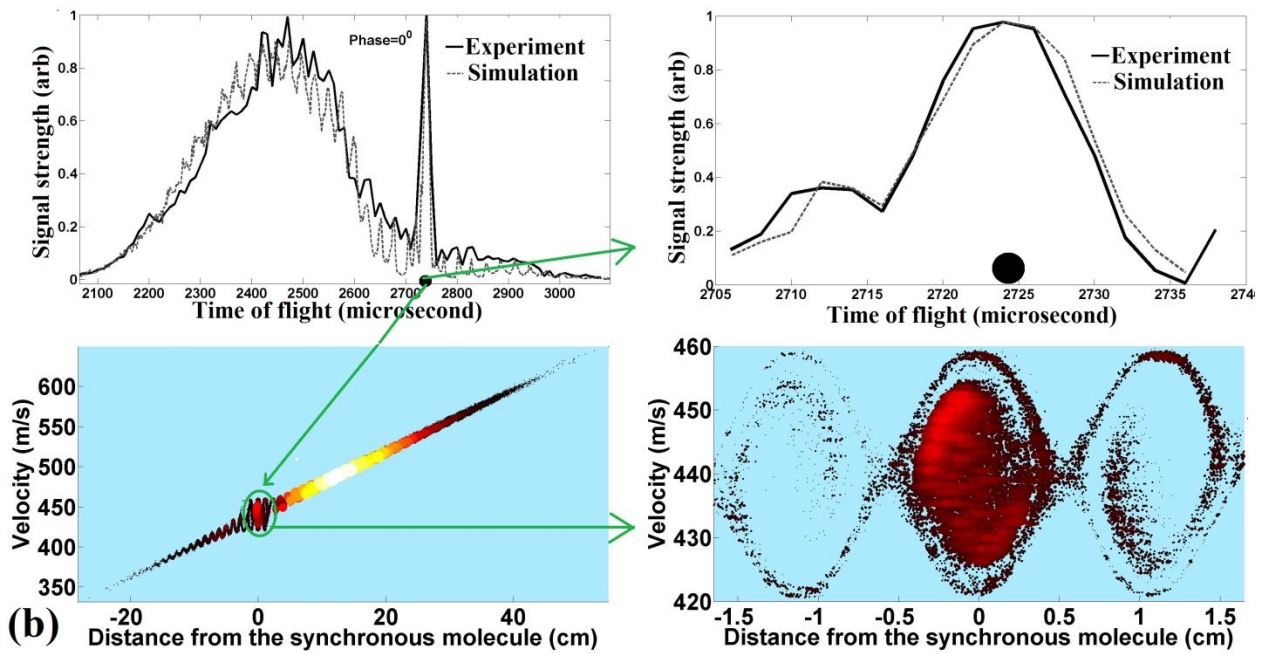
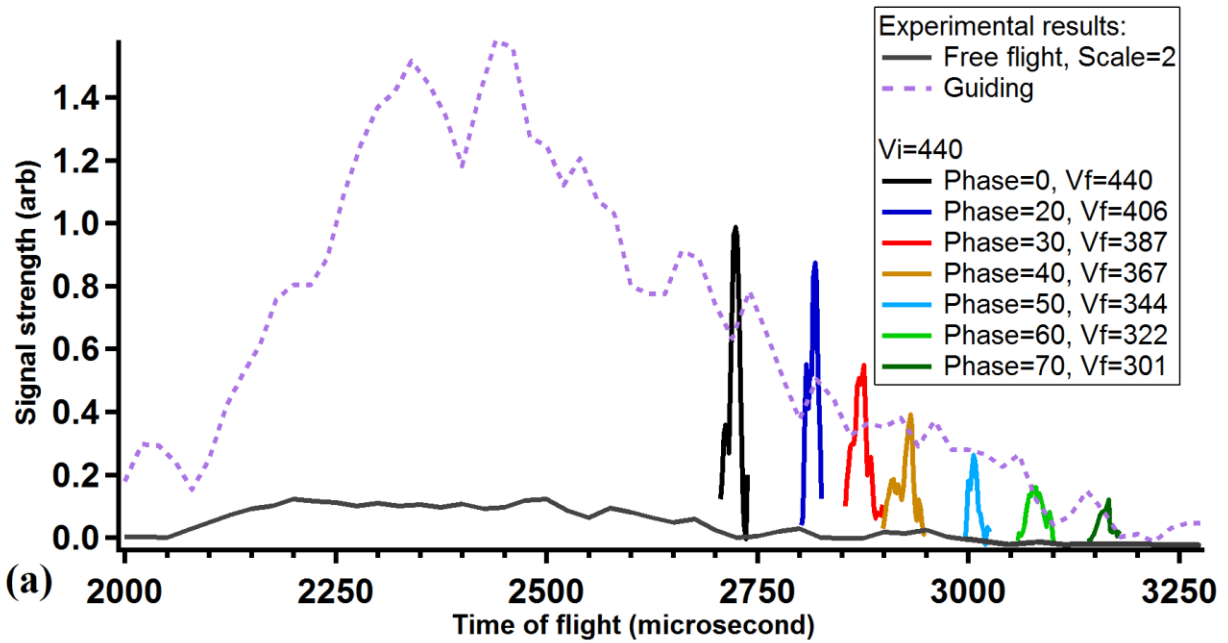
Velocity of the synchronous molecule: 440 *m/s*.

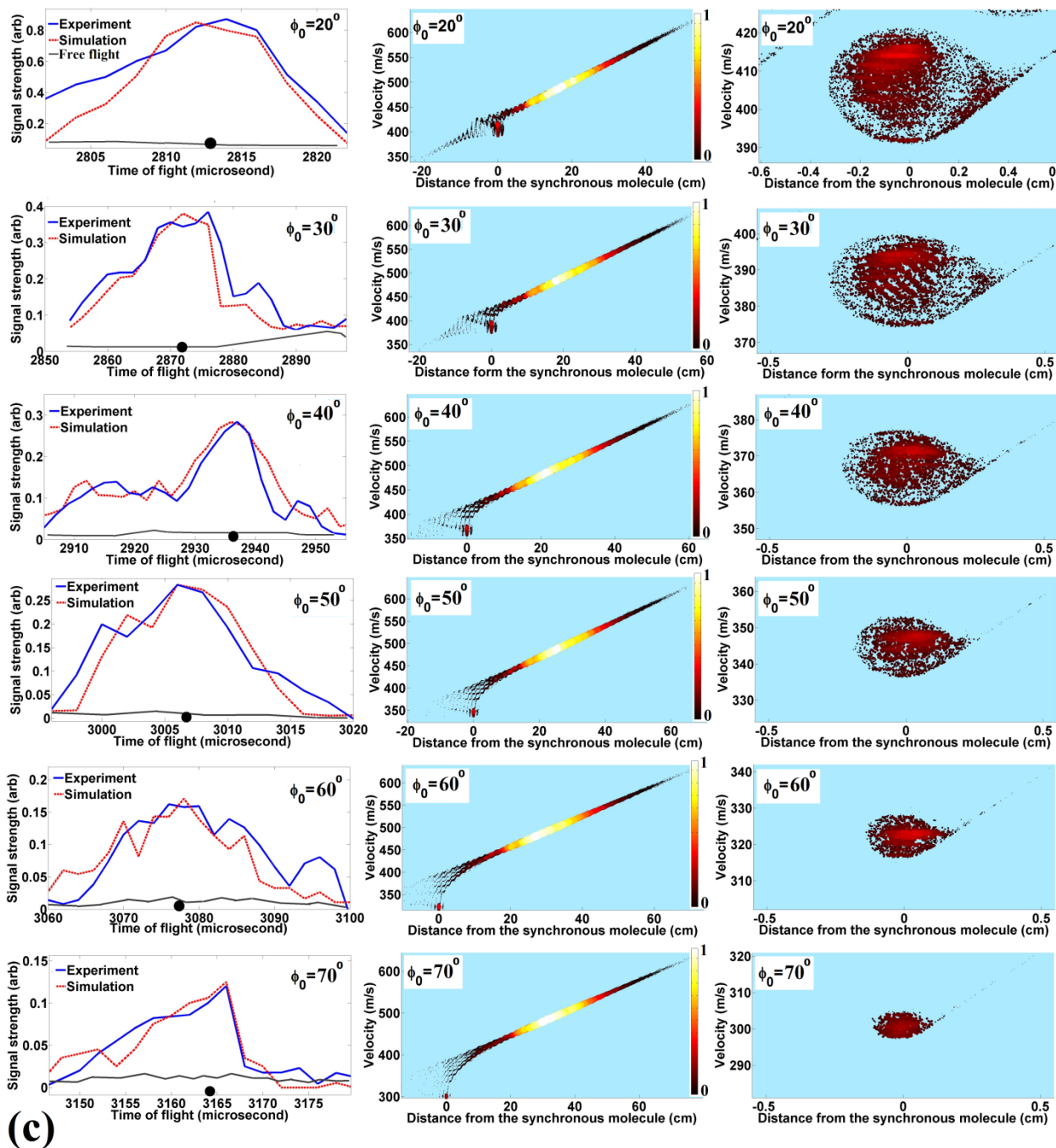
Phase of the synchronous molecule: from 0° to 20°

Deceleration down to: 415 *m/s*.

Figure (6-16) shows the deceleration results for this state.

The uncertainty for the signal intensity measurements at each data point was  $\sim \pm 15\%$ , that were obtained from the standard deviation of repeated measurements.





**(c)** **Figure 6-15:** Deceleration of *SD* radical. (a) Experimental results for the Stark deceleration of *SD* radical from  $440 \text{ m/s}$  down to  $301 \text{ m/s}$ , along with the free flight (black) and guiding mode (dashed) signals. (b) Right top: Simulation and experimental results for the full time of flight for phase= $0^\circ$ . Left top: the enlarged simulation and experimental results for the main packet with phase= $0^\circ$ . The black circle shows the expected arrival time for the synchronous molecule. Right bottom: the full phase-space distribution of the *SD* radicals that could reach to the detection point for phase= $0^\circ$ . Left bottom: the Phase-space distribution of the main packet for phase= $0^\circ$ . (c) Left panels: The simulation (red), experimental (blue), and free flight (black) for the time of flight of the main packet for different phases. Middle panel: the full phase-space diagram for each phase. Right panel: the phase-space distribution for the main packet for each phase.

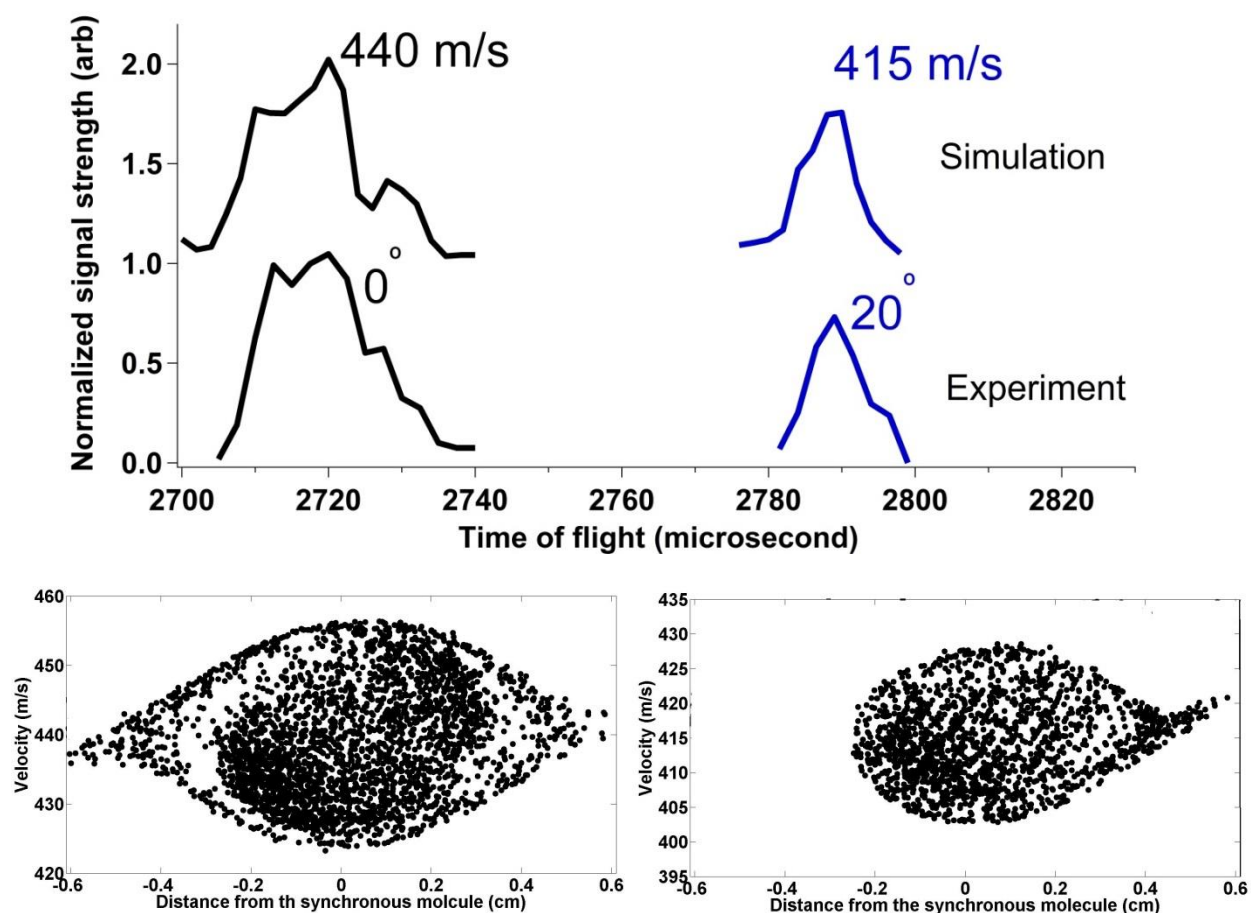


**Figure 6-16:** Top: Deceleration of SD radicals in  $|X^2\Pi_{3/2}, J = 5/2, M_J = -5/2\rangle$  state from  $440\text{ m/s}$  down to  $415\text{ m/s}$ . Bottom: Corresponding phase-space distribution for the decelerated packets.

### 6.2.6 State purity of the decelerated packets

The possibility of decelerating molecules in higher rotational states relies on the state selective behaviour of the Stark decelerator. This can provide an important tool for collision experiments and investigating the quantum mechanical aspects of molecular reactions. However when using a Stark decelerator as a state purifier, one has to carefully investigate the behaviour of the molecules in all of the energy states as they travel inside the decelerator. Fitch et al. have previously investigated the state purity of Stark decelerated ammonia molecules, in which they concluded that under their experimental circumstances the Stark decelerator was not able to state purify the decelerated ammonia packets [128]. This is true in most of the cases, but it is not a general rule.

In our case, SD radicals in  $|X^2\Pi_{3/2}, J = 5/2, M_J = -5/2\rangle$  and  $|X^2\Pi_{3/2}, J = 3/2, M_J = -3/2\rangle$  states have about  $0.3 \text{ cm}^{-1}$  Stark shift difference at the maximum possible electric field of our decelerator ( $126 \text{ kV/cm}$  on the molecular beam axis). For this experiment we focus on the behaviour of molecules in  $J = 3/2$  and  $J = 5/2$ , due to their abundance in our molecular beam. In our experiments the higher rotational states are not populated enough to be considered in this analysis. However, it is expected that higher rotational numbers have a shallower Stark potential depth due to their smaller Stark shift, which means that molecules in these states feel less confining potential. As a result it is expected that the results of comparison between molecules in  $J = 3/2$  and  $J = 5/2$  can be extended to higher rotational numbers. However a firm conclusion can only be made when one does the required analysis for all of the higher rotational states. Here we limit our discussion to  $J = 5/2$  and  $J = 3/2$  states.

Figure (6-17) shows the Stark potential energy of the SD radical versus its position between two parallel electrode pairs of our decelerator.

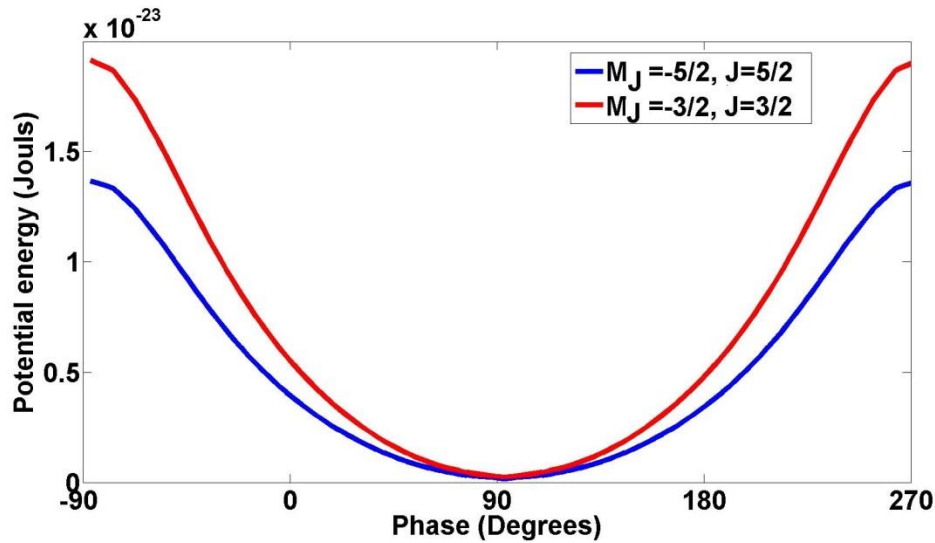


**Figure 6-17:** Stark potential energy for  $|X^2\Pi_{3/2}, J = 3/2, M_J = -3/2\rangle$  and  $|X^2\Pi_{3/2}, J = 5/2, M_J = -5/2\rangle$

For operational deceleration phases of less than  $50^\circ$  and with an initial velocity of  $440 \text{ m/s}$ , choosing the synchronous molecule to be from  $|X^2\Pi_{3/2}, J = 5/2, M_J = -5/2\rangle$  or  $|X^2\Pi_{3/2}, J = 3/2, M_J = -3/2\rangle$  states cannot purify the energy states of the decelerated packets for SD radicals under our experimental condition. The reason is that for these phases the molecular

packets of molecules in both states not only remain stable in phase-space, but also manage to end up with almost the same final velocity. Thus, a decelerated packet can contain molecules from both states. Figure (6-14) shows the frequency spectrum obtained from the decelerated packet, when the decelerator was operated at phase  $20^\circ$  with the synchronous molecule in  $|X^2\Pi_{3/2}, J = 3/2, M_J = -3/2\rangle$ . The frequency spectrum for the decelerated packet, when the decelerator was operated at phase  $20^\circ$  with the synchronous molecule in  $|X^2\Pi_{3/2}, J = 5/2, M_J = -5/2\rangle$  was similar to figure (6-14), which confirmed the presence of both states. Figure (6-18) compares the behaviour of the target molecules in both states, when the switching of the Stark electrodes is calculated for each of the above states. Each data point in figure (6-18) corresponds to the position and velocity of the target molecules in each energy state after each deceleration stage. The target molecules are assumed to have the same initial condition just before the deceleration, except their energy state. As shown in the graph, when the timing is calculated for a synchronous molecule in  $|X^2\Pi_{3/2}, J = 5/2, M_J = -5/2\rangle$ , the molecule in  $|X^2\Pi_{3/2}, J = 3/2, M_J = -3/2\rangle$  will oscillate around the synchronous molecule, and reaches to the a very close final velocity as the velocity of synchronous molecule. But when the timing is calculated for a synchronous molecule in  $|X^2\Pi_{3/2}, J = 3/2, M_J = -3/2\rangle$ , after a certain phase (in this case  $50^\circ$ ) the molecule in  $|X^2\Pi_{3/2}, J = 5/2, M_J = -5/2\rangle$  becomes unstable, that results in an unstable phase-space oscillation for the molecules in  $|X^2\Pi_{3/2}, J = 5/2, M_J = -5/2\rangle$ . Figure (6-18-e) demonstrates this situation for phase  $70^\circ$ . Therefore purifying the decelerated packet in a way that only molecules from  $|X^2\Pi_{3/2}, J = 3/2, M_J = -3/2\rangle$  are present requires to operate the decelerator with a timing calculated at high phases for a synchronous molecule in  $|X^2\Pi_{3/2}, J = 3/2, M_J = -3/2\rangle$ . A pure decelerated packet of molecules in  $|X^2\Pi_{3/2}, J = 5/2, M_J = -5/2\rangle$  state could be even more interesting for collision experiments. In order to get a pure decelerated packet for  $|X^2\Pi_{3/2}, J = 5/2, M_J = -5/2\rangle$ , it is required to terminate the switching at a time when the molecules in  $|X^2\Pi_{3/2}, J = 5/2, M_J = -5/2\rangle$  are still stable in phase-space. Figure (6-18-g) shows one of the possible schemes. In this scheme the decelerator was operated at phase  $10^\circ$  for the first 130 stages of deceleration, and then at  $70^\circ$  for the rest of the stages, which resulted in  $\sim 15$  m/s velocity difference for the molecules of the two packets. Figure (6-18-h) shows that if we calculate the timing for  $|X^2\Pi_{3/2}, J = 5/2, M_J = -5/2\rangle$  and use the same deceleration

scheme as figure (6-18-g), the final velocities of the two states remain close. The phase-space distributions for deceleration of an ensemble of molecules from both states with the scheme described in figures (6-18-g) and (6-18-h) are also shown in figure (6-18-bottom). The phase-space distribution clearly shows the separation of ensembles of molecules in each state from each other for the deceleration scheme of figure (6-18-g), while for the deceleration scheme of figure (6-18-h) they were mixed. To elaborate the situation for parts (g) and (h) in figure (6-18), the position of target molecules in  $J = 3/2$  and  $J = 5/2$  right before the switching are monitored in figure (6-19). One period of Stark potential corresponds to from 0 to 1.1 *cm* in length (from  $-90^\circ$  to  $270^\circ$  in figure (6-17)). As long as the position of the target molecules is within this range, their corresponding phase-space distribution remains stable. When the timing is set for  $J = 5/2, M_J = -5/2$ , the position of the target molecule in  $J = 3/2, M_J = -3/2$  deviates slowly toward the centre of the potential and returns to the position of the target molecule in  $J = 5/2$ , and its final velocity remains close to the velocity of the synchronous molecule. When the timing is calculated for  $J = 3/2, M_J = -3/2$ , the target molecule in  $J = 5/2, M_J = -5/2$  deviates slowly toward the edge of the potential well. For low phases (below  $50^\circ$ ) the potential depth for  $J = 5/2, M_J = -5/2$  is large enough to push the molecule back toward the position of the synchronous molecule (such as figure (6-18-a and c), but for larger phases the target molecule has enough energy to overcome the potential, and hence it cannot return back toward the position of the synchronous molecule and leaves the phase-stable area (such as figure (6-18-e)). This can be useful in purifying the energy state of the decelerated packet for  $J = 3/2$ , but it leaves no trace of  $J = 5/2$ . With the current experimental setup, in order to get well defined and separated decelerated packets for both of the energy states; it was required to only use the last stages of deceleration for separation, to minimize losing the molecules in  $J = 5/2$  due to instability of their phase-space. The number of stages for which the decelerator should operate in high phases depends on the initial velocity and the desired phase, final velocity, and separation. Operating the decelerator first in low phases can help in bunching the molecules in both states, especially in our case where the population of molecules in  $J = 5/2$  is low. Figure (6-20) shows the simulation and experimental result for the time of flight measurement of the SD radicals when using the scheme described in figure (6-18-g). The central velocity of the beam was 490 *m/s* and the initial velocity of the synchronous molecule was 440 *m/s*. Experimentally, the time of flights are monitored by using two different transitions,  $qQ_1P_{21}(1.5)$  for the red trace ( $J = 3/2$ ),

and  $qQ_1P_{21}(2.5)$  for the blue trace ( $J = 5/2$ ). The time of flight signals are normalized to the peak value for  $J = 3/2$  at  $\sim 2.79$  ms. The experimental time of flight for ( $J = 5/2$ ) is 10 times scaled up to be clearly seen. The initial number of molecules for the simulation was assumed to be the same, however under our experimental conditions we know that the population of the molecules in the  $J = 5/2$  state is much less than  $J = 3/2$ .

In order to check the state purity of the decelerated packets two separate frequency scans were recorded, once at the time of flight corresponding to the  $J = 5/2$  packet ( $\sim 2.76$  ms), and once at the time of flight corresponding to the  $J = 3/2$  ( $\sim 2.78$  ms). The results are shown in figure (6-21). The recorded signals are normalized to the peak value of the  $qQ_1P_{21}(1.5)$  transition in figure (2-21-a). The results show that for  $J = 3/2$  TOF peak there is no trace of  $J = 5/2$ , which means that the molecules arriving at this time are from  $J = 3/2$ , as it can be seen from figure (6-20-a). Figure (2-21-b) shows the frequency spectrum recorded for  $J = 5/2$  packet. The result shows a significant enhancement for  $qQ_1P_{21}(2.5)$  transition which indicates the presence of molecules in  $J = 5/2$ . However there is a small trace of  $qQ_1P_{21}(1.5)$  in the spectrum that indicates there are still some molecules from  $J = 3/2$  at this time. When comparing this spectrum with part (a), we realize that its magnitude is less than 5 % of the magnitude of the same transition in part (a). Also when comparing the magnitude of  $qQ_1P_{21}(1.5)$  transition with  $qQ_1P_{21}(2.5)$  in part (b), we can see that  $qQ_1P_{21}(1.5)$  is much smaller in magnitude.

The presented scheme was the first attempt to prove the possibility of separating decelerated SD radicals in  $J = 3/2$  and  $J = 5/2$ . The next step in this experiment would be to optimize the electrode switching timing sequences and improve the experimental condition, in order to get separated decelerated packets at desired final velocities or time of flights.

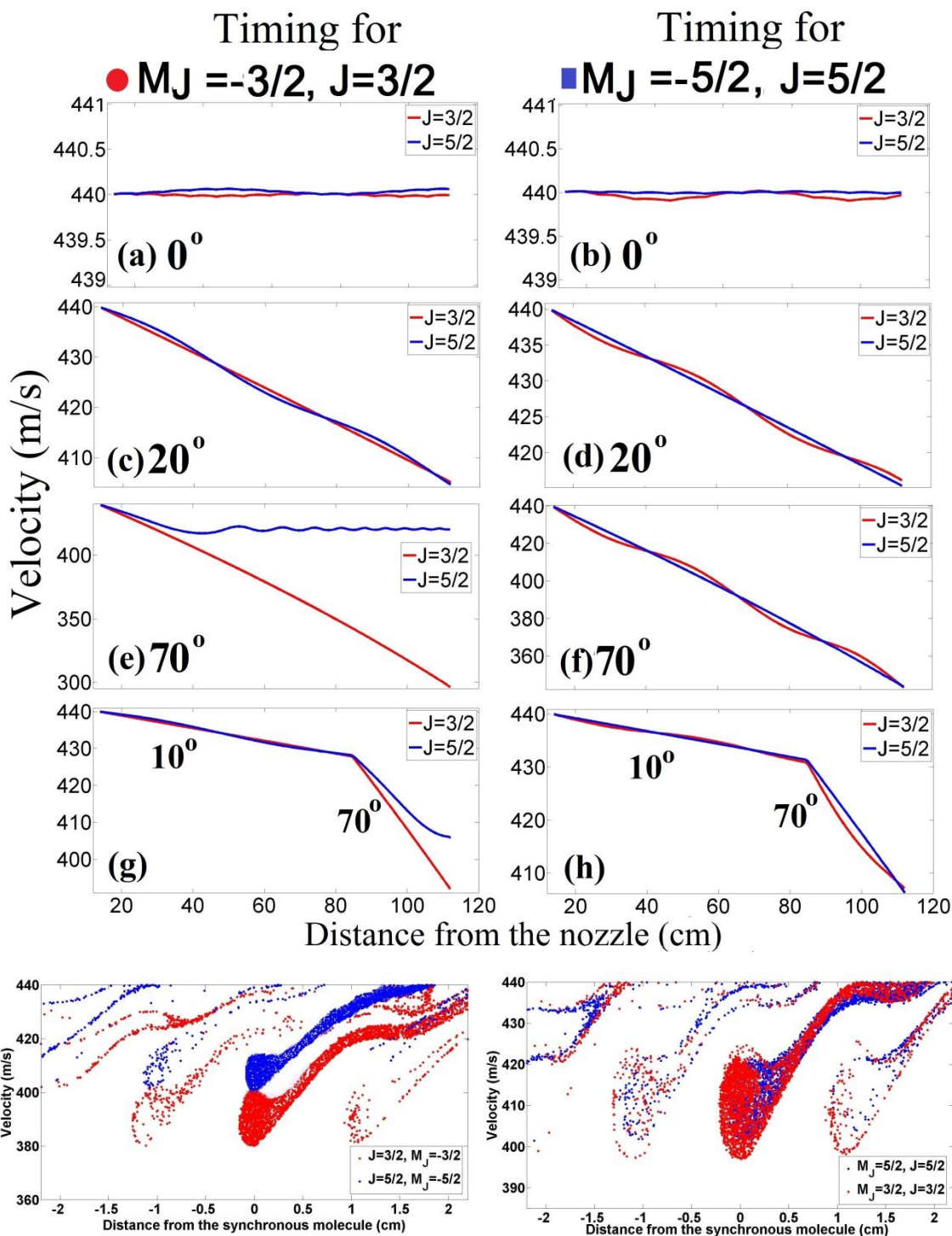


**Figure 6-18:** Top: The behaviour of target molecules in  $|X^2\Pi_{3/2}, J = 3/2, M_J = -3/2\rangle$  and  $|X^2\Pi_{3/2}, J = 5/2, M_J = -5/2\rangle$  states. Left: when timing calculated for  $|X^2\Pi_{3/2}, J = 3/2, M_J = -3/2\rangle$ , Right: When timing is calculated for  $|X^2\Pi_{3/2}, J = 5/2, M_J = -5/2\rangle$ . Bottom: Phase-space distribution for parts (g) and (h), right after the decelerator.

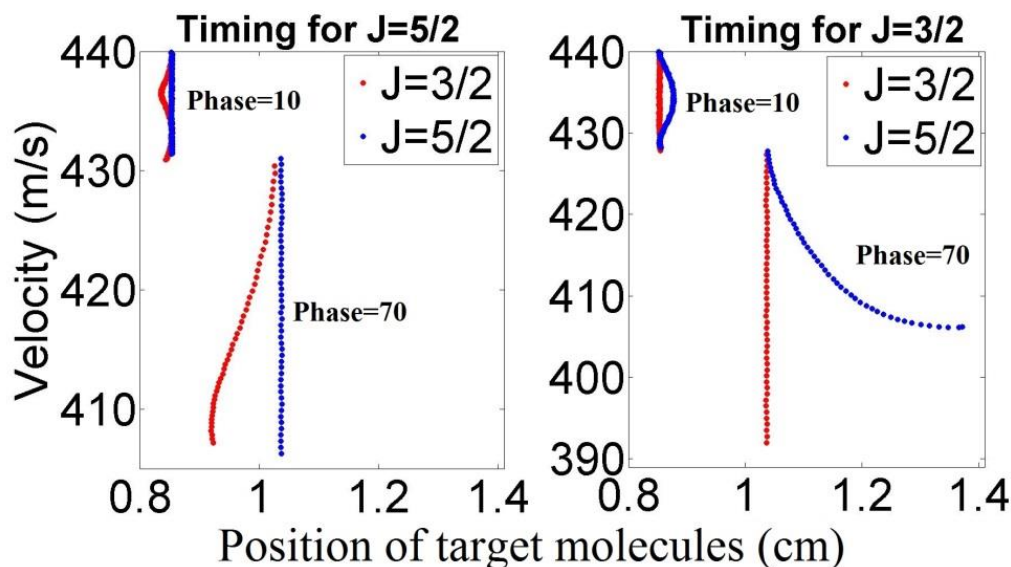


**Figure 6-19:** Position of target molecules in  $|X^2\Pi_{3/2}, J = 3/2, M_J = -3/2\rangle$  and in  $|X^2\Pi_{3/2}, J = 5/2, M_J = -5/2\rangle$  with respect to the Stark potential period ( $0 - 1.1 \text{ cm}$ ) when the first 130 stages are operated with phase= $10^\circ$ , and the next 50 stages with phase= $70^\circ$ .

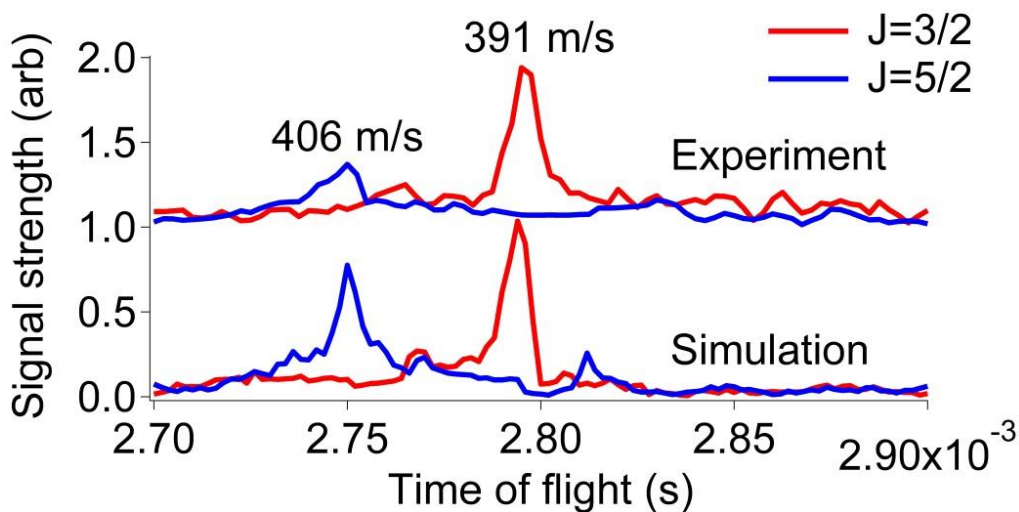


**Figure 6-20:** Simulation and experimental results for the time of flight of the separated SD radicals in  $|X^2\Pi_{3/2}, J = 3/2, M_J = -3/2\rangle$  and in  $|X^2\Pi_{3/2}, J = 5/2, M_J = -5/2\rangle$  energy states, when the first 130 stages are operated with phase= $10^\circ$ , and the next 50 stages with phase= $70^\circ$ . The uncertainty for the signal intensity measurements at each data point was  $\sim \pm 10\%$  for  $J = 3/2$ , and  $\sim \pm 15\%$  for  $J = 5/2$ , that were obtained from the standard deviation of repeated measurements.

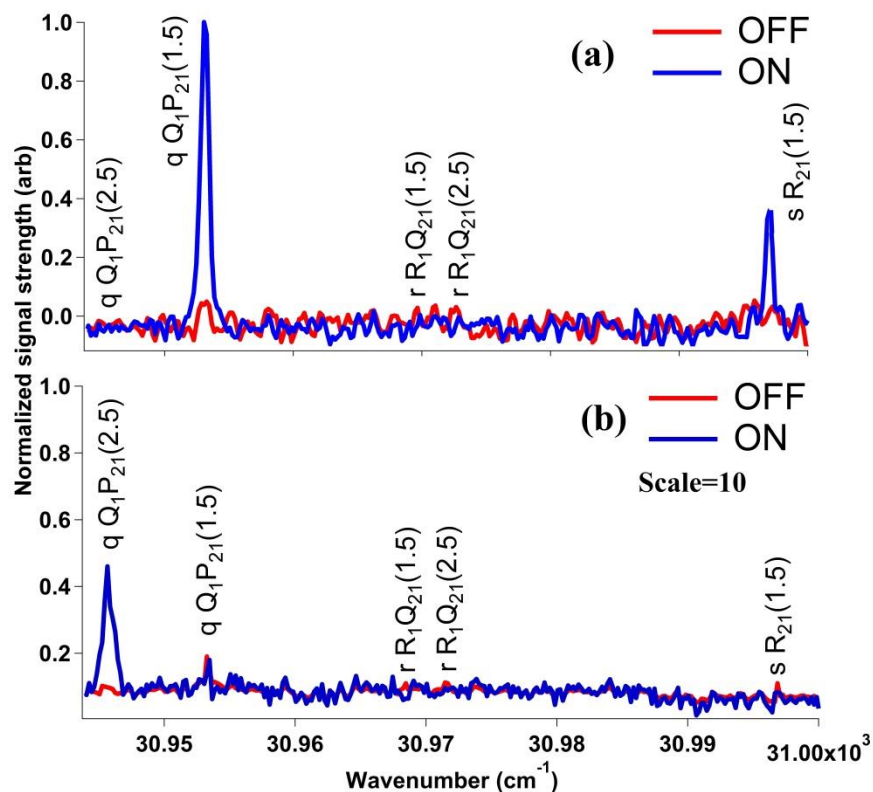


**Figure 6-21:** Frequency spectrum for the separated decelerated packets; (a) for the decelerated molecules corresponding to  $J = 3/2$  at  $t = 2.78 \text{ ms}$  (b) for the decelerated molecules corresponding to  $J = 5/2$  at  $t = 2.76 \text{ ms}$ . The uncertainty of the wavenumber was  $\pm 0.1 \text{ cm}^{-1}$ , which is obtained by the dye laser's minimum possible step size. The uncertainty for the signal intensity measurements at each data point was  $\sim \pm 10 \%$  for  $J = 3/2$ , and  $\sim \pm 15 \%$  for  $J = 5/2$ , that were obtained from the standard deviation of repeated measurements

### 6.2.7 CELIF detection

While writing this thesis, CELIF measurements of the Stark decelerated molecular packet are still in progress. The results are expected to be obtained in a few months. At the moment the challenge is improving the signal-to-noise ratio at the detection chamber after the decelerator. The problem is due to the low density of the molecules at the detection point which limits the CELIF measurements to the photon counting regime. The LabView code and the cavity characterizations are already prepared, but since the single photons emitted from the sample after excitation are very narrow in width, it is challenging to detect them with the current scope card available on the computer. The resolution of the scope needed to measure the CELIF narrow peaks depends on the PMT signal characteristic. The scope card in use is Alazar ATS9350 (12 bit, 500 MS/s, 250 MHz full power bandwidth, rise time 1.4 ns). The measured photon signal rise time is a quadrature combination of the rise time of the PMT (0.57 ns) and the scope, which

gives  $\sim 1.51$  ns. According to the data sheet available for our PMT, the FWHM for each single photon is 2.5 times of the rise time of the PMT, which gives  $\sim 3.78$  ns. Since the maximum sampling rate of the scope card is  $500$  MS/s, it is possible that at least one digitization point falls within the FWHM of the photon signal. It is also possible that two photons arrive so close in time that their signals merge above the photon counting threshold and get counted as one photon instead of two. Hence careful attention must be paid to the incident laser power to keep the fluorescence rate low enough to avoid this undercounting of photons. This means a very good signal to noise ratio should be available for the detection that can work at such low powers. While writing this thesis finding a proper way to improve, amplify and broaden the CELIF photon signal is in progress.

In order to characterize the CELIF setup a set of measurements were done in the test chamber with the cavity mirrors assembly. Since these test measurements were done at a distance close to the nozzle, the number of molecules was high enough not to be worried about photon counting issues. The cavity ring down behaviour and the frequency spectrum were recorded. Before presenting the experimental results the method of data acquisition should be explained. For the CELIF measurements depending on the number density of the molecules within the detection area two different methods could be implemented to record the signal. If the number density is low, getting a continuous fluorescence from the molecules within the cavity ring down time is not possible, hence a photon counting scheme should be used. When the density of the sample is high enough to get a continuous LIF decay signal, then a scheme similar to what was explained in section (6-2-1) for an ordinary LIF measurement should be implemented. In both schemes in a CELIF measurement the integrated LIF signal has to be normalized to the integrated ring down signal for each single laser shot. For the photon counting scheme this means normalizing the number of detected photons to the integrated ring down signal for each laser shot. In the photon counting scheme a LabView code uses a set threshold to distinguish the signal from the noise. This means that if two or more photons arrive close to each other in time and merge they will count as one. Figure (6-22) shows the experimental results for one shot for each of the two possible CELIF schemes, along with the experimental cavity ring down measurement for the  $TEM_{00}$  mode of the cavity.

It is important to measure the cavity ring down at the beginning of each measurement to make sure that the cavity mirrors are aligned correctly. The ring down shape would have been different

than what is shown if some other mode or a combination of other modes were on resonance for cavity. The theoretical ring down time constant for the cavity can be calculated by:

$$\tau = \frac{L}{C \ln(r)} \quad (6.1)$$

Where  $C$  is the speed of light in vacuum,  $L$  is the length of cavity, and  $r$  is the mirror reflectivity. For our cavity the calculated cavity ring down time was  $\tau = 1.499 \times 10^{-6}$  s. As shown in figure (6-22), this value was in agreement with the experimental measurement. The experimental ring down signal shown in figure (6-22-(a)) was collected by a photodiode (Thorlabs PDA36A) which was mounted behind the back mirror of the cavity. The ring down signal became weak after  $\sim 7 \mu\text{s}$ . In addition the signal close to the time zero could contain some scattered light. The signal integration gates were set between these two limits. The integration had to be done for each single laser shot. For each time of flight or frequency measurement an average of several shots per point was calculated by the LabView code. A frequency spectrum that was obtained by CELIF method is shown in figure (6-23). The measurement was done in the test chamber, and the scheme used for the integration was the scheme mentioned in figure (6-22-(b)).

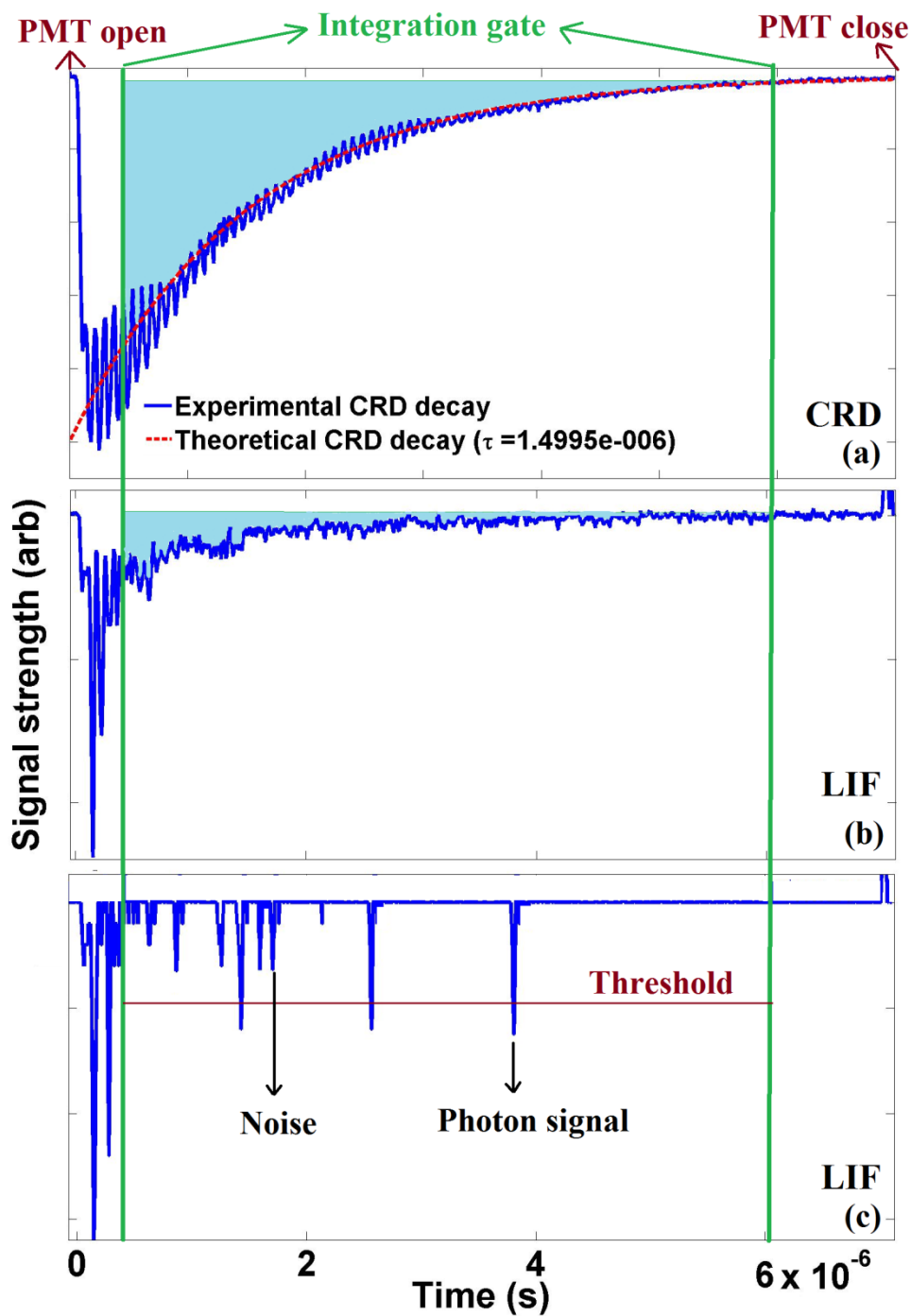


**Figure 6-22:** Signal recording scheme for CELIF detection method. (a): The experimental cavity ring-down signal. (b): The PMT signal obtained experimentally for the Fluorescence of *SD* radicals by CELIF method, when the gain and density were high at the test chamber. (c): The same as (b), but with lower concentration and gain. Therefore photon counting scheme was employed. Note that the gate for recording the signal was chosen in a way that includes less noise and stray light.

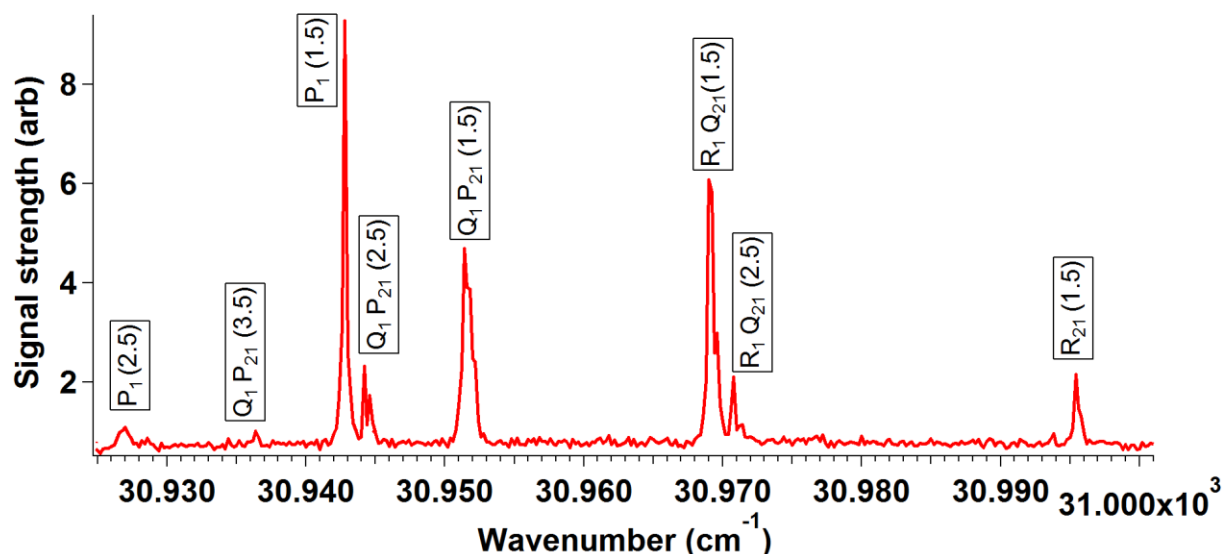


**Figure 6-23:** Frequency spectrum obtained by CELIF method for *SD* radicals at the test chamber. Note the higher resolution in this spectrum compared to the LIF measurement (figure 6-13). The peaks in this figure are narrower than the LIF measurement due to having less power broadening. The laser power just before hitting the cavity mirror for the first time was  $300 \pm 50 \mu\text{J}/\text{pulse}$ . The uncertainty of the wavenumber was  $\pm 0.1 \text{ cm}^{-1}$ , which is obtained by the dye laser's minimum possible step size.

There are two significant points to mention about the frequency spectrum above. First, although the laser intensity inside the cavity is much less than an ordinary LIF measurement, the signal to noise ratio of both methods is about the same. This happens due to the long integration time for the CELIF measurement in which the laser light reflects back and forth for several times between the two cavity mirrors, and each time excites a number of molecules. On the other hand in a LIF measurement the signal is recorded when the laser light hits the molecules only once, but with a higher intensity and larger diameter than CELIF. Second, the frequency spectrum has a better resolution in the CELIF measurement compared to the LIF measurement. This is mainly due to the fact that CELIF method uses much lower laser power than LIF, therefore the power broadening of the transitions is lower in CELIF method. As a result in CELIF it is possible to distinguish the transitions from the upper and lower  $\Lambda$ -doublets for each  $J''$ .

### 6.2.8 The first CELIF detection of *SD* radicals after the decelerator

In this section the result for the first successful detection of *SD* radicals with CELIF method is presented. The scheme used for detection was the same as figure (6-22-c). Due to the technical difficulties that were mentioned in section (6.2.7), although we could get a correct time of flight measurement, the obtained signal is not yet fully applicable for a precise absolute density

measurement. Particularly a better signal to noise ratio is required to measure the Rayleigh scattering of laser light from nitrogen molecules. Therefore there is still more work to do to improve the condition for our experiment. However as the first step toward implementing the CELIF method for density measurement, being able to see the time of flight for the molecular packet after the decelerator is very promising.

In figure (6-24) the time of flight was recorded for operating the decelerator with  $\varphi_0 = 0^\circ$  for SD radicals in  $|X^2\Pi_{3/2}, J = 3/2, M_J = -3/2\rangle$ . The frequency scan for a frequency range close to the  $Q_1P_{21}(1.5)$  transition of SD radicals is also shown in figure (6-24). The signal for each data point was averaged over 2000 shots to improve the signal to noise ratio. The initial and final velocity of the synchronous molecule were  $440\text{ m/s}$ , and the beam condition was the same as the LIF measurements. For a better comparison the same measurement was done with the decelerator being off.

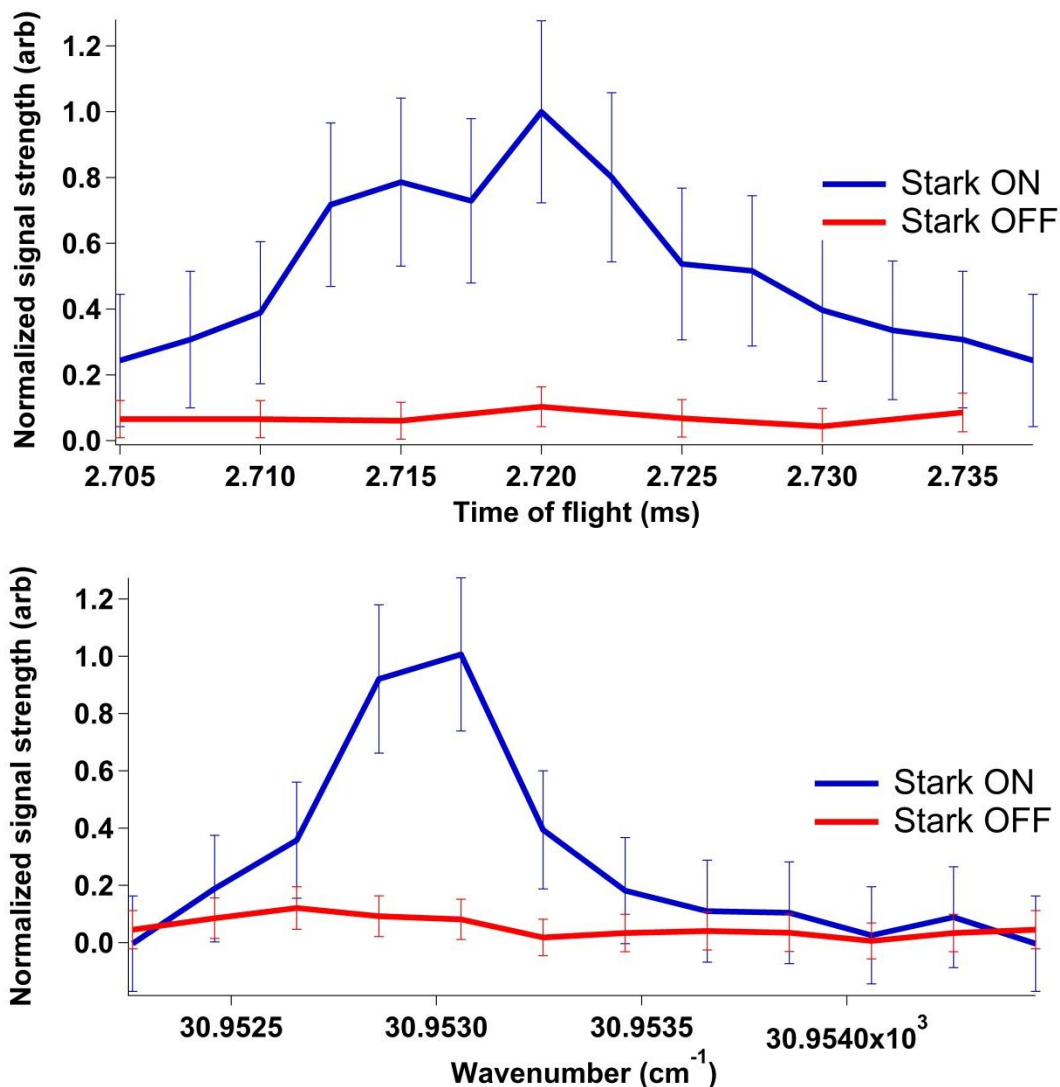


**Figure 6-24:** Time of flight (top) and frequency scan (bottom) for molecules in  $|X^2\Pi_{3/2}, J = 3/2, M_J = -3/2\rangle$  state after the decelerator and with the decelerator operating at  $\varphi_0 = 0^\circ$ , recorded by CELIF detection method. The laser power just before hitting the cavity mirror for the first time was  $300 \mu\text{J}/\text{pulse}$ . The uncertainty at each point is  $\pm\sigma$  (standard deviation from the mean value). The uncertainty of the wavenumber was  $\pm 0.1 \text{ cm}^{-1}$ , which is obtained by the dye laser's minimum possible step size.

### 6.2.9 Future work on CELIF

The detection of the Stark decelerated packet with the CELIF method is still in progress. Generally as soon as a good signal to noise ratio for the photon counting measurements at the detection point after the decelerator is found, two sets of measurement are needed to complete the absolute density measurement of the Stark decelerated packet. First, is to measure the CELIF signal while the *SD* molecules are present at the detection point and the system is under vacuum, and second, is to use the CELIF method to detect the Rayleigh scattering of the laser light from

the Nitrogen molecules at different pressures inside the detection chamber (while keeping all the other experimental factors the same as the *SD* CELIF measurement). Then using the method described in section (3-3) we can obtain the absolute density of the molecules in a Stark decelerated packet.

### **6.3 Experimental results for superconducting microwave cavity**

The theory and application of superconducting microwave cavities in the cold molecule studies was mentioned in section (4-4). In this section the setup used to characterize our prototype superconducting microwave cavity is described. A longer version of our prototype cavity was later designed and made for the purpose of deceleration and focusing experiments, which is now in use in our lab.

The rotational transitions,  $\Lambda$ -doublet transitions of  $\Pi$  electronic states, and low frequency vibrational transitions of most simple molecules fall between 1 – 100 GHz ( $\lambda \sim 0.003 - 0.3$  m). This range of wavelength is comparable with the size of the pulsed molecular beams. A microwave cavity provides an enhanced standing wave. Our prototype MW cavity was designed in a cylindrical shape with two small holes at the centre of its two end caps to allow the molecular beam to fly through it. In order to maintain a high quality factor, it was required that the diameter of the holes be much smaller than the microwave wavelength. Figure (6-24) shows the design for our prototype superconducting MW cavity.

The cylindrical cavity consists of a copper main body and two copper end caps. The inner surface of the copper cavity was electrochemically plated with an alloy of lead and tin (Pb/Sn). Copper was used for the body of the cavity because of its good thermal conductivity. The plating of the copper was preferred over using a common superconductor such as Niobium. The reason was that although a high quality factor was needed to increase the potential depth of the cavity, too high a quality factor could increase the response time of the cavity to a value that was not suitable for the fast switching of the field.

The plating process was done under the supervision and with the help of Professor Walter Hardy at UBC. Details of the plating procedure are presented in appendix II. The critical temperature for the Pb/Sn alloy is  $T_c = \sim 7$  K [129]. A cryostat was used to cool the cavity. The main container of the cryostat was filled with liquid helium and was connected to the cavity via a

copper plate. The outer layer of the cryostat was filled with liquid nitrogen to shield the main part from outside. After pumping on the liquid helium a temperature of  $2.7\text{ K}$  was obtained which was kept during the experiments. Short microwave pulses of  $1\text{ ms} - 100\text{ ms}$  were applied to the cavity in order to reduce the thermal load on the cavity when using high microwave powers. The temperature of the cavity increased by  $0.2\text{ K}$  when a  $100\text{ ms}$  pulse with  $5\text{ W}$  power was applied.

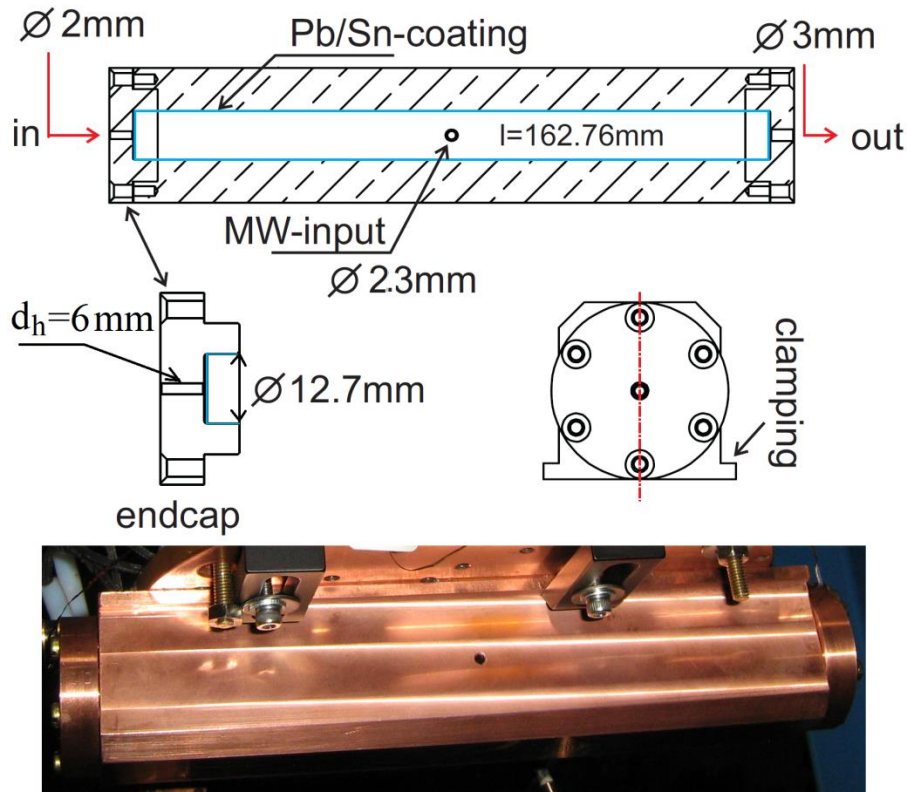


**Figure 6-25:** Top: The design and dimensions for prototype superconducting microwave cavity. Bottom: The outside view of the actual cavity.

Two custom made loop antennas with a diameter of  $\sim 1.5\text{ mm}$  were inserted through the side holes of the cavity, one responsible for magnetically coupling microwave power into the cavity, and one responsible for monitoring the microwave magnetic fields inside the cavity. The monitoring antenna was weakly coupled to the cavity to prevent lowering the quality factor. The tip of a coaxial cable (Coax, SC-219/50-SCN-CN,  $2.2\text{ mm}$  diameter, silver plated cupro-nickel) was bent to form a loop. These antennas had low transmission loss and low thermal conductivity, and were connected to the helium bath to prevent them heating up. The insertion length of the

antennas to the cavity was controlled by a translational stage from outside the cryostat. The ability to adjust the insertion length of the antenna into the cavity from outside the cryostat was important in order to be able to compensate for the length contractions of the antennas at low temperatures. Optimizing the insertion length was obtained by minimizing the reflected power from the cavity, which could be monitored simultaneously by the increase in the transmission signal that was picked up by the monitoring antenna. To improve temperature stability, the body of the cavity and all the elements connected to the cavity were also in thermal contact with the Helium bath through clamps and copper made meshes. A temperature sensor attached to the body of the cavity was used to monitor the temperature of the cavity.

The end-caps each had a hole in the middle to let the molecular beam pass through the cavity. Since the presence of the holes in the cavity reduces the quality factor small diameter holes were preferred. The diameter had to be large enough to let the arriving molecular beam pass through it. In this design we assumed a molecular beam with  $2\text{ mm}$  width. The exit diameter was  $3\text{ mm}$  to make sure that even molecules with transverse divergence from the beam axis can reach to the detection point. The location of the seam between the end-cap and the main body of the cavity was  $6.6\text{ mm}$  away from each end of the cavity to minimize the longitudinal surface current at the seam line for  $TE_{11p}$  mode with  $p = 13$  at about  $18.4\text{ GHz}$ .

The loaded quality factor of the cavity ( $Q_L$ ) was measured with two different methods, first by measuring the resonance line width of a frequency scan around the resonance, and second by measuring the transient signal for a microwave pulse, as was explained in the section (4-4). The setup for these measurements is shown in figure (6-25).

The microwave generator was *Anritsu MG3693C*, the isolator was *ATI 18 GHz – 26.5 GHz*, the power amplifier was a solid-state *Cernex CNP 18183040 – 01 (18 GHz – 18.5 GHz)*, the circulator was a *10W ATC 18 GHz – 26.5 GHz*, the detector was *AT 8473C*, and the attenuator was *MIDISCO 52335 MDC8165 – 30*.

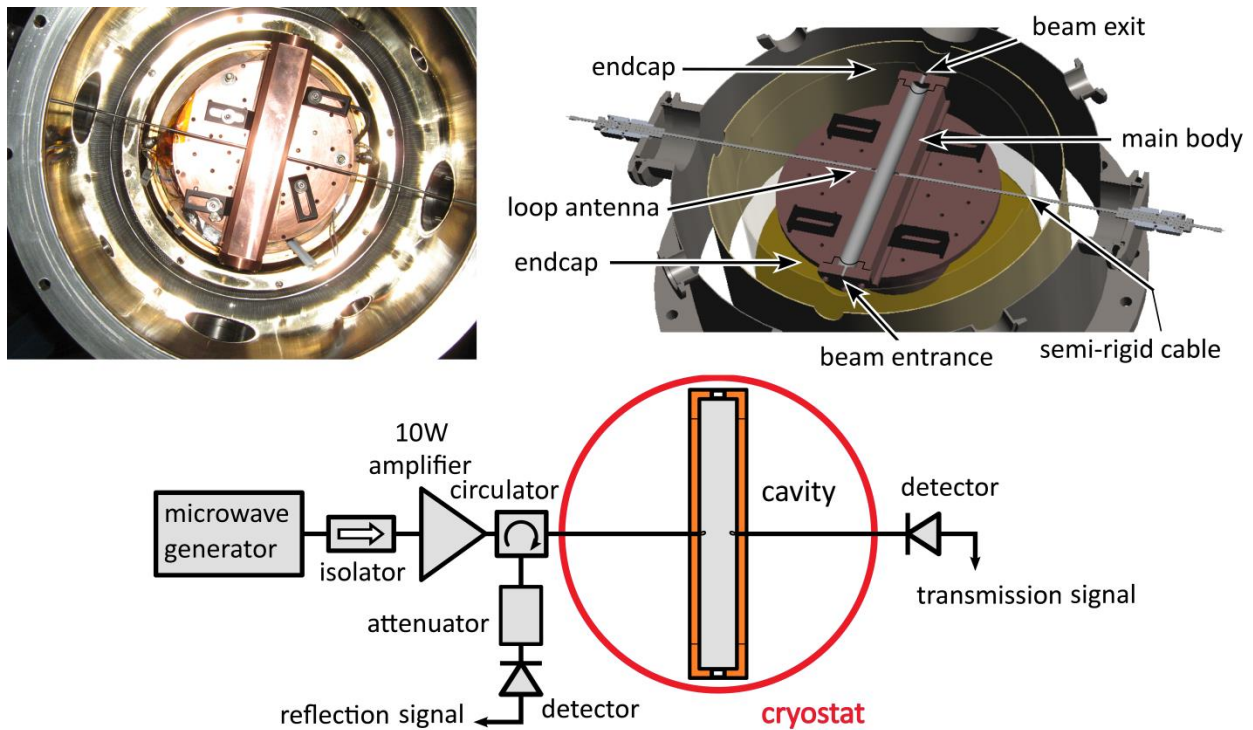


**Figure 6-26:** Top right: Schematic view of the characterizing experiment for the prototype superconducting cavity. Top Left: The actual experimental view. Bottom: The signal delivery and signal collection design.

The microwaves generated by the microwave generator passed through an isolator which blocked any reflection to the power supply. The amplified microwaves ( $\sim 10\text{ W}$ ) passed through a circulator, which separated the input to the antenna from the reflected wave from the cavity. The power of the microwaves delivered to the cavity was dropped to  $5\text{ W}$  due to the loss in the semi-rigid cable in use between the antenna and the circulator. The reflected power from the cavity to the circulator was  $2\text{ W}$  at non-resonant frequencies, which was first attenuated and then monitored by a diode detector (Agilent, 8473C). The transmitted signal after passing through a DC amplifier was monitored by the same detector model on the other side of the cavity. The transmitted and reflected signals were simultaneously recorded.

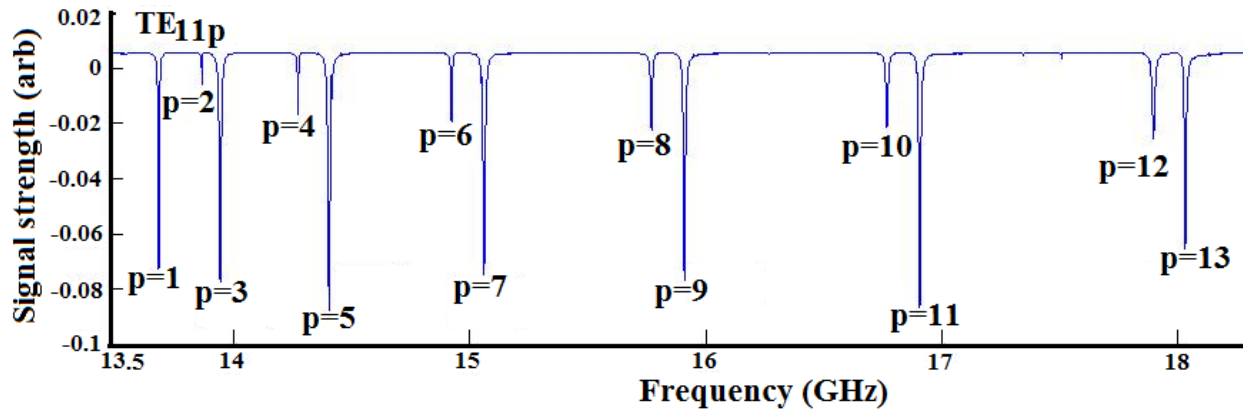


**Figure 6-27:** Resonance frequencies between **13.5 GHz** to **18 GHz** for  $TE_{11p}$  modes of the cavity at room temperature. Note that the peaks for the even- $p$  numbers are shorter than the odd- $p$  numbers. The reason is mainly due to the presence of the antenna at the location of an anti-node at the centre of the cavity for  $p$ -even numbers. However one can minimize this effect by adjusting the insertion of the antenna to the cavity. Also note that the resonances from the other modes are not present in this range.

In the frequency domain and for the line-width measurement, CW microwaves with 20 mW power were applied to produce a  $TM_{010}$  mode in the cavity. The measured resonance frequency at the critical coupling was 17994.7 MHz with a line width of 32 kHz, from which the loaded quality factor was calculated  $Q_L = 5 \times 10^5$ . Critical coupling refers to the condition in which the reflected power is negligible ( $\sim 0$ ). The reflected power could be optimized by adjusting the insertion length of the input coupler. From this quality factor the unloaded quality factor was calculated to be  $Q_0 = 1 \times 10^6$ . The same procedure was performed to measure the quality factor at 77 K, which yielded  $Q_L = 3 \times 10^3$ . Figure (6-27) shows the signals measured for the measurement at 2.7 K in which the Pb/Sn coating is superconducting.

In the time domain microwave pulses with 5 W power were applied to the cavity. The transient signals from the decay of the standing wave for the  $TM_{010}$  mode and pulse durations of 1 ms, 10 ms and 100 ms were monitored. The decay constants obtained from these measurements were 4.5  $\mu s$ , 3.9  $\mu s$ , and 3.1  $\mu s$  respectively. Using  $Q_L = 2\pi\nu_p\tau$  the loaded quality factor was calculated as  $\sim 5 \times 10^5$ , which was consistent with the frequency domain measurement. This measurement showed that the quality factor could be maintained for 100 ms pulses of 5 W microwaves, which was promising for the deceleration and trapping experiments. The experiment was then repeated with a supersonic molecular beam present (mixture of  $CH_3CN$  in  $N_2$ ) for  $10^4$  beam pulses to check its impact on the quality factor of the cavity. The result showed no change in the quality factor. Also no discharge due to the intense microwave field

inside the cavity was observed. Figure (6-29) shows the decay of the reflected and transmitted transient signals that were explained above.

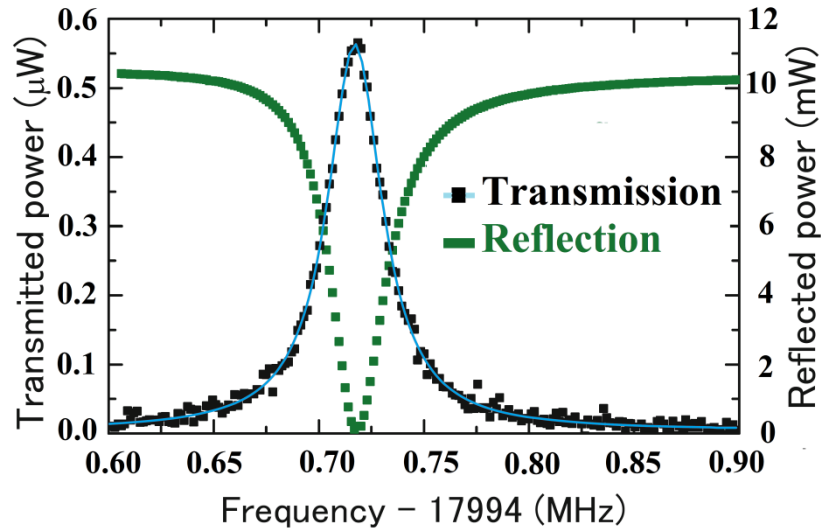


**Figure 6-28:** The transmission and reflection signal recorded for the prototype superconducting MW cavity at critical coupling.

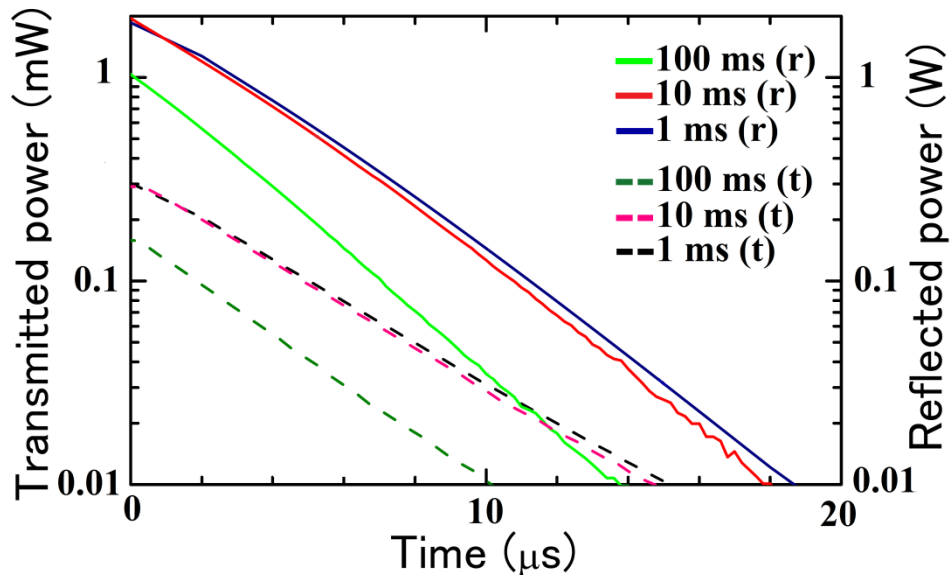


**Figure 6-29:** The power decay signal recorded for prototype superconducting MW cavity. The filled lines refer to reflected signals, while the dashed lines refer to the transmitted signal. Signal for **100 ms** long MW pulse (Green), Signal for **10 ms** long MW pulse (Red), signal for **1 ms** long MW pulse (Blue).

Power loss in the cavity can occur for several reasons, such as Ohmic loss ( $P_r$ ) and diffraction loss ( $P_d$ ). By assuming that  $R_{res}$  is negligibly small (typically  $\sim 0.1 \mu\Omega$  for a clean surface), and by using the equations (4-17) and (4-18) mentioned in section (4-3-2), the surface resistance of pure lead was estimated to be  $R_s = 23 \mu\Omega$  at 2.7 K, at 18 GHz. For  $TE_{11p}$  and  $TM_{010}$  modes the

corresponding quality factor was estimated to be  $Q_r = 2 \times 10^7$ . Since the diffraction loss due to the two end holes was negligible ( $Q_d > 10^{10}$ ), the maximum expected unloaded quality factor of the cavity at 2.7 K was estimated to be  $Q_0 \sim 2 \times 10^7$ , which was about ten times more than the experimental value ( $\sim 10^6$ ). The reason for this difference could be because of having a higher residual resistance ( $R_{res}$ ) for the Pb/Sn than the one we assumed for the pure Pb. Also in the estimation above we did not consider the contact resistances among the different parts of the cavity and antennas.

Theoretically it is possible to improve the quality factor of the cavity, if required, by lowering the temperature. For example the quality factor can improve 40 times if the temperature is lowered to 1.5 K.

The stored energy for the 100 ms pulse (5 W) measurement was less than the other two measurements (Figure (2-28)). The temperature of the cavity was increased by 0.2 K for this measurement, which resulted in a 20 kHz shift in the resonance frequency. The thermal expansion coefficient of copper is negligibly small ( $\sim 10^{-9} K^{-1}$  at 2.7 K), therefore expansion of the cavity could not be the reason for the frequency shift. The thermal expansion can affect the antenna and change the insertion length of the antenna into the cavity. The shift to lower resonance frequency for longer antenna insertion lengths was confirmed by manually adjusting the position of antenna. Also the London penetration depth of the Pb/Sn coating of the cavity could be different at a higher temperature, which could have contributed to the frequency shift. The measured resonance frequency shift for the 10 ms pulse was  $\sim 5$  kHz while for the 1 ms pulse it was negligible. Fortunately for the deceleration experiments the accumulated duration of the microwave pulse train is expected to be  $\sim 10$  ms, for which heating is not problematic. However for the trapping experiments the power loss should be compensated by gradually shifting the microwave frequency to the lower frequencies in a manner that it follows the frequency drift.

In order to decelerate the molecular samples, depending on their Stark shift, kinetic energy, and mass, different numbers of deceleration stages are needed. For example, by using a longer version of our prototype cavity (designed for  $TE_{11p=80}$ ) and for an input power of 5 W at 18.3 GHz, the maximum electric field inside the cavity would be  $E_0/2 \sim 11$  kV/cm. This

means that ideally for acetonitrile with a transition dipole moment of  $\mu_{eg} = 2.26 D$  a translational energy of  $\sim 25 K$  can be extracted from the molecule. If we consider the finite phase-space volume of the molecular packet and the time delay required to switch the microwaves, then acetonitrile molecules with a kinetic energy of up to  $\sim 20 K$  ( $90 m/s$ ) can be stopped.

The switching delay has to be taken into account for deceleration purposes since the standing wave has to be switched on and off much faster than the flight time of a molecule per each potential. This means that the rise and fall times of the standing wave have to be much shorter than one period of the standing wave. The flight time of the molecular beam per potential can be obtained from  $\lambda_{guide}/2v_x$  where  $\lambda_{guide} = 1/\sqrt{(\nu/c)^2 - (x'_{11}/2\pi a)^2}$  is the guide wavelength. Since  $W(t) = W(0)\exp(-2\pi\nu t/Q_L)$ , it is required that  $Q_L \ll \pi\nu\lambda_g/\nu = 1.6 \times 10^7$ , which is satisfied in our case ( $Q_L \sim 2 \times 10^6$ ). This is the main reason that the Pb/Sn coating method was preferred over using Niobium to make our cavity.

If another sample with a lower mass and higher AC Stark effect is chosen it is possible to decelerate molecules even at higher initial velocities. Extending the length of the cavity and using higher mode numbers ( $p$ ) in  $TE_{11p}$  can also help in decelerating molecules with higher initial velocities. However as the cavity length increases the plating and cooling of the cavity becomes more difficult. A cavity for  $TE_{11p=80}$  with the same design as mentioned above was made in our lab and coupled to a counter-rotating nozzle experiment. The counter-rotating nozzle can produce a molecular beam with a tunable final velocity. The experiment to focus and decelerate acetonitrile molecules from an initial velocity of about  $90 m/s$  by using a superconducting microwave cavity is still in progress at the moment in our lab by another member of our group. The current setup is suited for decelerating the pre-cooled molecules in HFS states. The DC Stark decelerator decelerates molecules in the LFS states in the presence of the DC electric fields. In a MW decelerator, a rotational state can be HFS or LFS depending on the detuning of the MW frequency ( $\nu$ ) from the transition frequency ( $\nu_{eg}$ ). Therefore it can be attached after our DC Stark decelerator, which only works for LFS states, for further deceleration of the molecules, and even trapping.

## Chapter 7: Conclusion

This thesis presented the first set of experiments successfully performed with the DC Stark decelerator that was constructed at UBC. With this decelerator the deceleration of ammonia molecules, previously performed by other groups, was reproduced to characterize the decelerator [45]. The ammonia molecules were decelerated via our Stark decelerator from  $445\text{ m/s}$  to  $27.9\text{ m/s}$ . Even further deceleration for ammonia molecules was possible, however for the purpose of characterization the presented result was sufficient. The numerical simulations were adjusted to reproduce the experimental results. Doing so, a reliable simulation was obtained. With the simulation it became possible to verify the improvement of the signal by optimizing the spacing of the detection ion optics after the decelerator, and also by removing the  $35\text{ cm}$  long hexapole from our original design. The new contribution in this part was improving the signal by bunching the molecules before the deceleration, and also by removing the hexapole from the setup.

After characterizing the setup by decelerating ammonia molecules, deceleration of SD radicals in  $J = 3/2$  from  $440\text{ m/s}$  to  $301\text{ m/s}$  was performed. This proved that our decelerator can work for any Stark decelerator compatible molecule, and confirmed the reliability of the simulations. Further deceleration of SD radicals was limited by the signal-to-noise ratio. The SD radicals were produced from the dissociation of  $D_2S$  molecules via glow discharge, and the molecular beam was characterized in a test chamber. The findings from the beam characterization, such as the transition frequencies and velocity distributions at different discharge voltages, were used for the deceleration simulations and experiments.

SD radicals in the next rotational level ( $J = 5/2$ ) were also decelerated from  $440\text{ m/s}$  down to  $415\text{ m/s}$ . Further deceleration of molecules in this state was not detectable due to the poor signal-to-noise ratio.

A deceleration scheme was presented to demonstrate the possibility of separating decelerated packets with different rotational numbers, and the state purity of the decelerated packets was investigated.

After successfully decelerating SD radicals, the first steps toward measuring the absolute density of the Stark decelerated molecular packets via CELIF detection were taken and are presented in

this thesis. All the experiments, simulations, and analysis related to the SD radical deceleration in this thesis are new contributions to the field.

In addition to the work done on the DC Stark decelerator, a superconducting microwave cavity was made and characterized. The work was done in collaboration with Dr. Katsunari Enomoto from the University of Toyama and Prof. Walter Hardy from UBC, with the purpose of improving the quality factor of the previously demonstrated molecular microwave decelerator [45]. The measured quality factor,  $Q$ , of the superconducting cavity was  $5 \times 10^5$ . The quality factor of the cavity used in Gerard Meijer's group ( $TE_{11,12}$  mode, with maximum electric field strength of  $1.4 \text{ kV/cm}$ ) was  $9.15 \times 10^3$ , and they could decelerate ammonia molecules from  $20 \text{ m/s}$  down to  $16.9 \text{ m/s}$ . Since the electric field strength inside the cavity is proportional to  $\sqrt{P_{MW} \times Q}$  (see equation (4-12)), the improved quality factor enhances the potential barrier by  $\sim 10$  times, which makes it possible to decelerate molecules with much higher initial velocities. One possibility is to use a longer cavity and decelerate molecules with more deceleration stages, and hence remove the previously required pre-deceleration step. The new contribution of this experiment to the field of cold molecules is improving the efficiency of the MW molecular decelerator by improving the quality factor of the MW cavity. The ability to make a cavity with the desired quality factor, in way that the MW rise and fall times are fast enough for deceleration purposes, is also an important result of this experiment.

## 7.1 Future work

At the moment we are working on improving our signal acquisition instrumentation for the CELIF measurements. We hope to have experimental results in the near future. Knowing the absolute density of the molecules will provide an accurate tool for collision, chemical reaction, and spectroscopy measurements.

We are also investigating the possibility of applying the CELIF detection method to ammonia molecules. Ammonia molecules are easily detectable with REMPI detection. We can try detecting ammonia molecules with their fluorescence light, and apply the CELIF method for their detection. A carefully power-controlled two-photon transition with a  $305 \text{ nm}$  laser can bring the ammonia molecules from their ground state  $X$  to their  $C'$  electronic excited state. This transition followed by relaxation to the  $A$  electronic state via fluorescence at  $565 \text{ nm}$  [130]. The

fluorescence light then can be used for detection. The first benefit of working with ammonia over the SD radical is its easier Stark deceleration. Second, the fluorescence wavelength of ammonia is at a different wavelength than its excitation wavelength. Therefore the scattered laser light and unwanted wavelengths can easily be filtered with an optical filter. There are two factors that might limit applying the CELIF method to ammonia. First, a two-photon transition probability is less than a one photon transition, which can affect the detection efficiency. Second, when using a cavity, the laser power inside the cavity is much less than outside (in the CELIF method we do not build up a standing wave inside the cavity). Since the two-photon transition depends on the laser power, this might also be a drawback for the experiment. So overall we can discuss the efficiency of using ammonia molecules for CELIF detection after we do the experiment.

In order to reach lower final velocities for decelerated SD radicals we plan to use Xenon as the carrier gas. Simulations show that if the initial velocity of the beam is  $321\text{ m/s}$ , by operating the decelerator at  $\varphi_0 = 70^\circ$  a final velocity of  $14\text{ m/s}$  can be achieved. This final velocity is suitable for trapping the molecules. In addition, other interesting experiments can be done with the decelerated packet, such as collision experiments or spectroscopic measurements.

The scheme presented in this thesis for obtaining separated decelerated SD radicals with different rotational numbers was the first attempt to prove its possibility. The decelerator's operational phases can vary depending on the initial velocity of the molecules, the desired final velocity of molecules, and the desired packet arrival time separation. Different combination of phases should be tried to optimize the desired result. In the experiment presented in this thesis the population of molecules in the rotational states higher than  $J = 3/2$  was low. Investigating methods to prepare more molecules in these states in the molecular beam can improve the detection limitations imposed by the signal to noise ratio. One way to do this would be to use Xenon as the carrier gas to reduce the mean velocity of the molecular beam, and then increase the discharge voltage.

As mentioned above, one way to improve the signal-to-noise ratio is to optimize the SD radical production. This can be done by optimizing the discharge. Also, other methods of producing SD radicals such as photo dissociation of  $D_2S$  by a  $193\text{ nm}$  laser pulse should be investigated [106]. Further reduction of stray light from the detected signal can also help. It is also possible to improve the fluorescence collecting optics by adding a spherical reflecting mirror to it. The

mirror should be placed beneath the detection point with its focal point at the detection point. The excited molecules emit in all directions; hence adding a mirror is equivalent to collecting light from a larger effective area. If CELIF measurement is not needed, one can try the REMPI detection of SD radicals to check if a better signal-to-noise ratio can be obtained.

In CELIF density measurements, in order to get an accurate calibration it is required to improve the accuracy of pressure readings when measuring the Rayleigh scattering of nitrogen at different pressures. The pressure sensors in use in our setup are not very accurate, and we expect the pressure readings not be very accurate. However, they are reliable for measuring the order of magnitude of the density of the decelerated packet. At the moment I am working on reading the pressure from the CRD ring-down signal. The ring-down time constants obtained at different pressures give the concentrations of the nitrogen molecules in the chamber, provided that all the experimental conditions are kept the same. This is experimentally challenging since the mirrors of the cavity can move when the chamber is pressurized. So it is important to fix the position of the mirrors.

A longer version of our prototype superconducting microwave cavity (50.7 *cm*) has already been made in our lab. The new version has been added to a counter-rotating nozzle setup. Experiments on decelerating acetonitrile and acetone molecules from an initial velocity of 100 *m/s* are in progress in our lab. It is also possible to combine the superconducting microwave decelerator with the Stark decelerator for further deceleration of species that have been pre-decelerated by the Stark decelerator.

The long term goal of combining DC Stark and superconducting MW decelerators is to bring the molecules to the trappable velocities, and then use a Febry-Prot superconducting MW cavity to trap the molecules and cool them by evaporative cooling in order to reach to the ultra-cold regime. There are advantages and disadvantages in this combination. Using the DC Stark decelerator as the pre-cooling method limits the deceleration to the LFS molecules only, because our DC Stark decelerator can only decelerate molecules in LFS states. This means that the molecules in the absolute ground state (HFS state) cannot be prepared with this method. However one can resonantly transfer the molecules from the LFS state to the ground state prior to trapping. The molecules in the absolute ground state are more stable in the trap due to the fact that they have elastic collisions. The other disadvantage of this combination is that only a small

portion of molecules are accepted in the phase-space acceptance of the DC Stark decelerator. Therefore not many molecules are introduced to the MW cavity after the decelerator. The higher the operational phase of the DC Stark decelerator is, the lower number of molecules will arrive to the MW cavity. However, using a superconducting MW cavity enables us to decelerate the molecules from higher initial velocities. This means that it is not required to operate the DC Stark decelerator at high phases. The superconducting MW cavity can produce three-dimensional deep potentials (K range), and can be used for further deceleration. Compared to the other available methods, using a resonant superconducting MW cavity provides much larger interaction volume and more accurate control on the electric field distribution. Therefore an open Fabry-Prot type MW trap with tunable trap depth can be utilized for evaporative cooling of the trapped molecules, while it provides access to the molecules in the trap. After trapping, many interesting experiments can be done such as cold collisions and precision spectroscopy. Improving the trap lifetime can help a lot in increasing the interaction time with molecules and hence getting a more accurate result.

## References

- [1] J. R. Ensher, “The first experiments with Bose-Einstein condensation of 87Rb,” University of Colorado, 1998.
- [2] S. Jochim, “Bose-Einstein Condensation of Molecules,” Leopold- Franzens- University, 2004.
- [3] J. Klaers, J. Schmitt, F. Vewinger, and M. Weitz, “Bose–Einstein condensation of photons in an optical microcavity,” *Nature*, vol. 468, no. 7323, pp. 545–548, Nov. 2010.
- [4] D. N. Sob’yanin, “Theory of Bose-Einstein condensation of light in a microcavity,” *Bull. Lebedev Phys. Inst.*, vol. 40, no. 4, pp. 91–96, Apr. 2013.
- [5] L. D. Carr, D. DeMille, R. V. Krems, and J. Ye, “Cold and ultracold molecules: science, technology and applications,” *New J. Phys.*, vol. 11, no. 5, p. 055049, May 2009.
- [6] H. L. Bethlem and G. Meijer, “Production and application of translationally cold molecules,” *Int. Rev. Phys. Chem.*, vol. 22, no. 1, pp. 73–128, Jan. 2003.
- [7] A. André, D. DeMille, J. M. Doyle, M. D. Lukin, S. E. Maxwell, P. Rabl, R. J. Schoelkopf, and P. Zoller, “A coherent all-electrical interface between polar molecules and mesoscopic superconducting resonators,” *Nat. Phys.*, vol. 2, no. 9, pp. 636–642, Sep. 2006.
- [8] D. DeMille, “Quantum Computation with Trapped Polar Molecules,” *Phys. Rev. Lett.*, vol. 88, no. 6, Jan. 2002.
- [9] J. L. Bohn, M. Cavagnero, and C. Ticknor, “Quasi-universal dipolar scattering in cold and ultracold gases,” *New J. Phys.*, vol. 11, no. 5, p. 055039, May 2009.
- [10] S. Jochim, M. Bartenstein, A. Altmeyer, G. Hendl, S. Riedl, C. Chin, J. H. Denschlag, and R. Grimm, “Bose-Einstein condensation of molecules,” *Science*, vol. 302, no. 5653, pp. 2101–2103, 2003.
- [11] T. Köhler, K. Góral, and P. Julienne, “Production of cold molecules via magnetically tunable Feshbach resonances,” *Rev. Mod. Phys.*, vol. 78, no. 4, pp. 1311–1361, Dec. 2006.
- [12] H. R. Thorsheim, J. Weiner, and P. S. Julienne, “Laser-induced photoassociation of ultracold sodium atoms,” *Phys. Rev. Lett.*, vol. 58, no. 23, p. 2420, 1987.
- [13] J. M. Doyle, B. Friedrich, J. Kim, and D. Patterson, “Buffer-gas loading of atoms and molecules into a magnetic trap,” *Phys. Rev. A*, vol. 52, no. 4, p. R2515, 1995.
- [14] H. L. Bethlem, G. Berden, and G. Meijer, “Decelerating neutral dipolar molecules,” *Phys. Rev. Lett.*, vol. 83, no. 8, p. 1558, 1999.
- [15] H. Tsuji, T. Sekiguchi, T. Mori, T. Momose, and H. Kanamori, “Stark velocity filter for nonlinear polar molecules,” *J. Phys. B At. Mol. Opt. Phys.*, vol. 43, no. 9, p. 095202, May 2010.
- [16] S. Hogan, C. Seiler, and F. Merkt, “Rydberg-State-Enabled Deceleration and Trapping of Cold Molecules,” *Phys. Rev. Lett.*, vol. 103, no. 12, Sep. 2009.
- [17] S. Zhou, “Zeeman deceleration of Methyl Radical,” University of British Columbia, 2014.
- [18] K. Enomoto and T. Momose, “Microwave Stark decelerator for polar molecules,” *Phys. Rev. A*, vol. 72, no. 6, Dec. 2005.
- [19] R. Fulton, A. I. Bishop, M. N. Schneider, and P. F. Barker, “Controlling the motion of cold molecules with deep periodic optical potentials,” *Nat. Phys.*, vol. 2, no. 7, pp. 465–468, Jul. 2006.

- [20] M. Tarbutt, H. Bethlem, J. Hudson, V. Ryabov, V. Ryzhov, B. Sauer, G. Meijer, and E. Hinds, “Slowing Heavy, Ground-State Molecules using an Alternating Gradient Decelerator,” *Phys. Rev. Lett.*, vol. 92, no. 17, Apr. 2004.
- [21] A. Osterwalder, S. A. Meek, G. Hammer, H. Haak, and G. Meijer, “Deceleration of neutral molecules in macroscopic traveling traps,” *Phys. Rev. A*, vol. 81, no. 5, May 2010.
- [22] J. Riedel, S. Hoekstra, W. Jäger, J. J. Gilijamse, S. Y. T. van de Meerakker, and G. Meijer, “Accumulation of Stark-decelerated NH molecules in a magnetic trap,” *Eur. Phys. J. D*, vol. 65, no. 1–2, pp. 161–166, Nov. 2011.
- [23] J. F. Barry and D. Demille, “A chilling effect for molecules,” *Nature*, vol. 491, pp. 539–540, Nov. 2012.
- [24] S. Chervenkov, X. Wu, J. Bayerl, A. Rohlfes, T. Gantner, M. Zeppenfeld, and G. Rempe, “Continuous Centrifuge Decelerator for Polar Molecules,” *Phys. Rev. Lett.*, vol. 112, no. 1, Jan. 2014.
- [25] J. D. Weinstein, R. deCarvalho, T. Guillet, B. Friedrich, and J. M. Doyle, “Magnetic trapping of calcium monohydride molecules at millikelvin temperatures,” *Nature*, vol. 395, pp. 148–150, Aug. 1998.
- [26] N. R. Hutzler, H.-I. Lu, and J. M. Doyle, “The Buffer Gas Beam: An Intense, Cold, and Slow Source for Atoms and Molecules,” *Chem. Rev.*, vol. 112, no. 9, pp. 4803–4827, Sep. 2012.
- [27] M. Gupta and D. Herschbach, “A Mechanical Means to Produce Intense Beams of Slow Molecules,” *J. Phys. Chem. A*, vol. 103, no. 50, pp. 10670–10673, Dec. 1999.
- [28] M. Strebel, F. Stienkemeier, and M. Mudrich, “Improved setup for producing slow beams of cold molecules using a rotating nozzle,” *Phys. Rev. A*, vol. 81, no. 3, Mar. 2010.
- [29] S. Spieler, W. Zhong, P. Djuricanin, O. Nourbakhsh, I. Gerhardt, K. Enomoto, F. Stienkemeier, and T. Momose, “Microwave lens effect for the  $J = 0$  rotational state of  $\text{CH}_3\text{CN}$ ,” *Mol. Phys.*, vol. 111, no. 12–13, pp. 1823–1834, Jul. 2013.
- [30] W. Zhong, “Manipulation of the motion of polyatomic molecules in the rotational ground state: microwave lens effect by AC Stark dipole force,” 2013.
- [31] R. V. Krems, W. C. Stwalley, and B. Friedrich, Eds., *Cold molecules: theory, experiment, applications*. Boca Raton: CRC Press, 2009.
- [32] M. Schnell and G. Meijer, “Cold Molecules: Preparation, Applications, and Challenges,” *Angew. Chem. Int. Ed.*, vol. 48, no. 33, pp. 6010–6031, Aug. 2009.
- [33] B. K. Stuhl, “Ultracold molecules for the masses: evaporative cooling and magneto-optical trapping,” University of Colorado, 2012.
- [34] S. Hogan, D. Sprecher, M. Andrist, N. Vanhaecke, and F. Merkt, “Zeeman deceleration of H and D,” *Phys. Rev. A*, vol. 76, no. 2, Aug. 2007.
- [35] E. Narevicius, C. G. Parthey, A. Libson, J. Narevicius, I. Chavez, U. Even, and M. G. Raizen, “An atomic coilgun: using pulsed magnetic fields to slow a supersonic beam,” *New J. Phys.*, vol. 9, no. 10, pp. 358–358, Oct. 2007.
- [36] L. P. Parazzoli, N. Fitch, D. S. Lobser, and H. J. Lewandowski, “High-energy-resolution molecular beams for cold collision studies,” *New J. Phys.*, vol. 11, no. 5, p. 055031, May 2009.
- [37] J. Gilijamse, J. Küpper, S. Hoekstra, N. Vanhaecke, S. van de Meerakker, and G. Meijer, “Optimizing the Stark-decelerator beamline for the trapping of cold molecules using evolutionary strategies,” *Phys. Rev. A*, vol. 73, no. 6, Jun. 2006.

- [38] L. Scharfenberg, H. Haak, G. Meijer, and S. van de Meerakker, "Operation of a Stark decelerator with optimum acceptance," *Phys. Rev. A*, vol. 79, no. 2, Feb. 2009.
- [39] S. Y. T. van de Meerakker, "Deceleration and electrostatic trapping of OH radicals," s.n.], S.I., 2006.
- [40] H. L. Bethlem, M. R. Tarbutt, J. Küpper, D. Carty, K. Wohlfart, E. A. Hinds, and G. Meijer, "Alternating gradient focusing and deceleration of polar molecules," *J. Phys. B At. Mol. Opt. Phys.*, vol. 39, no. 16, pp. R263–R291, Aug. 2006.
- [41] S. A. Meek, M. F. Parsons, G. Heyne, V. Platschkowski, H. Haak, G. Meijer, and A. Osterwalder, "A traveling wave decelerator for neutral polar molecules," *Rev. Sci. Instrum.*, vol. 82, no. 9, p. 093108, 2011.
- [42] K. Wohlfart, F. Filsinger, F. Grätz, J. Küpper, and G. Meijer, "Stark deceleration of OH radicals in low-field-seeking and high-field-seeking quantum states," *Phys. Rev. A*, vol. 78, no. 3, Sep. 2008.
- [43] S. Hoekstra, J. Gilijamse, B. Sartakov, N. Vanhaecke, L. Scharfenberg, S. van de Meerakker, and G. Meijer, "Optical Pumping of Trapped Neutral Molecules by Blackbody Radiation," *Phys. Rev. Lett.*, vol. 98, no. 13, Mar. 2007.
- [44] S. Y. T. van de Meerakker, I. Labazan, S. Hoekstra, J. Kupper, and G. Meijer, "Production and deceleration of a pulsed beam of metastable NH ( $a1\Delta$ ) radicals," *OURNAL P HYSICS B TOMIC M OLECULAR O PTICAL P HYSIC*, vol. 39, pp. 1077–1084, 2006.
- [45] S. Merz, N. Vanhaecke, W. Jäger, M. Schnell, and G. Meijer, "Decelerating molecules with microwave fields," *Phys. Rev. A*, vol. 85, no. 6, Jun. 2012.
- [46] P. Jansen, M. Quintero-Pérez, T. E. Wall, J. E. van den Berg, S. Hoekstra, and H. L. Bethlem, "Deceleration and trapping of ammonia molecules in a traveling-wave decelerator," *Phys. Rev. A*, vol. 88, no. 4, Oct. 2013.
- [47] H. L. Bethlem, M. Kajita, B. Sartakov, G. Meijer, and W. Ubachs, "Prospects for precision measurements on ammonia molecules in a fountain," *Eur. Phys. J. Spec. Top.*, vol. 163, no. 1, pp. 55–69, Oct. 2008.
- [48] H. L. Bethlem, G. Berden, F. M. H. Crompvoets, R. T. Jongma, A. J. A. van Roij, and G. Meijer, "Electrostatic trapping of ammonia molecules," *Nature*, vol. 406, pp. 491–494, Aug. 2000.
- [49] H. Bethlem, F. Crompvoets, R. Jongma, S. van de Meerakker, and G. Meijer, "Deceleration and trapping of ammonia using time-varying electric fields," *Phys. Rev. A*, vol. 65, no. 5, May 2002.
- [50] X. Wang, M. Kirste, G. Meijer, and S. Y. T. van de Meerakker, "Stark Deceleration of NO Radicals," *Z. Für Phys. Chem.*, p. 130617035227002, Jun. 2013.
- [51] E. Hudson, C. Ticknor, B. Sawyer, C. Taatjes, H. Lewandowski, J. Bochinski, J. Bohn, and J. Ye, "Production of cold formaldehyde molecules for study and control of chemical reaction dynamics with hydroxyl radicals," *Phys. Rev. A*, vol. 73, no. 6, Jun. 2006.
- [52] S. K. Tokunaga, J. M. Dyne, E. A. Hinds, and M. R. Tarbutt, "Stark deceleration of lithium hydride molecules," *New J. Phys.*, vol. 11, no. 5, p. 055038, May 2009.
- [53] T. E. Wall, J. F. Kanem, J. M. Dyne, J. J. Hudson, B. E. Sauer, E. A. Hinds, and M. R. Tarbutt, "Stark deceleration of CaF molecules in strong- and weak-field seeking states," *Phys. Chem. Chem. Phys.*, vol. 13, no. 42, p. 18991, 2011.
- [54] M. Tarbutt, H. Bethlem, J. Hudson, V. Ryabov, V. Ryzhov, B. Sauer, G. Meijer, and E. Hinds, "Slowing Heavy, Ground-State Molecules using an Alternating Gradient Decelerator," *Phys. Rev. Lett.*, vol. 92, no. 17, Apr. 2004.

- [55] N. E. Bulleid, R. J. Hendricks, E. A. Hinds, S. A. Meek, G. Meijer, A. Osterwalder, and M. R. Tarbutt, "Traveling-wave deceleration of heavy polar molecules in low-field-seeking states," *Phys. Rev. A*, vol. 86, no. 2, Aug. 2012.
- [56] J. E. van den Berg, S. C. Mathavan, C. Meinema, J. Nauta, T. H. Nijbroek, K. Jungmann, H. L. Bethlem, and S. Hoekstra, "Traveling-wave deceleration of SrF molecules," *J. Mol. Spectrosc.*, vol. 300, pp. 22–25, Jun. 2014.
- [57] O. Bucicov, M. Nowak, S. Jung, G. Meijer, E. Tiemann, and C. Lisdat, "Cold SO<sub>2</sub> molecules by Stark deceleration," *Eur. Phys. J. D*, vol. 46, no. 3, pp. 463–469, Mar. 2008.
- [58] K. Wohlfart, F. Grätz, F. Filsinger, H. Haak, G. Meijer, and J. Küpper, "Alternating-gradient focusing and deceleration of large molecules," *Phys. Rev. A*, vol. 77, no. 3, Mar. 2008.
- [59] E. Narevicius, A. Libson, C. Parthey, I. Chavez, J. Narevicius, U. Even, and M. Raizen, "Stopping supersonic oxygen with a series of pulsed electromagnetic coils: A molecular coilgun," *Phys. Rev. A*, vol. 77, no. 5, May 2008.
- [60] T. Momose, Y. Liu, S. Zhou, P. Djuricanin, and D. Carty, "Manipulation of translational motion of methyl radicals by pulsed magnetic fields," *Phys Chem Chem Phys*, vol. 15, no. 6, pp. 1772–1777, 2013.
- [61] M. Motsch, P. Jansen, J. A. Agner, H. Schmutz, and F. Merkt, "Slow and velocity-tunable beams of metastable  $^4\text{He}$  by multistage Zeeman deceleration," *Phys. Rev. A*, vol. 89, no. 4, Apr. 2014.
- [62] S. D. Hogan, "Cold atoms and molecules by Zeeman deceleration and Rydberg-Stark deceleration," Habilitationsschrift ETH Zürich, 2012, 2012.
- [63] F. B. Dunning and R. G. Huet, *Atomic, Molecular, and optical Physics: Atoms and Molecules*, vol. 9B. Academic press, 1996.
- [64] G. Scoles, *Atomic and Molecular Beam Methods*, vol. 1. Oxford University Press.
- [65] G. W. Thomson, "The Antoine equation for vapor-pressure data," *Chem. Rev.*, vol. 38, no. 1, pp. 1–39, 1946.
- [66] G. Brusdeylins, H. D. Meyer, and I. R. Campargue, *Rarefied gas dynamics, Proceedings of the 11th International Symposium*, vol. 2. Commissariat à l'Energie Atomique, Paris, France, 1979.
- [67] W. Christen and K. Rademann, "Cooling and slowing in high-pressure jet expansions," *Phys. Rev. A*, vol. 77, no. 1, Jan. 2008.
- [68] M. H. Havenith, *Infrared Spectroscopy of Molecular Clusters: An Introduction to Intermolecular Forces (Springer Tracts in Modern Physics)*, vol. 176. Springer, 2002.
- [69] O. F. Hagen, "Cluster Formation in Expanding Supersonic Jets: Effect of Pressure, Temperature, Nozzle Size, and Test Gas," *J. Chem. Phys.*, vol. 56, no. 5, p. 1793, 1972.
- [70] B. Sawyer, "Cold polar molecules for novel collision experiments at low energies," 2010.
- [71] W. L. Meerts and A. Dymanus, "A Molecular Beam Electric Resonance Study of the Hyperfine A Doubling spectrum of OH OD SH and SD," *Can J Phys*, vol. 53, p. 2123, 1975.
- [72] T. D. Hain and T. J. Curtiss, "Controlling the Orientation of Hexapole-Selected Hydroxyl (OH) Radicals," *J. Phys. Chem. A*, vol. 102, no. 48, pp. 9696–9701, Nov. 1998.
- [73] M. Kirste, "OH-NO scattering at the quantum level," Freie Universität Berlin, 2012.

- [74] B. K. Stuhl, M. T. Hummon, M. Yeo, G. Quéméner, J. L. Bohn, and J. Ye, “Evaporative cooling of the dipolar hydroxyl radical,” *Nature*, vol. 492, no. 7429, pp. 396–400, Dec. 2012.
- [75] J. Senekowitsch, H.-J. Werner, P. Rosmus, E.-A. Reinsch, and S. V. O’Neil, “Ab initio calculations of radiative transition probabilities in SH, SH<sup>+</sup>, and SH<sup>-</sup>,” *J. Chem. Phys.*, vol. 83, no. 9, p. 4661, 1985.
- [76] I. Yamamura, K. Kawaguchi, and S. T. Ridgway, “Identification of SH  $\Delta v = 1$  Rovibrational Lines in R Andromedae,” *Astrophys. J. Lett.*, vol. 528, no. 1, p. L33, 2000.
- [77] R. P. Wayne, *Chemistry of Atmospheres*, Third. Oxford University Press, 2000.
- [78] W. W. Dular, T. J. Millar, and D. A. Williams, *MNRAS*, vol. 192, p. 945, 1980.
- [79] J. B. Milan, W. J. Buma, and C. A. de Lange, “Two-photon resonance enhanced multiphoton ionization photoelectron spectroscopy of the SH (SD) radical below and above the lowest ionization threshold,” *J. Chem. Phys.*, vol. 105, no. 16, p. 6688, 1996.
- [80] S. C. Herndon and A. R. Ravishankara, “Kinetics of the Reaction of SH and SD with NO<sub>2</sub>,” *J. Phys. Chem. A*, vol. 110, no. 1, pp. 106–113, Jan. 2006.
- [81] M. Mozurkewich and S. W. Benson, “Negative activation energies and curved Arrhenius plots. 1. Theory of reactions over potential wells,” *J. Phys. Chem.*, vol. 88, no. 25, pp. 6429–6435, 1984.
- [82] Y.-P. Chang, F. Filsinger, B. G. Sartakov, and J. Küpper, “CMIstark: Python package for the Stark-effect calculation and symmetry classification of linear, symmetric and asymmetric top wavefunctions in dc electric fields,” *Comput. Phys. Commun.*, vol. 185, no. 1, pp. 339–349, Jan. 2014.
- [83] Q. Wei, S. Kais, B. Friedrich, and D. Herschbach, “Entanglement of polar symmetric top molecules as candidate qubits,” *J. Chem. Phys.*, vol. 135, no. 15, p. 154102, 2011.
- [84] J. V. Hajnal and G. I. Opat, “Stark effect for a rigid symmetric top molecule: exact solution,” *J. Phys. B At. Mol. Opt. Phys.*, vol. 24, no. 12, p. 2799, 1991.
- [85] P. Jansen, “Polyatomic molecules for probing a possible variation of the proton-to-electron mass ratio,” 2013.
- [86] J. Schleipen, “State-To-State cross sections for rotational excitation of NH<sub>3</sub> and OH by collisions with He, Ar, and H<sub>2</sub>,” Radboud University Nijmegen, 1964.
- [87] M. N. R. Ashfold, R. Dixon, R. J. Stickland, and C. M. Western, *Chem Phys Lett*, vol. 138, p. 201, 1987.
- [88] G. Herzberg, *Molecular spectra and molecular structure, II. Infrared and Raman spectra of polyatomic molecules*, 7th ed. D. Van Nostrand company, INC, 1945.
- [89] P. Bunker, *Molecular Symmetry and Spectroscopy*. Academic press, INC., 1979.
- [90] H. Tsuji, Y. Okuda, T. Sekiguchi, and H. Kanamori, “Velocity distribution of the pulsed ND<sub>3</sub> molecular beam selected by a quadrupole Stark velocity filter,” *Chem. Phys. Lett.*, vol. 436, no. 4–6, pp. 331–334, Mar. 2007.
- [91] S. Höjer, H. Ahlberg, and A. Rosén, “Infrared laser Stark shift spectroscopy in ammonia,” *Appl. Phys. B*, vol. 52, no. 3, pp. 200–210, 1991.
- [92] R. Zare, *Angular Momentum; Understanding spatial aspects in Chemistry and Physics*. Wiley-Interscience, 1988.
- [93] E. J. Durig and J. K. Watson, *Aspects of Quartic and sextic centrifugal effects on rotational levels in “Vibrational spectra and structure,”* vol. 6. Elsevier, Amsterdam, 1977.
- [94] J. M. Brown and A. Carrington, *Rotational spectroscopy of diatomic molecules*. Cambridge; New York: Cambridge University Press, 2003.

- [95] R. A. Frosch and H. M. Foley, “Magnetic hyperfine structure in diatomic molecules,” *Phys. Rev.*, vol. 88, no. 6, p. 1337, 1952.
- [96] X. Zheng, J. Wu, Y. Song, and J. Zhang, “Ultraviolet photodissociation of the SD radical in vibrationally ground and excited states,” *Phys. Chem. Chem. Phys.*, vol. 11, no. 23, p. 4699, 2009.
- [97] E. Klisch, T. Klaus, S. P. Belov, A. Dolgner, R. Schieder, and G. Winnewisser, “The rotational spectrum of SH and SD,” *Astrophys. J.*, vol. 437, pp. 1118–1124, 1996.
- [98] P. Andresen and E. W. Rothe, “Analysis of chemical dynamics via  $\Lambda$  doubling: Directed lobes in product molecules and transition states,” *J. Chem. Phys.*, vol. 82, p. 3634, 1985.
- [99] K. F. Freed, “Theory of the Hyperfine Structure of Molecules: Application to  $3\Pi$  States of Diatomic Molecules Intermediate between Hund’s Cases (a) and (b),” *J. Chem. Phys.*, vol. 45, p. 4214, 1966.
- [100] D. A. Ramsay, “Absorption Spectra of SH and SD Produced by Flash Photolysis of H<sub>2</sub>S and D<sub>2</sub>S,” *J. Chem. Phys.*, vol. 20, no. 12, p. 1920, 1952.
- [101] D. DeMille, D. R. Glenn, and J. Petricka, “Microwave traps for cold polar molecules,” *Eur. Phys. J. D*, vol. 31, no. 2, pp. 375–384, Nov. 2004.
- [102] L. M. C. Janssen, M. P. J. van der Loo, G. C. Groenenboom, S.-M. Wu, D. Č. Radenović, A. J. A. van Roij, I. A. Garcia, and D. H. Parker, “Photodissociation of vibrationally excited SH and SD radicals at 288 and 291 nm: The S(<sup>1</sup>D<sub>2</sub>) channel,” *J. Chem. Phys.*, vol. 126, no. 9, p. 094304, 2007.
- [103] G. H. Dieke and H. M. Crosswhite, “The ultraviolet bands of OH Fundamental data,” *J. Quant. Spectrosc. Radiat. Transf.*, vol. 2, no. 2, pp. 97–199, Apr. 1962.
- [104] J. B. Milan, W. J. Buma, C. A. de Lange, C. M. Western, and M. N. R. Ashfold, “Two-photon resonance enhanced MPI-PES above the lowest ionization threshold. Observation of the [a mA]5p<sup>rr</sup> state of the SH (SD) radical,” *Chem. Phys. Lett.*, vol. 239, pp. 326–331, 1995.
- [105] S. E. Sanders, O. R. Willis, N. H. Nahler, and E. Wrede, “Absolute absorption and fluorescence measurements over a dynamic range of  $10^6$  with cavity-enhanced laser-induced fluorescence,” *ArXiv Prepr. ArXiv13081989*, 2013.
- [106] A. Mizouri, L. Z. Deng, J. S. Eardley, N. H. Nahler, E. Wrede, and D. Carty, “Absolute density measurement of SD radicals in a supersonic jet at the quantum-noise-limit,” *Phys. Chem. Chem. Phys.*, vol. 15, no. 45, p. 19575, 2013.
- [107] M. N. R. Ashfold, S. R. Langford, R. A. Morgan, A. J. Orr-Ewing, C. M. Western, C. R. Scheper, and C. A. De Lange, “Resonance enhanced multiphoton ionization (REMPI) and REMPI-photoelectron spectroscopy of ammonia,” *Eur. Phys. J. -At. Mol. Opt. Plasma Phys.*, vol. 4, no. 2, pp. 189–197, 1998.
- [108] H. L. Bethlem, G. Berden, A. J. Van Roij, F. M. Cromptvoets, and G. Meijer, “Trapping neutral molecules in a traveling potential well,” *Phys. Rev. Lett.*, vol. 84, no. 25, p. 5744, 2000.
- [109] T. E. Wall, S. K. Tokunaga, E. A. Hinds, and M. R. Tarbutt, “Nonadiabatic transitions in a Stark decelerator,” *Phys. Rev. A*, vol. 81, no. 3, Mar. 2010.
- [110] H. Odashima, S. Merz, K. Enomoto, M. Schnell, and G. Meijer, “Microwave Lens for Polar Molecules,” *Phys. Rev. Lett.*, vol. 104, no. 25, Jun. 2010.
- [111] K. Enomoto, P. Djuricanin, I. Gerhardt, O. Nourbakhsh, Y. Moriwaki, W. Hardy, and T. Momose, “Superconducting microwave cavity towards controlling the motion of polar molecules,” *Appl. Phys. B*, vol. 109, no. 1, pp. 149–157, Oct. 2012.

- [112] C. G. Montgomery, *Technique of Microwave Measurements*. McGraw-Hill, New York, 1947.
- [113] D. M. Pozar, *Microwave Engineering*. Wiley, Hoboken, 2005.
- [114] S. Merz, C. Brieger, N. Vanhaecke, G. Meijer, and M. Schnell, "Manipulating the motion of polar molecules with microwave radiation," *Mol. Phys.*, vol. 111, no. 12–13, pp. 1855–1864, Jul. 2013.
- [115] P. Schmuser, "Superconductivity in high energy particle accelerators," vol. 49, no. 1, p. 155, 2002.
- [116] J. Bardeen, L. N. Cooper, and J. R. Schrieffer, "Theory of superconductivity," *Phys. Rev.*, vol. 108, no. 5, p. 1175, 1957.
- [117] N. A. McDonald, *IEEE Trans Microw. Theory Tech*, vol. 20, p. 689, 1972.
- [118] R. V. Latham, *High Voltage Vacuum Insulation: Basic Concepts and Technological Practice*, 1st ed. Academic press, 1995.
- [119] K. Luria, W. Christen, and U. Even, "Generation and Propagation of Intense Supersonic Beams," *J. Phys. Chem. A*, vol. 115, no. 25, pp. 7362–7367, Jun. 2011.
- [120] R. W. Anderson, "Tracks of symmetric top molecules in hexapole electric fields," *J. Phys. Chem. A*, vol. 101, no. 41, pp. 7664–7673, 1997.
- [121] S. J. Greaves, E. L. Flynn, E. L. Futcher, E. Wrede, D. P. Lydon, P. J. Low, S. R. Rutter, and A. Beeby, "Cavity Ring-Down Spectroscopy of the Torsional Motions of 1,4-Bis(phenylethynyl)benzene," *J. Phys. Chem. A*, vol. 110, no. 6, pp. 2114–2121, Feb. 2006.
- [122] W. C. Wiley and I. H. McLaren, "time of flight mass spectrometer with improved resolution.pdf," *Rev. Sci. Instrum.*, vol. 26, p. 1150.
- [123] S. T. Pratt, "Photoionization dynamics of the B1E" state of ammonia," *J. Chem. Phys.*, vol. 117, no. 3, 2002.
- [124] F. Crompvoets, R. Jongma, H. Bethlem, A. van Roij, and G. Meijer, "Longitudinal Focusing and Cooling of a Molecular Beam," *Phys. Rev. Lett.*, vol. 89, no. 9, Aug. 2002.
- [125] R. R. Friedl, W. H. Brune, and J. G. Anderson, "Radiative and predissociative lifetimes of the  $V'=0$  level of the  $A\ 2\Sigma^+$  state of SH and SD from chemical and spectroscopic studies," *J. Chem. Phys.*, vol. 79, p. 4227, 1983.
- [126] M. Kawasaki, H. Sato, G. Inoue, and M. Suzuki, "Fluorescence lifetimes of  $SD(A\ 2\Sigma^+, v'=0, N')$  radicals and rotational distribution of  $SD(X\ 2\Pi_{3/2}, v'=0, J')$  photofragments generated in photodissociation of  $D_2S$  and  $C_2H_5SD$  at 193 nm," *J. Chem. Phys.*, vol. 91, no. 11, p. 6758, 1989.
- [127] J. Senekowitsch, H.-J. Werner, P. Rosmus, E.-A. Reinsch, and S. V. O'Neil, "Ab initio calculations of radiative transition probabilities in SH, SH<sup>+</sup>, and SH<sup>-</sup>," *J. Chem. Phys.*, vol. 83, no. 9, p. 4661, 1985.
- [128] N. J. Fitch, D. A. Esteves, M. I. Fabrikant, T. C. Briles, Y. Shyur, L. P. Parazzoli, and H. J. Lewandowski, "State purity of decelerated molecular beams," *J. Mol. Spectrosc.*, vol. 278, pp. 1–6, Aug. 2012.
- [129] W. H. Warren, "Superconductivity Measurements in Solders Commonly Used for Low Temperature Research," *Rev. Sci. Instrum.*, vol. 40, no. 1, p. 180, 1969.
- [130] C. Brackmann, O. Hole, B. Zhou, Z. S. Li, and M. Aldén, "Characterization of ammonia two-photon laser-induced fluorescence for gas-phase diagnostics," *Appl. Phys. B*, vol. 115, no. 1, pp. 25–33, Apr. 2014.
- [131] E. R. Hudson, "Experiments on cold molecules produced via Stark deceleration," 2006.

- [132] J. Liu, H.-T. Kim, and S. L. Anderson, "Multiphoton ionization and photoelectron spectroscopy of formaldehyde via its 3p Rydberg states," *J. Chem. Phys.*, vol. 114, no. 22, p. 9797, 2001.

## Appendices

### Appendix 1: REMPI detection for formaldehyde

Stark deceleration of formaldehyde molecule has been studied before; therefore there is nothing new about its deceleration. However since it is being known as a good candidate for Stark deceleration experiments it is possible to use it for the future experiments in our lab, such as trapping them for spectroscopic studies. To my knowledge the Stark deceleration experiments on formaldehyde have used the LIF detection method in which  $\sim 353\text{ nm}$  photons were used to excite the molecules from  $|1_1 1\rangle$  ground state to the  $\tilde{A}^1A_2$  electronically excited state. About 60 % of the excited molecules then emit distributed fluorescence from  $350\text{ nm}$  to  $610\text{ nm}$ , which can be collected and filtered optically and then be sent to the PMT [131].

With the current setup Stark decelerator setup we have it seems that working with REMPI detection is less problematic, provided that a good REMPI scheme is available to monitor the sample molecules in the desired state.

The neutral ground state of formaldehyde is  $\tilde{X}^1A_1$ . A good REMPI detection scheme that can be used for formaldehyde detection is two-photon resonant (2+1) in the region of the  $^1A_2(3p_x)$ ,  $^1A_1(3p_y)$ , and  $^1B_2(3p_z)$  states of formaldehyde. The corresponding wavelength for the two-photon transition is between  $272\text{ nm} - 312\text{ nm}$ , among which the  $0_0^0$  transitions at  $\sim 295\text{ nm}$  can be used for monitoring the molecules in the desired state [132].

## Appendix 2: Pb/Sn coating procedure

The technique of electroplating presented here is the one used for our prototype microwave cavity. Professor Walter Hardy and his colleagues in his lab at UBC shared their valuable knowledge in this procedure with us. Here I briefly present the steps taken for electroplating our cavity.

Electroplating was done in a solution bath. The steps to set up the bath and to plate the cavity were as follows:

- 1- Make the glue solution. The glue used in our experiment was made from horse nail, and was responsible for providing binding between metal and solutions. 1 *gr* of the glue was first dissolved in distilled water and then filtered. We needed 10 *mL* of the solution.
- 2- Dilute 40 *mL* of  $Pb(BF_4)_2$  with 200 *mL* distilled water, and add to the 10 *mL* glue solution.
- 3- Add some boric acid crystals to the solution.
- 4- Clean the electrodes and metals and all the surfaces with chemicals. For stainless steel we first used trichloroethylene, then rinsed it in ethanol, then rinsed in distilled water, then put the part in dilute sulfuric acid, then rinsed it in distilled water, then put it on NaOH (12.5 %) solution soak, then rinsed it with distilled water. For Sn electrode all the above procedure was done except the sulfuric acid part. Also the stainless steel and Sn electrodes were dipped into 12 % fluoboric acid right before plating. Cu surfaces were cleaned by etching.
- 5- Plate at 30  $mA/cm^2$  for half an hour. Be sure to carefully plate the corners as well.
- 6- Rinse with distilled water.
- 7- Rinse with acetone.
- 8- Blow to dry.

Figure below shows the electroplating for a typical cavity.

Our DC Stark decelerator setup is also shown in the next page.

